# Experimental and simulation studies of mesoscale phenomena in gas-solid fluidized beds by PTV and CFD-DEM

**Dissertation**
zur Erlangung des akademischen Grades

**Doktoringenieur**
**(Dr.-Ing.)**

von M.Sc. Zhaochen Jiang
geb. am 28.11.1987 in Zhenjiang, China

genehmigt durch die Fakultät für Verfahrens- und Systemtechnik
der Otto-von-Guericke-Universität Magdeburg

Promotionskommission:     Prof. Dr. lr. Berend van Wachem (Vorsitz)

Prof. Dr.-Ing. habil. Evangelos Tsotsas (Gutachter)

Prof. Dr.-Ing. Andreas Bück (Gutachter)

Prof. Dr.-Ing. habil. Dominique Thévenin (Gutachter)

eingereicht am 08.04.2020

Promotionskolloquium am 25.08.2020

# Abstract

Particle formation processes in spray fluidized beds are widely applied in chemical industries to produce particulate materials with designed properties. These processes are very complex by the presence of multi-phase transport phenomena at multiscales, and by the coupling of an array of sub-processes (spraying, wetting, drying and solidifying). The understanding of mesoscale phenomena between the individual particle scale and the process unit is critical to achieving efficient operation and improved particle product quality.

In this thesis, the experimental technique of particle tracking velocimetry (PTV) and the numerical approach that combines computational fluid dynamics with the discrete element method (CFD-DEM) are used to investigate mesoscale particle dynamics related to particle formation processes in gas-solid fluidized beds.

Motion of non-spherical particles is conveniently studied by DEM. The rebound behavior of irregularly shaped particles is predicted by DEM simulations using the multi-sphere and superquadric models, in terms of the distributions of total and normal coefficients of restitution and corresponding relationships with the rotation speed after collision and the absolute difference of incidence angle and rebound angle. Compared with PTV measurements, the multi-sphere model well predicts the macroscopic particle-wall collision behavior of irregular non-convex particles.

In pseudo-2D fluidized beds, PTV is used to measure dynamics of mono-disperse and poly-disperse particles by means of new methods for particle segmentation and particle tracking. Using synthetic images generated from CFD-DEM simulation, the entire PTV methodology can be comprehensively verified with respect to segmentation bias, segmentation ratio, recovery ratio and error ratio. The collision event is determined by the variation of measured trajectories of individual particles. Compared to the theoretical collision model in the kinetic theory of granular flow, the experimental collision frequency tends to be relatively constant or even decrease after exceeding a critical solid volume fraction. The average collision velocity correlates linearly with the average square root of particle granular temperature. The mixing degree of differently sized particles is measured by color-PTV. Additionally, CFD-DEM simulations are performed according to the PTV measurements in pseudo-2D fluidized beds. The simulation results are in agreement with measurements in terms of volumetric flux of particles, granular temperature, particle collision velocity and mixing degree. The correction

for the size dispersity effect in the drag model is essential to improve the accuracy of CFD-DEM simulations of poly-disperse particle systems.

CFD-DEM simulations are applied to investigate the particle circulation and residence times in different zones in a Wurster fluidized bed. Simulated ideal cycle times and residence times are in good agreement to the available positron emission particle tracking measurement data. Moreover, a coupled CFD-DEM and Monte Carlo approach is developed to investigate inter- and intra-particle coating uniformity in the Wurster fluidized bed. On the basis of the spherical centroidal Voronoi tessellation, the Monte Carlo approach can model the deposition and splashing of spray droplets on the surface of individual particles. The intra-particle layer thickness distributions predicted by the simulation are in good agreement with X-ray micro-computed tomography measurements.

# Zusammenfassung

Partikelbildungsprozesse in Sprühwirbelbetten werden in der chemischen Industrie häufig angewendet, um partikuläre Materialien mit definierten Eigenschaften herzustellen. Diese Prozesse sind sehr komplex durch das Vorhandensein von Mehrphasentransportvorgängen auf mehreren Skalen und die Kopplung einer Reihe von Teilprozessen (Sprühen, Benetzen, Trocknen und Erstarren). Das Verständnis mesoskaliger Phänomene zwischen der Einzelpartikelebene und der Prozesseinheit ist entscheidend für einen effizienten Betrieb und eine verbesserte Produktqualität.

In diese Arbeit werden die „Partikel-Tracking-Velocimetry" (PTV) und ein gekoppelter Ansatz von Methoden der numerischen Strömungsmechanik und der diskreten Elementmethode (CFD-DEM) verwendet, um die mesoskalige Partikeldynamik bei Partikelbildungsprozessen in Gas-Feststoff-Wirbelschichten zu untersuchen.

Das Rückprallverhalten unregelmäßig geformter Partikel wird durch DEM-Simulationen unter Verwendung der Multi-Sphere- und Superquadric-Modelle vorhergesagt. Das untersuchte Verhalten umfasst die Verteilung der Gesamt- und Normalwerte des Restitutionskoeffizienten sowie die entsprechenden Beziehungen zur Rotationsgeschwindigkeit nach der Kollision und zur absoluten Differenz von Einfallswinkel und Rückprallwinkel. Im Vergleich zu PTV-Messungen sagt das Mehrkugelmodell das makroskopische Kollisionsverhalten von Partikelwänden unregelmäßiger, nichtkonvexer Partikel gut voraus.

In Pseudo-2D-Wirbelschichten wird PTV eingesetzt, um die Dynamik von monodispersen und polydispersen Partikeln mithilfe neuer Methoden zur Partikelsegmentierung und Partikelverfolgung zu erfassen. Unter Verwendung synthetischer Bilder, die in CFD-DEM-Simulationen erzeugt wurden, kann die gesamte PTV-Methodik hinsichtlich Segmentierungsverzerrung, Segmentierungsverhältnis, Wiederherstellungsverhältnis und Fehlerverhältnis umfassend verifiziert werden. Das Kollisionsereignis wird durch die Variation der gemessenen Trajektorien individueller Partikeln bestimmt. Im Vergleich zum theoretischen Kollisionsmodell in der kinetischen Theorie des granularer Materialien (KTGF) ist die experimentelle Kollisionsfrequenz nach Überschreiten eines kritischen Feststoffvolumenanteils relativ konstant oder nimmt sogar ab. Die mittlere Kollisionsgeschwindigkeit korreliert linear mit der mittleren Quadratwurzel der granularen Partikeltemperatur. Der Mischungsgrad von Partikeln unterschiedlicher Größe wird durch Farb-PTV gemessen. Zusätzlich werden CFD-DEM-Simulationen gemäß den PTV-Messungen in Pseudo-2D-Wirbelschichten durchgeführt. Die Simulationsergebnisse stimmen mit Messungen hinsichtlich des Volumenflusses der Partikel, der

granularen Temperatur, der Partikelkollisionsgeschwindigkeit und des Mischungsgrades überein. Die Korrektur des Größendispersitätseffekts im Widerstandsmodell ist wichtig, um die Genauigkeit von CFD-DEM-Simulationen polydisperser Partikelsysteme zu verbessern. CFD-DEM-Simulationen werden eingesetzt, um die Partikelzirkulation und Verweilzeiten in verschiedenen Zonen in einem Wurster-Apparat zu untersuchen. Die simulierten idealen Zykluszeiten und Verweilzeiten stimmen gut mit den verfügbaren Messdaten aus der Positronenemissionspartikelverfolgung überein. Darüber hinaus wird ein gekoppelter CFD-DEM- und Monte-Carlo-Ansatz entwickelt, um die Gleichmäßigkeit der Beschichtung zwischen und innerhalb von Partikeln im Wurster-Prozess zu untersuchen. Auf der Grundlage der sphärischen Schwerpunkt-Voronoi-Tessellation kann der Monte-Carlo-Ansatz die Ablagerung und das Ausbreitung von Sprühtröpfchen auf der Oberfläche einzelner Partikel modellieren. Die durch die Simulation vorhergesagten Schichtdickenverteilungen innerhalb der Partikel stimmen gut mit Daten aus Röntgenmikrocomputertomographie-Messungen überein.

# Contents

# Nomenclature

*In this thesis, the symbols used in the chapters are defined chapter-wise.*

| Chapter 2 | | |
|---|---|---|
| $A$, $B$ | constants in relaxation method | $[-]$ |
| $d$ | diameter | [m] |
| $\boldsymbol{d}$ | displacement vector between two particles | [pixel] |
| $I$, $\bar{I}$ | intensity and mean intensity of pixels in raw image | $[-]$ |
| $L_b$ | bias of the segmentation location | [pixel] |
| $L_{minor}$, $L_{major}$ | lengths of major and minor axes | [pixel] |
| $\mathbb{P}_{ij}$, $\tilde{\mathbb{P}}_{ij}$ | normalized matching probability, non-normalized matching probability | $[-]$ |
| $\mathbb{Q}_{ij}$ | contribution of neighboring particles to matching probability | $[-]$ |
| $\boldsymbol{r}$ | particle centroid (vector) | [pixel] |
| $R_e$ | error ratio | $[-]$ |
| $R_r$ | recovery ratio | $[-]$ |
| $R_s$ | segmentation ratio | $[-]$ |
| $s$, $\bar{s}$ | intensity and mean intensity of pixels in template particle | $[-]$ |
| $S_f$ | scale factor | [pixel/mm] |
| $t$, $\Delta t$ | time, time step | [s] |
| $T$ | searching radius in relaxation method | [pixel] |
| $\boldsymbol{r}$ | particle velocity (vector) | [pixel] |
| $x$, $y$, $z$ | Cartesian coordinates | [m] |
| | | |
| *Greek symbols* | | |
| $\gamma$ | normalized cross-correlation coefficient | $[-]$ |
| $\theta_o$ | orientation | [°] |
| | | |
| *Subscripts* | | |
| $i$, $j$, $k$, $l$, $m$ | indices | |
| $p$ | particle, order | |
| $q$ | order | |

| **Chapter 3** | | |
|---|---|---|
| $A$, $B$, $C$ | constants to calculate capillary force | [−] |
| $d$ | diameter | [m] |
| $d_{inter}$ | inter-particle distance | [m] |
| $d_{32}$ | Sauter mean diameter | [m] |
| $D_r$ | rupture distance | [m] |
| $e$ | coefficient of restitution | [-] |
| $E$ | Young's modulus | [Pa] |
| $\boldsymbol{f}''$ | sum of non-dominant forces (vector) | [N] |
| $\boldsymbol{f}_{capillary}$ | capillary force (vector) | [N] |
| $\boldsymbol{f}_c$ | particle-particle interaction force (vector) | [N] |
| $\boldsymbol{f}_d$ | drag force (vector) | [N] |
| $\boldsymbol{f}_i$ | local mean value of force on particle due to particle-fluid interaction (vector) | [N] |
| $\boldsymbol{f}'_i$ | force due to variations of fluid stress (vector) | [N] |
| $\boldsymbol{f}_{pf}$ | particle-fluid interaction force (particle level, vector) | [N] |
| $\boldsymbol{f}_{vis}$ | viscous force (vector) | [N] |
| $\boldsymbol{f}_{\nabla p}$ | pressure gradient force (vector) | [N] |
| $\boldsymbol{f}_{\nabla \cdot \tau}$ | viscous force due to fluid shear stress tensor (vector) | [N] |
| $\boldsymbol{F}_{pf}$ | particle-fluid interaction force (cell level, vector) | [N] |
| $\boldsymbol{g}$ | gravity vector | [m/s$^2$] |
| $G$ | shear modulus | [Pa] |
| $k$ | stiffness (elastic) coefficient | [N/m] |
| $k_r$ | rolling friction coefficient | [−] |
| $m$ | mass | [kg] |
| $\boldsymbol{n}$ | unit vector | [−] |
| $r$ | radial distance | [m] |
| $\boldsymbol{r}$ | position vector | [m] |
| $R$ | radius of particle | [m] |
| $\boldsymbol{S}$ | Reynolds stress for solids | [Pa] |
| $S_{cube}$ | constant factor in BPM | [−] |
| $t$, $\Delta t$ | time, time step | [s] |
| $T_t$ | tangential torque (vector) | [N · s] |
| $T_r$ | rolling torque (vector) | [N · s] |
| $\boldsymbol{u}$ | fluid velocity (vector) | [m/s] |
| $\boldsymbol{v}$, $\boldsymbol{v}_p$ | particle velocity (vector) | [m/s] |
| $v_{c,max}$ | maximum collision velocity | [m/s] |
| $V_p$ | volume of particle | [m$^3$] |
| $U_{mf}$ | minimum fluidization velocity | [m/s] |
| $U_g$ | superficial gas velocity | [m/s] |
| $V_p$ | volume of particle | [m$^3$] |

| $V_l$ | volume of liquid bridge | [m³] |
|---|---|---|
| $x$, $y$, $z$ | Cartesian coordinates | [m] |

*Greek symbols*

| | | |
|---|---|---|
| $\alpha_d$ | damping ratio | [−] |
| $\beta_{pf}$ | momentum exchange coefficient | [kg/(m³ · s)] |
| $\gamma$ | normalized cross-correlation coefficient | [−] |
| $\delta$ | overlap between two particles | [m] |
| $\epsilon$ | volume fraction | [−] |
| $\eta$ | damping coefficient | [(N · s)/m] |
| $\theta$ | contact angle | [°] |
| $\Theta$ | particle granular temperature | [m²/s²] |
| $\mu_f$ | fluid dynamic viscosity | [Pa · s] |
| $\mu_g$ | gas dynamic viscosity | [Pa · s] |
| $\mu_{fc}$ | friction coefficient | [−] |
| $\boldsymbol{\xi}$ | fluid stress tensor | [Pa] |
| $\boldsymbol{\xi}^s$ | solid stress tensor | [Pa] |
| $\rho$ | density | [kg/m³] |
| $\sigma_f$ | surface tension of fluid | [N/m] |
| $\sigma$ | Poisson's ratio | [Pa · s] |
| $\tau_H$ | Hertzian collision time | [s] |
| $\tau_f$ | fluid stress tensor | [Pa] |
| $\varphi$ | polar angle | [°] |
| $\boldsymbol{\Phi}$ | local mean value of particle-particle interaction force | [N] |
| $\psi$ | azimuthal angle | [°] |
| $\boldsymbol{\omega}$ | particle angular velocity (vector) | [rad/s] |

*Subscripts*

| | |
|---|---|
| eq | equivalent |
| f | fluid |
| i, j, k | indices |
| l | liquid |
| n | normal direction, time step |
| p | particle |
| d | droplet |
| r | relative |
| s | solid |
| t | tangential direction |

| **Chapter 4** | | |
|---|---|---|
| $A_I$ | area of particle image | [pixel] |
| $C_I$ | circumference of particle image | [pixel] |

| | | |
|---|---|---|
| $A, B, C$ | constants in the capillary force | [−] |
| $d_{32}$ | Sauter mean diameter | [m] |
| $d_p$ | diameter of particle | [m] |
| $d_{cell}$ | diameter of cell | [m] |
| $D_r$ | rupture distance | [m] |
| $e$ | coefficient of restitution | [−] |
| $E$ | Young's modulus | [Pa] |
| $k$ | stiffness coefficient | [N/m] |
| $m$ | mass of particle | [kg] |
| $S_f$ | scale factor | [pixel/mm] |
| $SPHT$ | sphericity of particle | [−] |
| $U_{mf}$ | minimum fluidization velocity | [m/s] |
| $v_{c,max}$ | maximum impact velocity | [m/s] |
| $V$ | volume | [m³] |
| $x, y, z$ | Cartesian coordinates | [m] |

| | | |
|---|---|---|
| Greek symbols | | |
| $\alpha$ | damping ratio | [−] |
| $\varepsilon$ | overlap | [m] |
| $\eta$ | damping coefficient | [N · s/m] |
| $\mu_{fc}$ | friction coefficient | [−] |
| $\rho_p$ | particle density | [kg/m³] |
| $\rho_{solid}$ | solid density | [kg/m³] |
| $\sigma$ | Poisson's ratio | [Pa · s] |

| | | |
|---|---|---|
| Subscripts | | |
| $2D$ | two dimensional | |
| $l$ | liquid | |
| $eq$ | equivalent | |
| $p$ | particle | |

| **Chapter 5** | | |
|---|---|---|
| $A_I$ | area of particle image | [pixel] |
| $C_I$ | circumference of particle image | [pixel] |
| $d_{32}$ | Sauter mean diameter | [m] |
| $d_s$ | diameter of sphere | [m] |
| $e$ | coefficient of restitution | [−] |
| $\boldsymbol{e}$ | unit axis of rotation (vector) | [−] |
| $E$ | Young's modulus | [Pa] |
| $\boldsymbol{f}_c$ | particle-particle interaction force (vector) | [N] |
| $\boldsymbol{F}_{sum}$ | total force (vector) | [N] |
| $\boldsymbol{G}$ | coordinate vector of centroid of gravity | [m] |
| $I$ | intensity in raw image | [−] |

| | | |
|---|---|---|
| $I_i$ | moment of inertia in space-fixed system | [kg·m$^2$] |
| $\hat{I}_i$ | principal moments of inertia | [kg·m$^2$] |
| $L_{minor}, L_{major}$ | lengths of major and minor axes | [m] |
| $k$ | stiffness coefficient | [N/m] |
| $m$ | mass of particle | [kg] |
| $N_s$ | number of spheres | [−] |
| $N_{s,c}$ | number of spheres in individual contact | [−] |
| $\boldsymbol{n}$ | unit vector of contact force | [−] |
| $\boldsymbol{q}$ | quaternion (vector) | [−] |
| $\boldsymbol{r}$ | particle centroid (vector) | [m] |
| $r_{s,c}$ | radius of sphere in individual contact | [m] |
| $R$ | particle radius | [s] |
| $R_A$ | aspect ratio | [−] |
| $S_f$ | scale factor | [pixel/mm] |
| $SPHT$ | sphericity of particle | [−] |
| $St_v$ | viscous Stokes number | [−] |
| $T$ | threshold intensity | [−] |
| $\boldsymbol{T}$ | sum of all torques acting on particle $i$ in space-fixed frame | [N·m] |
| $t, \Delta t$ | time, time step size | [s] |
| $\boldsymbol{v}$ | particle velocity (vector) | [m/s] |
| $V$ | volume | [m$^3$] |
| $w$ | weighted mean of intensity | [−] |
| $\boldsymbol{W}$ | angular velocity in body-fixed system (vector) | [rad/s] |
| $x, y, z$ | Cartesian coordinates | [m] |

Greek symbols

| | | |
|---|---|---|
| $\alpha$ | damping ratio | [−] |
| $\varepsilon$ | overlap | [m] |
| $\eta$ | damping coefficient | [N·s/m] |
| $\theta$ | angle between velocity vector and vertical axis | [°] |
| $\theta_e$ | Euler angle | [°] |
| $\theta_o$ | orientation | [°] |
| $\Lambda$ | transformation matrix | [−] |
| $\mu_{fc}$ | friction coefficient | [−] |
| $\rho_p$ | particle density | [kg/m$^3$] |
| $\rho_{solid}$ | solid density | [kg/m$^3$] |
| $\sigma$ | Poisson's ratio | [Pa·s] |
| $\omega$ | rotational speed | [1/s] |

Subscripts

| | |
|---|---|
| 0 | initial condition |
| 1, 2 | different time steps, before or after collision |

| | | |
|---|---|---|
| $2D, 3D$ | two dimensional, three dimensional | |
| $b$ | background, body-fixed | |
| $eq$ | equivalent | |
| $i, j, k$ | indices | |
| $n$ | normal direction | |
| $opt$ | optimal | |
| $p$ | particle | |
| $s$ | space-fixed | |
| $t$ | tangential direction | |

**Chapter 6**

| | | |
|---|---|---|
| $A, B$ | constants in relaxation method | $[-]$ |
| $d_p$ | particle diameter | [mm] |
| $\boldsymbol{d}$ | displacement vector between two particles | [pixel] |
| $f_c$ | particle and average particle collision frequency | [1/s] |
| $g_0$ | radial distribution function | $[-]$ |
| $I, \bar{I}$ | intensity and mean intensity in the matrix of raw image | $[-]$ |
| $L_c$ | distance of two particle centers | [m] |
| $L_i$ | distance to the front wall | [m] |
| $n$ | particle number concentration | $[1/\text{m}^3]$ |
| $\boldsymbol{n}$ | unit vector between two particles | [pixel] |
| $\dot{n}_c$ | particle collision rate | $[1/(\text{m}^3 \cdot \text{s})]$ |
| $m_c$ | total number of candidate particles | $[-]$ |
| $N_c$ | number of particle collisions | $[-]$ |
| $N_p$ | number of particles | $[-]$ |
| $P_{ij}, \tilde{P}_{ij}$ | normalized matching probability, non-normalized matching probability | $[-]$ |
| $Q_{ij}$ | contribution of neighboring particles to matching probability | $[-]$ |
| $R_r$ | recovery ratio | $[-]$ |
| $s, \bar{s}$ | intensity and mean intensity in the matrix of template particle | $[-]$ |
| $S_f$ | scale factor | [pixel/mm] |
| $St$ | Stokes number | $[-]$ |
| $St_v$ | viscous Stokes number | $[-]$ |
| $T$ | searching radius in relaxation method | [pixel] |
| $t, \Delta t$ | time, time step size | [s] |
| $u_c$ | magnitude of impact velocity (scalar) | [m/s] |
| $\boldsymbol{u}_f$ | fluctuation particle velocity (vector) | [m/s] |
| $\boldsymbol{u}_p$ | particle velocity (vector) | [m/s] |
| $\boldsymbol{u}_{r,c}$ | impact velocity (vector) | [m/s] |
| $U_{mf}$ | minimum fluidization velocity | [m/s] |

| $U$ | superficial gas velocity | [m/s] |
| $x, y, z$ | Cartesian coordinates | [m] |

*Greek symbols*

| $\gamma$ | normalized cross-correlation coefficient | $[-]$ |
| $\delta$ | contact threshold value | [pixel] |
| $\epsilon_s$ | solid volume fraction | $[-]$ |
| $\epsilon_{s,max}$ | maximum solid volume fraction | $[-]$ |
| $\theta$ | angle between two velocity vectors | [°] |
| $\Theta$ | granular temperature | $[m^2/s^2]$ |
| $\rho_p$ | particle density | $[kg/m^3]$ |
| $\tau_p$ | life time of particle | [s] |
| $\Phi$ | volume flux of solid particles | $[m^3/(s \cdot m^2)]$ |
| $\chi$ | collision model parameter | [1/s] |

Subscripts

| $1, 2$ | different particles, or time steps |
| $2D$ | two dimensional space |
| $c$ | imaginary collision moment |
| $i, j, k$ | indices |
| $p$ | particle |
| $fit$ | fitting curve |

**Chapter 7**

| $c$ | volume fraction of the smallest particle in each sample | $[-]$ |
| $d_p$ | particle diameter | [mm] |
| $d_{32}$ | Sauter mean diameter | [mm] |
| $e$ | coefficient of restitution | $[-]$ |
| $E$ | Young's modulus | [Pa] |
| $k$ | stiffness coefficient | $[-]$ |
| $k_r$ | rolling coefficient | $[-]$ |
| $m$ | mass of particle | [kg] |
| $N_e$ | equivalent number of particles in each sample | $[-]$ |
| $N_s$ | number of samples | $[-]$ |
| $P_s$ | global volume fraction of the smallest particle in a mixture | $[-]$ |
| $S_f$ | scale factor | [pixel/mm] |
| $S^2$ | actual variance of particle volume fraction of the smallest particle | $[-]$ |
| $x, y, z$ | Cartesian coordinates | [m] |

*Greek symbols*

| $\alpha$ | damping ratio | $[-]$ |
|---|---|---|
| $\beta_{pf}$ | momentum exchange coefficient | $[\mathrm{kg}/(\mathrm{m}^3 \cdot \mathrm{s})]$ |
| $\eta$ | damping coefficient | $[-]$ |
| $\mu_g$ | gas dynamics viscosity | $[\mathrm{Pa} \cdot \mathrm{s}]$ |
| $\mu_{fc}$ | friction coefficient | $[-]$ |
| $\rho$ | density | $[\mathrm{kg}/\mathrm{m}^3]$ |
| $\sigma$ | Poisson's ratio | $[\mathrm{Pa} \cdot \mathrm{s}]$ |
| $\tau_H$ | Hertzian collision time | $[\mathrm{s}]$ |

*Subscripts*

| $eq$ | equivalent |
|---|---|
| $i, j, k$ | indices |
| $n$ | normal direction |
| $p$ | particle |
| $t$ | tangential direction |

## Chapter 8

| $a$ | scale constant | $[-]$ |
|---|---|---|
| $d$ | diameter | $[\mathrm{m}]$ |
| $d_{32}$ | Sauter mean diameter | $[\mathrm{mm}]$ |
| $e$ | coefficient of restitution | $[-]$ |
| $E$ | Young's modulus | $[\mathrm{Pa}]$ |
| $L$ | length ratio | $[-]$ |
| $m$ | mass | $[\mathrm{kg}]$ |
| $N_d$ | number of droplet | $[-]$ |
| $r_n$ | number ratio of ideal cycles to overall cycles | $\%$ |
| $R_d$ | droplet deposition rate | $[\mathrm{mg}/\mathrm{s}]$ |
| $S_{cube}$ | the constant factor | $[-]$ |
| $t$ | time | $[\mathrm{s}]$ |
| $v_c$ | collision (impact) velocity | $[\mathrm{m}/\mathrm{s}]$ |

Greek symbols

| $\tau_H$ | Hertzian collision time | $[\mathrm{s}]$ |
|---|---|---|
| $\varphi$ | volume ratio of different zones | $[\%]$ |

Subscripts

| $c$ | cycle |
|---|---|
| $d$ | droplet |
| $eq$ | equivalent |
| $i, j$ | indices |
| $ic$ | ideal cycle |
| $s$ | spray |
| $t$ | tube |

| **Chapter 9** | | |
|---|---|---|
| $A$ | area | [m$^2$] |
| $A, B, C$ | dimensionless regression parameters in the capillary force | [$-$] |
| $d$ | diameter | [m] |
| $d_{inter}$ | inter-particle distance | [m] |
| $D_r$ | rupture distance | [m] |
| $e$ | coefficient of restitution | [$-$] |
| $E$ | Young's modulus | [Pa] |
| $F$ | normalized drag force | [$-$] |
| $\boldsymbol{f}_{pf}$ | particle-fluid interaction force (particle level, vector) | [N] |
| $\boldsymbol{f}_c$ | particle-particle interaction force (vector) | [N] |
| $\boldsymbol{f}_{capillary}$ | capillary force (vector) | [N] |
| $\boldsymbol{f}_d$ | drag force (vector) | [N] |
| $\boldsymbol{F}_{pf}$ | particle-fluid interaction force (cell level, vector) | [N] |
| $g$ | constant probability density function | [$-$] |
| $\boldsymbol{g}$ | acceleration due to gravity (vector) | [m/s$^2$] |
| $G$ | shear modulus | [Pa] |
| $h$ | layer thickness | [m] |
| $I$ | moment of inertia | [kg $\cdot$ m$^2$] |
| $I_{A_c}$ | indicator function | [$-$] |
| $k$ | stiffness coefficient | [N/m] |
| $k_r$ | rolling coefficient | [$-$] |
| $L_{min}$ | minimum orthodromic distance | [m] |
| $m, M$ | mass | [kg] |
| $\dot{m}$ | drying rate | [kg/(m$^2 \cdot$ s)] |
| $\dot{M}$ | mass flow rate | [kg/s] |
| $N_1$ | number of particles in interactions | [$-$] |
| $N_2$ | number of liquid bridges | [$-$] |
| $N_3$ | number of particles in a CFD cell | [$-$] |
| $N_{dep}$ | number of deposition panels | [$-$] |
| $N_p$ | number of particles in the bed | [$-$] |
| $N_{p,MC}$ | number of particles in Monte Carlo domain | [$-$] |
| $p$ | pressure | [Pa] |
| $r_1, r_2, r_3$ | random numbers in Monte Carlo simulations | [$-$] |
| $R$ | particle radius | [m] |
| $R_{ic}$ | number ratio of ideal to total cycles | [$-$] |
| $Re$ | Reynolds number | [$-$] |
| $s$ | cumulative sum of weights | [$-$] |
| $S_p$ | size of high porosity region | [$-$] |
| $Sc$ | Schmidt number | [$-$] |
| $Sh$ | Sherwood number | [$-$] |

| $t,\ \Delta t$ | time, time step | [s] |
|---|---|---|
| $T_t$ | tangential torque (vector) | [N $\cdot$ s] |
| $T_r$ | rolling torque (vector) | [N $\cdot$ s] |
| $\boldsymbol{v}_p$ | particle velocity (vector) | [m/s] |
| $v_{c,max}$ | maximum collision velocity | [m/s] |
| $v_{rel}$ | normal impact velocity between particle and droplet | [m/s] |
| $V$ | volume | [m$^3$] |
| $V_i$ | Voronoi region | [$-$] |
| $V_s$ | volume swept by moving particle | [m$^3$] |
| $We$ | Weber number | [$-$] |
| $x,\ y,\ z$ | Cartesian coordinates | [m] |
| $Y$ | moisture content of gas | [kg/kg] |

Greek symbols

| $\alpha_d$ | damping ratio | [$-$] |
|---|---|---|
| $\alpha_l$ | volume ratio of liquid bridge to two particles | [$-$] |
| $\beta$ | mass transfer coefficient of gas side | [m/s)] |
| $\beta_{pf}$ | momentum exchange coefficient | [kg/(m$^3 \cdot$ s)] |
| $\gamma$ | droplet surface tension | [N/m] |
| $\delta$ | diffusion coefficient between water and air | [m$^2$/s] |
| $\epsilon$ | volume fraction, porosity | [$-$] |
| $\varepsilon$ | overlap between particles | [m] |
| $\eta$ | damping coefficient | [N $\cdot$ s/m] |
| $\theta$ | contact angle | [°] |
| $\mu_f$ | gas dynamic viscosity | [Pa $\cdot$ s] |
| $\mu_{fc}$ | friction coefficient | [$-$] |
| $\rho$ | density | [kg/m$^3$] |
| $\sigma$ | Poisson's ratio | [Pa $\cdot$ s] |
| $\tau_H$ | Hertzian collision time | [s] |
| $\tau_f$ | fluid stress tensor | [Pa] |
| $\Psi$ | coating coverage | [$-$] |
| $\boldsymbol{\omega}$ | particle angular velocity (vector) | [rad/s] |
| $\boldsymbol{\omega}_r$ | relative particle angular velocity (vector) | [rad/s] |

Subscripts

| $1, 2$ | different time steps |
|---|---|
| $2D$ | two-dimensional space |
| $A_c$ | start of a new cycle |
| $c$ | coupling |
| $con$ | conservative |
| $d$ | droplet |
| $dis$ | dissipative |

| | |
|---|---|
| *eq* | equivalent |
| *f* | fluid |
| *g* | gas |
| *i, j, k* | indices |
| *l* | liquid solution |
| *m* | Monte Carlo, mean |
| *n* | normal direction |
| *p* | particle |
| *s* | spray zone |
| *sat* | saturation |
| *t* | tangential direction, Wurster tube |

*Abbreviations of all chapters.*

| **Abbreviations** | |
|---|---|
| API | active pharmaceutical ingredient |
| BPM | big particle method |
| CFD | computational fluid dynamics |
| CoV | coefficient of variation |
| COR | coefficient of restitution |
| CPU | central processing unit |
| CVT | centroidal Voronoi tessellation |
| DE | dextrose equivalent |
| DEM | discrete element method |
| DIA | digital image analysis |
| DPVM | divided particle volume method |
| FOV | field of view |
| HSD | Hertzian spring-dashpot |
| KTGF | kinetic theory of granular flow |
| LBM | lattice Boltzmann method |
| LSD | Linear spring-dashpot |
| MBVK | mono-disperse Beetstra drag model |
| MC | Monte Carlo |
| MCC | microcrystalline cellulose |
| MPIA | micro particle interaction analyzer |
| MS | multi-sphere |
| PBM | population balance modeling |
| PBVK | poly-disperse Beetstra drag model |
| PCM | particle centroid method |
| PEPT | positron emission particle tracking |
| PIV | particle imaging velocimetry |
| PISO | pressure-implicit split-operator |
| PMF | probability mass function |

| | |
|------|----------------------------|
| PTV  | particle tracking velocimetry |
| RGB  | red-green-blue color space |
| RTD  | residence time distribution |
| SEM  | scanning electron microscope |
| SD   | standard deviation |
| SQ   | superquadric |

# Chapter 1

# Introduction

## 1.1 Motivation

Fluidized beds are encountered in many important industrial operations that involve multiphase flow. Due to the fluidization of solid particles, fluidized beds can offer unique features such as large interfacial area between fluid (gas or liquid) and the particles, excellent heat and mass transfer, uniformity of temperature, and the ability to design a wide range of particle properties and a large quantity of particulate materials. The term "fluidization" reflects the conferment of fluid-like properties onto the solid particles when the fluid rises through the bed of particles with a sufficient flow rate [1, 2]. Fluidized beds are applied for many physical processes, such as mixing, drying, *particle formation* (coating, layering granulation and agglomeration), heating and cooling of bulk solids; and many chemical processes, such as coal gasification, combustion, water purification, catalytic reactions. In most applications of fluidized beds, the fluidizing medium is a gas, rather than a liquid.

*Particle formation in spray fluidized beds*

Particle formation processes in spray fluidized beds are used in a wide range of industries, including pharmaceutics, foods, fertilizers, detergents, mineral processing and specialty chemicals [3]. Particle formation processes can enhance the flowability, compressibility, stability and dissolution of materials. Spray fluidized bed processes are considerably complex, caused by the integration of a number of sub-processes, including spraying, wetting, drying and solidifying; by the presence of different process zones with different controlling parameters; and by the presence of multiphase transport at multi-scale level. Owing to the complexity, various definitions and names are used for spray fluidized bed processes and their products in the literature and industrial appilcations. Tsotsas and Mujumdar [4] clarify the terminology in spray fluidized bed processes. Figure 1.1 distinguishes agglomeration, granulation and coating by means of basic principles and product structures. *Agglomeration* is a process of aggregating smaller particles (powders) to larger and semipermanent structures (snowball). *Granulation* is a process of successive layering solidified shells on particles (seeds) by means

of orderly spreading, drying and solidifying atomized liquid. The final granule has an onion structure. *Coating* is essentially the same as layering, with the difference of thin layer of another material on particles (carriers). A spray droplet can dry after deposition on the particle surface; or form a liquid bridge, when interacting with more than one particle. Indeed, agglomeration competes with granulation and coating to acquire more droplets that can form liquid bridges.
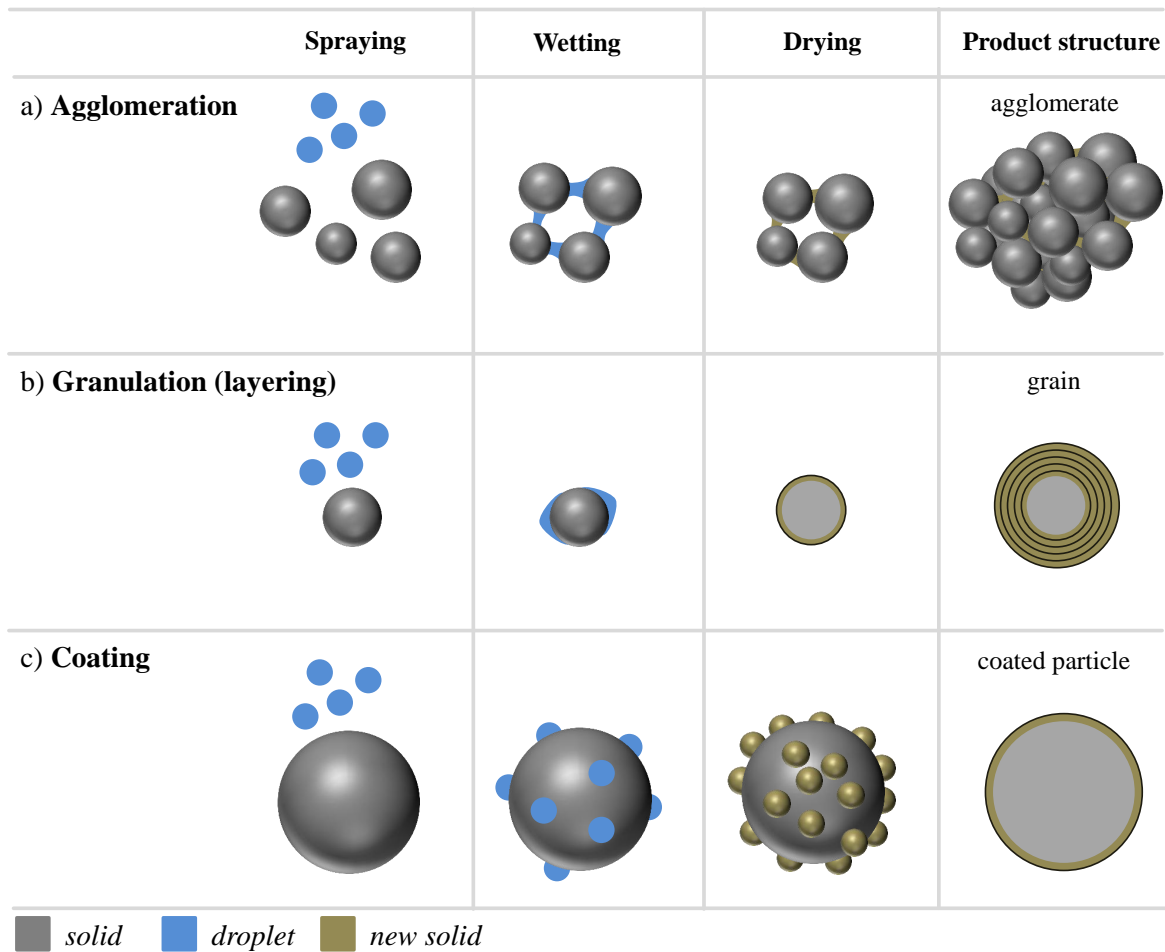
| | Spraying | Wetting | Drying | Product structure |
|---|---|---|---|---|
| **a) Agglomeration** | | | | agglomerate |
| **b) Granulation (layering)** | | | | grain |
| **c) Coating** | | | | coated particle |

■ *solid*   ■ *droplet*   ■ *new solid*

Figure 1.1: Basic principles of spray fluidized bed processes: a) agglomeration, b) granulation (layering), c) coating [4].

Spray fluidized bed equipment is mainly composed of the gas inlet chamber, the gas distributor, the process chamber, the spray system and the exhaust chamber. The critical process option can be characterized by the spray nozzle orientation, for instance, top-spray processing (in or on bed), bottom-spray processing (with or without inserts) and tangential-spray processing [5]. Additional opportunities of new product structures and high product quality require manipulation of the gas distributor, the process chamber and the spray system [4]. Two successful examples of such combinations are the Wurster equipment [6–8] and the horizontal fluidized bed [9, 10].

*Mesoscale phenomena*

As pointed out in "Towards Engineering Mesoscience" (a joint virtual special issue of *Chemical Engineering Science, Powder Technology and Particuology*) [11], an understanding of mesoscale phenomena that take place between single element scale and system scale is a grand challenge not only for chemical engineering, but also for the whole spectrum of science and engineering. It has been gradually recognized that an upgraded knowledge of mesoscale phenomena is necessary in order to increase our capability to resolve main tasks of chemical engineering including the design of materials, scaling-up reactors, and system optimization.

As shown in Figure 1.2, particle formation in spray fluidized beds is a multi-scale process in both space and time involving multi-phase flow (solid particles, spray droplets and carrier gas), in which the particle scale and the process unit (spray fluidized bed) constitute a kind of boundaries. At the particle scale, we can understand flow and the transport of single particles based on fundamentals of transport phenomena [1, 12]; and we can characterize properties (such as size, shape and morphology) of both, single primary particles and single product particles, by means of different measurement techniques, for instance, scanning electron microscopy (SEM), white light interferometry, X-ray micro-computed tomography ($\mu$-CT) [13, 14]. At the system scale, we have accumulated knowledge to change the overall performance of particle formation in the desired direction by adjusting gas flow rate, spray rate, binder content in sprayed liquid, atomization pressure, drying conditions and composition of suspension, equipment design and so on [4, 15–18].

However, the knowledge about what happens at the mesoscale between single particles and the whole process unit is still very limited, which is the main gap that needs to be closed to achieve efficient operations in industry. In order to further improve a spray particle formation process, we must answer the questions: How do the particles and the droplets interact in the real system? How do these interactions correlate to the performance of particle formation processes and influence final product properties? How to understand the transition from phenomena that govern the formation of the solid phase at the microscale to the macroscale behavior of particle systems in industrial equipment? [19].

In spray fluidized beds, the motion of particles is not only influenced by aerodynamic transport and turbulent effects, but is also significantly affected by particle-particle (droplet) interactions. Moreover, the particle-particle and particle-droplet collisions are the prerequisites to form new particles. *Particle collision* is an important mesoscale phenomenon, which can be characterized by collision frequency, collision (impact) velocity and coefficient of restitution. The particle collision frequency, defined as the number of collisions of one single particle per unit time, measures the possibility for the single particle to form a new structure with other particles or to break the existing unstable structures. Supposed that the viscous and capillary forces due to liquid bridges are the only cohesion sources, collisions occurring at dry contact points cannot form new structures; but they can transfer the momentum between particles. However,
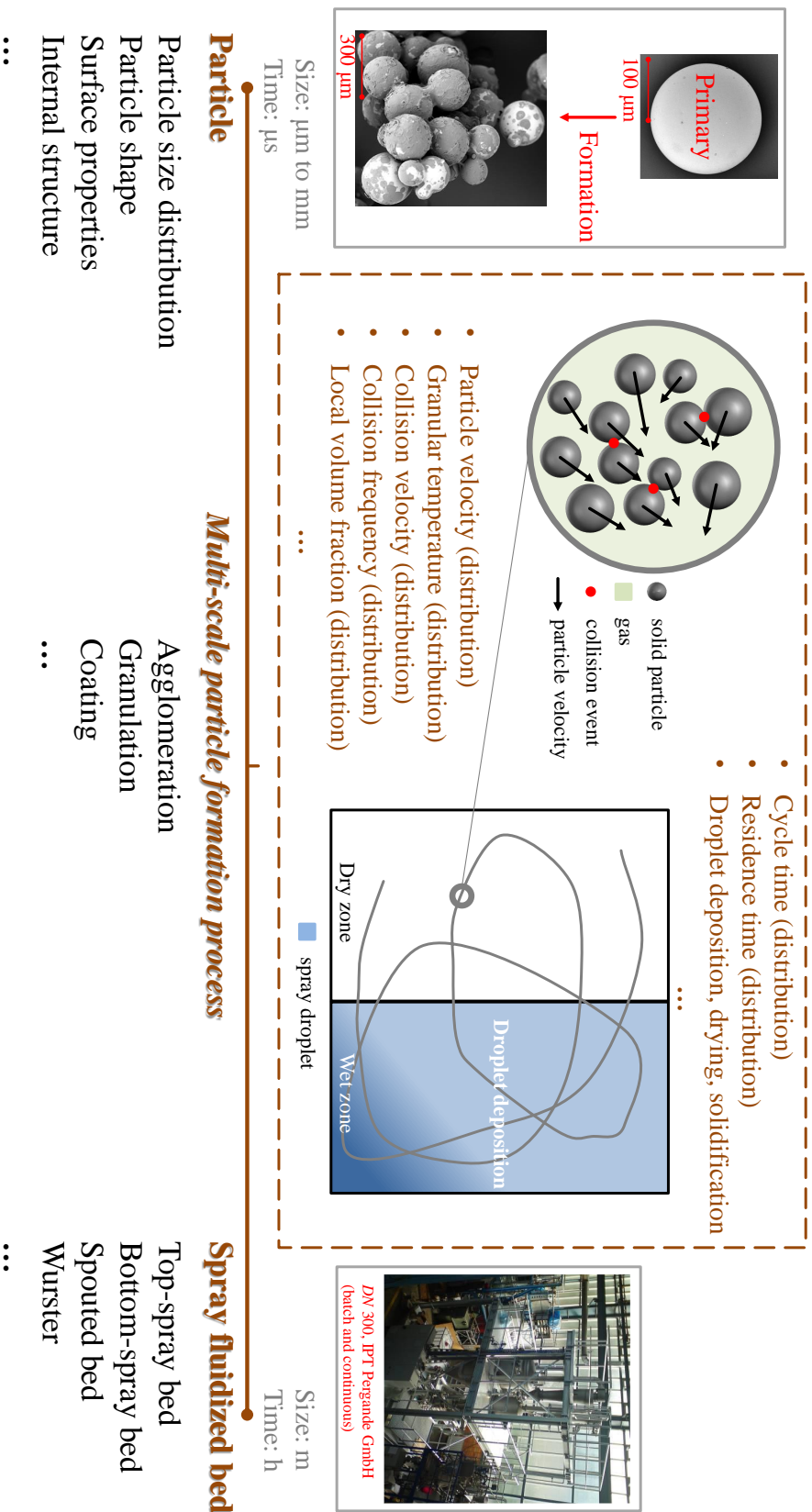
Figure 1.2: Multi-scale particle formation processes in fluidized beds.

not all collisions occurring at wet spots enable coalescence. As shown in the SEM image of an agglomerate in Figure 1.2, there are some obvious positions with different sizes covered by dried liquid binder (relatively dark color) due to particle-particle collisions with different intensities (impact velocities). These positions imply that: i) some particle-particle collisions that happened at wet spots failed to result in coalescence and ii) some particle-particle collisions led to the breakage of previously formed unstable agglomerates. In wet two-body collisions, Ennis et al. [20] modelled the first case by assuming that successful coalescence occurs if the kinetic energy of impact is entirely dissipated by viscous forces in the fluid and elastic losses in the solid phase. Most of numerical and experimental studies of wet collisions focused on the two-body system, where the only two possible outcomes are agglomeration and rebound affected by particle sizes, the impact velocity and angle, and wetting properties of liquid layer [21–24]. For the three-body system, Donahue et al. [25] measured the outcome of normal collisions between an incoming striker particle and two initially agglomerated particles (due to liquid bridge) by observing Stoke's cradle via high-speed imaging. Liu et al. [26] investigated the outcome of collisions between a primary particle and a small unstable agglomerate (predefined by a constant cohesive force) in various pre-collisional configurations by DEM simulations. The understanding of the dynamics of collisions between primary particles and small unstable agglomerates is required to well control wet particle formation processes. Note that most particles used in industry are non-spherical and irregular, which makes the investigation of particle-particle interactions more complex and challenging.

As shown in Figure 1.2, there are typically at least one dry zone and one wet zone in the spray fluidized bed to successively achieve the processes of wetting, drying and solidification. Therefore, the precise control of the residence times in different zones and the total cycle time are critical for the final product quality. Particle residence time distributions were experimentally measured in different configurations, for instance in Wurster fluidized beds using positron emission particle tracking and particle image velocimetry combined with conductivity probes [27, 28], and in horizontal fluidized beds using colored tracer particles [9, 10]. The residence time distribution (RTD) is the model parameter required in Monte Carlo modeling [29] and population balance modeling [6, 8, 16] of particle formation in spray fluidized beds. Meanwhile, the non-uniform distribution of spray droplets is influenced by the location of spray nozzle, the bed geometry, and particle motion in the bed; and the droplet size distribution influenced by both liquid properties (surface tension, density and viscosity) and gaseous (stream) flow properties (velocity, density and viscosity) [30], which makes the study of droplet deposition on particles and cohesive particle-particle interactions more complex in real applications. Experiments of single droplet impact on dry or wet flat surfaces [31] and dry particles [32–34] were conducted to investigate droplet impact hydrodynamics such as deposition, spreading, recoiling, splashing and rebound.

In order to further improve spray fluidized bed processes, different experimental techniques are essential to measure the particle-scale and mesoscale quantities; and accordingly, a multi-scale numerical approach for particulate system should be developed and

applied to reveal particle dynamics in the fluidized beds that are difficult to measure by current techniques; and (or) to directly predict the spray fluidized bed process.

*Particle tracking techniques for fluidized beds*

Although the use of fluidized beds is extensive, their operation is very complex; and an improved understanding of fundamental particle dynamics from advanced experimental techniques is always necessary to develop process improvements and optimization, as well as develop and validate fundamental models for their operation. With this information, more economical processes can be achieved yielding high quality products.

Generally, advanced experimental systems for multiphase flow in fluidized beds should have: i) high spatial and temporal resolution for local phase velocity field measurement as well as local phase fraction measurement, and ii) the capabilities to provide instantaneous and time history of granular flow field. Obviously, it is impossible to use one measurement technique to capture all detailed meso-scale phenomena in the fluidized beds, including particle collision velocity (distribution), particle collision frequency (distribution), solid volume fraction (distribution), particle velocity (distribution), and residence time (distribution).

The principal difficulty in characterizing, quantifying and tracking granular flows in fluidized beds is the fact that the systems are typically opaque, which requires either the
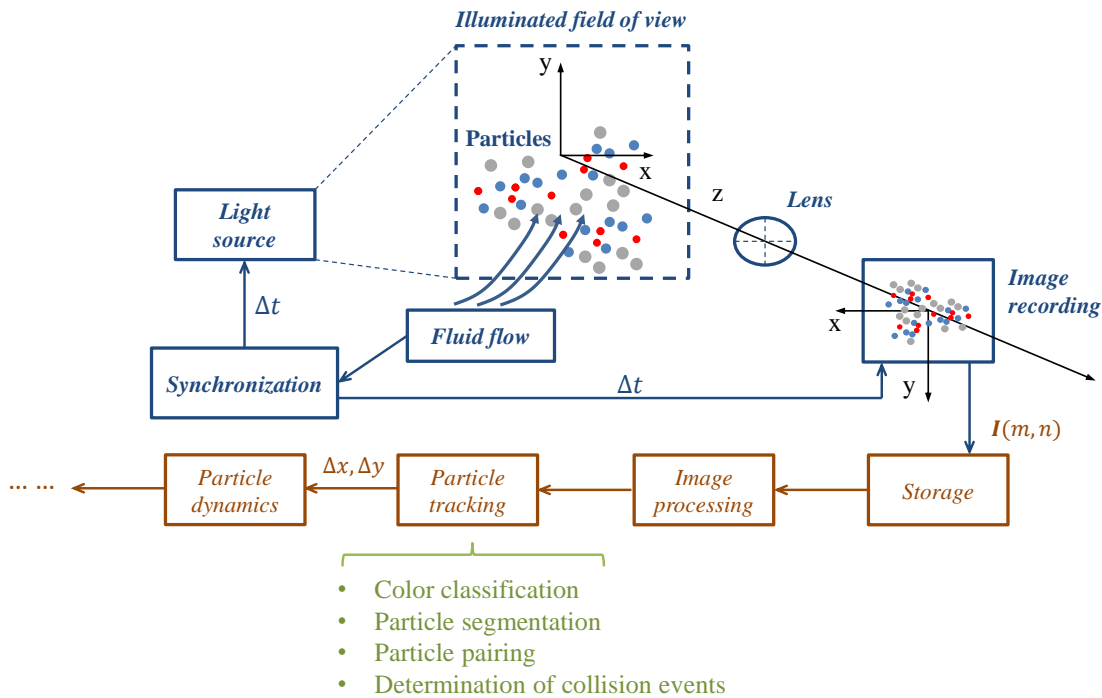


Figure 1.3: Elements and procedure of particle tracking velocimetry (PTV) for the measurement of granular flow.

use of invasive measurement probes or special noninvasive methods. The weakness of invasive probes is that they can change the flow field and interfere with the real processes. Noninvasive particle tracking techniques mainly include particle tracking velocimetry (PTV), magnetic particle tracking (MPT), positron emission particle tracking (PEPT), magnetic resonance imaging (MRI) and X-ray particle tracking velocimetry (XPTV). The advantages and disadvantages of these techniques, and corresponding quantities that can be measured are summarized in Table 1.1.

Appilcations of particle tracking velocimetry (PTV) technique for the measurement of particulate flows originated from the powerful particle-image velocimetry (PIV) technique, which has became a standard tool for experimental fluid mechanics in the last three decades [35]. For tracking the motion of particles in the visualized beds, PTV consists of a light source to illuminate particles in the field of view, a high-speed camera (or high-speed color camera) to record images of particle motion, and a computer for data storage and further post-processsing, as shown in Figure 1.3. Signals from lighting system and fluid flow system are synchronized. In addition, particle tracking algorithms need to be developed according to different target quantities of measurement, such as, particle collision frequency, particle collision velocity and mixing or segregation of particles.

The positron emission particle tracking (PEPT) technique requires tracer particles (up to three) labelled with a radionuclide, a positron camera together with two position-sensitive detectors, and algorithms to calculate the position of particle based on the intersection of several $\gamma$-trajectories pairing by the two detectors [36]. However, PEPT cannot separate the trajectories of two particles which are closer than the intrinsic spatial resolution of the positron camera (about 6 mm for most systems); in other words, PEPT is unlikely to reveal details of inter-particle collisions even though more than one tracer particle are used.

The magnetic particle tracking (MPT) technique involves a magnetic marked particle, a magnetic monitoring system and the algorithm to reconstruct the position and the orientation of particle based on the analysis of quasi-static magnetic field around the marked particle [37].

The magnetic resonance imaging (MRI) technique is performed with special particles containing liquid-like centers (such as poppy seeds), a spectrometer operated at different frequencies for gas and liquid, a birdcage radio-frequency coil to excite and detect signals from particles and gas, and the algorithms to calculate motions by the sine-shaped encoding gradients of magnetic resonance pulse sequence [38].

The X-ray particle tracking velocimetry (XPTV) technique comprises a X-ray stereography imaging system (including two X-ray sources, and two X-ray detectors connected with CCD cameras) and tracer particles (with inserted small pieces of high density material). The algorithms to identify particle locations and track one and the same particle in two successive image frames are similar to those used in normal PTV [39].

Table 1.1: Overview of five noninvasive particle tracking techniques used in fluidized beds (particle tracking velocimetry (PTV), positron emission particle tracking (PEPT), magnetic particle tracking (MPT), magnetic resonance imaging (MRI), X-ray particle tracking velocimetry (XPTV)).

| Technique | Obtained quantity | Advantage and disadvantage | Reference |
|---|---|---|---|
| PTV | • translational particle velocity <br> • volume fraction <br> • collision behavior <br> • mixing and segregation <br> • cycle time (distribution) | (+) spatial resolution; (+) temporal resolution <br> (++) a large number of particles <br> (−) 2D near wall, visualization configuration <br> (−) tracking time <br> (+) cost; (+) operation; (+) interpretation | [40–45] |
| PEPT | • translational particle velocity <br> • residence time (distribution) <br> • cycle time (distribution) | (+) spatial resolution; (o) temporal resolution <br> (++) tracking time <br> (−) maximum 3 radio-active tracer particles <br> (−) cost; (−) operation; (+) interpretation | [27, 36, 46–50] |
| MPT | • translational particle velocity <br> • rotational particle speed <br> • residence time (distribution) <br> • cycle time (distribution) | (o) spatial resolution; (o) temporal resolution <br> (++) particle orientation; (++) tracking time <br> (−−) single particle, large size of tracer particle <br> (+) cost; (+) operation; (+) interpretation | [37, 51, 52] |
| MRI | • translational particle velocity <br> • fluid velocity <br> • volume fraction | (+) spatial resolution; (+) temporal resolution <br> (−) particles must contain a liquid-like center <br> (−) cost; (−) operation; (+) interpretation | [38, 53–55] |
| XPTV | • translational particle velocity <br> • residence time (distribution) <br> • cycle time (distribution) | (+) spatial resolution; (−) temporal resolution <br> (o) tracking time; (o) particle number <br> (−) cost; (−) operation; (+) interpretation | [39, 56–58] |

[*] ++ very good; + good; o moderate; − poor; −− very poor.

*Numerical simulation of fluidized bed processes*

In addition to experimentation, numerical modeling of particulate flow in fluidized beds is an alternative approach to study mesoscale phenomena.

The Eulerian-Eulerian (EE) framework is used to denote simulation and modeling techniques, in which both solids and the carrier phase are treated as inter-penetrating continuous media. The phase volume fractions are introduced in the governing equations for the sake of dividing volume occupied by different phases. Since the trajectories of individual particles are not tracked in EE approach, it is affordable to perform simulations on the pilot or industrial scale. For example, EE approach can be used to predict residence time distribution in industrial scale horizontal fluidized bed by the species method and the multi-solid method [59]. However, the accuracy of EE approach heavily depends on the sub-models associated with particle-scale processes, such as particle-particle collisions and drag forces. The kinetic theory of granular flow and friction flow theory are often used to provide constitutive or closure relations for the solid phase [60].

The Lagrangian-Eulerian (LE) framework is used to denote simulation and modeling techniques, in which the particles (droplets) are represented in a Lagrangian reference frame while the carrier phase is represented in a Eulerian reference frame. Subramaniam [61] gives a comprehensive review of foundation, modeling issues, and numerical implementation of different LE methods for multiphase flows. In the area of particulate flows in fluidized beds, the LE approach consisting of computational fluid dynamics (CFD) and the discrete element method (DEM) has become more and more popular due to its inherent advantage in accurately modeling particle-fluid and particle-particle interactions. In CFD-DEM, the continuum fluid is modeled by the volume-averaged Navier–Stokes equations in the Eulerian framework; simultaneously, the motion of each
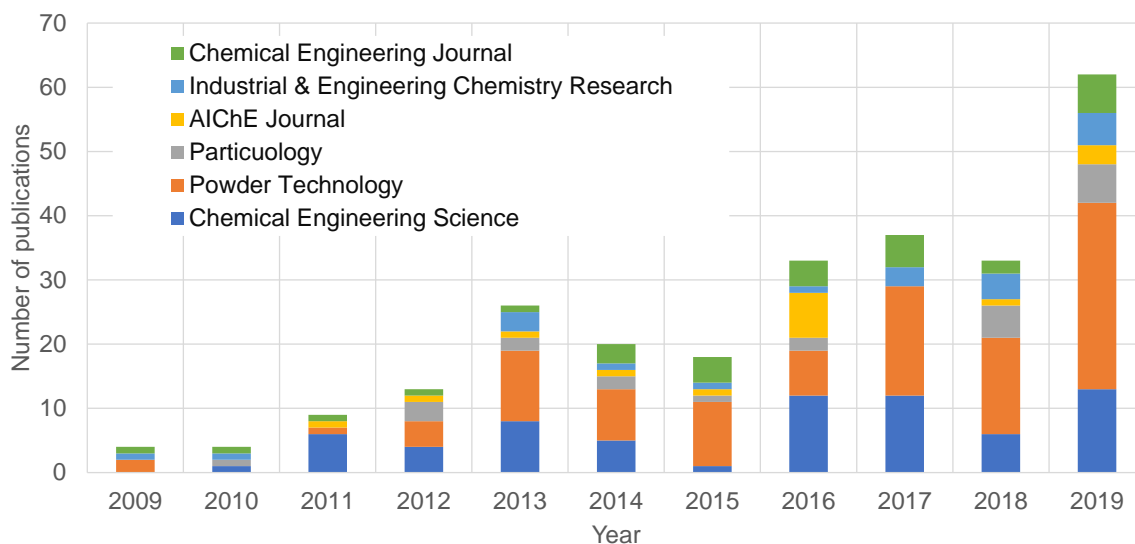


Figure 1.4: Number of publications using keywords "CFD-DEM" and "fluidized bed" from 2009 to 2019 (source: *Web of Science*).

individual dispersed particle is governed by Newton's second law of motion in the Lagrangian framework accounting for particle-particle (wall) interactions and particle-fluid interactions. Compared with the traditional two-fluid EE method closed by the kinetic theory of granular flow, the main advantage of CFD–DEM is that it can provide particle-scale information in the complex granular flow associated with, for instance, non-spherical particle shape, cohesion model, and mixing or segregation of poly-disperse systems.

Table 1.2: Summary of popular topics of CFD-DEM publications in Figure 1.4.

| Topics | Number of publications | Typical references |
|---|---|---|
| Mixing/segregation behavior | 17 | [62–66] |
| Heat and mass transfer | 15 | [67–71] |
| Non-spherical particles | 12 | [63, 72–76] |
| Coarse-grain model | 12 | [66, 77–80] |
| Cohesion model | 12 | [81–85] |
| Liquid fluidized bed | 10 | [86–90] |
| Circle and residence time | 10 | [91–95] |

According to a survey of literatures from 2009 to 2019 (as shown in Figure 1.4), the number of publications using CFD-DEM approach to investigate particle behavior in fluidized beds has gradually increased, as a result of, on the one hand, requirements to employ discrete particle simulation to reveal detailed information on multi-scale necessary for improvements of various processes in fluidized beds but difficult to obtain experimentally; on the other hand, rapid development of open source codes (such as CFDEM Project and MFIX) on the basis of advanced computer science. The publications in Figure 1.4 cover various popular topics, including mixing and segregation behavior, heat and mass transfer, non-spherical particle system, coarse-grain model, cohesion model, liquid fluidized bed, circle and residence time; as summarized in Table 1.2.

Some featured works associated with wet particle formation processes in fluidized beds are listed in Table 1.3. The great challenge of CFD-DEM simulation is the huge computational cost that exponentially increases with increasing the number of particles in large-scale systems. If non-spherical particles, cohesion forces (van der Waals force, electrostatics, capillary force and viscous force), or heat and mass transfer are taken into account, the computational effort further increases. The storage and further post-processing of CFD-DEM simulation data face the same problem. Currently, for a personal computer or a workstation, the number of particles in three-dimensional simulations is limited to $10^5$ [96], however, the number of particles in a lab-scale spray fluidized bed often surpasses $10^9$ that is much beyond the capacity of common computers.

Table 1.3: Selected CFD-DEM simulations from open literature associated with particle formation processes in fluidized beds.

| Paper | Configuration | Variables | Remarks |
|---|---|---|---|
| Askarishahi et al. (2017) [70] | Top-spray bed Packed bed *Particles*: 0.14 mm, $6 \times 10^4$ and $10^6$ *Droplets*: 20 $\mu$m (only in CFD) | Particle and gas temperature Liquid content of particles Liquid and vapor mass loading | • A framework for tracking different species and the temperature in the gas phase • Models for droplet deposition on particles (rate of deposition), evaporation of liquid from free droplets and deposited droplets on particles • Identification of characteristic droplet-in-suspension time (fast deposition or over-spray) |
| Lichtenegger et al. (2017) [97] | Bubbling fluidized bed *Particles*: 1 mm, $5.7 \times 10^4$ and $9.5 \times 10^4$ | Particle temperature Recurrence plots | • Employ recurrence nature of bubbling bed in CFD-DEM for modeling heat transfer • Extrapolate fields from recurrence process without the need to continuously solve the dynamic equations • The new approach requires 1/300 of the runtime of conventional CFD-DEM to model heat transfer • Particle temperatures are compared with infrared thermography measurements |
| Sutkar et al. (2016) [98] | Spout fluidized bed (with and without draft plates) *Particles*: 1 mm, $8.2 \times 10^4$ *Droplets*: 60 $\mu$m, $7.2 \times 10^5$ 1/s | Particle and gas temperature Moisture content | • Assumption that particle-droplet collisions generate an uniform liquid layer around the individual particles • Varied coefficient of restitution that depends on Stokes number is used to model wet particle collisions • Particle temperatures are compared with infrared thermography measurements |
| Fries et al. (2013) [91] | Top-spray granulator Wurster coater Spouted bed *Particles*: 2 mm, $1.5 \times 10^5$ | Residence time Collision frequency and velocity Particle rotation (in different zones) | • CFD-DEM was used to investigate particle collision dynamics • Comparisons between different configurations • DEM model can offer large potential for process intensification |
| Hillton et al. (2013) [99] | Wurster coater *Particles*: 2 mm, $7 \times 10^3$ *Droplets*: 20 $\mu$m (normal distribution, treated as soft spheres) | Coating coverage Deposited droplet volume Coefficient of variation | • Spray droplets are modelled as individual Stokesian particles • The radially symmetric Gaussian shape is used to model droplet and particle impact • Coating coverage was mapped over individual particles based on the spherical harmonic formulation |

One solution to this problem is the DEM coarse grain model, in which several real particles are lumped into a computational parcel for the sake of reducing computational cost while retaining essential dynamics of the granular system. Accordingly, the drag force and contact force need to be scaled based on the coarse graining ratio. The coarse grain method can be applied to both mono-disperse and poly-disperse systems [66, 77]. Note that in some literature, coarse graining also refers to the method to map (average) from particle-scale quantities (DEM) to macroscopic quantities (CFD) [100].

Recently, DEM/CFD-DEM based on graphical processing units (GPUs), instead of traditional central processing units (CPUs), has been increasingly applied to various systems with spherical or non-spherical particles and moving wall boundaries [96, 101]. Besides, GPU simulation can be extended to other cases of discrete modeling, for instance, the simulation of particle breakage by time-driven constant-number Monte Carlo method [102]. The GPU-based parallel simulation and computation is one of the most promising techniques to accelerate simulation of granular systems [103].

## 1.2   Objective and outline

The aim of the present work is to investigate some important mesoscale phenomena for particle formation in spray fluidized beds, including coefficient of restitution of irregularly shaped particles, particle-particle collision frequency and impact velocity, mixing degree of poly-disperse particle system, residence time in Wurster fluidized bed, droplet deposition events, cohesion collisions, by means of PTV measurements and DEM/CFD-DEM simulations. These mesoscale phenomena are essential to directly or indirectly improve product quality in particle formation processes, but are not clearly understood by experimental or numerical approaches so far.

In Chapter 2, the detailed experimental algorithms used in the particle segmentation procedure and the particle tracking procedure are first described. Then, the entire PTV method is thoroughly verified based on synthetic images generated from CFD-DEM simulation of a poly-disperse particle system. In Chapter 3, the suitable set of formulations in CFD-DEM (LE) for the simulation of fluidized beds is clarified, starting from the derivation of traditional two-fluid method (EE). The sub-models of CFD-DEM used in this thesis, including drag models for mono- and poly-disperse systems, the mapping model, contact model, cohesion model and rolling model, are described. The experimental and simulation studies are mainly conducted in two pseudo-2D fluidized beds and a Wurster fluidized bed. In Chapter 4, all experimental and simulation setups are systemically introduced.

In Chapter 5, the collision behavior between irregular maltodextrin particles and horizontal substrates is experimentally measured by PTV method. In addition, the measurement data is compared with DEM simulations using the multi-sphere model and the superquadric model, regarding the distributions of total and normal coefficients of restitution and corresponding relationships with the rotational speed after collision and the absolute difference of incidence angle and rebound angle.

In Chapter 6, PTV method is used to measure complex granular flows in a pseudo-2D fluidized bed. The particle granular temperature, particle collision frequency and impact velocity are systematically investigated under various operation conditions. Collision events are identified by a self-developed algorithm based on the variation of individual particle trajectories. Measurement data are compared with CFD-DEM simulations. In Chapter 7, an extended color-PTV method is used to measure velocities of individual particles in poly-disperse particle systems. Experimental results are compared with CFD-DEM simulations using different drag models, in terms of the mixing index, time-averaged volumetric particle flux, distributions of individual particle velocity as well as distributions of particle granular temperature.

In Chapter 8, CFD-DEM is applied to investigate the residence time and collision velocity in different processing zones of a Wurster fluidized bed. Ideal and nonideal circulating motions of particles are distinguished to evaluate distributions of cycle times. Solid-like droplets are injected and simulated inside a predefined spray zone to study the droplet deposition rate. In Chapter 9, a coupled CFD-DEM-Monte Carlo approach is developed to investigate intra- and inter-particle coating uniformity in a Wurster fluidized bed by considering gas flow, particle motion, droplet deposition, and the drying and solidifying of droplets on particle surfaces. Based on the spherical centroidal Voronoi tessellation (CVT), the Monte Carlo approach can model the deposition and splashing of spray droplets on the surface of individual particles. The capillary force induced by liquid bridges between particles is accounted for in the DEM to investigate its influence on the coating and agglomeration behavior.

In Chapter 10, the main results of the thesis are summarized and an outlook to future studies is given.

In the appendices, supplementary measurement data and simulation results are summarized.

# Chapter 2

# Particle tracking velocimetry (PTV) methodology

*Parts of this chapter are based on Jiang et al. [104], Jiang et al. [45] and Jiang et al. [105].*

The granular flow in fluidized beds is characterized by three features: *i)* high solid volume fraction, *ii)* strong fluctuation velocity generated by particle-particle, particle-wall collisions and non-spherical shapes, and *iii)* high flow gradient on the scale of several particle diameters due to bubble motion, which raises issues in both particle segmentation and particle tracking procedures [40, 106]. Thus, reliable and accurate algorithms of particle segmentation and particle tracking are required to accurately measure complex granular flows in fluidized beds.

Based on sequences of images acquired from a high-speed imaging system, particle tracking velocimetry (PTV) consisting of the particle segmentation and particle tracking procedures can be used to recover the trajectories of all individual particles in the field of view, as depicted in Figure 2.1. The main task of the particle segmentation procedure is to detect the centroids of individual particles in each frame. Besides, other particle information such as the area, size and orientation can also be identified in this procedure. Then, the particle tracking procedure pairs identical particles in different frames using the particle centroids in two or multiple subsequent frames. After these two procedures, the trajectories of all individual particles, encompassing both centroids and velocity vectors, can be reconstructed. The algorithms of the procedures schematically represented in Figure 2.1 will be elaborated in this chapter.

## 2.1 Particle segmentation algorithms

### 2.1.1 Particle-mask correlation method

For relatively large spherical particles with a certain size, the particle-mask correlation method, proposed by Takehara and Etoh [107], can detect accurately their geometric centers, which correspond to the locations of the cross-correlation coefficient peaks. The
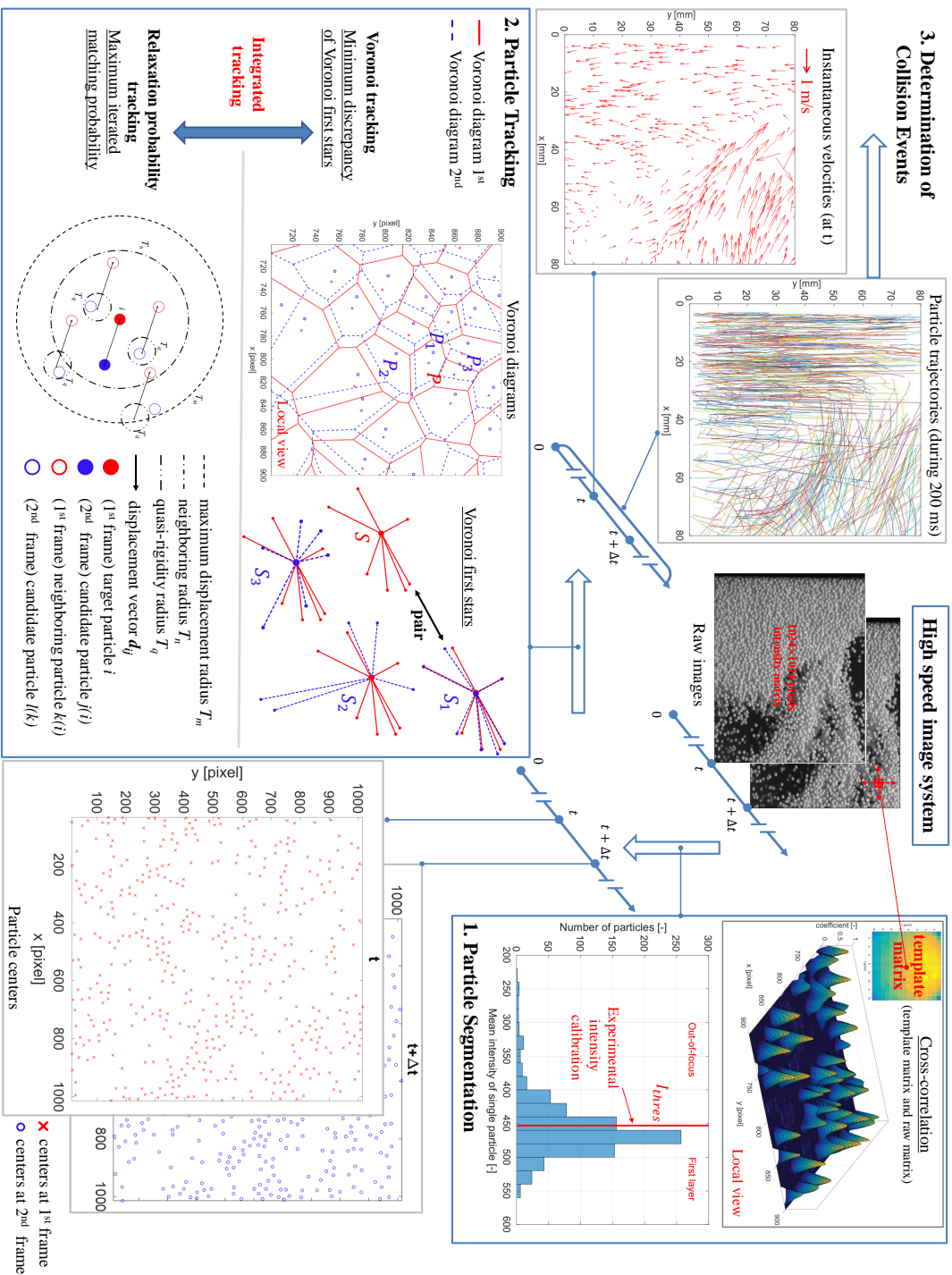
Figure 2.1: Schematic representation of the methodology of particle tracking velocimetry (PTV) for measuring complex granular flow.

Table 2.1: Summary of equations used in the particle segmentation procedure.

---

*Particle-mask cross-correlation + intensity filtering (spherical particles)*

*Normalized cross-correlation*

$$\gamma(x,y) = \frac{\sum\limits_{i=x-m/2}^{x+m/2} \sum\limits_{j=y-m/2}^{y+m/2} [I(i,j) - \bar{I}][s(i,j) - \bar{s}]}{\sqrt{\sum\limits_{i=x-m/2}^{x+m/2} \sum\limits_{j=y-m/2}^{y+m/2} [I(i,j) - \bar{I}]^2 \sum\limits_{i=x-m/2}^{x+m/2} \sum\limits_{j=y-m/2}^{y+m/2} [s(i,j) - \bar{s}]^2}} \tag{2.1}$$

*Intensity filtering*

$$\bar{I}_{p,k} \geq I_{thres}, \bar{I}_{p,k} = \sum_{i}^{N_{p,k}} I(i)/N_{p,k} \tag{2.2}$$

---

*Image moment (non-spherical particles in dilute systems)*

*Raw image moment*

$$M_{pq} = \sum_x \sum_y x^p y^q I(x,y) \tag{2.3}$$

*Centroid*

$$(\bar{x}, \bar{y}) = (\frac{M_{10}}{M_{00}}, \frac{M_{01}}{M_{00}}) \tag{2.4}$$

*Normalized central moment*

$$\mu_{pq} = \sum_x \sum_y (x - \bar{x})^p (y - \bar{y})^q I(x,y)/M_{00} \tag{2.5}$$

*Covariance matrix*

$$cov(I(x,y)) = \begin{bmatrix} \mu_{20} & \mu_{11} \\ \mu_{11} & \mu_{02} \end{bmatrix} \tag{2.6}$$

*Orientation*

$$\theta_o = \frac{1}{2} \arctan\left(\frac{2\mu_{11}}{\mu_{20} - \mu_{02}}\right) \tag{2.7}$$

*Lengths of major and minor axes*

$$L_{major} = \sqrt{2}\sqrt{\mu_{20} + \mu_{02} + \sqrt{(\mu_{20} - \mu_{02})^2 + 4\mu_{11}^2}} \tag{2.8}$$

$$L_{minor} = \sqrt{2}\sqrt{\mu_{20} + \mu_{02} - \sqrt{(\mu_{20} - \mu_{02})^2 + 4\mu_{11}^2}} \tag{2.9}$$

---

intensity pattern of this type of particles always has a clear peak in the center, and the intensity concentrically decreases as the distance from the central location increases. The merits of this segmentation approach are: (i) only particles with complete contour are identified, even when intensity peaks do not coincide with particle centers, (ii) the effects of linear elements and background elements on segmentation performance are avoided automatically [108].

The normalized cross-correlation coefficient $\gamma$ of the template particle (m $\times$ m pixels) with any interrogation region of the same size in the raw image, centered at $(x, y)$, can be calculated by Eq. (2.1) in Table 2.1. The quantity $I(i, j)$ is the intensity in the matrix of the interrogation region in the raw image, $s(i, j)$ is the intensity in the matrix of the template particle. $\bar{I}$ and $\bar{s}$ are the spatially averaged intensities of the interrogation region of the raw image and the template particle, respectively. The template particle matrix is a square matrix with the edge size $m$ equal to $\sqrt{2}d_p \cdot S_f/2$ pixel (spherical particles).

For each measurement, several complete and smooth particles are required to be manually selected from the raw image, and the intensity fields of these particles are used to average the intensity field of the template particle in a way that eliminates the influence of random noise. The obtained template particle is used to scan the entire raw image pixel by pixel, which produces a matrix of the normalized cross-correlation coefficient. Then, the locations of qualified peaks in the coefficient matrix correspond to particle centers $\boldsymbol{r}_k(x_k, y_k)$. The locations of peaks are identified by a peak finder approach, including the evaluations of 2-D median filtering, convolution and local maxima.

Particles that depart from the first layer, still having similar intensity distribution but much lower intensity value, will be recognized by the particle-mask correlation method. Most of these particles are found in the dilute region, in which particles rarely overlap with neighboring particles, and thus, show the complete intensity distribution. Therefore, the threshold mean intensity $I_{thres}$, obtained from the intensity calibration (detailed method given in Section 4.2.1), is used to re-check the mean intensity of each detected individual particle $\bar{I}_{p,k}$, expressed as Eq. (2.2) in Table 2.1. $N_{p,k}$ is the number of pixels that belong to particle $k$. This procedure filters the out-of-focus particles identified by intensity value. Contrary, there is a high probability that an optical overlap with neighboring particles will occur when particles in the dense region depart from the first layer. As a consequence, the intensity distributions of these particles deviate from that of the template particle, and they cannot be detected by the particle-mask correlation segmentation approach. Hence, the particle-mask correlation method together with intensity filtering enable to adapt to different solid volume fractions.

## 2.1.2   Thresholding, watershed segmentation and image moment

For non-spherical particles, even though owning a certain particle geometry (for example, tablets in Figure 2.2a), the performance of the mask correlation method rapidly
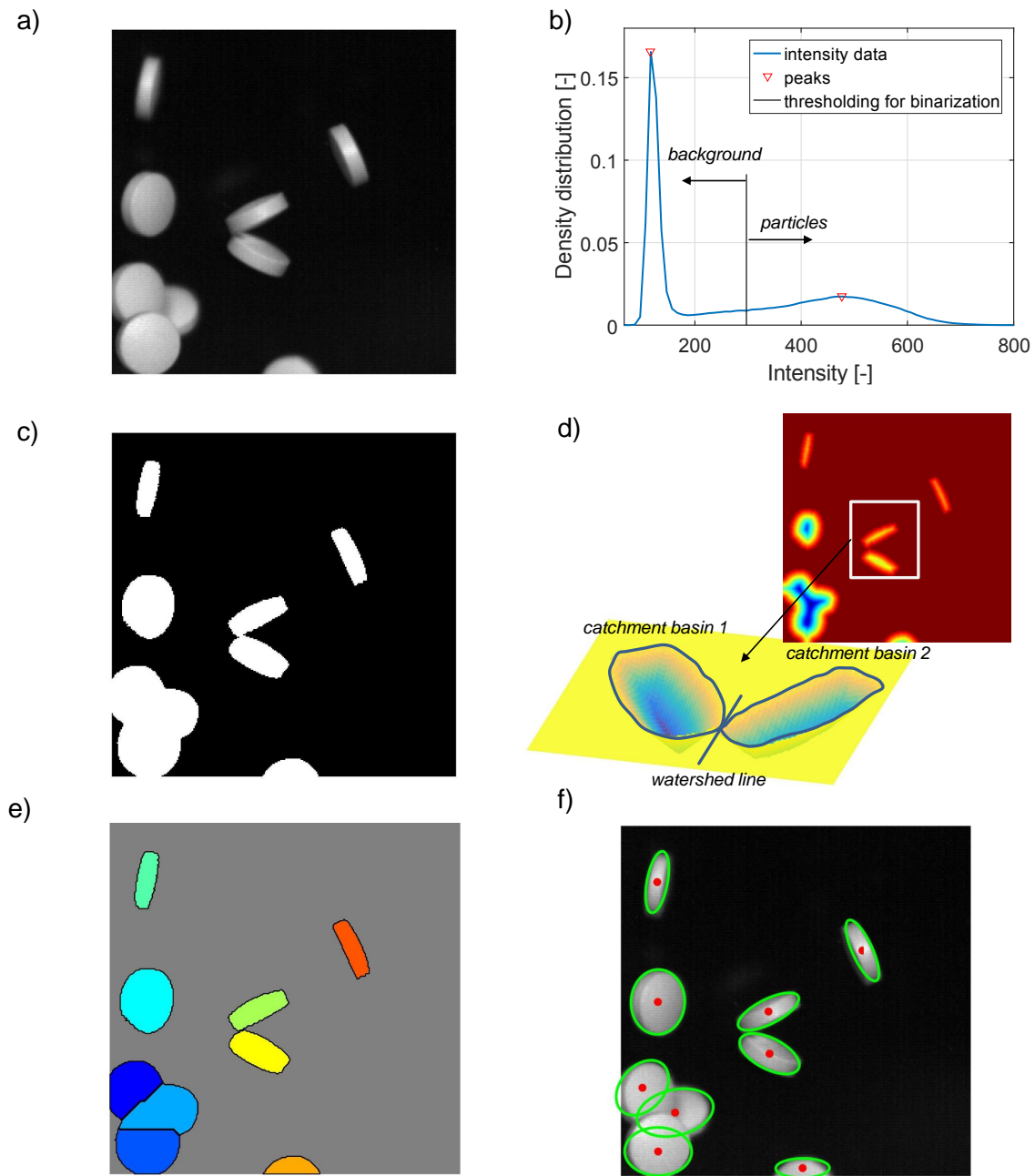
Figure 2.2: Illustration of the binarization by the automatic thresholding and the watershed segmentation: a) original gray-scale image (with tablets), b) determination of the threshold intensity by analysis of the pixel intensity distribution, c) binary image of tablets, d) distance transformation based on the binary image and an example of catchment basins and watershed line of two slightly overlapping tablets, e) connected regions after the watershed segmentation, f) particle centroids and equivalent ellipses owning the same normalized second order image moments as the segmented regions.

decreases due to the orientation of particles. The problem becomes even worse for irregularly shaped particles with wider size and shape distributions (for instance, maltodextrin particles in Figure 4.2a). Indeed, selection and segmentation of irregular objects within the image is an important prerequisite for most measurements and analyses. In this thesis, the segmentation of non-spherical particles is achieved by binarization, distance transformation and watershed processes; then, the image moment is used to get important properties related to particle shape.

*Binarization by thresholding*

The objective of binarization is to separate features representing particles from the background, so that further counting and measurement can be performed. The binarization can be achieved by the thresholding intensity value, or combining different color channels (RGB or HSV, discussion in Section 7.2). After binarization, the regions of particles and background are assigned values of unity and zero, respectively. For each image, the threshold intensity was estimated by the analysis of density distribution of pixel intensities, as shown in Figure 2.2b. Normally, two peaks exist in the profile of density distribution; one belongs to the background with a relatively narrow width, the other is the result of the particle regions with a larger width. The intensity located at the midpoint of these two peaks is selected as the threshold intensity. The result of binarization by thresholding is shown in Figure 2.2c. However, the binary image is not perfect to identify the features of every individual particle, due to the difficulty arising from overlapping particles.

*Distance transformation and watershed segmentation*

The distance transformation is a tool that gives new features to the binary image to reproduce a gray-scale image, as shown in Figure 2.2d. The definition of distance transformation is simple enough: each pixel in the foreground is assigned a brightness value equal to its straight line distance to the nearest pixel in the background. The distance transformation can enhance the convex features of touching particles, which is a benefit in efficiently performing the watershed segmentation. Imagining that the brightness values of each pixel after the distance transformation correspond to a physical elevation; then the features appear as mountain peaks or sometimes the distances need to be negated to change mountains to catchment basins. As shown in Figure 2.2d, after distance transformation, two slightly overlapping particles are converted into two adjacent basins separated by a watershed line. The placement of the watershed line depends on the relative depth and area of the adjacent basins. The detailed algorithm was proposed by Meyer [109]. As shown in Figure 2.2e, overlapping particles can be separated by watershed segmentation; and each color stands for one individual particle reckoned as a connected region.

*Image moment*

After having identified the connected regions of individual particles, the image moment, related to well known algebraic invariants, can be used to calculate important geometrical properties based on the intensity of segmented pixels. Hu [110] published the first

significant paper on the use of image moment invariants for two-dimensional pattern recognition applications. For a two-dimensional digital image with intensity $I(x, y)$ of individual pixels, raw image moments $M_{pq}$ with of order $p + q$ can be calculated by Eq. (2.3) in Table 2.1. $I(x, y)$ of particles equals to unity in a binary image. The centroid $(\bar{x}, \bar{y})$ of the particle can be evaluated using raw image moments according to Eq. (2.4), in which $M_{00}$ is the area of particle (total number of pixels).

In addition, the normalized central moment, defined by Eq. (2.5), can be used to further analyze the covariance matrix, giving the orientation, and the major and minor axes of particles. Indeed, if only the second order $(p + q = 2)$ central moments are considered, the particle is completely equivalent to an ellipse centered at the particle centroid $(\bar{x}, \bar{y})$ with a certain size and orientation [111]. The orientation of a particle calculated by Eq. (2.7) can be evaluated from the covariance matrix calculated by Eq. (2.6). In this way, the orientation specifies the angle in a range from $-90°$ to $90°$ between the horizontal axis and the major axis of the covariance matrix. It is constructed from the second central moments $\mu_{11}$, $\mu_{02}$ and $\mu_{20}$. The expressions for $L_{major}$ and $L_{minor}$ are given by Eq. (2.8) and Eq. (2.9), respectively.

## 2.2 Particle tracking algorithms

The objective of particle tracking is to pair particles between frames based on the two sets of particle centroids $\boldsymbol{r}_{i,1}$ and $\boldsymbol{r}_{j,2}$ obtained from particle segmentation procedure. The pairing $\{i(k), j(k)\}$ means that particle $P_i$ on the first frame and particle $P_j$ on the second frame are the same physical particle $k$. Considering a time interval $\Delta t$ between two subsequent frames, the individual particle velocity can be calculated by

$$\boldsymbol{v}_k = \frac{\boldsymbol{r}_{i(k),2} - \boldsymbol{r}_{j(k),1}}{\Delta t}. \tag{2.10}$$

Different algorithms can be used to track particles depending on the solid volume fraction and the features of motion.

### 2.2.1 Minimum displacement tracking method

If the time interval between two frames is short enough and the mean free paths between particles are large enough, it is reasonable to match each particle in the first frame to the nearest particle in the second frame. This simple algorithm is the *minimum displacement tracking*, which is a good choice to track individual particles in the dilute region, especially when the general motion of particles is predictable. The best global match of all particles $P_i$ in the second frame can be achieved by minimizing the objective function

$$\sum_{k=1}^{n_1} dis_p(P_{i(k),1}, P_{j(k),2}), \tag{2.11}$$

where the particle displacement $dis_p(P_{i(k),1}, P_{j(k),2})$ is the standard Euclidean distance of two paired particles corresponding to physical particle $k$ between first and second

frame. In two-dimensional Cartesian coordinates, the Euclidean distance of particles $P_a$ and $P_b$ is given by

$$dis_p(P_a, P_b) = \sqrt{(x_a - x_b)^2 + (y_a - y_b)^2}. \tag{2.12}$$

The sum over the displacements of all matching pairs is calculated to find the best global matching. If the motion of a particle is predictable, the number of candidate particles $P_{j,2}$ can be narrowed by introducing a search circle with diameter estimated from the maximum detected particle velocity.

### 2.2.2   Voronoi tracking method

However, it is challenging to simultaneously track a large number of individual particles in the dense region of a fluidized bed, where the particles undergo a complex motion that is caused by traveling bubbles and particle-particle or particle-wall interactions. To address these problems, Capart et al. [40] and Hagemeier et al. [42] used tracking methods with favorable features of Voronoi structures (generated from centroids of detected particles) to pair particles in two consecutive frames with short interval. The Voronoi star is a matching token assembled by the target particle (center of star) and corresponding natural neighboring particles (endpoints of the extremities of the star), which is relatively stable even in complex granular flows. Thus, the discrepancy of Voronoi stars in two subsequent frames is considered as the measure of identification.

Consider a set of particles $P_i$ that occupy positions $\boldsymbol{r}_i(x_i, y_i)$ in the plane ($i = 1, ..., n$). The _Voronoi diagram_ designates the tiling of the plane into $n$ polygonal regions such that each polygon encompasses the region which is closer to particle $P_i$ than to any other particle, as shown in Figure 2.1. The particles characterized by Voronoi diagram sharing an edge are termed _natural neighbors_ of each other; and the graph that connects natural neighbors defines the _Delaunay triangulation_. The _Voronoi first star_ $S_i$ of $P_i$ is defined as the set of natural neighbors including itself, which can be visualized as a "star of spokes".

The applicability and detailed Voronoi algorithm for tracking particles in the fluidized bed have been well explained by [40, 42], mainly including the estimation of candidate particles and calculation of the discrepancy of Voronoi first stars. Briefly, the match candidate particles $j$ in the second frame are selected as the four nearest natural neighbors of target particle $i$ in the first frame. Expressed as Eq. (2.13) in Table 2.2, the discrepancy of Voronoi first stars $dis_S(S_i, S_j)$ reflects the degree of deviation between the patterns formed by two stars. Three steps are included in Eq. (2.13): i) a linear translation is conducted to coincide the centers of two stars, in which the subscript 0 of $\boldsymbol{r}$ means the center of star; ii) an inner loop, based on the minimum Euclidean norm, to find the nearest extremity of $S_2$ for each extremity $\boldsymbol{r}_{k1,1}$ of $S_1$; iii) an outer loop based on the median norm, whereby the median value obtained from the inner loop is adopted as an overall measure of the discrepancy of Voronoi first stars. This method allows comparisons between any two stars, without the requirement of them having the

Table 2.2: Summary of equations used in the integrated particle tracking algorithm.

---

*Voronoi tracking method*

---

*Discrepancy of Voronoi first stars*

$$dis_S(S_1, S_2) = \underset{k_1=1\ldots N_1}{\text{median}} \left[ \min_{k_2=1\ldots N_2} |(\boldsymbol{r}_{k1,1} - \boldsymbol{r}_{0,1}) - (\boldsymbol{r}_{k2,2} - \boldsymbol{r}_{0,2})| \right] \quad (2.13)$$

$$match(P_{i,1}) = min(dis_S(S_{i,1}, S_{j,2}))) \quad (2.14)$$

---

*Probability relaxation method*

---

*Quasi-rigidity condition*

$$|\boldsymbol{d}_{ij(i)} - \boldsymbol{d}_{k(i)l(k)}| < T_q, \quad (2.15)$$

$$\sum_{j(i)=1}^{m_{c(i)}} \mathbb{P}_{ij(i)} + \mathbb{P}_i^* = 1, \quad (2.16)$$

$$\mathbb{Q}_{ij(i)}^{(n-1)} = \sum_{k(i)=1}^{m_{n(i)}} \sum_{l(k)=1}^{m_{c(k)}} \mathbb{P}_{k(i)l(k)}^{(n-1)}, \quad (2.17)$$

$$\tilde{\mathbb{P}}_{ij(i)}^{(n)} = A \cdot \mathbb{P}_{ij(i)}^{(n-1)} + B \cdot \mathbb{Q}_{ij(i)}^{(n-1)} \quad (2.18)$$

$$\mathbb{P}_{ij(i)}^{(n)} = \frac{\tilde{\mathbb{P}}_{ij(i)}^{(n)}}{\sum_{j(i)=1}^{m_{c(i)}} \tilde{\mathbb{P}}_{ij(i)}^{(n)} + \mathbb{P}_i^{*(n-1)}} \quad (2.19)$$

$$\mathbb{P}_i^{*(n)} = \frac{\mathbb{P}_i^{*(n-1)}}{\sum_{j(i)=1}^{m_{c(i)}} \tilde{\mathbb{P}}_{ij(i)}^{(n)} + \mathbb{P}_i^{*(n-1)}} \quad (2.20)$$

$$match(P_i) = max(\mathbb{P}_{ij(i)}) \quad (2.21)$$

---

*Integrated method*

$$M_{IT} = M_{VTM} \cup M_{PRM} \quad (2.22)$$

---

same number of extremities. The best match of target particle $i$ thus is the candidate with the minimum discrepancy of Voronoi first star, expressed as Eq. (2.14). Identifiers (IDs) are assigned to the two particles of each pair and all information related to shapes, locations and velocities is stored in the set $M_{VTM}$.

## 2.2.3 Probability relaxation method

Alternatively, the *probability relaxation method* has been widely used to track particles in complex fluid flows [106, 108, 112–114]. The underlying concept of the probability relaxation method is to iteratively match the target particle to one of its candidate particles in the second image based on the total probability of neighboring particles satisfying the quasi-rigidity condition. It assumes that the motion of neighboring particles is similar and the corresponding velocity gradients are relative small in short enough time intervals. As a result of successful iteration, the matching probability of correct pairs approaches almost unity while others tend to zero. Developed for motion analysis in the field of image recognition and computer vision [115], the original implementation of the probability relaxation method in fluid mechanics was proposed by Baek and Lee [112]. Because the original approach provided satisfactory recovery ratio, it has been used in the present work aiming at both accuracy of measurements and global reconstruction speed of particle trajectories. The basic scheme of the probability relaxation method is described in Figure 2.1, whereas detailed procedures employed here follow the study of Baek and Lee [112].

*Three selecting radii*

There are three special radii in the probability relaxation method. The maximum displacement radius $T_m$ is predefined to search candidate particles ($j$) of target particle ($i$) in the second frame. The neighboring radius $T_n$ is applied to find neighboring particles ($k$) of target particle ($i$) in the first frame. Similarly, candidate particles of neighboring particles $k$ (referred as $l$) are limited by the same maximum displacement radius $T_m$ in the second frame. Further, the quasi-rigidity radius $T_q$ is selected to determine which neighboring particles can be used to update the matching probability $\mathbb{P}_{ij(i)}$ of each candidate particle $j$ to the target particle $P_i$. The quasi-rigidity condition can be expressed as Eq. (2.15) in Table 2.2; where $\boldsymbol{d}_{ij(i)}$ is the displacement vector from target particle ($i$) to its candidate particles ($j$), and $\boldsymbol{d}_{k(i)l(k)}$ is that from neighboring particles ($k$) to their candidate particles ($l$). Generally, the matching probability $\mathbb{P}_{ij(i)}$ has to satisfy Eq. (2.16), in which $m_{c(i)}$ is the total number of candidate particles ($j$) of target particle ($i$), and non-matching probability $\mathbb{P}_i^*$ is the probability of target particle ($i$) to have no matching particle. The initial value of $\mathbb{P}_{ij(i)(0)}$ and $\mathbb{P}_i^{*(0)}$ can be given as $1/(m_{c(i)} + 1)$.

*Iteration formulation*

Then, the matching probability $\mathbb{P}_{ij(i)}$ is iterated by the sum probabilities of neighboring particles ($k$) meeting the quasi-rigidity condition (Eq. (2.15)), which is represented as Eq. (2.17). $m_{n(i)}$ is the total number of neighboring particles ($k$) of target particle

$(i)$, and $m_{c(k)}$ is the number of candidate particles $(l)$ of neighboring particle $(k)$. The superscript $n-1$ denotes the iteration step. Further, the contribution of neighboring particles $\mathbb{Q}_{ij(i)}^{(n-1)}$ can be included in the iteration formulation for updating the matching probability $\mathbb{P}_{ij(i)}$ by Eq. (2.18), in which $\tilde{\mathbb{P}}_{ij(i)}^{(n)}$ is the non-normalized probability that needs to be normalized before the next iteration step, by the expressions of Eqs. (2.19) and (2.20). In the iteration equation (Eq. (2.18)), A$(> 1)$ and B$(< 1)$ are constants and affect the convergence speed of the iteration. Note that the non-matching probability $\mathbb{P}_i^{*(n)}$ is not directly considered in the iteration equation, but iterated in the normalization process. Finally, the most probable matching particle for the objective particle $(i)$ is chosen as the one with the largest matching probability $\mathbb{P}_{ij(i)}$ approaching unity, expressed as Eq. (2.21). Identifiers (IDs) are assigned to the two particles of each pair and all information related to shapes, locations and velocities is stored in the set $M_{PRM}$.

The integrated tracking data $M_{IT}$ is based on the set union $(\cup)$ of pairing information in two matrices $M_{VTM}$ and $M_{PRM}$ . If the same particle (with a certain particle center) possesses different pairing information, the pairing with minimum velocity is retained.

## 2.3   Verification by synthetic images

### 2.3.1   Principle

The accuracy of measurement is a quantitative performance characteristic, expressing the agreement between a measurement result and the value of the quantity to be measured. With regards to the PTV measurements in fluidized beds, the measured quantity is the velocity distribution of a large number of individual particles under different fluidization conditions. According to Figure 2.3, the uncertainty sources associated with the PTV methodology include individual particle locations (related to the particle segmentation algorithm) and the performance of particle pairing in two consecutive frames (related to both the particle segmentation algorithm and the integrated particle tracking algorithm). Whether particles can be identified and further tracked affects, the global performance of PTV. After successful tracking, the evaluation of single particle velocity is directly influenced by the biases of particle location segmentation.

Hence, suitable criteria are essential for quantitatively evaluating the performance of the algorithms used in the proposed PTV methodology. First, the bias of individual location of segmented particle was used to identify the uncertainty of evaluation of individual particle velocity; this is defined as

$$L_{b,i} = \sqrt{(x_i - x_{i,t})^2 + (y_i - y_{i,t})^2}, \qquad (2.23)$$

where $(x_i, y_i)$ is the location vector of segmented particle $i$, and $(x_{i,t}, y_{i,t})$ is its true location vector. Following the works of Baek and Lee [112] and Hassan et al. [116], the segmentation ratio, the recovery ratio and the error ratio were used as criteria to
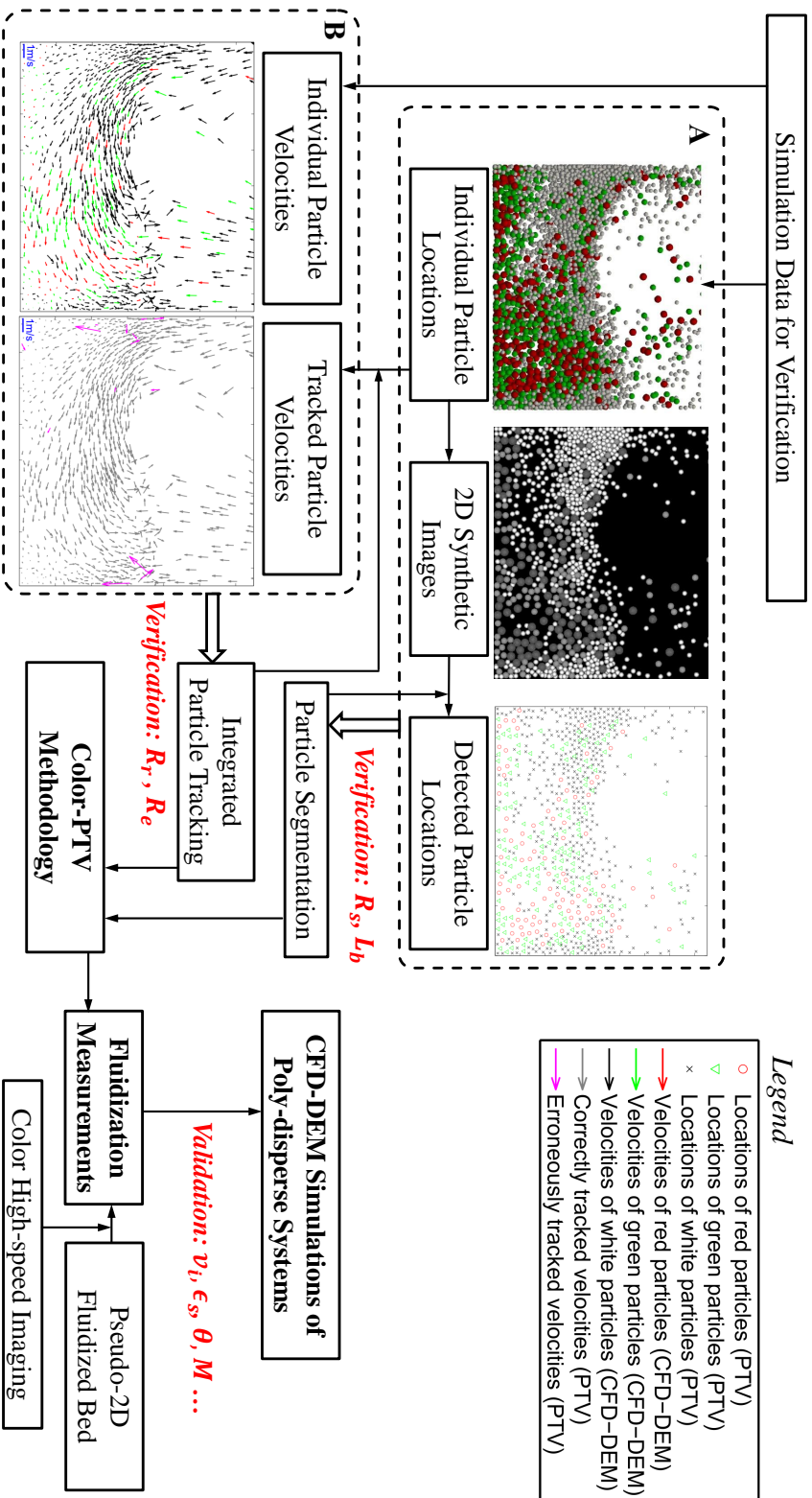
Figure 2.3: Schematic representation of the two-way verification/validation of PTV measurement and CFD-DEM simulation: block A illustrates the verification of the particle segmentation algorithm based on $R_s$ and $L_b$; block B describes the verification of the integrated particle tracking algorithm based on $R_r$ and $R_e$ (erroneously tracked vectors are marked in magenta to distinguish from correct vectors in the right sub-figure). The verified color-PTV methodology can be applied to images from fluidization measurements to validate corresponding CFD-DEM simulations.

verify the global performance of the particle segmentation algorithm and the integrated particle tracking algorithm. Specifically, the segmentation ratio $R_s$ is defined as

$$R_s = \frac{number\, of\, segmented\, particles}{total\, number\, of\, particles}; \qquad (2.24)$$

the recovery ratio $R_r$ is defined as

$$R_r = \frac{number\, of\, accurate\, vectors}{total\, number\, of\, recovered\, vectors}; \qquad (2.25)$$

and the error ratio $R_e$ is defined as

$$R_e = \frac{number\, of\, error\, vectors}{total\, number\, of\, recovered\, vectors}. \qquad (2.26)$$

However, it is difficult to directly acquire all quantities necessary in order to apply criteria from a large number of particles with complex motion by experiments. Therefore, data from CFD-DEM simulations, performed according to the experimental configuration and operating conditions, were instead used to verify the PTV methodology in the present work. The basic idea was similar to the synthetic (standard) images approach for evaluating PIV algorithms [117–119]. The main advantages in using CFD-DEM simulation data are:

1. As a well established simulation method, CFD-DEM can properly describe the motion of particles in granular systems (discussed in Chapter 3).

2. CFD-DEM simulation data can represent particle motion under different fluidization conditions.

3. All required variables in Eq. (2.23) to Eq. (2.26) can be easily retrieved from CFD-DEM data.

Therefore, the use of CFD-DEM simulation data is complementary to real experimental images because it is a powerful approach to investigate the effects of associated parameters (such as solid volume fraction, particle velocity, granular temperature, etc.) on the accuracy of particle velocity measurement, as well as to estimate the intrinsic limitations of the methodology.

Figure 2.3 shows the flow chart of verification of the color-PTV methodology based on synthetic images generating from simulation data, including block A for particle segmentation and block B for integrated particle tracking. After verification, the color-PTV methodology can be used to evaluate particle dynamics and mixing behavior based on color images acquired from fluidization measurements in the pseudo-2D fluidized bed. In addition, measurement data can be used to validate corresponding CFD-DEM simulations of poly-disperse particle systems. The detailed numerical setup of the CFD-DEM simulation is given in Section 4.3.3.

Corresponding to block A, synthetic images were generated to evaluate the performance of the segmentation algorithm by means of the bias $L_b$ and the segmentation ratio $R_s$. In order to be close to pseudo-2D conditions, only particles in the first layer were selected from three-dimensional CFD-DEM simulation data to generate two-dimensional synthetic images, which means that the normal distances from the centers of selected particles to the front wall were smaller than 3 mm. According to the descending order of the distances to the front wall, contours of individual particles with different sizes were created in each image based on the corresponding relative intensity distribution (details in Section 7.2). By this approach, the overlap between particles that is encountered in measurement images was intentionally introduced to inspect its effect on the particle segmentation. According to the analysis of measurement images, 0.1 % noisy pixels were randomly introduced to fit the real image quality. In terms of spatial resolution, the gray-scale synthetic image was the same as the raw image from measurements. Based on the particle-mask correlation segmentation, three template particles were separately used to process each synthetic image and to obtain the segmented locations of particles with different sizes. Then, the bias $L_b$ and the segmentation ratio $R_s$ were evaluated by the comparison of individual particles.

Corresponding to block B, the integrated particle tracking algorithm was verified by means of the recovery ratio $R_r$ and the error ratio $R_e$. Using a unique ID for each particle in the DEM solver, particle velocities can be easily evaluated from the location of each individual particle before and after a time step (Eq. (2.10)). However, a sequential labeling process was required to extract the pairing information obtained from integrated PTV method. In the first frame, unique IDs were assigned to all segmented particles. After successful pairing, each matched candidate particle in the second frame received the same ID as in the first frame. Candidate particles without a valid partner received a new ID. Then, tracked particle velocities can be also evaluated by Eq. (2.10). The process was repeated for all image sequences to obtain the trajectories of all individual particles. In order to gain the numerators in Eq. (2.25) and Eq. (2.26), particle velocities in the same time step obtained from PTV and CFD-DEM were compared one by one according to the locations and the lengths of vectors.

The thorough analysis of segmentation ratio, recovery ratio and error ratio with respect to particle velocity, solid volume fraction and granular temperature can be further conducted to assess the applicability of the PTV method to measure the dynamics of poly-disperse particle systems in different fluidization conditions.

## 2.3.2   Verification of segmentation algorithm

Figure 2.4 shows the cumulative distribution of bias $L_{b,i}$ of individual segmented locations according to analysis of approximately $2.5 \times 10^7$ particles. Due to the discrete nature of digital images, possible bias values were 0, 1, $\sqrt{2}$, 2, $\sqrt{5}$, $\sqrt{8}$, and 3 pixels. When the segmented particle location coincides with the corresponding particle location in DEM data, the bias $L_{b,i}$ is zero. Generally, the particle-mask correlation segmentation algorithm shows good performance for particles with different sizes. More than
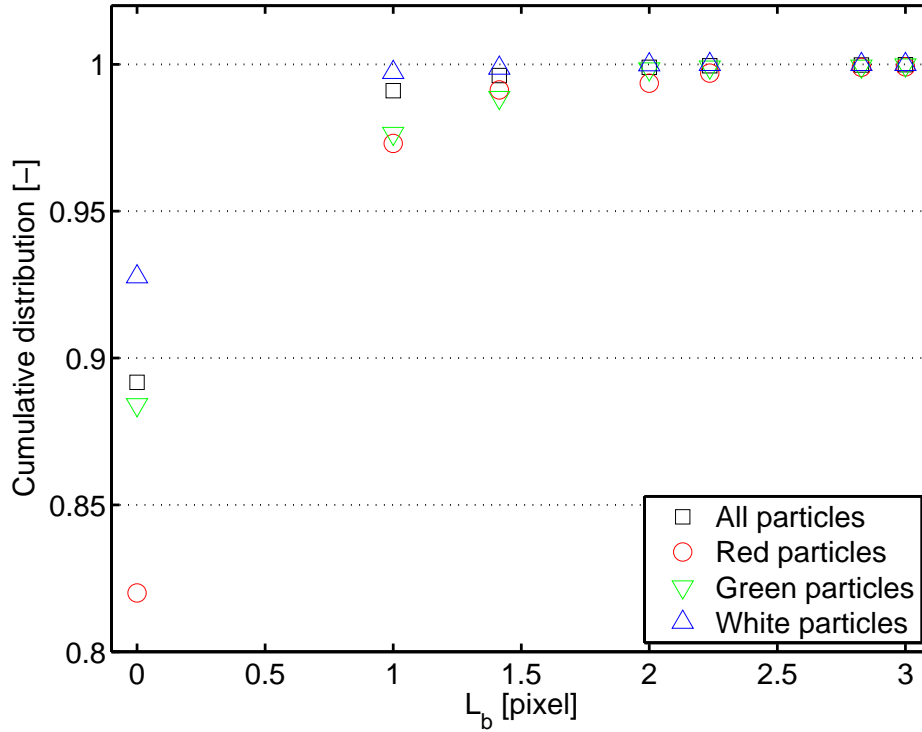
Figure 2.4: Cumulative distribution of the bias of particle-mask correlation segmentation (analysis of approximately $2.5 \times 10^7$ particles).

89 % of all particles can be identified without any error. The cumulative distribution for all particles reaches unity at $\sqrt{8}$ pixels, which indicates the high precision of particle segmentation. Smaller particles are more accurately located compared with larger particles. The mean values of bias $L_{b,i}$ of all particles, red particles, green particles and white particles were 0.11, 0.31, 0.13, and 0.07 pixel, respectively.

For the particle-mask correlation approach, the segmentation ratio was mainly influenced by the solid volume fraction that was calculated as the ratio of the total particle volume to the volume of the investigation region. To this end, the full image was divided into small investigation regions with a size of $75 \times 75$ pixels, and an overlap of 2/3 was set between two neighboring regions to obtain better spatial resolution. The Sauter mean diameter $d_{32}$ was considered as the depth of investigation region in this study. This method of partitioning the investigation region will be used in all following post-processing. For the case of the verification study, the mean value of solids volume fraction was 0.136 with a standard deviation of 0.120 for all data from 30 s simulation time.

Figure 2.5a shows the segmentation ratio $R_s$ for all three sizes of particles with respect to solid volume fraction $\epsilon_s$. The points are averages, where the two dash lines define the region covered by the standard deviation of data. Globally, the segmentation ratio for all particles is close to unity when the solid volume fraction is lower than 0.2. Then,
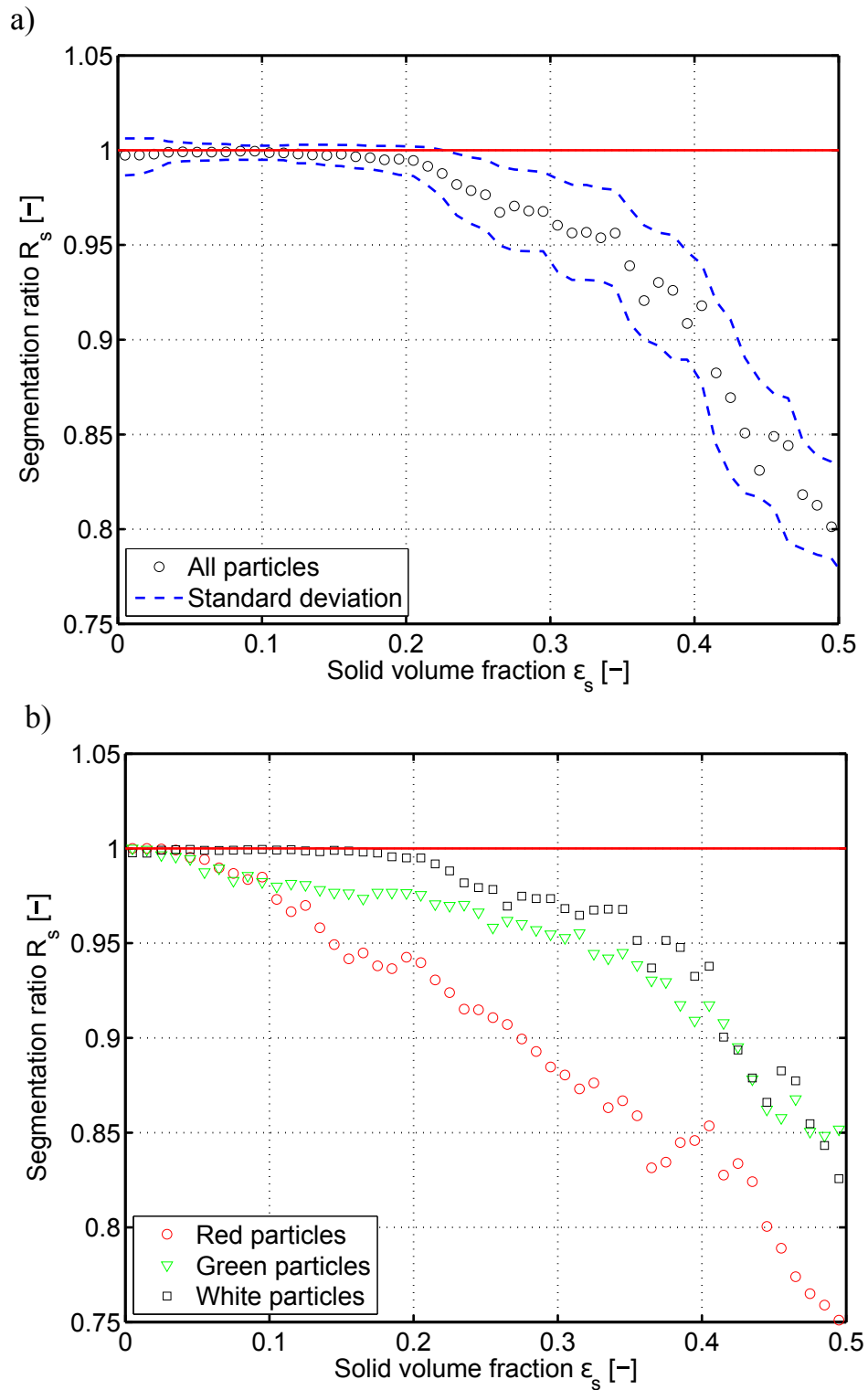
Figure 2.5: Segmentation ratio $R_s$: a) all particles with standard deviation, b) particles of different sizes (colors).

there is a decreasing tendency of the segmentation ratio when the solid volume fraction increases from 0.2 to 0.5. The standard deviation of segmentation ratio experiences a similar tend: it is small when the solid volume fraction is smaller than 0.2 and gradually increases after the solid volume exceeds 0.2. In fact, the standard deviation can be considered as a quantification of precision in respect to the random errors of measurements. Reasonably, the inevitable overlap of particles in the dense region led to a decrease of segmentation ratio and an increase of the corresponding standard deviation, since the segmentation algorithm depends on intensity distribution on the surface of individual particles.

Figure 2.5b shows the influence of different sizes (colors) on the segmentation ratio. The smaller the particle size (white), the better the performance of particle segmentation, because the gray-scale intensity distribution on the surface of small particles is more pronounced compared to other particles. In other words, the more pronounced the intensity distribution, the less is the interference of overlap of particles with the segmentation algorithm.

Nevertheless, the particle segmentation algorithm shows very good accuracy and precision in the primary range of solid volume fraction. For the largest solid volume fraction, the lowest value of segmentation ratio of red particles is still larger than 0.75. Notably, the intensity of individual particles is also affected by the shadowing effect of neighboring particles and the motion blur effect in real fluidization measurements, which were not included in the current verification study of particle segmentation. There should be a certain decrease in segmentation ratio to take account of these two negative effects in real measurements.

### 2.3.3 Verification of integrated tracking algorithm

Figure 2.6 shows the influence of different tracking algorithms on the recovery ratio with respect to solid volume fraction. The Voronoi method is more suitable in the dense region, in terms of both accuracy and precision. However, if the solid volume fraction is lower than 0.2, there is a large decrease in recovery ratio. In the dilute region, the mean free paths of neighboring particles (the extremities of Voronoi first order stars) are relatively large. Hence, the loss of single particles in the dilute region, caused by motion in third direction vertically to the front wall, can generate relatively large discrepancies of several nearby Voronoi first order stars, compared to the discrepancies generated by the in-plane motion of particles. This instability of Voronoi first order stars may cause erroneous pairing of target particles in the dilute region. However, the negative effect of this instability is very small in the dense region due to the naturally shorter mean free paths.

In case of the relaxation probability tracking method, the recovery ratio decreases gradually with increasing solid volume fraction, whereas the standard deviation is larger than that of the Voronoi method for most solid volume fractions. Remarkably, the Voronoi method and the relaxation method are complementary in terms of the recovery ratio, especially in the dilute region (solid volume fraction smaller than 0.1). As a consequence,
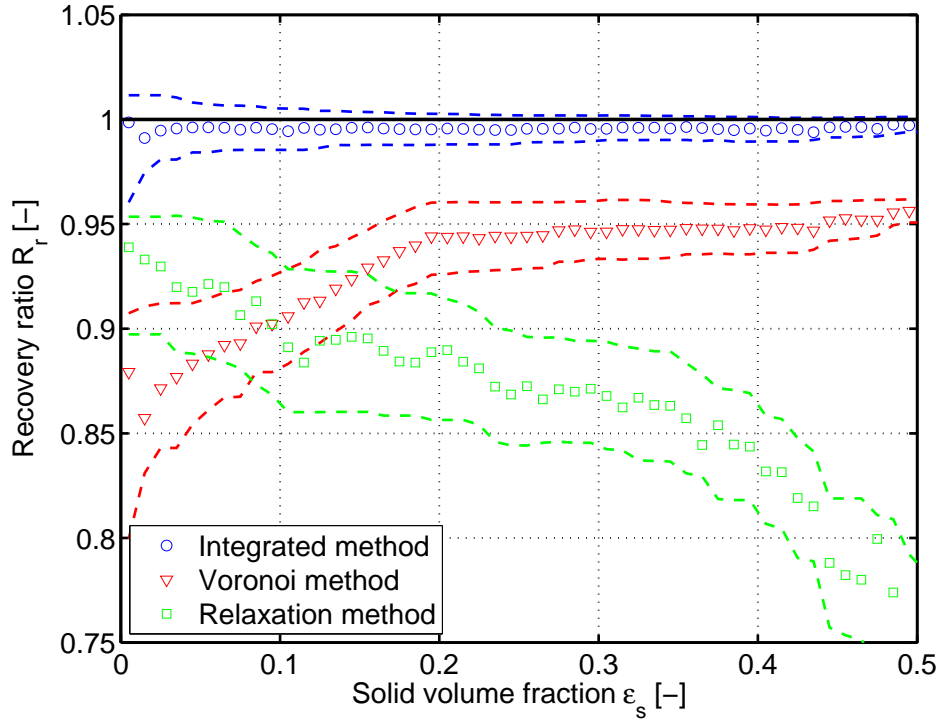
Figure 2.6: Comparison of recovery ratio $R_r$ from the integrated tracking method, the Voronoi tracking method and the relaxation probability tracking method (standard deviations for the different methods are labeled by two dashed lines of corresponding colors).

the final recovery ratio obtained by the integrated tracking method is very close to unity in almost the entire range of solid volume fractions. Moreover, the standard deviation of the integrated tracking method is smaller than that of either single tracking method. Hence, use of the integrated particle tracking helps to achieve high performance for all solid volume fractions. For all three tracking methods, the error ratio was lower than 0.005 and had no apparent dependence on the solid volume fraction.

It should be noted that the recovery ratio and error ratio were not only influenced by the solid volume fraction, but were also significantly affected by the local particle dynamics such as particle velocity and particle granular temperature. For the parameters of the verification study, the mean value of particle velocity was 0.311 m/s with a standard deviation of 0.206 m/s; and the mean value of the square root of particle granular temperature was 0.132 m/s with a standard deviation of 0.084 m/s.

Figure 2.7a shows the recovery ratio (left y axis) and the error ratio (right y axis) with respect to the local average particle velocity (magnitude) from the integrated method. When the particle velocity exceeds approximately 0.7 m/s, the recovery ratio evaluated by the integrated method deviates from desired value of unity and becomes more scattered. The error ratio slowly increases to a maximum value of approximately 0.006 as the particle velocity increases from 0 to 0.7 m/s. Figure 2.7b shows the recovery ratio
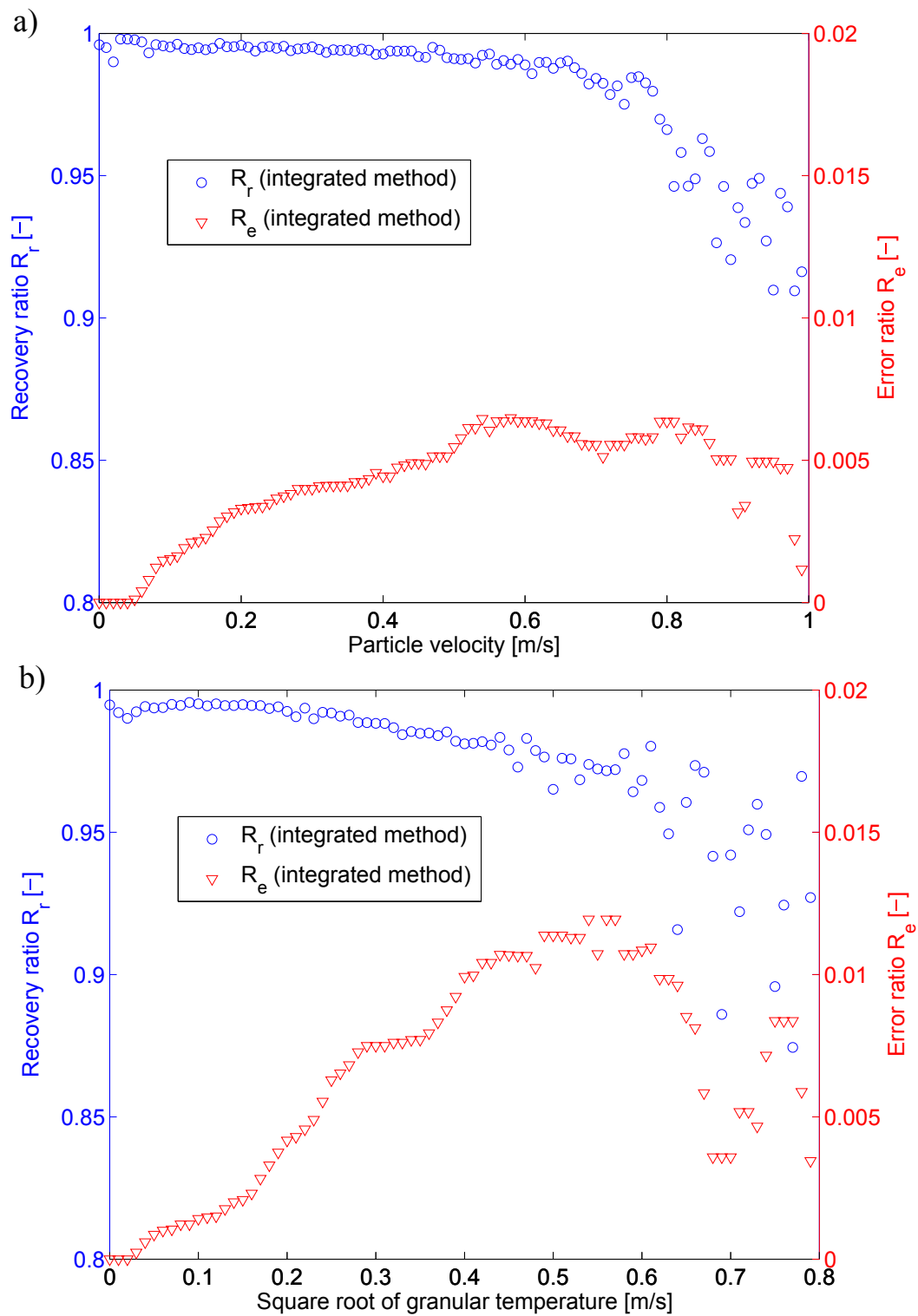
Figure 2.7: Recovery ratio $R_r$ and error ratio $R_e$: a) influence of particle velocity, b) influence of particle granular temperature.

and the error ratio with respect to the local average square root of particle granular temperature. When the square root of particle granular temperature increases from 0 to 0.6 m/s, the recovery ratio decreases from unity to 0.95; and the error ratio increases from 0 to 0.012. As the square root of particle granular temperature further increases, large fluctuations appear in both the recovery ratio and error ratio due to the low number of samples in this range. Based on statistical analysis, less than 1 % of particles in the investigation regions can experience velocity larger than 0.7 m/s or square root of granular temperature larger than 0.6 m/s. In total, the integrated particle tracking algorithm was able to achieve very good recovery ratio in most of the considered operating conditions. The increase of error ratio with increasing local particle velocity and granular temperature can be explained by the decrease of stability of neighboring structures associated with the mean free path (solid volume fraction).

According to the verification results, the PTV methodology can identify and track particles of different sizes with high accuracy and precision. Remarkably, the final recovery ratio obtained by the integrated tracking method is very close to unity for all solid volume fractions due to the good complementarity of Voronoi and relaxation probability tracking. Since the well-established CFD-DEM simulation can provide very similar fluidization conditions as observed in real measurements, including the solid volume fraction, the local velocity and the local particle granular temperate, measurements of poly-disperse particle dynamics using the PTV methodology are expected to be reasonably trustworthy. Moreover, CFD-DEM simulation data can be very useful in designing experiments and optimizing the parameters of the segmentation and the tracking algorithms. In order to achieve high segmentation ratio and low bias, the size of template particle in the segmentation can be adjusted according to the characteristics of intensity distribution. The frame rate of the high-speed camera has to be increased when insufficient recovery ratio appears in the primary ranges of solid volume fraction, particle velocity and granular temperature.

Based on the verified methodology, PTV will be applied to measure key aspects related to the particle formation process in fluidized beds. The collision velocity and collision frequency can be investigated based on the variations of particle trajectories, which will be described in Chapter 6. If colors of different particles in the system are distinguished, the mixing behavior can be studied based on color classification before particle segmentation, which will be discussed in Chapter 7. The measurement of irregularly shaped particles impacting on horizontal substrates will be presented in Chapter 5.

# Chapter 3

# CFD-DEM methodology

*Parts of this chapter are based on Jiang et al. [120], Jiang et al. [45] and Jiang et al. [121].*

## 3.1   Governing equations

### 3.1.1   Origin of models in two-fluid method

Since the fluid flow in CFD-DEM is still modelled on a macroscopic local level, it is necessary to start the discussion of CFD-DEM formulations from the two-fluid method (TFM). With the help of the local average method, Anderson and Jackson [122] directly derived the governing equation for the fluid phase on the basis of Navier-Stokes equations; and the governing equation for the solid phase on the basis of motion of a single solid particle, expressed as:

$$\epsilon_f \rho_f \left[ \frac{\partial \boldsymbol{u}}{\partial t} + \nabla \cdot (\boldsymbol{uu}) \right] = \nabla \cdot \boldsymbol{\xi} - n\boldsymbol{f}_i + \epsilon_f \rho_f \boldsymbol{g} \tag{3.1}$$

$$\epsilon_s \rho_s \left[ \frac{\partial \boldsymbol{v}}{\partial t} + \nabla \cdot (\boldsymbol{vv}) \right] = n\boldsymbol{\Phi} - \nabla \cdot \boldsymbol{S} + n\boldsymbol{f}_i + \epsilon_s \rho_s \boldsymbol{g} \tag{3.2}$$

where $\epsilon_f$ and $\epsilon_s = 1 - \epsilon_f$ are, respectively, volume fractions of fluid and particles; $\boldsymbol{u}$ is fluid velocity, $\boldsymbol{\xi}$ is fluid stress tensor, $\boldsymbol{f}_i$ is the local mean value of force on particle $i$ due to particle-fluid interactions, $n$ is the number of particles per unit volume $[1/\text{m}^3]$. $\boldsymbol{v}$ is particle velocity, $\boldsymbol{\Phi}$ is the local mean value of particle-particle interaction force, $\boldsymbol{S}$ is the tensor representing 'Reynolds stress' for solid particles. Comparing Eq. (3.1) and Eq. (3.2), the particle-fluid interaction force $\boldsymbol{f}_i$ is in the same form but with opposite sign, guaranteeing that Newton's third law is satisfied. The important precondition of the local average is that point variations can be decomposed into two contributions, of scales much smaller and much larger than the radius of weighting function. Then, constitutive equations relating $\boldsymbol{\xi}$, $\boldsymbol{f}_i$, $\boldsymbol{\Phi}$ and $\boldsymbol{S}$ to volume fractions, pressure and local mean velocity fields are required to determine the motion of fluid and particles.

When particles are fluidized, they can support the compressive stress by momentum exchange through particle-particle collisions without further motion, and simultaneously, any shear can generate a motion as long as the stress is maintained. Based on these features, Anderson and Jackson [122] introduced a solid stress tensor $\boldsymbol{\xi}^s$ by lumping 'Reynolds stress' for solid particles with particle-particle interactions, expressed as

$$\nabla \cdot \boldsymbol{\xi}^s = n\boldsymbol{\Phi} - \nabla \cdot \boldsymbol{S}.$$

$\boldsymbol{\xi}^s$ contains an isotropic term representing the elastic resistance of the particle assembly to compression, together with terms related to the rate of strain tensor representing the fluid-like behavior of the particle assembly. Both fluid stress tensor $\boldsymbol{\xi}$ and solid stress tensor $\boldsymbol{\xi}^s$ can be given by expressions analogous to the stress tensor of a Newtonian fluid, as follows (in Einstein notation):

$$\xi_{ij} = p\delta_{ij} + \lambda(\epsilon_f)\frac{\partial u_m}{\partial x_m}\delta_{ij} + \mu(\epsilon_f)\left[\frac{\partial u_i}{\partial x_j} + \frac{\partial u_j}{\partial x_i} - \frac{2}{3}\delta_{ij}\frac{\partial u_m}{\partial x_m}\right];$$

$$\xi_{ij}^s = p^s(\epsilon_s)\delta_{ij} + \lambda^s(\epsilon_s)\frac{\partial v_m}{\partial x_m}\delta_{ij} + \mu^s(\epsilon_s)\left[\frac{\partial v_i}{\partial x_j} + \frac{\partial v_j}{\partial x_i} - \frac{2}{3}\delta_{ij}\frac{\partial v_m}{\partial x_m}\right];$$

where $p$ is the local mean fluid pressure, $p^s$ represents the inter-particle pressure relating to $\epsilon_s$; $\lambda$ and $\mu$ are effective bulk and shear viscosities which take account of Reynold stress and mechanical stress; $\lambda^s$ and $\mu^s$ are effective bulk and shear viscosities for the particle assembly; $\delta_{ij}$ is Kronecker delta.

A single particle moving in the fluid was used to introduce the particle-fluid interactions. The total force due to particle-fluid interaction on a single particle in the fluid can be simply expressed as:

$$f = f_d(u) - V_p\frac{dp}{dx},$$

where $f_d$ represents the forces of surface friction and form drag arising from small scale distortions of fluid streamlines in the neighborhood of the particle; and $-V_p(dp/dx)$ represents the force generated by the large scale pressure gradients in the fluid. The buoyancy force, a result of the vertical pressure gradient induced by the gravitational body force, has been included in the second term. Accordingly, the total particle-fluid interaction forces $n\boldsymbol{f}_i$ can be decomposed into a component due to macroscopic variations in fluid stress tensor on a scale larger than the particle spacing, together with a component representing the interaction force due to variations of fluid stress tensor induced by fluctuations in velocity as the fluid passes around individual particles and through interstices between particles. That is,

$$n\boldsymbol{f}_i = n(V_p\nabla \cdot \boldsymbol{\xi})/V + n\boldsymbol{f}_i' = \epsilon_s\nabla \cdot \boldsymbol{\xi} + n\boldsymbol{f}_i'. \tag{3.3}$$

With the considerations of $\nabla \cdot \boldsymbol{\xi}^s = n\boldsymbol{\Phi} - \nabla \cdot \boldsymbol{S}$ and Eq. (3.3), Eq. (3.1) and Eq. (3.2) become

$$\epsilon_f\rho_f\left[\frac{\partial \boldsymbol{u}}{\partial t} + \nabla \cdot (\boldsymbol{u}\boldsymbol{u})\right] = \epsilon_f\nabla \cdot \boldsymbol{\xi} - n\boldsymbol{f}_i' + \epsilon_f\rho_f\boldsymbol{g} \tag{3.4}$$

$$\epsilon_s \rho_s \left[ \frac{\partial \boldsymbol{v}}{\partial t} + \nabla \cdot (\boldsymbol{vv}) \right] = \epsilon_s \nabla \cdot \boldsymbol{\xi} + n\boldsymbol{f}'_i + \epsilon_s \rho_s \boldsymbol{g} + \nabla \cdot \boldsymbol{\xi}^s \qquad (3.5)$$

To further eliminate the fluid stress tensor term $\nabla \cdot \boldsymbol{\xi}$, an equation was obtained by multiplying Eq. (3.4) with $\epsilon_s/\epsilon_f$ and subtracting from Eq. (3.5). This gives

$$\epsilon_s \rho_s \left[ \frac{\partial \boldsymbol{v}}{\partial t} + \nabla \cdot (\boldsymbol{vv}) \right] = \frac{n\boldsymbol{f}'_i}{\epsilon_f} - \epsilon_s \rho_f \boldsymbol{g} + \epsilon_s \rho_f \left[ \frac{\partial \boldsymbol{u}}{\partial t} + \nabla \cdot (\boldsymbol{uu}) \right] + \epsilon_s \rho_s \boldsymbol{g} + \nabla \cdot \boldsymbol{\xi}^s. \qquad (3.6)$$

Comparing Eq. (3.6) and Eq. (3.2), the total particle-fluid interaction force $n\boldsymbol{f}_i$ can be written as:

$$n\boldsymbol{f}_i = \frac{n\boldsymbol{f}'_i}{\epsilon_f} - \epsilon_s \rho_f \boldsymbol{g} + \epsilon_s \rho_f \left[ \frac{\partial \boldsymbol{u}}{\partial t} + \nabla \cdot (\boldsymbol{uu}) \right]. \qquad (3.7)$$

If the term $\epsilon_s \rho_f [\partial \boldsymbol{u}/\partial t + \nabla \cdot (\boldsymbol{uu})]$ approaches zero or becomes much smaller than $n\boldsymbol{f}'_i/\epsilon_f - \epsilon_s \rho_f \boldsymbol{g}$, the total particle-fluid interaction force can be simplified to

$$n\boldsymbol{f}_i = \frac{n\boldsymbol{f}'_i}{\epsilon_f} - \epsilon_s \rho_f \boldsymbol{g}. \qquad (3.8)$$

This restrictive assumption indicates that the fluid flow through the particle phase should be steady and uniform. Using this simplified equation, two alternative equations can be obtained based on Eq. (3.1) and Eq. (3.2), namely [123],

$$\epsilon_f \rho_f \left[ \frac{\partial \boldsymbol{u}}{\partial t} + \nabla \cdot (\boldsymbol{uu}) \right] = \nabla \cdot \boldsymbol{\xi} - \left( \frac{n\boldsymbol{f}'_i}{\epsilon_f} - \epsilon_s \rho_f \boldsymbol{g} \right) + \epsilon_f \rho_f \boldsymbol{g} \qquad (3.9)$$

$$\epsilon_s \rho_s \left[ \frac{\partial \boldsymbol{v}}{\partial t} + \nabla \cdot (\boldsymbol{vv}) \right] = \nabla \cdot \boldsymbol{\xi}^s + \left( \frac{n\boldsymbol{f}'_i}{\epsilon_f} - \epsilon_s \rho_f \boldsymbol{g} \right) + \epsilon_s \rho_s \boldsymbol{g} \qquad (3.10)$$

In the literature, there has been a lot of discussion on the precision of different forms of governing equations. The classification of governing equations related to previous derivations is given in Table 3.1. Gidaspow [60] distinguished model A and model B, mainly depending on whether the pressure gradient is shared by both phases (model A) or only contributes to the fluid phase (model B). Based on the work of Anderson and Jackson [122], Zhou et al. [123] proposed recommendations on the proper classification and usage of different models. They defined equation sets I, II, and III. Set I is the original model directly from the local average of Navier-Stokes equations and Newton's second law. Set II is derived by splitting the particle-fluid interaction force to a component of marcoscopic pressure gradient and a component of friction and drag contributions (virtual mass force and drag force). Set III is obtained from some mathematical manipulations of set I and set II, however a restrictive assumption that flow around particles is steady and uniform is required. According to the principle of Gidaspow to classify models A and B, set I should be an original model B. The model A is commonly used in commercial software Fluent (ANSYS) and CFX (ANSYS) to simulate bubbling fluidized beds and circulating fluidized beds.

Table 3.1: A summary of classifications of governing equations used in the two fluid method for fluidized beds.

| Equation | Classification | |
| --- | --- | --- |
| | Gidaspow [60] | Zhou et al. [123] |
| Eqs. (3.1) and (3.2) | - | set I (original model B) |
| Eqs. (3.4) and (3.5) | model A | set II |
| Eqs. (3.9) and (3.10) | model B | set III |

After clarifying the governing equations in the two-fluid approach for fluidized beds, the remaining chanllenge is to develop closure laws to determine solid flow parameters including particle pressure, effective bulk and shear viscosities for particles; and momentum transfer between particles and fluid. The most popular approach to solve this task is the kinetic theory of granular flow [60], in which particle pressure, effective bulk and shear viscosities for particles are expressed as a function of granular temperature. One additional equation is required to balance the granular temperature (a measure of the random kinetic energy per unit mass), which is analogous to the usual thermal temperature in kinetic theory of dense gases [124]. The detailed discussion of the determination of solid flow parameters in the two-fluid method is out of focus of this thesis, but coincidentally, the CFD-DEM approach provides a new angle to view this difficulty in the traditional method.

### 3.1.2 CFD-DEM formulations

*Particle phase*

The main difference between CFD-DEM and two-fluid method is the treatment of the particle phase. In original DEM proposed by Cundall and Strack [125], the motion of the individual particle $i$ with mass $m_i$ and moment of inertia $I_i$ is calculated in a Lagrangian frame by Newton's laws of motion:

$$m_i\frac{\mathrm{d}\boldsymbol{v}_{p,i}}{\mathrm{d}t} = \boldsymbol{f}_{pf,i} + \sum_{j=1,j\neq i}^{N_0} (\boldsymbol{f}_{c,ij}^n + \boldsymbol{f}_{c,ij}^t) + m_i\boldsymbol{g}, \tag{3.11}$$

$$I_i\frac{\mathrm{d}\boldsymbol{\omega}_i}{\mathrm{d}t} = \sum_{j=1,j\neq i}^{N_0} (\boldsymbol{T}_{t,ij} + \boldsymbol{T}_{r,ij}). \tag{3.12}$$

$\boldsymbol{v}_{p,i}$ and $\boldsymbol{\omega}_i$ are, respectively, the transitional and angular velocities of the individual particle $i$, and $N_0$ is the number of particles in interaction with particle $i$. $\boldsymbol{f}_{pf,i}$ is the particle-fluid interaction force on the particle scale, $\boldsymbol{f}_{c,ij}^n$ and $\boldsymbol{f}_{c,ij}^t$ are the particle-particle interaction forces in the normal and tangential directions, and $m_i\boldsymbol{g}$ is the gravitational force. The torque acting on particle $i$ by the particle $j$ includes two components: $\boldsymbol{T}_{t,ij}$ generated by the tangential force $\boldsymbol{f}_{c,ij}^t$, and $\boldsymbol{T}_{r,ij}$ generated by the rolling friction.

The particle-fluid interaction force on individual particle $\boldsymbol{f}_{pf,i}$ mainly includes drag force $\boldsymbol{f}_{d,i}$, pressure gradient force $\boldsymbol{f}_{\nabla p,i}$, viscous force $\boldsymbol{f}_{\nabla\cdot\tau,i}$ due to fluid shear stress tensor

and some other non-dominant forces $\boldsymbol{f}''$ (such as virtual mass force, Magnus force and Basset force [1]), expressed as

$$\boldsymbol{f}_{pf,i} = \boldsymbol{f}_{d,i} + \boldsymbol{f}_{\nabla p,i} + \boldsymbol{f}_{\nabla\cdot\tau,i} + \boldsymbol{f}''.$$

As pointed out by Zhou et al. [123], one important aspect of CFD-DEM implementation is how to couple the particle-fluid interaction force at the particle scale for solid phase ($\boldsymbol{f}_{pf,i}$) and the particle-fluid interaction force at the CFD cell for fluid phase ($n\boldsymbol{f}_i$ or $\boldsymbol{F}_{pf}$). Due to the particle oriented feature, first, the $\boldsymbol{f}_{pf,i}$ for all individual particles in the CFD cell were calculated; and then the volumetric particle-fluid interaction force in the CFD cell was calculated by summation of all individual forces and dividing by the volume of the CFD cell $\Delta V$. This coupling scheme can be described by

$$n\boldsymbol{f}_i = \frac{1}{\Delta V}\sum_{j=1}^{N_1}(\boldsymbol{f}_{pf,i}) = \frac{1}{\Delta V}\sum_{j=1}^{N_1}(\boldsymbol{f}_{d,i} + \boldsymbol{f}_{\nabla p,i} + \boldsymbol{f}_{\nabla\cdot\tau,i} + \boldsymbol{f}''), \tag{3.13}$$

where $N_1$ is the total number of particles in the CFD cell.

*Fluid phase*

The mass conservation for fluid phase is expressed by

$$\frac{\partial}{\partial t}(\epsilon_f\rho_f) + \nabla\cdot(\epsilon_f\rho_f\boldsymbol{u}) = 0. \tag{3.14}$$

For most cases in gas fluidized beds, the fluid compressibility is not essential. The divergence of fluid stress tensor in Eq. (3.1) can be expressed as

$$\nabla\cdot\boldsymbol{\xi} = -\nabla p + \nabla\cdot\boldsymbol{\tau}_f, \tag{3.15}$$

where viscous stress $\boldsymbol{\tau}_f$ is

$$\boldsymbol{\tau}_f = \mu_f\left[\nabla\boldsymbol{u} + (\nabla\boldsymbol{u})^T\right] - \frac{2}{3}\mu_f(\nabla\cdot\boldsymbol{u})\boldsymbol{I}.$$

Accordingly, Eq. (3.3) can be rewritten as

$$n\boldsymbol{f}_i = -\epsilon_s\nabla p + \epsilon_s\nabla\cdot\boldsymbol{\tau}_f + n\boldsymbol{f}_i'. \tag{3.16}$$

Keeping the consistency with Eq. (3.13) and Eq. (3.16),

$$n\boldsymbol{f}_i' = \frac{1}{\Delta V}\sum_{j=1}^{N_1}(\boldsymbol{f}_{d,i} + \boldsymbol{f}''). \tag{3.17}$$

Introducing Eq. (3.15) into the equations of fluid phase in equation-sets I, II and III for the two-fluid method, three different governing equations of the fluid phase for the

Table 3.2: Different momentum equations and corresponding fluid-particle interaction forces used in the CFD-DEM simulation for solid-fluid multiphase flow according to three sets in the two-fluid method.

---

*Momentum conservation*

**set I**

$$\frac{\partial}{\partial t}(\epsilon_f \rho_f \boldsymbol{u}) + \nabla \cdot (\epsilon_f \rho_f \boldsymbol{u}\boldsymbol{u}) = -\nabla p + \nabla \cdot \boldsymbol{\tau}_f - \boldsymbol{F}_{pf} + \epsilon_f \rho_f \boldsymbol{g} \qquad (3.18)$$

$$\boldsymbol{F}_{pf} = n\boldsymbol{f}_i = \frac{1}{\Delta V} \sum_{j=1}^{N_1} (\boldsymbol{f}_{d,i} + +\boldsymbol{f}_{\nabla p,i} + \boldsymbol{f}_{\nabla \cdot \tau,i} \boldsymbol{f}'') \qquad (3.19)$$

$$\boldsymbol{f}_{pf,i} = \boldsymbol{f}_{d,i} + \boldsymbol{f}_{\nabla p,i} + \boldsymbol{f}_{\nabla \cdot \tau,i} + \boldsymbol{f}'' \qquad (3.20)$$

---

**set II** (model A)

$$\frac{\partial}{\partial t}(\epsilon_f \rho_f \boldsymbol{u}) + \nabla \cdot (\epsilon_f \rho_f \boldsymbol{u}\boldsymbol{u}) = -\epsilon_f \nabla p + \nabla \cdot (\epsilon_f \boldsymbol{\tau}_f) - \boldsymbol{F}_{pf} + \epsilon_f \rho_f \boldsymbol{g} \qquad (3.21)$$

$$\boldsymbol{F}_{pf} = n\boldsymbol{f}'_i = \frac{1}{\Delta V} \sum_{i=1}^{N_1} (\boldsymbol{f}_{d,i} + \boldsymbol{f}'') \qquad (3.22)$$

$$\boldsymbol{f}_{pf,i} = \boldsymbol{f}_{d,i} + \boldsymbol{f}_{\nabla p,i} + \boldsymbol{f}_{\nabla \cdot \tau,i} + \boldsymbol{f}'' \qquad (3.23)$$

---

**set III** (model B)

$$\frac{\partial}{\partial t}(\epsilon_f \rho_f \boldsymbol{u}) + \nabla \cdot (\epsilon_f \rho_f \boldsymbol{u}\boldsymbol{u}) = -\nabla p + \nabla \cdot \boldsymbol{\tau}_f - \boldsymbol{F}_{pf} + \epsilon_f \rho_f \boldsymbol{g} \qquad (3.24)$$

$$\boldsymbol{F}_{pf} = n\boldsymbol{f}'_i/\epsilon_f - \epsilon_s \rho_f \boldsymbol{g} = \frac{1}{\epsilon_f \Delta V} \sum_{i=1}^{N_1} (\boldsymbol{f}_{d,i} + \boldsymbol{f}'') - \frac{1}{\Delta V} \sum_{i=1}^{N_1} (V_{p,i} \rho_f \boldsymbol{g}) \qquad (3.25)$$

$$\boldsymbol{f}_{pf,i} = (\boldsymbol{f}_{d,i} + \boldsymbol{f}'')/\epsilon_f - V_{p,i} \rho_f \boldsymbol{g} \qquad (3.26)$$

Only valid under the condition that the fluid flow through the particle phase is steady and uniform.

CFD-DEM approach can be derived, as summarised in Table 3.2. As emphasized by Zhu et al. [126], the coupling of the particle-fluid interaction force acting on particles $\boldsymbol{f}_{pf,i}$ and volumetric particle-fluid interaction force in the CFD cell $\boldsymbol{F}_{pf}$ must obey Netwon's third law of motion. Note that in set II, the pressure gradient force $-\epsilon_s \nabla p$ and the viscous force $\epsilon_s \nabla \cdot \boldsymbol{\tau}_f$ on particles have been separated from $\boldsymbol{F}_{pf}$ in momentum balance Eq. (3.21). However, the application of set III is only valid if the fluid flow is steady, that is

$$\epsilon_s \rho_f \left[ \frac{\partial \boldsymbol{u}}{\partial t} + \nabla \cdot (\boldsymbol{u}\boldsymbol{u}) \right] = 0. \tag{3.27}$$

As suggested by Zhou et al. [123], Tsuji et al. [127], Goniva et al. [128], for the CFD-DEM simulations of fluidized beds, the model A (set II), given by Eqs. (3.21) to (3.23), together with the mass conservation Eq. (3.14) will be used in this thesis.

## 3.2 Drag model

On the basis of different drag models, the momentum exchange coefficient $\beta_{pf}$ can be calculated to account for the interaction forces between particles and fluid phase. Therefore, accurate drag force models are of great importance in achieving high simulation accuracy.

Before discussion of different drag models, the definition of drag force has to be clarified. Generally, when a fluid percolates through assemblies of particles, each particle experiences two main forces from the fluid phase, namely a buoyancy force due to average pressure gradient $\boldsymbol{f}_{\nabla p,i}$ and a force resulting from the local frictional losses (friction between fluid and particle surface) $\boldsymbol{f}_{d,i}$. In literature, both $\boldsymbol{f}_{d,i}$ [60, 129] and $\boldsymbol{f}_{d,i} + \boldsymbol{f}_{\nabla p,i}$ [130] are sometimes referred as the drag force. The two definitions for the drag force differ by a factor of $1 - \epsilon_s$. According to the discussion of Eq. (3.3) and Eq. (3.13), only the friction-caused force was considered as the drag force in this work. The drag models discussed in this chapter were derived for spherical particles. Drag models for non-spherical particles can be found in papers of Hölzer and Sommerfeld [131] and Zastawny et al. [132], and references therein.

### 3.2.1 Gidaspow drag model

The relation between pressure drop and momentum exchange coefficient $\beta_{pf}$, also named as friction coefficient, can be simply derived from one-dimensional momentum balance for the fluid phase without acceleration, wall friction and gravity, expressed as

$$- \epsilon_f \frac{\partial p}{\partial x} - \beta_{pf} (u - v_i) = 0, \tag{3.28}$$

where $v_i$ is the velocity of particles and $\epsilon_f$ is fluid volume fraction. Based on experimental studies with packed beds, Ergun [133] suggested an expression that described the effects of volume fractions ($\epsilon_f$, $\epsilon_s$) and superficial gas velocity $\boldsymbol{U}$ on the pressure drop in

the dense regions (fixed dense bed of spherical particles). Wen and Yu [134] derived an expression for pressure drop prediction in dilute regions by fluidization experiments, in which they measured the terminal velocity of sedimenting spherical particles. Gidaspow [60] proposed a drag model based on the Ergun equation for the dense region and the Wen-Yu correlation for the dilute region, as follows

$$
\beta_{pf} = \begin{cases} \left(150\frac{\epsilon_s^2}{\epsilon_f} + 1.75\frac{\epsilon_s}{\epsilon_f}Re_p\right)\frac{\mu_f}{d_p^2}, \ \epsilon_s > 0.2 \\ \frac{3}{4}Re_pC_D\frac{\mu_f\epsilon_s}{d_p^2}\epsilon_f^{-2.65}, \epsilon_s \leq 0.2 \end{cases}, \tag{3.29}
$$

where the particle Reynolds number $Re_p$ and superficial gas velocity can be expressed as

$$
Re_p = \frac{\epsilon_f\rho_f \left| \boldsymbol{u} - \boldsymbol{v}_i \right| d_p}{\mu_f} = \frac{\rho_f \left| \boldsymbol{U} \right| d_p}{\mu_f}, \qquad \boldsymbol{U} = \epsilon_f \cdot (\boldsymbol{u} - \boldsymbol{v}_i). \tag{3.30}
$$

The expression for the drag coefficient is

$$
C_D = \begin{cases} 24\left(\frac{1 + 0.15Re_p^{0.687}}{Re_p}\right), \ Re_p < 1000 \\ 0.44, \ Re_p \geq 1000 \end{cases} \tag{3.31}
$$

After having obtained the momentum exchange coefficient $\beta_{pf}$, the drag force $\boldsymbol{f}_{d,i}$ can be calculated by

$$
\boldsymbol{f}_{d,i} = \frac{V_{p,i}}{\epsilon_s}\beta_{pf}(\boldsymbol{u} - \boldsymbol{v}_i). \tag{3.32}
$$

### 3.2.2 Beetstra drag model

In addition to experiments, fully resolved simulations have been considered as a promising tool to derive drag models, in which the inter-phase interaction is not modeled via empirical assumptions but follows from boundary conditions at the surface of the particles. Koch and Hill [130] first performed lattice Boltzmann method (LBM) simulations over a range of particle Reynolds numbers and solid volume fractions, and proposed a functional representation which could precisely fit to the simulation data. Different expressions were used for different ranges of particle Reynolds numbers and solid volume fractions. Note that two points in their original work were different from the convention in literature of fluidization dynamics: 1) the particle radius, rather than the particle diameter, was used to calculate particle Reynolds number; and 2) the buoyancy force was accounted in the drag force. The drag model proposed by Koch and Hill [130] only covers parts of the ranges of solids volume fraction or Reynolds number encountered in fluidized beds.

Based on the work of Hoef et al. [135] for low particle Reynolds numbers, extensive LBM simulations were performed by Beetstra et al. [136, 137] to propose a drag model

(referred to as MBVK) for mono-disperse systems in a wider range of solid volume fractions, $\epsilon_s \in [0.1, 0.6]$, and particle Reynolds numbers $Re_p \in [20, 1000]$. Their expression is given by

$$F(\epsilon_s, Re_p)_{mono} = \frac{10\epsilon_s}{\epsilon_f^2} + \epsilon_f^2(1+1.5\epsilon_s^{0.5}) + \frac{0.413Re_p}{24\epsilon_f^2}\left[\frac{\epsilon_f^{-1} + 3\epsilon_s\epsilon_f + 8.4Re_p^{-0.343}}{1 + 10^{3\epsilon_s} \cdot Re_p^{-(1+4\epsilon_s)/2}}\right]. \quad (3.33)$$

Under the assumption of laminar flow with an isolated single particle, the Stokes (Stokes-Einstein) drag $\boldsymbol{f}_{d,s}$ is defined as the force of viscous fluid exerted on a small sphere (friction force on single particle), that is

$$\boldsymbol{f}_{d,s} = 3\pi d_p \mu_f \boldsymbol{U}. \quad (3.34)$$

It is natural to use this expression to normalize the drag force obtained from LBM simulations at arbitrary packing fractions and flow velocities, expressed as

$$F(\epsilon_s, Re_p) = \frac{\boldsymbol{f}_{d,i}}{3\pi d_p \mu_f \boldsymbol{U}}. \quad (3.35)$$

Comparing Eqs. (3.32) and (3.35), the relationship between normalized drag force $F(\epsilon_s, Re_p)$ and momentum exchange coefficient $\beta_{pf}$ can be written as

$$\beta_{pf} = \frac{18\mu_f\epsilon_s\epsilon_f}{d_p^2}F(\epsilon_s, Re_p). \quad (3.36)$$

An accurate drag model is of great importance for the performance in the prediction of complex particle-fluid flows, especially in poly-disperse systems. In the example of a binary system, if the volume fraction of small particles is somewhat smaller than the averaged solid volume fraction (including both large and small particles), then an over-prediction of the drag force on small particles results. Inversely, the drag force is under-predicted for the large particles. Beetstra et al. [136, 137] found that a correction for the effect of poly-dispersity was essential to improve the accuracy of simulations. The correction factor $F_p$ depends on the solid and fluid volume fractions ($\epsilon_s$ and $\epsilon_f$), and on the diameter ratio $y_i$ of the diameter of a certain class of particles $d_{p,i}$ and the Sauter mean diameter $d_{32}$ of the entire particle system. The detailed poly-disperse Beetstra drag model (PBVK) can be written as

$$F(\epsilon_s, Re_p)_{poly} = F_p \cdot F(\epsilon_s, Re_p)_{mono}, \quad (3.37)$$

$$F_p = \epsilon_f y_i + \epsilon_s y_i^2 + 0.064\epsilon_f y_i^3, \quad (3.38)$$

in which, the Sauter mean diameter $d_{32}$ instead of $d_p$ was used in Eq. (3.30) to calculate particle Reynolds number. The expressions of the Sauter mean diameter $d_{32}$ and the diameter ratio $y_i$ are

$$d_{32} = \frac{\sum_{i=1}^{c} N_i d_{p,i}^3}{\sum_{i=1}^{c} N_i d_{p,i}^2}, \quad (3.39)$$

$$y_i = \frac{d_{p,i}}{d_{32}}. \quad (3.40)$$

### 3.2.3   Tang drag model

More recently, Tang et al. [138] further improved the drag model using an iterative immersed boundary method coupled with LBM, which is almost independent of the grid resolution. The Tang drag correlation combining the existing drag correlations for low-Re flows and single-sphere flows (from MBVK) fits the entire dataset with an average relative deviation of 4 %, with the form of

$$
\begin{aligned}
F(\epsilon_s, Re_p) =& \frac{10\epsilon_s}{\epsilon_f^2} + \epsilon_f^2(1 + 1.5\epsilon_s^{0.5}) \\
&+ \left[ 0.11\epsilon_s\,(1 + \epsilon_s) - \frac{0.00456}{\epsilon_f^4} + (0.169\epsilon_f + \frac{0.0644}{\epsilon_f^4})Re_p^{-0.343} \right] Re_p.
\end{aligned}
\tag{3.41}
$$

This correlation is so far the best possible expression for the drag force in monodisperse static arrays of spheres, and is the most accurate basis to simulate particle motion
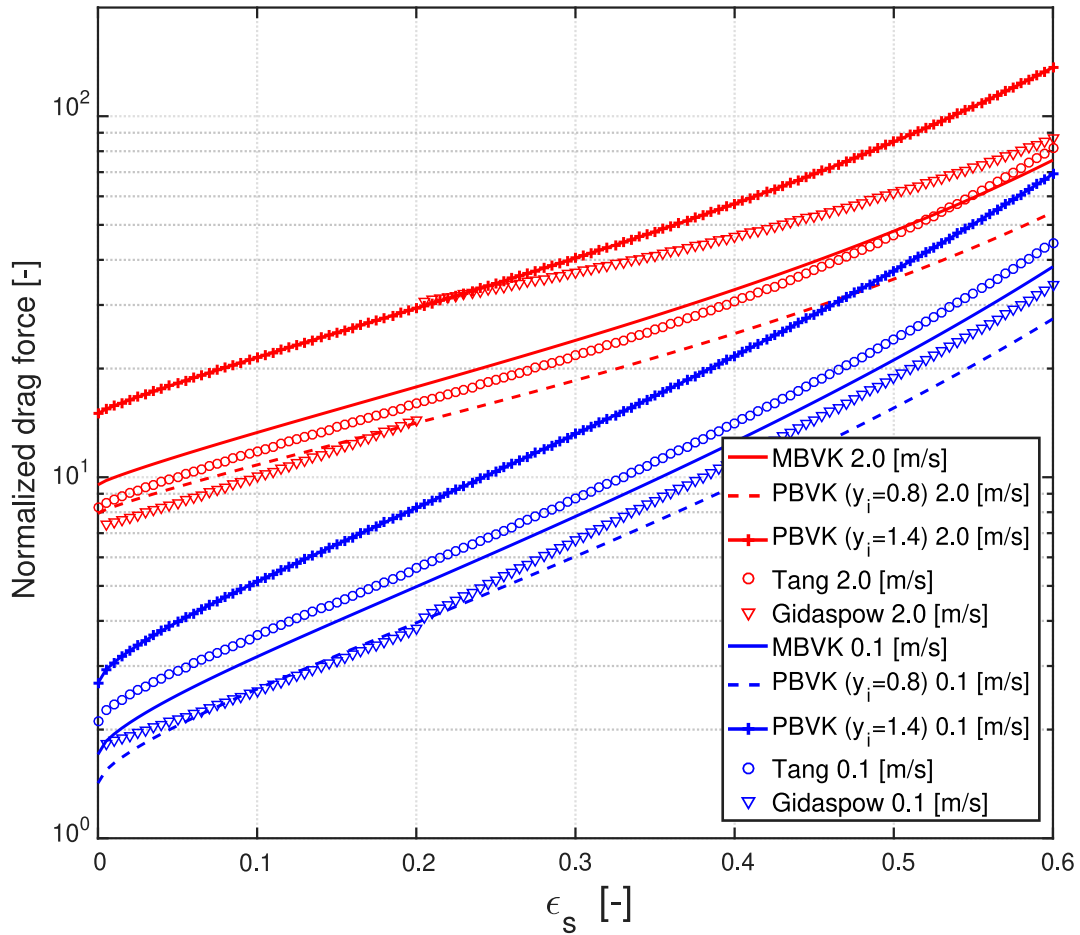


Figure 3.1: Normalized drag force $F(\epsilon_s, Re_p)$ [-] as a function of solid volume fraction $\epsilon_s$ under conditions of different relative velocities $|\boldsymbol{u} - \boldsymbol{v}_i|$ (0.1 m/s with color blue and 2 m/s with color red).

in fluidized beds. Figure 3.1 summarizes the normalized drag forces predicted by the different drag models discussed in Section 3.2 under different operation conditions.

## 3.3 Mapping model

In CFD-DEM, the effects of particle-fluid interactions on the fluid phase are mainly accounted in continuity and momentum equations, through the presence of the following two terms: solid volume fraction $\epsilon_s$ and particle-fluid interaction forces $\boldsymbol{F}_{pf}(\epsilon_s, \boldsymbol{u}, \boldsymbol{v}_i)$. Based on the CFD cells, these quantities are obtained from positions, sizes, shapes and velocities of each individual particle as well as local mean fluid velocity. Therefore, the mapping from particle-scale quantities to macroscopic quantities can profoundly influence the accuracy of CFD-DEM simulations. The mapping procedure should ideally conserve relevant physical quantities and handle particles both in the interior cells and the cells near boundaries (including processing boundaries in parallel simulation).

The simplest mapping method is the *particle centroid method* (PCM), where only the particles, the centroids of which fall within a cell are counted for calculating continuum quantities. The main drawback of this method is that non-physical values are generated if the particle centroid is located near interfaces of neighboring cells, leading to a non-smooth solid particle volume field with large gradients.

Instead of counting the entire particle volume to the cell containing the centroid of the particle, the *divided particle volume method* (DPVM) equally distributes the volume of the particle among all cells overlapped by the particle. In this work, each particle is first divided into 29 sub-regions of equal volume. As shown in Figure 3.2, the volumes of center sphere, first spherical shell and second spherical shell are $V_p/29$, $(14V_p)/29$, and $(14V_p)/29$, respectively. The radial distances $r_{s,1}, r_{s,2}$ of the centroids of sub-regions in the spherical shells can be calculated by

$$r_{s,1} = \frac{3}{4}\frac{r_2{}^4 - r_1{}^4}{r_2{}^3 - r_1{}^3}, r_{s,2} = \frac{3}{4}\frac{R^4 - r_2{}^4}{R^3 - r_2{}^3}. \tag{3.42}$$

In each shell, 14 sets of azimuthal angle $\psi$ and polar angle $\varphi$ are selected to determine the centroids of 14 sub-regions. Then, the centroids of all 29 sub-regions are used to distribute the volume of the particle into all involved cells in a manner similar to the particle centroid method.

From the numerical point of view, fine CFD cells (much smaller than the particle size) are desirable to be used in some special regions, to obtain the details of gas flow and guarantee grid-independent solution, for example, in the spray zone of a Wurster bed. In such cases, the *big particle model* (BPM) was used on the basis of the work of Link et al. [139]. A constant factor $S_{cube}$ was used to calculate an effective porous cube representing the influence of a single particle on neighboring CFD cells, i.e. $d_{cube} = d_p \cdot S_{cube}$. The porosity of the porous cube representing the particle can be easily calculated as

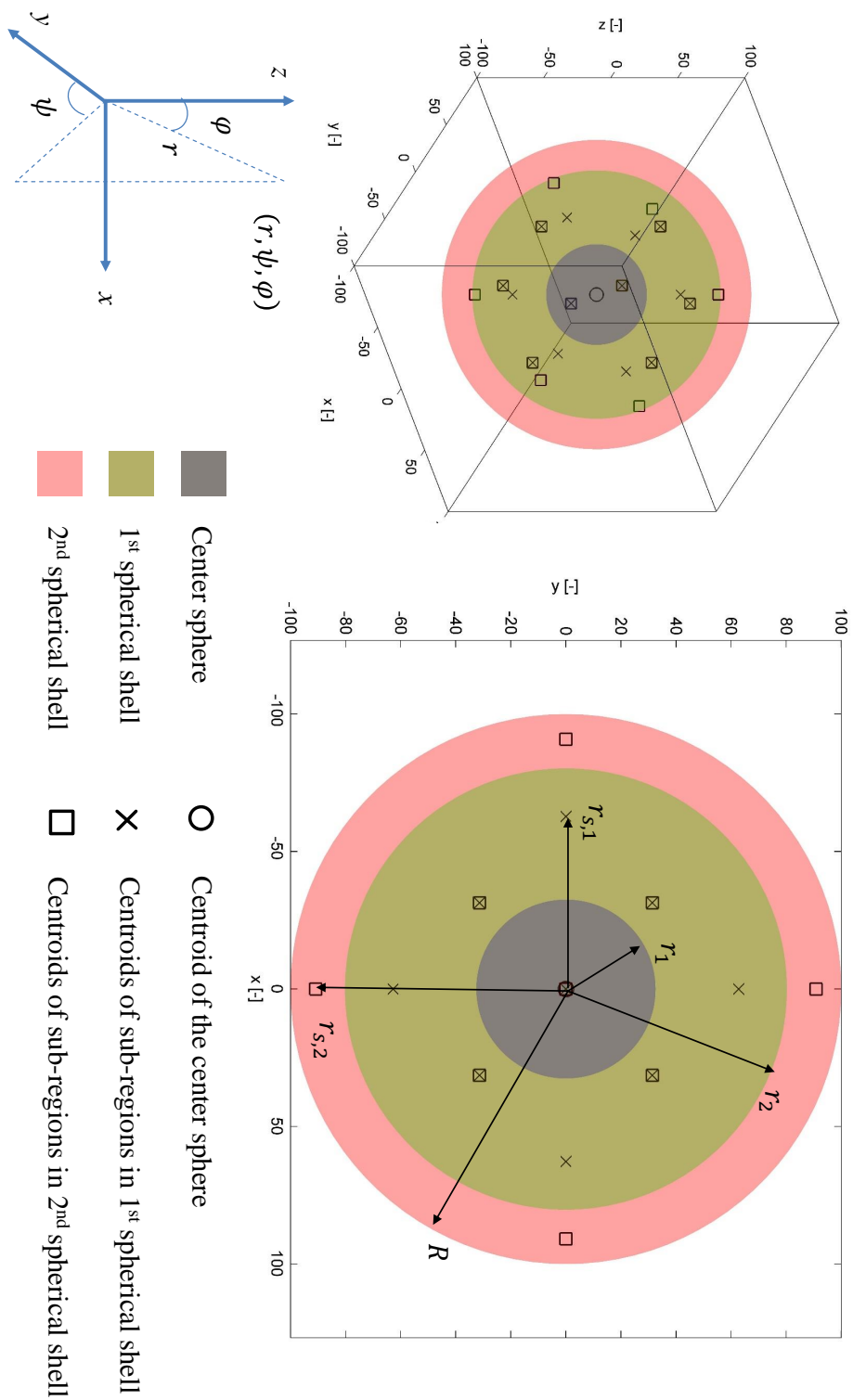$$\epsilon_{cube} = 1 - \frac{V_p}{V_{cube}} = 1 - \frac{\pi}{6 \cdot S_{cube}^3}. \tag{3.43}$$

Figure 3.2: Divided particle volume mapping method.

Different from the real particles, the effective cubes were allowed to overlap in CFD cells. The solid volume fraction in each cell can be expressed as

$$\epsilon_{s,cell} = (1 - \epsilon_{cube}) \cdot N_{cube}, \tag{3.44}$$

in which $N_{cube}$ is the number of effective cubes covering the cell. In this way, grid refinement will not lead to a non-smooth solid particle volume field with large gradients. Note that the total volume of all particles is kept constant in the entire simulation domain.

## 3.4 Contact model

Generally, there are two types of contact models to deal with the interactions between particles. In the *hard-sphere model*, the interactions between particles are treated instantaneously in a pair-wise manner. The collisions are processed one by one according to the order in which the events occur. For the simulation of dilute systems, the hard-sphere model is very efficient. However, the adaptability of the hard-sphere model to dense systems is poor due to the occurrence of multiple collisions [140]. The *soft-sphere model*, originally proposed by Cundall and Strack [125], assumes that a slight overlap is existent between the particles during the collision period to represent the deformation at the contacting surface. This phenomenon can be simulated by different contact force models in which physical laws are more or less simplified. Tsuji et al. [127] firstly applied a soft-sphere model to compute the motion of particles in a fluidized bed, in which the linear spring and dashpot model was used. DEM simulations rely on realistic contact force models, however, too many details make both implementation and interpretation prohibitively difficult. The contact forces discussed in this section focus on particles with sizes larger than 10 $\mu$m. For powders with sizes in the range of 0.1 to 10 $\mu$m, the review of Luding [141] and references therein provide comprehensive discussion of issues related to cohesion and friction.

Two spherical particles are in mechanical contact if $(R_i + R_j - |\boldsymbol{r}_i - \boldsymbol{r}_j|) > 0$, i.e. the sum of radii of the two particles exceeds the distance of the two centers of particles, as shown in Figure 3.3. The overlap $\delta_{ij}$ can be expressed as

$$\delta_{ij} = \max\left[0, (R_i + R_j - |\boldsymbol{r}_i - \boldsymbol{r}_j|)\right]. \tag{3.45}$$

The detection of contacts is much more complicated for irregularly shaped particles. The normal and tangential components of contact force can be written in the form of

$$\boldsymbol{f}_{c,ij}^n = f_{c,ij}^n \cdot \boldsymbol{n}^n, \boldsymbol{f}_{c,ij}^t = f_{c,ij}^t \cdot \boldsymbol{n}^t; \tag{3.46}$$

where $\boldsymbol{n}^n$ and $\boldsymbol{n}^t$ are unit vectors. The normal force $f_{c,ij}^n$ changes the translational motion of particles, whereas the tangential force $f_{c,ij}^t$ changes the rotational motion of particles. Both components of the contact force are related to the relative position of particles $\boldsymbol{r}_i - \boldsymbol{r}_j$ and the relative velocity of particles $\boldsymbol{v}_i - \boldsymbol{v}_j + (R_i\boldsymbol{\omega}_i \times \boldsymbol{n}^n + R_j\boldsymbol{\omega}_j \times \boldsymbol{n}^n)$.
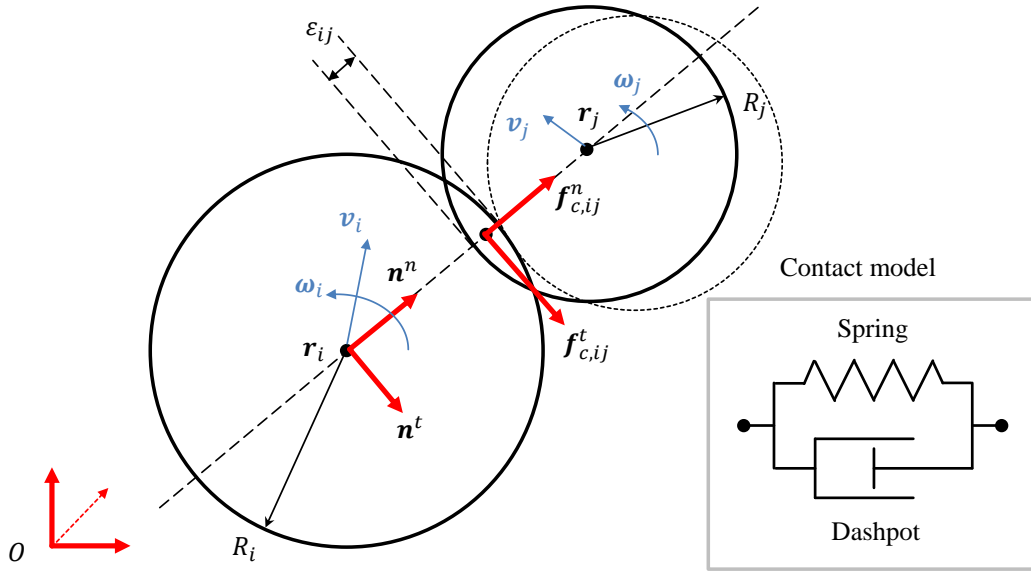
Figure 3.3: Soft-sphere particle-particle contact model.

### 3.4.1 Hertzian spring-dashpot model

*Normal direction*

The non-linear damped Hertzian spring-dashpot (HSD) model was developed to phenomenologically describe the inelastic collision of two particles (with a 'loss' of kinetic energy) in normal direction. For simplicity of the notation, the indices $ij$ of forces are omitted. The normal contact force $f_c^n$ consists of a conservative force and a dissipative force, expressed as

$$f_c^n(\delta, \dot{\delta}) = -f_{cons}(\delta) - f_{dis}(\delta, \dot{\delta}) = \min(0, -k_n\delta - \eta_n v_{r,n}). \tag{3.47}$$

The normal stiffness coefficient (or elastic coefficient) $k_n$ and the normal damping coefficient (or dissipative coefficient) $\eta_n$ can be written as

$$k_n = \frac{4}{3}E_{eq}\sqrt{R_{eq}\delta}, \tag{3.48}$$

$$\eta_n = \alpha_d(e)\sqrt{k_n m_{eq}}. \tag{3.49}$$

The relative velocity in normal direction at the contact point $v_{r,n}$ can be calculated by

$$v_{r,n} = (\boldsymbol{v}_i - \boldsymbol{v}_j)\boldsymbol{n}^n, \tag{3.50}$$

in which $\boldsymbol{n}^n = (\boldsymbol{r}_i - \boldsymbol{r}_j)/|\boldsymbol{r}_i - \boldsymbol{r}_j|$. The expressions for equivalent properties of the pair of particles are listed in Table 3.3.

Table 3.3: The expressions for equivalent properties in the contact model.

*Young's modulus*

$$E_{eq} = \left( \frac{1 - \sigma_i^2}{E_i} + \frac{1 - \sigma_j^2}{E_j} \right)^{-1} \tag{3.51}$$

*Radius*

$$R_{eq} = \left( \frac{1}{R_i} + \frac{1}{R_j} \right)^{-1} \tag{3.52}$$

*Shear modulus*

$$G_{eq} = \left( \frac{1 - \sigma_i}{G_i} + \frac{1 - \sigma_j}{G_j} \right)^{-1}, \quad G_i = \frac{E_i}{2(1 + \sigma_i)} \tag{3.53}$$

*Mass*

$$m_{eq} = \left( \frac{1}{m_i} + \frac{1}{m_j} \right)^{-1} \tag{3.54}$$

The minimum operator in Eq. (3.47) is used to cut off the artificially attractive force $(-k_n\delta - \eta_n\dot{\delta}$ is a positive value) between two particles as $\delta > 0$, $\dot{\delta} < 0$, as shown in Figure B.1.

Different from the work of Cundall and Strack [125], the contribution of the coefficient of restitution $e$ (the ratio of relative velocities of particles before and after collisions) is used in the determination of normal damping coefficient $\eta_n$ by introducing the damping ratio $\alpha_d(e)$. The analytical expression for the damping ratio is given in the work of Tsuji et al. [142] based on linear spring–dashpot (LSD) model. The analytical expression for $\alpha_d(e)$ based on Hertzian spring-dashpot (HSD) model is [143]

$$\alpha_d(e) = \begin{cases} -\sqrt{5}\dfrac{\ln e}{\sqrt{(\ln e)^2 + \pi^2}}, & e > 0, \\ -\sqrt{5}, & e = 0. \end{cases} \tag{3.55}$$

*Tangential direction*

Considering the Coulomb frictional limit, the tangential contact force $f_c^t$ can be written as [128]

$$f_c^t = \begin{cases} -k_t\delta_t - \eta_t v_{r,t}, & f_c^t < \mu_{fc}|f_c^n|, \\ -\mu_{fc}|f_c^n|, & f_c^t > \mu_{fc}|f_c^n|, \end{cases} \tag{3.56}$$

where the tangential stiffness coefficient $k_t$ and the tangential damping coefficient $\eta_t$ can be written as

$$k_t = 8G_{eq}\sqrt{R_{eq}\delta}, \tag{3.57}$$

$$\eta_t = \sqrt{\frac{2}{3}}\alpha_d\sqrt{k_t m_{eq}}. \tag{3.58}$$

Moreover, $v_{r,t}$ is the relative tangential velocity (slip velocity) at the contact point, expressed as

$$\boldsymbol{v}_{r,t} = (\boldsymbol{v}_i - \boldsymbol{v}_j) - v_{r,n}\boldsymbol{n}^n + (R_i\boldsymbol{\omega}_i \times \boldsymbol{n}^n + R_j\boldsymbol{\omega}_j \times \boldsymbol{n}^n). \tag{3.59}$$

The unit vector in tangential direction is

$$\boldsymbol{n}^t = \frac{\boldsymbol{v}_{r,t}}{|\boldsymbol{v}_{r,t}|}. \tag{3.60}$$

The tangential deformation of the particle surfaces $\delta_t$ since the time when two particles came into contact, $t_{c,0}$, can be expressed as

$$\delta_t = \int_{t_{c,0}}^{t} v_{r,t}dt. \tag{3.61}$$

### 3.4.2   Rolling model

A slight non-sphericity of particles can be considered by the rolling model, which introduces an additional torque even when the relative tangential velocity at the contact point is zero. According to the work of Ai et al. [144], rolling friction torque $\boldsymbol{T}_{r,ij}$ can be modelled by

$$\boldsymbol{T}_r = -k_r k_n \delta \frac{\boldsymbol{\omega}_r}{|\boldsymbol{\omega}_r|}R_{eq}; \tag{3.62}$$

in which $k_r$ is a model parameter; and the relative angular velocity is defined as

$$\boldsymbol{\omega}_r = \frac{R_i\boldsymbol{\omega}_i + R_j\boldsymbol{\omega}_j}{R_i + R_j}. \tag{3.63}$$

### 3.4.3   Cohesion model

Cohesive forces between particles, including capillary force and viscous force (liquid induced), electrostatic force, and van der Waals force, may significantly affect particle dynamics in the system. The effects become more pronounced in the case of fine particle system (diameter less than 100 $\mu m$) [145, 146].

Two forces induced by liquid bridges are considered in this work. The static capillary force $f_{capillary}$, associated with the liquid bridge, can be considered as the sum of two components: 1) the surface tension acting on the three-phase contact line; and 2) the pressure difference $\Delta p$ across the gas-liquid interface [147]. Besides, wet particles encounter a viscous force resisting motion, which can be derived from lubrication theory [148].
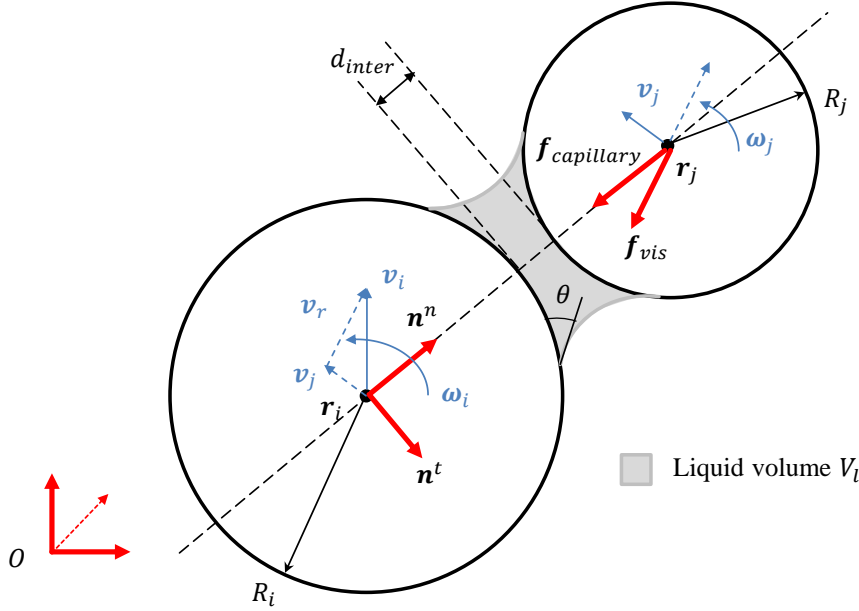
Figure 3.4: Cohesion forces induced by liquid bridge.

Limited to spherical particles, the equation for calculating the capillary force in a particle-pair geometry was obtained by fitting the set of discrete solutions of the Laplace equation [149], expressed as:

$$f_{capillary} = \pi \sigma_f \sqrt{R_i R_j} \left[ C + \exp \left( A \frac{d_{inter}}{\max(R_i, R_j)} + B \right) \right], \tag{3.64}$$

where $R_i$ and $R_j$ are radii of the two particles, $d_{inter}$ is the inter-particle distance, and $\sigma_f$ is the surface tension, as shown in Figure 3.4. By means of numerical solutions, the coefficients $A$, $B$ and $C$ can be expressed as functions of liquid volume $V_l$, contact angle $\theta$ (radian) and larger particle radius $R_{max} = \max(R_i, R_j)$:

$$A = -1.1 \left( \frac{V_l}{R_{max}^3} \right)^{-0.53}, \tag{3.65}$$

$$B = \left[ -0.148 \ln \left( \frac{V_l}{R_{max}^3} \right) - 0.96 \right] \theta^2 - 0.0082 \ln \left( \frac{V_l}{R_{max}^3} \right) + 0.48, \tag{3.66}$$

$$C = 0.0018 \ln \left( \frac{V_l}{R_{max}^3} \right) + 0.078. \tag{3.67}$$

The liquid volume of the bridge is assumed to be evenly distributed between the two particles when the inter-particle distance becomes larger than the rupture distance

$$D_r = (1 + 0.5\theta) \cdot V_l^{1/3}. \tag{3.68}$$

The viscosity force $f_{vis}$ in the normal and tangential direction can be calculated as [148]:

$$f_{vis,n} = 6\pi\mu_f \ R_{eq}v_{r,n}\frac{R_{eq}}{d_{inter}}, \tag{3.69}$$

$$f_{vis,t} = 6\pi\mu_f \ R_{eq}v_{r,t}(\frac{8}{15}\ln\frac{R_{eq}}{d_{inter}} + 0.9588); \tag{3.70}$$

where $\mu_f$ is the fluid viscosity, $R_{eq}$ is the equivalent radius; and $v_{r,n}$ and $v_{r,t}$ are relative velocities of the two particles in normal and tangential direction, respectively. In the simulation, the capillary force and the viscous force are included into the contact forces $\boldsymbol{f}^n_{c,ij}$ and $\boldsymbol{f}^t_{c,ij}$ in Eqs. (3.11) and (3.12) to solve the motion of each individual particle. Although Eq. (3.69) and Eq. (3.70) predict an unbounded magnitude of the viscous force with infinitely small particle separation gaps, in DEM simulations, the surface roughness limits the approach of the spheres. Hence, a minimum value for $d_{inter}$, corresponding to an average asperity height of particle surface $h_a$, is used, and the viscous force remains constant below this cutoff value.

## 3.5   Summary

Figure 3.5 summarizes the coupling routine of CFD-DEM with following steps:

1) DEM solver calculates particle positions, velocities (both translational and rotational) based on the governing equations for solid phase (Section 3.1.2); and all possible forces (Section 3.4). The coupling simulations start from the DEM solver.

2) DEM data are passed to the CFD solver and mapped to corresponding CFD cells. The solid volume fraction and mean local particle velocity are calculated in each cell (Section 3.3).

3) The momentum exchange coefficient and the drag force on each particle are calculated based on solid volume fraction (Section 3.2). The volumetric particle-fluid interaction force is calculated by ensemble averaging over all particles in a CFD cell (Section 3.1.2). The solid-fluid interaction forces on individual particles are passed back to the DEM solver.

4) CFD solver calculates fluid velocity based on the governing equations for fluid phase (Section 3.1.2). In addition, other scalar transport equations can be calculated, for instance, the liquid content and species concentration [70].

5) Routine repeats from step 1.

In the step 1, the integration of Newton's equations of motion (Eqs. (3.11) and (3.12)) for granular particle systems is achieved by velocity-Verlet method. The implementation scheme of this algorithm is: 1) calculate the velocity at $t + 1/2\Delta t$ by the force at $t$, 2) calculate the location at $t + \Delta t$ by the velocity at $t + 1/2\Delta t$, 3) update force at $t + \Delta t$, and 4) update the velocity at $t + \Delta t$ by the force at $t + \Delta t$. The Verlet integration provides numerical stability without significant extra computation cost compared with the simple Euler method [150]. In step 4, the pressure-implicit split-operator (PISO) algorithm, following one predictor (velocity) and two corrector procedures, was used to solve the governing equations for the fluid phase [128].
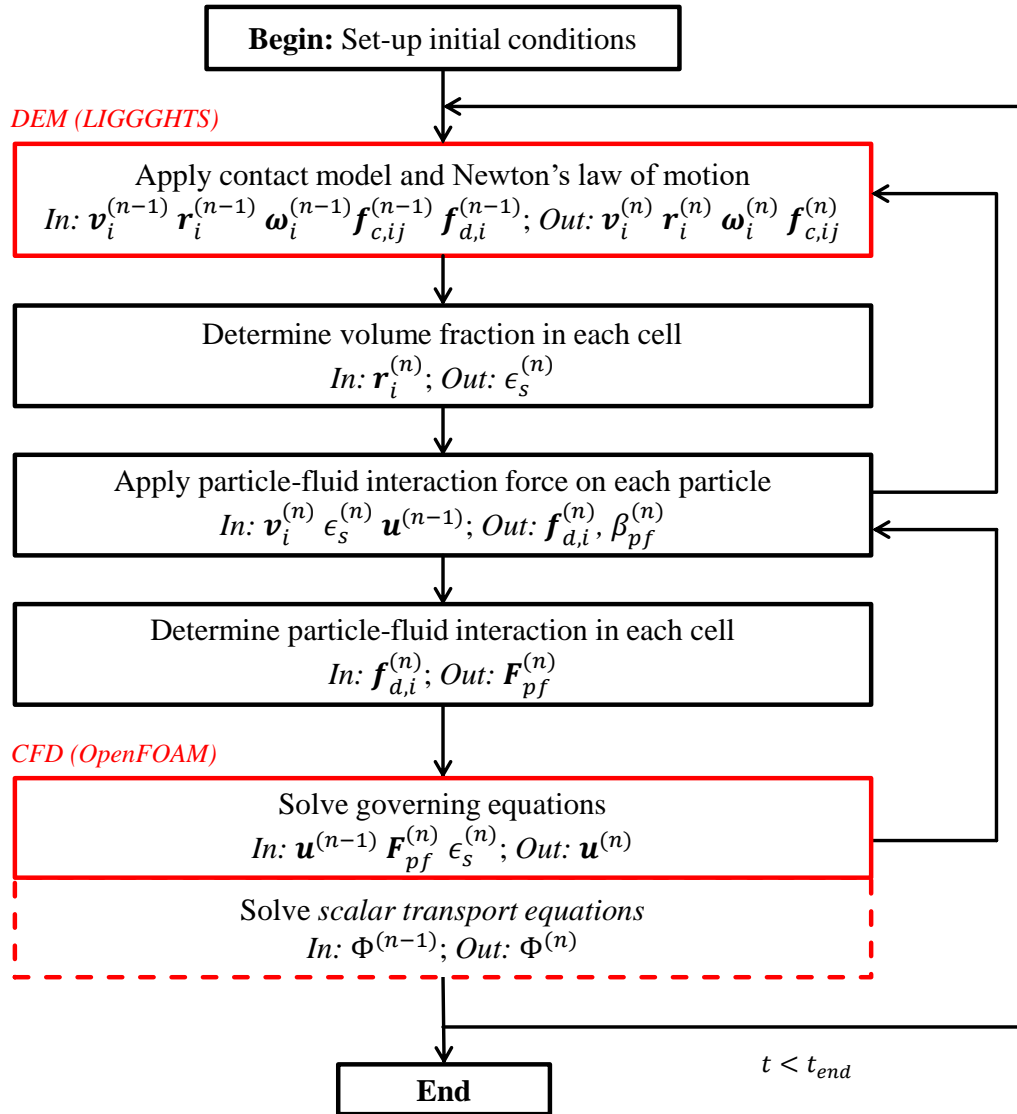
Figure 3.5: CFD-DEM coupling routine.

# Chapter 4

# Experimental and simulation setups

*This chapter is based on parts of Jiang et al. [104], Jiang et al. [45], Jiang et al. [105], Jiang et al. [120] and Jiang et al. [121].*

In this thesis, single collisions between irregular or spherical particles and horizontal substrates were measured using high-speed imaging and a vibratory feeder. Different **pseudo-2D fluidized beds** were applied to investigate important mesoscale phenomena in mono-disperse and poly-disperse particle systems by PTV measurements and CFD-DEM simulations. The residence time distribution and inter- and intra-particle coating uniformity in the **Wurster fluidized bed** were studied by CFD-DEM simulations. All associated experimental and simulation setups are presented in this chapter.

## 4.1 Single particle collision

A range of applications in the chemical, pharmaceutical, food and power industries involve the transportation and the processing of particles, where particle interactions are of great importance to particle motion and the overall performance of the processes.

The coefficient of restitution (COR, also $e$) is defined as the ratio of relative velocities of particles before and after a collision event, which is widely used to characterize the energy dissipation during individual particle-particle or particle-wall interactions. As a major particle property, the COR is required in multi-scale modeling of complex granular flows with strong solid phase interactions, such as two-fluid CFD simulations closed by the kinetic theory of granular flow (KTGF) [60], discrete element method (DEM) using the hard-sphere [140] or Hertzian spring-dashpot (HSD) or linear spring-dashpot (LSD) model [103, 125, 143, 145, 151], and coupled CFD-DEM simulations [103, 127, 140]. The COR is essential in predictions of particle formation processes in spray fluidized beds by Monte Carlo and population balance modeling (PBM) approaches [20, 152–155]. As a liquid layer is present on the surface of particles during the particle formation process, Ennis et al. [20] used the viscous Stokes number $St_v$ to predict whether a particle-particle collision will result in coalescence. The COR is the key parameter to determine the critical viscous Stokes number. However, the COR is

not a physical material property, instead, it is a function of the material parameters of particles, the masses and radii of particles, the impact velocities, and angular orientations (irregular sharped particles) [156]. Therefore, the measurement of COR is the basis for experimental and simulation study of complex fluidized bed systems.

### 4.1.1  High-speed imaging and vibratory feeder

The collision behavior between different particles and horizontal substrates was measured using a high-speed imaging system and a vibratory feeder. Besides, the PTV method was improved to reconstruct the trajectories of individual particles. The rotation speeds of individual particles can be evaluated for irregular shapes.

As shown in Figure 4.1a, the motion of particles was observed with a Photron high-speed camera (LaVision, CMOS chip, 1024 × 1024 pixel) that is located in front of the target substrate. The effective spatial resolution of this camera decreased when the frame rate was larger than 1000 fps. It was operated at a frame rate of 5000 fps and the corresponding spatial resolution was 384 × 384 pixels. The high-speed imaging system was fixed on optical rails; in addition, two linear stages were used to precisely control the relative position between the high-speed camera and target substrates in both vertical and horizontal directions. The system was controlled by the DaVis image acquisition software (LaVision). As summarized in Table 4.1, an optical lens with 60 mm focal length was employed to obtain a suitable field of view (FOV). Two continuously illuminating 400 W halogen lamps were utilized as light sources; and the exposure time was selected as 1/10000 s. The f-number, relative focal length to effective aperture, was set at the minimum value of 2.8, which yields a minimum depth of field and a maximum light exposure. In order to capture the entire impact process, the FOV was adjusted to about 13.5 × 13.5 mm$^2$, which corresponds to an approximate scale factor of 28.4 pixel/mm. This value was obtained from the standard geometry calibration process in the DaVis software.

The vibratory feeder with a V-shaped channel (Fritsch, Germany) was used to continuously release a group of particles from the tip of the channel, which was exactly located on top of the effective region of the camera. The release rate of particles was controlled by the vibration frequency of the feeder (50 to 80 Hz). The height from the tip of the channel to the substrate was set to 150 mm in all measurements. As depicted in Figure 4.1b, the impact process can be a normal impact or an oblique impact due to the vibratory release approach and irregular particle features.

### 4.1.2  Material properties

The experimental setup and corresponding PTV algorithms are flexible enough to measure irregular or spherical particles with characteristic lengths ranging from 100 $\mu m$ to several mm. Irregular maltodextrin particles with a characteristic size of approximately 100 $\mu m$ were the smallest particles in measurements. Therefore, measurements with maltodextrin are discussed in detail.
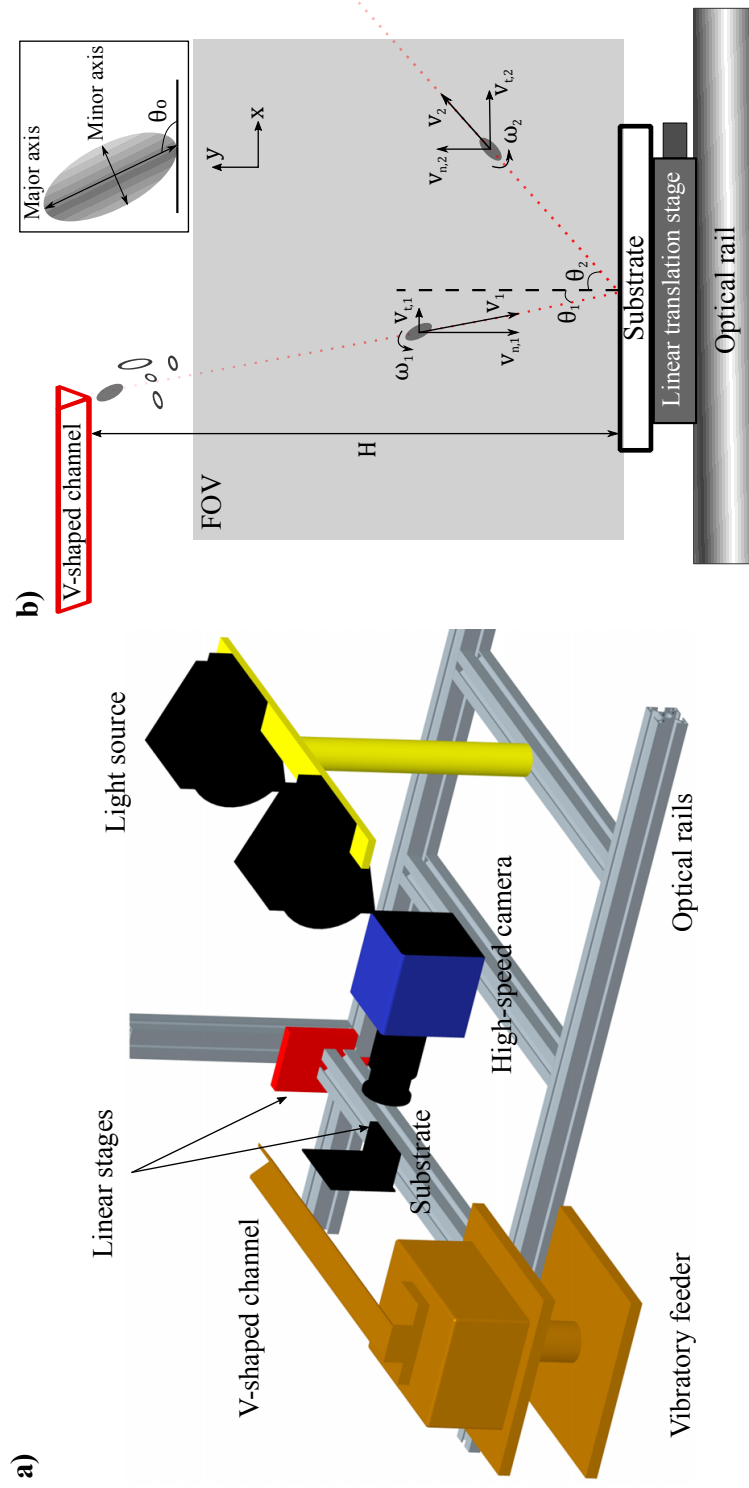
Figure 4.1: Schematic diagrams: a) experimental setup for testing collision behavior of irregular particles, and b) representation of the impact between irregular particles and the horizontal substrate.

Table 4.1: Parameters of the imaging system and maltodextrin particles.

| Parameter | Value | Unit |
|---|---|---|
| *Imaging system* | | |
| CMOS size | $384 \times 384$ | pixel |
| frame rate | 5000 | fps |
| exposure time | 1/10 000 | s |
| scale factor | 28.4 | pixel/mm |
| dynamic range | 10 | bit |
| local length | 60 | mm |
| f-number | 2.8 | – |
| depth of FOV | 0.1 | mm |
| halogen lamp | 400 | W |
| *Material* | | |
| bulk density | 500 | kg/m$^3$ |
| particle density $\rho_p$ | 900 | kg/m$^3$ |
| solid density $\rho_{solid}$ | 1500 | kg/m$^3$ |
| sphericity $SPHT$ | 0.783 | – |
| DE value | 5-8 | – |
| Sauter mean diameter $d_{32}$ | 137 | $\mu$m |
| Young's modulus $E$ | $10^7$ | Pa |
| Poisson ratio $\sigma$ | 0.21 | – |
| friction coefficient $\mu_{fc}$ | 0.5 | – |
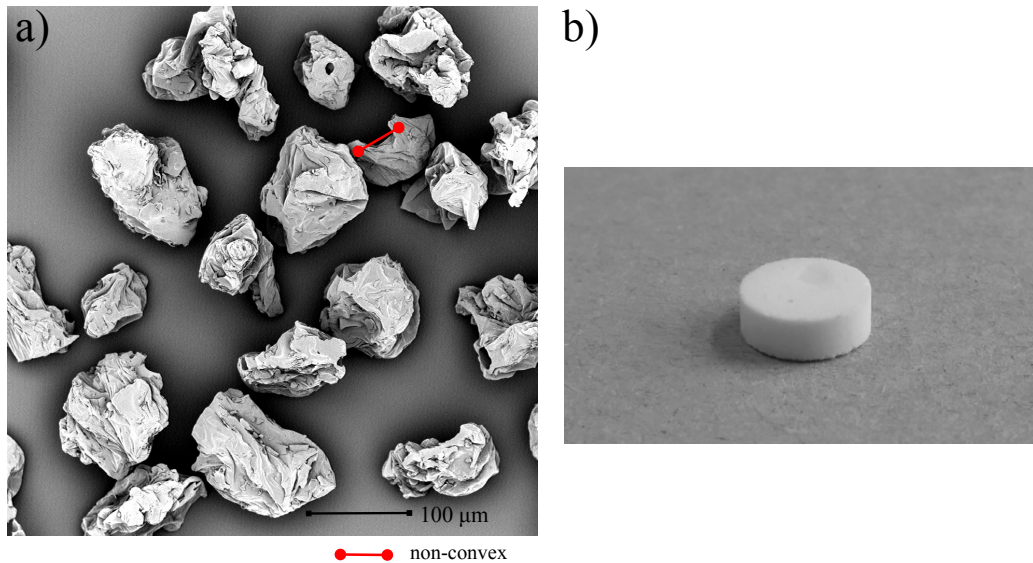


Figure 4.2: Material and substrate: a) SEM of angular, irregular, and non-convex maltodextrin (DE 6) particles, and b) picture of a maltodextrin tablet.

The maltodextrin shown in Figure 4.2a (Glucidex IT, Roquette, France) is a carbo-hydrate mixture that is produced by hydrolysis of starch and can be characterized by dextrose equivalent (DE). This material was widely used to study particle agglomer-ation in spray fluidized bed [155, 157]. Material properties are listed in Table 4.1. The particle size was measured by a Camsizer (Retsch Technology, Germany), which is a photo-optical system acquiring the images of freely falling irregularly shaped par-ticles. For individual particles, the area $A_I$ and the circumference $C_I$ in pixels can be obtained by image processing. The diameter of an individual particle refers to the diameter of a circle with the same area. The Sauter mean diameter $d_{32}$ was calculated based on the normalized size distribution related to particle number. The sphericity of irregularly shaped particles was estimated based on particle area and circumference ($SPHT = 4\pi A_I/C_I^2$). The density of the solid maltodextrin without pore volume $\rho_{solid}$ was measured by a helium pycnometer (Grabner Instruments, Austria, type: Minidens TCO).

The substrates used in the measurements were maltodextrin tablets and a microscopy slide made of glass. As shown in Figure 4.2b, the tablet used as the substrate was made of maltodextrin powder by a hydraulic press (pressure 1.3 MPa). The mass of the tablets ranges from 226 to 268 mg. The microscope slide is a thin flat piece of soda–lime glass ($75\times26\times1$ mm$^3$). The maltodextrin tablet and the glass slide were fixed on the rigid support base. To guarantee stationary conditions, the temperature and relative humidity of environment were adjusted to relatively constant values before all experiments. The mean temperature and mean relative humidity during all experiments were 20.2 °C and 46.2%, respectively.

The improvements of PTV algorithms for irregular particles, measurement results and the detailed comparisons with non-spherical DEM simulations will be given in Chapter 5.

## 4.2 Pseudo-2D fluidized bed with mono-disperse particle system

As studied by Hagemeier et al. [42, 43], the pseudo-2D fluidized is a favorable con-figuration to conduct PTV measurements. Collision dynamics are the focus of PTV measurements in mono-disperse system.

### 4.2.1 Pseudo-2D fluidized bed

Experiments were conducted using $\gamma$-alumina particles with a mean diameter of $d_p = 1.8$ mm and an apparent density of $\rho_p = 945$ kg/m$^3$ (Geldart class D). The minimum fluidization velocity $U_{mf}$ for these particles is 0.56 m/s [134]. A total mass of 0.5 kg particles (static height of 145 mm) was fluidized in a pseudo-2D fluidized bed, as depicted schematically in Figure 4.3. The parameters of the pseudo-2D fluidized bed and the imaging system are listed in Table 4.2. The dimensions of the process chamber were
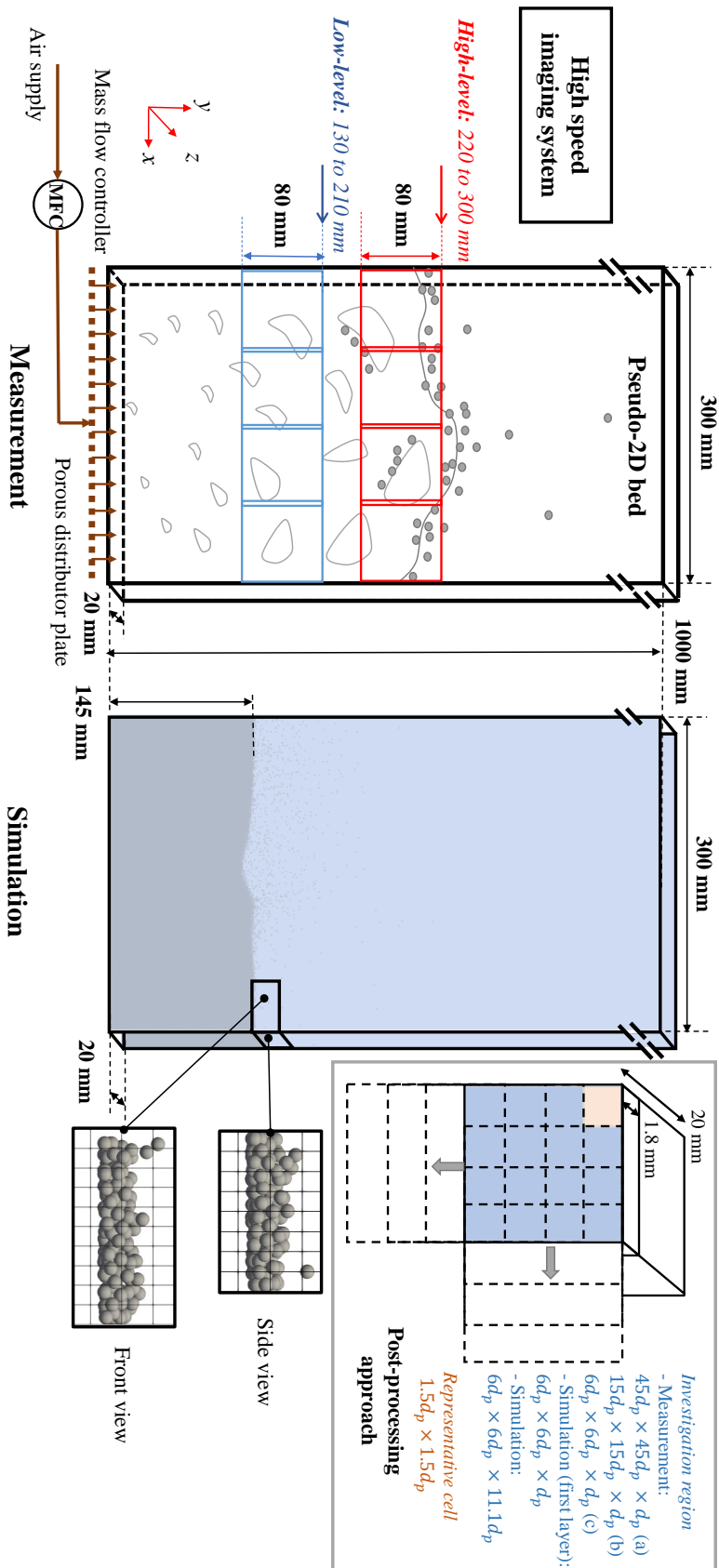
Figure 4.3: Sketch of the experiment and simulation setup as well as the post-processing approach; 8 different experimental locations at the "low-level" and the "high-level" bed heights are used in measurements.

300 mm, 1000 mm and 20 mm in width, height and depth, respectively. The maximum solid volume fraction (packed bed) was $\epsilon_{s,max} \approx 0.61$. The ratio between depth and particle diameter $d_p$ is very important for the particle flow behavior in the chamber. The depth has to be sufficiently small to present pseudo-2D flow of particles, but large enough to avoid extreme particle-wall collisions and attrition [158, 159]. A depth-width ratio of 1/15 and a depth-diameter ratio of 11 were realized in this configuration. The front and back walls were made of shatter-proof glass. Special surface treatment (plastic film) was made to protect the glass from abrasion by particle contacts. The side walls were made of aluminum. Pressurized air was used as the fluidization gas. Accurate control of the inlet gas flow rate was achieved by application of a calibrated mass flow controller. A 3 mm porous plate distributor with a mean pore size of 10 $\mu$m was used to generate a relatively homogeneous gas distribution over the entire bed bottom. The same configuration has been used to conduct fiber optical probe (FOP), laser Doppler velocimetry (LDV) and particle tracking velocimetry (PTV) measurements by Börner et al. [28], Hagemeier et al. [43] and Meyer et al. [44].

Table 4.2: Parameters of the pseudo-2D fluidized bed and imaging system for the mono-disperse system.

| Parameter | Value | Unit |
|---|---|---|
| *Pseudo-2D fludized bed* | | |
| chamber size ($x \times y \times z$) | $300 \times 1000 \times 20$ | mm$^3$ |
| particle diameter $d_p$ | 1.8 | mm |
| particle density $\rho_p$ | 945 | kg/m$^3$ |
| particle sphericity | 0.96 | $-$ |
| minimum fluidization velocity $U_{mf}$ | 0.56 | m/s |
| superficial gas velocity $U$ | $3.0U_{mf}/2.5U_{mf}/2.0U_{mf}$ | m/s |
| total mass | 0.5 | kg |
| static bed height | 145 | mm |
| *Imaging system* | | |
| CMOS size | $1024 \times 1024$ | pixel |
| frame rate | 1000 | fps |
| exposure time | $1/10\,000$ | s |
| dynamic range | 10 | bit |
| local length | 60 | mm |
| f-number | 2.8 | $-$ |
| halogen lamp | 400 | W |

## 4.2.2 Imaging system

Motion of particles was observed with the Photron high-speed camera (LaVision, CMOS chip, $1024 \times 1024$ pixel). It was operated at full spatial resolution with a frame rate of 1000 fps, an exposure time of 1/10000 s and a dynamic range of 10 bit. The light sources, optical lens and imaging control system are the same as those used in measurements of

COR (Section 4.1.1). The f-number was set at the minimum value of 2.8. The depth of field was approximately 10 mm in measurements. In order to satisfy the requirement of high spatial resolution for PTV algorithms and the evaluation of particle collisions, the field of view was adjusted to $80 \times 80$ mm$^2$, which corresponds to an approximate spatial resolution scale factor $S_f$ of 12.8 pixel/mm. This value was obtained from the standard geometry calibration process in the DaVis software.

For each gas velocity, the camera was positioned at eight locations on two height levels, namely "high-level" and "low-level", as shown in Figure 4.3. Specifically, the "low-level" ranges from $y = 130$ mm to $y = 210$ mm (center height $y_m = 170$ mm), and the "high-level" ranges from $y = 220$ mm to $y = 300$ mm (center height $y_m = 260$ mm). There is a small overlap between two adjacent FOVs at the same level and both side walls are included in the adjoining FOVs. The four horizontal locations are named as "left", "left-center", "right-center" and "right" from left to right in order, respectively. The detailed center position of each measurement location is listed in Table 4.3 in terms of the aspect ratio of the height $y_m$ and the distance to the left wall $x_m$. Two typical features of particle movement in fluidized beds were observed in these regions: the upwards oriented transport of particles by rising gas bubbles in the center, and particles sliding down the side walls. Three different target superficial gas velocities $U$ were selected as $2.0U_{mf}$, $2.5U_{mf}$ and $3.0U_{mf}$. For each measurement, the gas flow rate and the corresponding superficial gas velocity are also given in Table 4.3. Since only one camera was used, the measurement data of these eight positions for each operation condition cannot be acquired at the same time. The maximum number of images stored in each measurement was 5000 (5 s measurement time), which was sufficient to represent the periodicity of particle flow in the pseudo-2D fluidized bed [43].

Table 4.3: Measurement locations and inlet conditions.

| Case | Aspect ratio [-] | Gas flow rate [kg/h] | | | Gas velocity [m/s] | | |
|---|---|---|---|---|---|---|---|
| Low left | 1:0.229 | 28.65 | 35.75 | 42.92 | 1.123 | 1.401 | 1.682 |
| Low left-center | 1:0.665 | 28.48 | 35.62 | 42.69 | 1.116 | 1.396 | 1.673 |
| Low right-center | 1:1.100 | 28.39 | 35.77 | 42.76 | 1.113 | 1.402 | 1.676 |
| Low right | 1:1.535 | 28.66 | 35.59 | 42.70 | 1.123 | 1.395 | 1.674 |
| High left | 1:0.150 | 28.52 | 35.64 | 42.80 | 1.118 | 1.397 | 1.678 |
| High left-center | 1:0.434 | 28.69 | 35.78 | 42.71 | 1.124 | 1.403 | 1.674 |
| High right-center | 1:0.719 | 28.53 | 35.80 | 42.96 | 1.118 | 1.403 | 1.684 |
| High right | 1:1.004 | 28.44 | 35.68 | 42.93 | 1.115 | 1.399 | 1.683 |

## 4.2.3   CFD-DEM simulation setup

In addition to PTV measurements, CFD-DEM simulations were performed for the pseudo-2D bed to study collision dynamics. The physical properties and simulation parameters are summarized in Table 4.4. Particle interactions were calculated by the Hertzian contact model (HSD) with tangential history tracking (Section 3.4.1). In this soft-sphere contact model, the effects of spring and dashpot appear through stiffness $k$

Table 4.4: Physical properties and simulation parameters.

| Parameter | Value | Unit |
|---|---|---|
| *Simulation chamber* | | |
| Dimensions in x, y, z directions | $300 \times 1000 \times 20$ | mm |
| Grid numbers in x, y, z directions | $60 \times 300 \times 4$ | – |
| Size ratio $d_{cell}/d_{32}$ | 2.42 | – |
| *Particle phase* | | |
| *Contact model: hertzian, inelastic, with friction, rolling and tangential history* | | |
| Particle diameter $d_p$ | 1.8 | mm |
| Particle density $\rho_p$ | 945 | kg/m$^3$ |
| Coefficient of restitution $e$ | 0.79 | – |
| Young's modulus $E$ | $10^8$ | Pa |
| Poisson ratio $\sigma$ | 0.25 | – |
| Friction coefficient $\mu_f$ | 0.1 | – |
| Rolling coefficient $k_r$ | 0.1 | – |
| *Gas phase* | | |
| Gas density | 1.2 | kg/m$^3$ |
| Dynamic viscosity | $1.84 \times 10^{-5}$ | Pa · s |
| Superficial gas velocity | 1.68 | m/s |
| Boundary condition | *Slip* | – |
| *Coupling simulation parameters* | | |
| CFD time step $\Delta t_{CFD}$ | $5 \times 10^{-5}$ | s |
| DEM time step $\Delta t_{DEM}$ | $10^{-6}$ | s |
| Simulation time $t_{sim}$ | 10 | s |

and damping coefficient $\eta$, which were determined by the physical material properties of Poisson ratio $\sigma$, Young's modulus $E$ and the COR. The COR of $\gamma$-alumina particles was measured by the method used in Section 4.1. The COR for particle-particle interaction and particle-wall interaction were considered identical in the simulation. The $\gamma$-alumina particles were assumed to be less stiff than they are in reality, in order to avoid the requirement to use excessively small DEM time steps. A Young's modulus of $10^8$ Pa was used, which provided negligible differences as compared to simulation with the typical Young's modulus of $10^{10}$ Pa of $\gamma$-alumina particles [160]. Artificial softening of particles is universally used in CFD-DEM simulations of gas-solid flow in fluidized beds. Coulomb's friction law was applied to account for particle sliding, in which the friction coefficient $\mu_f$ was taken from Fries et al. [91]. The rolling coefficient $k_r$ in the directional constant rolling friction model (Section 3.4.2) was taken from Goniva et al. [128]. The drag force of individual particles was calculated by Tang et al. [138] (Section 3.2).

The chamber was divided into $60 \times 300 \times 4$ cells in $x$, $y$ and $z$ direction, respectively. The cuboid grids used in CFD-DEM simulation are depicted in Figure 4.3. The size ratio $d_{cell}/d_{32}$ was approximately 2.42. The divided particle volume mapping method was used according to Section 3.3. The time step should be set smaller than a critical

value to conform with physical laws and guarantee stability of the DEM and CFD solvers. The CFD time step was set to $5 \times 10^{-5}$ s, which ensured that the maximum Courant number was less than 0.5. The collision time $\tau_H$ can be estimated based on Hertz contact theory [161], expressed as:

$$\tau_H = 2.87 \Big( \frac{m_{eq}^2}{R_{eq} E_{eq}^2 v_{c,max}} \Big)^{0.2}. \tag{4.1}$$

Assuming a maximum collision velocity $v_{c,max}$ of 1.5 m/s in the whole bed [104], the estimated collision time $\tau_H$ for two particles is approximately $2.6 \times 10^{-5}$ s. Hence, the DEM time step was selected as $10^{-6}$ s, less than $\tau_H/20$ for the entire granular system, to ensure an accurate performance of the contact model. In the CFD, the pressure-implicit with split-operator (PISO) pressure-velocity coupling algorithm was used to solve the Navier-Stokes equations for unsteady flow. The k-$\epsilon$ model was applied to simulate mean flow characteristics for turbulent conditions. The coupling interval between DEM and CFD solvers was 50 times the DEM time step. Besides, different investigation regions for the spatial averages of PTV measurement data and CFD-DEM simulation data were also demonstrated in Figure 4.3.

The intensity calibration and determination of collision events used in PTV to evaluate particle collision dynamics and detailed comparisons with CFD-DEM simulations will be given in Chapter 6.

## 4.3 Pseudo-2D fluidized bed with poly-disperse particle system

Poly-disperse systems (with particles of different sizes, different densities, or both different sizes and densities) are commonly encountered in practical applications. As an important phenomenon in poly-disperse fluidization, the segregation and mixing of particles strongly influences particle formation processes. The PTV technique for the mono-disperse system can be readily extended to poly-disperse systems of particles with different sizes marked by distinguishable colors. Using a relatively small pseudo-2D fluidized bed, the mixing index was studied by color-PTV measurements in binary and ternary mixture systems.

### 4.3.1 Pseudo-2D fluidized bed

As shown schematically in Figure 4.4, the dimensions of the laboratory fluidized bed are 100 mm, 340 mm and 14 mm in width, height and depth, respectively. The front and side walls were made of acrylic glass and the back wall was made of aluminum. Pressurized air was used as fluidization gas. Accurate control of inlet gas flow rate was achieved by application of a calibrated mass flow controller. A 3 mm porous plate distributor with a mean pore size of 10 $\mu$m was used to generate a relatively uniform gas distribution.
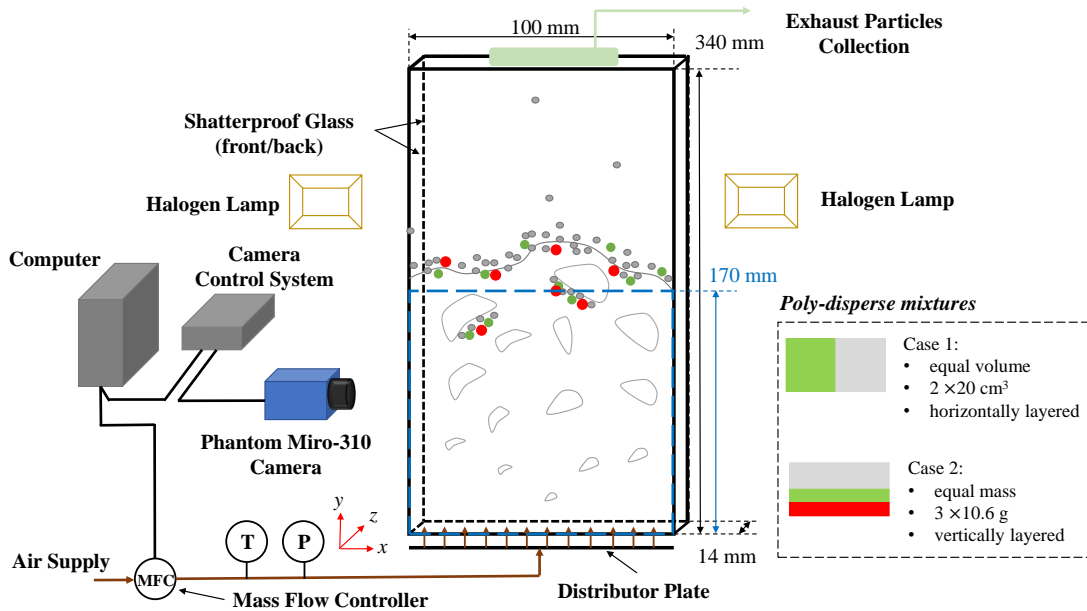
Figure 4.4: Sketch of laboratory-scale pseudo-2D fluidized bed configuration for poly-disperse systems with apparatus dimensions and initial mixture characteristics.

Three different fractions of $\gamma$-alumina particles with diameter $d_p$ of 3.0 mm, 2.5 mm and 1.8 mm (Geldart class D) were used in measurements, and detailed particle properties and operation conditions for two cases are summarized in Table 4.5. The size and sphericity of particles were measured by Camsizer (Retsch GmbH). The density of particles was measured by a pycnometer (GeoPyc 1360, Micromeritics GmbH). The COR of particles was, again, measured by the method used in Section 4.1. The minimum fluidization velocities $U_{mf}$ of different particles were calculated using the correlation of Wen and Yu [134]. Regarding the initial conditions, different particles are vertically layered with equal volume of 20 cm$^3$ in *Case 1*, and horizontally layered with equal mass of 10.6 g in *Case 2*, as also shown in Figure 4.4. The static height in both cases was approximately 28.5 mm. The Sauter mean diameter $d_{32}$ in both cases was approximately 2.15 mm. In each case, the gas flow rate was manually increased from zero to a superficial gas velocity of 2.8 m/s in approximately 1 s. The gas flow velocities experienced fluctuations of 0.02 m/s during the measurements.

## 4.3.2 Imaging system

Motion of particles in the poly-disperse particle systems was observed with a high-speed color camera (Phantom Micro-310, CMOS chip, 1280 × 800 pixels). It was operated at full spatial resolution with a frame rate of 1000 fps, an exposure time of 1/8000 s and a dynamic range of 12 bit. The imaging system was controlled by the DaVis image acquisition software (LaVision).

To capture the whole bed width, the FOV was adjusted to 100 × 170 mm$^2$, which corresponds to an approximate spatial resolution scale factor $S_f$ of 7.5 pixel/mm. This

Table 4.5: Particle properties, characteristics of mixtures and operation conditions.

| $d_p$ [mm] | $\rho_p$ [kg/m$^3$] | Sphericity [-] | e [-] | $U_{mf}$ [m/s] | Color |
|---|---|---|---|---|---|
| *Particle properties* | | | | | |
| 3.0 | 1478 | 0.97 | 0.79 | 1.05 | Red |
| 2.5 | 1450 | 0.97 | 0.81 | 0.91 | Green |
| 1.8 | 985 | 0.96 | 0.81 | 0.53 | White |

| Case | Bed mass [g] | | | Height [mm] | $U_g$ [m/s] |
|---|---|---|---|---|---|
| | 3.0 mm | 2.5 mm | 1.8 mm | | |
| *Characteristics of mixtures and operating conditions* | | | | | |
| 1 | - | 20.2 | 13.5 | 28.5 | $2.8 \pm 0.02$ |
| 2 | 10.6 | 10.6 | 10.6 | 28.5 | $2.8 \pm 0.02$ |

factor was obtained from the standard geometry calibration process in the DaVis software. Note that only 170 mm bed height can be observed by the imaging system, as marked in Figure 4.4. However, most of fluidization characteristics can be observed in this field of view. The depth of field was approximately 8 mm using the same light sources, optical lens, f-number as those used in Section 4.1.1.

The raw color images acquired from the high-speed camera are in the red-green-blue (RGB) space, which is defined by the three chromatic levels of red, green and blue additive primaries. The number of images stored in each measurement was 5000 (5 s measurement time), which included the initial (start-up) period.

### 4.3.3    CFD-DEM simulation setup

As mentioned in the verification of PTV methodology by synthetic images in Section 2.3, CFD-DEM simulations are performed for poly-disperse systems. The physical properties and simulation parameters are listed in Table 4.6. Particle interactions were also calculated by the Hertzian contact model with tangential history tracking (Section 3.4.1). The setups of Young's modulus $E$, COR, Poisson ratio $\sigma$, friction coefficient $\mu_f$ and rolling coefficient $k_r$ are the same as in Section 4.2.3. The drag model MBVK for mono-disperse system and PBVK for poly-disperse system are applied according to descriptions in Section 3.2.

Cuboid grids were used in the simulations. The chamber was divided into $20 \times 100 \times 3$ cells in $x$, $y$ and $z$ direction, respectively. The size ratio $d_{cell}/d_{32}$ was approximately 2.3 for both simulated cases, where $d_{cell} = \sqrt[3]{V_{cell}}$ was an effective length based on the volume of each CFD cell. For the purpose of examination of grid independence (results shown in section Section 7.3.1), two further CFD grids with size ratios of 2.0 (finer grid) and 2.7 (coarser grid) were also built. The accurate simulation of granular flow in fluidized beds is very sensitive to the correct calculation of cell solid volume fraction [162]. The divided particle volume mapping method was used according to Section 3.3, which is able to generate smooth solid volume fraction fields for poly-disperse particle systems.

Table 4.6: Physical properties and simulation parameters.

| Parameter | Value | Unit |
|---|---|---|
| *Simulation chamber* | | |
| Dimensions in x, y, z directions | $100 \times 340 \times 14$ | mm |
| Grid numbers in x, y, z directions | $20 \times 100 \times 3$ | − |
| Size ratio $d_{cell}/d_{32}$ | 2.3 | − |
| | 2.0, 2.7 (independence study) | − |
| *Particle phase* | | |
| *Contact model: hertzian, inelastic, with friction, rolling and tangential history* | | |
| Particle diameter $d_p$ | Table 4.5 | mm |
| Particle density $\rho_p$ | Table 4.5 | kg/m$^3$ |
| Coefficient of restitution $e$ | Table 4.5 | − |
| Young's modulus $E$ | $10^8$ | Pa |
| Poisson ratio $\sigma$ | 0.25 | − |
| Friction coefficient $\mu_f$ | 0.1 | − |
| Rolling coefficient $k_r$ | 0.1 | − |
| *Gas phase* | | |
| Gas density | 1.2 | kg/m$^3$ |
| Dynamic viscosity | $1.84 \times 10^{-5}$ | Pa · s |
| Superficial gas velocity | 2.8 | m/s |
| Boundary condition | *Slip* | − |
| *Coupling simulation parameters* | | |
| CFD time step $\Delta t_{CFD}$ | $5 \times 10^{-5}$ | s |
| DEM time step $\Delta t_{DEM}$ | $10^{-6}$ | s |
| Simulation time $t_{sim}$ | 30 | s |

$\Delta t$ is 1 ms according to the frame rate of the imaging system.

The PISO algorithm and k-$\epsilon$ model were used in the CFD solver. The CFD time step was set to $5 \times 10^{-5}$ s, which ensured that the maximum Courant number was less than 0.5. The collision time $\tau_H$ can be estimated based on Eq. (4.1). Assuming a maximum collision velocity $v_{c,max}$ of 1.5 m/s in the whole bed [104], the estimated collision time $\tau_H$ for two 1.8 mm particles (the smallest objects occurring in the system) is approximately $2.6 \times 10^{-5}$ s. Hence, the DEM time step was selected as $10^{-6}$ s, less than $\tau_H/20$ for the entire granular system, to ensure an accurate performance of the contact model. The coupling interval between DEM and CFD solvers was 50 times the DEM time step.

The algorithm of color-classification in PTV and detailed comparisons of different drag models used in CFD-DEM simulations of poly-disperse systems will be given in Chapter 7.

## 4.4 Wurster fluidized bed

An important characteristic of the Wurster fluidized bed is that particles continuously circulate in different zones to experience sub-processes of droplet deposition, drying

and solidification. Based on motion of individual particles, residence time distributions (RTDs) are investigated by CFD-DEM simulations in a Wurster fluidized bed.

## 4.4.1   Geometry of bed

The geometry of the Wurster fluidized bed was built according to the positron emission particle tracking (PEPT) experiments of Li et al. [27]. The configuration with detailed dimensions and structured meshes is illustrated in Figure 4.5. The diameter and length of the concentric cylindrical Wurster tube are 50 mm and 150 mm, respectively. There is a 15 mm partition gap between tube bottom and the distributor plate. A circular symmetric spray zone with inflection boundaries [28] was pre-defined in the simulation, where the maximum penetration was 75 mm and spray angle was about 52.5 degree, as plotted with red lines in Figure 4.5. The tip of the spray nozzle was located 10 mm higher than the distributor plate. The volumes of the spray zone and the Wurster tube were $0.19 \times 10^{-3}$ m$^3$ and $1.18 \times 10^{-3}$ m$^3$, respectively. A relatively large nozzle (5 mm diameter) was purposely used in the PEPT measurements [27], which is a benefit in avoiding numerical difficulties caused by the high speed atomization gas flow in CFD-DEM simulation.
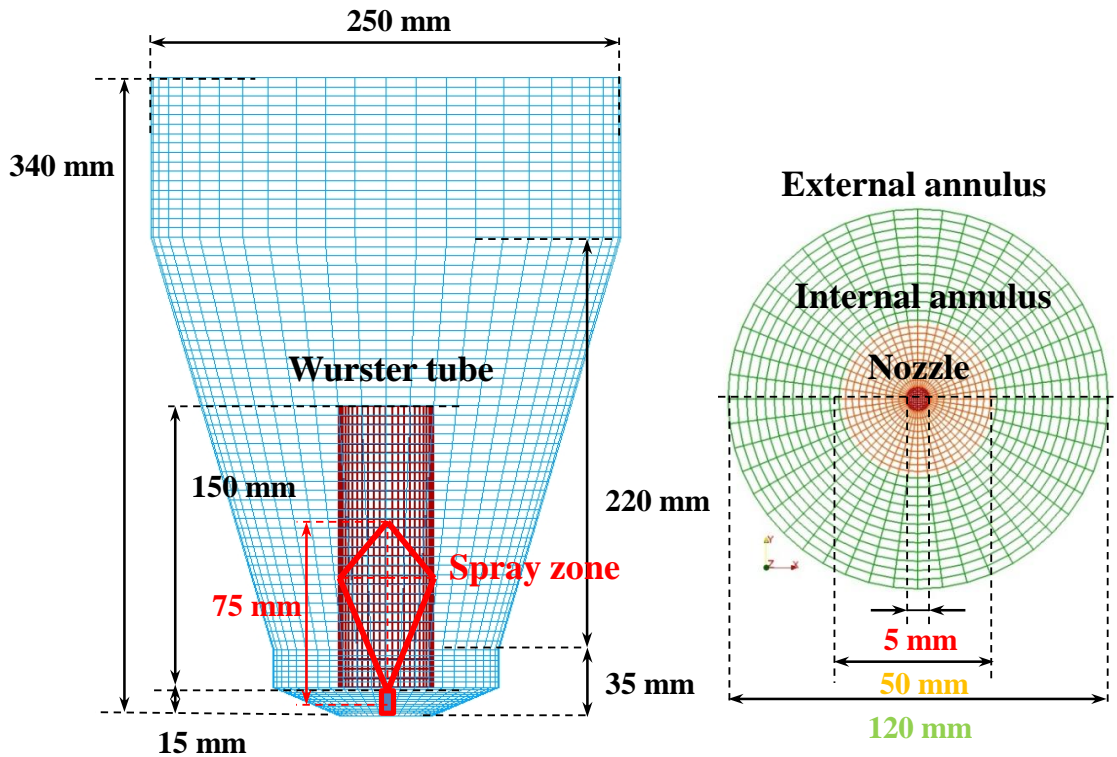


Figure 4.5: Geometry and structured grids of the Wurster fluidized bed together with specific dimensions (boundaries of the pre-defined axisymmetric spray zone are plotted as red lines).

## 4.4.2 Operation conditions and material properties

*Poly-disperse particle system*

The CFD-DEM simulation was conducted for the binary mixture system according to the runs number 11 and 12 in Li et al. [27]. The main objective of this simulation is to evaluate RTDs and interactions between particles and solid-like droplets, which will be fully discussed in Chapter 8. The total batch mass of 1.75 mm and 2.67 mm microcrystalline cellulose (MCC) particles was 200 g with equal mass fractions. The numbers of small particles and large particles inserted into the bed were 25000 and 7400, respectively. The detailed material properties of microcrystalline cellulose particles [93, 128, 163, 164], and operation conditions [27, 93] are listed in Table 4.7. The atomizer gas flow rate is 4.32 m$^3$/h; and the fluidization gas flow rate is 80.3 m$^3$/h. Only one tracer particle was used in each run of PEPT measurement. Therefore, the RTDs were evaluated from the long trajectory of a single particle (about 1.5 hours) based on the principle of ergodicity.

In a real coating process, fine coating droplets are generated by a two-fluid nozzle, involving complex break-ups from the liquid sheet to ligaments and droplets [30, 165]. From the perspective of numerical simulation, the modeling of the real droplets spray is beyond the scope of this study. Instead, solid-like droplets (without serious deformation)

Table 4.7: The detailed material properties of MCC particles and solid-like droplets and simulation parameters.

| Parameter | Value | Unit |
|---|---|---|
| *MCC particle* | | |
| Particle diameter | 1.75, 2.67 | mm |
| Particle density | 1420, 1387 | kg/m$^3$ |
| Poisson ratio | 0.3 | – |
| Young's modulus | $10^6$ | Pa |
| Coefficient of restitution | 0.69 | – |
| Friction coefficient | 0.53 | – |
| Rolling coefficient | 0.1 | – |
| *Solid-like droplet* | | |
| Droplet diameter | 0.1 | mm |
| Droplet density | 1000 | kg/m$^3$ |
| Coefficient of restitution | 0.1 | – |
| *Fluidization gas* | | |
| Density | 1.2 | kg/m$^3$ |
| Dynamic viscosity | $1.84 \times 10^{-5}$ | Pa·s |
| Number of structured CFD cells | 81600 | – |
| CFD time step $\Delta t_{CFD}$ | $5 \times 10^{-5}$ | s |
| DEM time step $\Delta t_{DEM}$ | $10^{-6}$ | s |
| CFD-DEM coupling $\Delta t_{c,1}$ | $5 \times 10^{-5}$ | s |

with diameter of 0.1 mm were injected into the bed with a liquid flow rate of $10^{-3}$ m$^3$/h. The initial velocity of droplets was set to zero and they are accelerated by the high velocity gas (without swirl) generated by the spray nozzle. The main material properties of the solid-like droplets were considered to be the same as those of the real particles, except of the COR which was set to 0.1 to take account of high energy dissipation due to particle-liquid interactions. Because of the small mass of solid-like droplets, the influence of droplets on the particle motion was very limited and did not affect the comparisons with PEPT measurement results. Furthermore, it was assumed that the droplets can be deleted when they pass through the spray zone boundaries, which limited the life-time of droplets and the total number of droplets in the simulation domain.

*Mono-disperse particle system*

The CFD-DEM simulation was conducted for the mono-disperse system according to the run number 16 in Li et al. [27]. The droplet deposition on individual particles was accounted for in the CFD-DEM simulation by a Monte Carlo approach, which will be thoroughly explained in Chapter 9. The total batch mass of 1.75 mm MCC particles is 200 g (about 50000 particles). The atomizer gas flow rate is 3.5 m$^3$/h; and the fluidization gas flow rate is 80.3 m$^3$/h. No solid-like droplets were used in this simulation.

## 4.4.3   Simulation parameters

*Poly-disperse particle system*

The HSD model and rolling model were used to calculate the particle-particle interactions (Section 3.4). The Young's modulus $E$ and the friction coefficient $\mu_f$ were taken from Li et al. [93]. The Poisson ratio $\sigma$ was measured by Roberts et al. [166]. The rolling coefficient $k_r$ in the directional constant rolling friction model was taken from Goniva et al. [128].

The Gidaspow drag model was applied using the Sauter mean diameter $d_{32}$ (Section 3.2). Assuming a maximum collision velocity of 1.5 m/s in the Wurster coater, the estimated collision time $\tau_H$ for two solid-like droplets (the smallest bodies occurring in the system) is about $1.5 \times 10^{-5}$ s by Eq. (4.1). Therefore, the DEM time step was selected as $10^{-6}$ s, less than $\tau_H/15$ for the entire granular system, to ensure an accurate performance of the Hertz contact model. The PISO algorithm and k-$\epsilon$ model were used in the CFD solver. The CFD time step was set to $5 \times 10^{-5}$ s, which ensured that the maximum Courant number was less than 0.5. The coupling interval between the DEM and CFD solvers $t_{c,1}$ was set to 50 times the DEM time step, i.e. 50 $\mu$s.

The DEM simulation was firstly performed to insert particles into the simulation domain, and this preliminary DEM simulation ended when all particles were almost static. Initially, large and small particles were separated, with large particles at the bottom. After particle insertion, the CFD-DEM simulation started and the flow rates of fluidization gas and atomization gas were linearly increased from 0 to the target values

in 2 s time. The insertion of solid-like droplets started from the time mark 2 s of the CFD-DEM simulation. In order to accurately analyze cycle time and RTDs, at least 30 seconds simulation time had to be completed based on Li et al. [93], while the first 5 s simulation results were not used in the analysis to avoid an influence of initial separation on the circulation motion of particles. In DEM, the impact (collision) velocity is defined as the relative velocity of two particles at their first moment of contact. The impact velocity can significantly affect the appearance of particle agglomeration in the Wurster coater.

*Mono-disperse particle system*

Assuming a maximum collision velocity $v_{c,max}$ of 1.5 m/s in the whole bed, the estimated collision time $\tau_H$ for two 1.75 mm particles is approximate $2.6 \times 10^{-5}$ s. Hence, the DEM time step was set as $10^{-6}$ s, less than $\tau_H/20$. The CFD time step and coupling interval are the same as those for poly-disperse particle system. The drag model MBVK was used in this simulation (Section 3.2). The setup of contact model is similar to the poly-disperse system.

To investigate the effect of cohesion forces on particle circulation in the Wurster bed, the capillary force induced by liquid bridge, Eq. (3.64), was also taken into account in the DEM simulation. The capillary force was related to the separation (inter-particle) distance $d_{inter}$, the surface tension of the liquid $\sigma_f$, and the dimensionless regression parameters $A$, $B$, $C$, Eqs. (3.65) to (3.67), obtained from the solution of the Laplace-Young equation [149]. Liquid bridges appear if the inter-particle distance between two particles is shorter than the rupture distance $D_r$ (Eq. (3.68)) or during the collision of two particles. Note that the inter-particle distance was considered zero in the latter case, where the magnitude of capillary force had a constant value. Moreover, the capillary force disappears when the separation distance increases to the point of bridge rupture. When implementing the liquid bridge force model into DEM simulations, some assumptions are used: i) the capillary force only exists in the Wurster tube and spray zone; ii) the volume of all individual liquid bridges is equal and constant (without effects of drying and bridge rupture); and iii) there is no capillary force during particle-wall interactions. The parameter $\alpha_l$, which defines the ratio of the volume of liquid bridge $V_l$ and the total volume of two primary particles $2V_p$ (mono-disperse), was a model parameter to calculate the volume of liquid bridge.

It is important to note that the drag force acting on the solid phase might be reduced due to the decrease of inter-phase surface for relatively large agglomerate [167]. Normally, the drag force can be scaled by a constant factor or a dynamic factor related to the structure of the agglomerate and the number of primary particles in the agglomerate [84]. In the present work, no scaling of the drag force was attempted in consideration of the relatively small size and instability of the agglomerates induced by the liquid bridge.

### 4.4.4   Mesh independence

Since a structured grid is important for the mapping procedure, the orthogonal grid method was used to build hexahedral grids. The grid was relatively fine near the center axis, in which the gas experiences high velocity due to the influence of the spray. The detailed orthogonal grid method using the built-in *OpenFOAM* function *blockMesh* is given in Section B.5.

The first 5 s of CFD-DEM simulation were performed for the three different sets of computational grids (numbers of cells 81600, 122400, 163200, respectively). The average velocity of gas in the axial direction was evaluated in the circular plane 15 mm above the bottom distributor for the time range 4 s to 5 s, as shown in Figure 4.6. Clearly, only little differences exist for the three sets of grids. The spray nozzle generates high gas velocity close to the axis; then the gas velocity gradually decreases to almost zero when reaching the Wurster tube; and the axial gas velocity keeps a relative constant value in the horizontal transport zone except the regions close to the walls. Based on these results, the set with smallest cell number (81600) was used in all CFD-DEM simulations. From the numerical point of view, fine CFD cells (smaller than the particle size) are desirable to be used in some special regions, in order to obtain the details of gas flow and guarantee grid-independent solution, for example in the spray zone. However, fine CFD cells will pose the problem of accurate evaluation of local solid volume fraction.
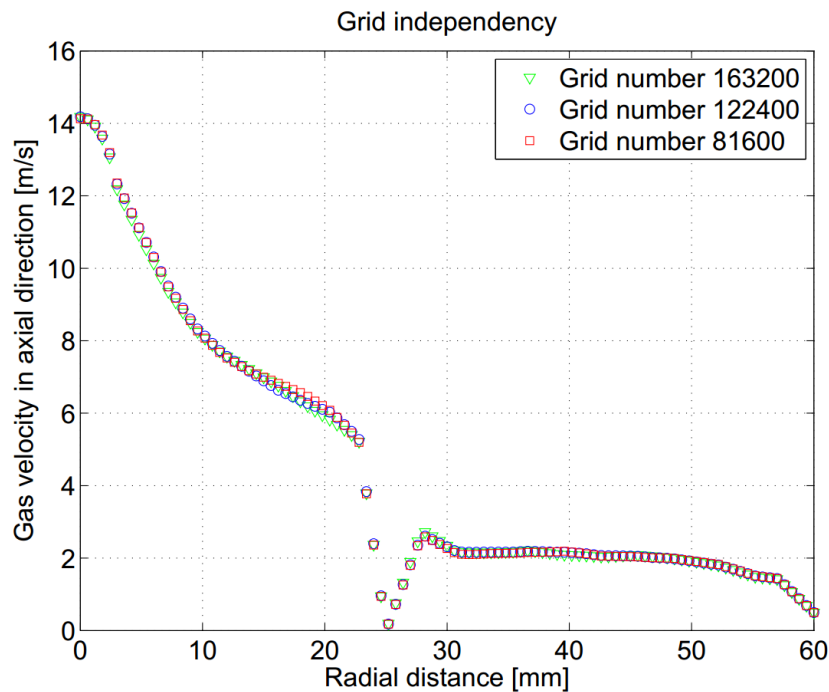


Figure 4.6: Grid independence with respect to average gas velocity in the axial direction (for a circular cross-section located at 15 mm above the bottom distributor).

Thus, the big particle model (Section 3.3) was used in the fine grid region, in which the constant factor $S_{cube}$ was set to 3.

All experiments and simulations conducted in this thesis are summarized in Table A.1 and Table B.1, respectively.

# Chapter 5

# PTV experiments and DEM simulations of the coefficient of restitution for irregular particles impacting on horizontal substrates

*This chapter is based on Jiang et al. [105].*

## 5.1 Coefficient of restitution

Due to its significance, there are a lot of results about the measurement of the coefficient of restitution (COR) for spherical particles in cases of normal impacts [24, 168, 169] or oblique impacts [170–173] at both dry and wet conditions.

However, particles are almost always irregular in real applications. Reported experimental studies with irregularly shaped particles are relatively limited, for instance, for pharmaceutical tablets [164], polyethylene pellets [174, 175], polyethylene glycol flakes [176], maize grains [177, 178] and coke particles [175]. Most measurements of the COR use high-speed imaging systems to capture the particle drop and the subsequent rebound, since the early work of Labous et al. [179]. The measurement accuracy with irregular particles is influenced by the out-of-plane motion of particles that results from various particle properties (such as, the shape and the surface roughness) and the method to initialize the particle movement. The out-of-plane motion of particles can be captured by two synchronized high-speed cameras [173, 180] or one high-speed camera with an additional mirror [174], on account of narrowing the distribution of measured COR. In order to detect the complete impact process, a high enough temporal resolution must be used, resulting in an inevitable decrease of the spatial resolution. Besides, the COR can be measured by, for example, the analysis of sound-sensor signals obtained from a piezoelectric sensor [181], the micro particle interaction analyzer (MPIA) [169], or the stroboscopic illumination technique [182].

Moreover, recent years have seen a substantial increase of interest in DEM simulations of particulate systems with non-spherical particles, in which the contact force is quite

complicated and closely related to the contact geometry including the contact area and the specific geometry of overlap region. Comprehensive reviews about the theoretical development and applications of non-spherical DEM simulations are given by Zhong et al. [103] and Lu et al. [183]. Despite a range of methods having been proposed for representing the shapes of non-spherical particles, for instance, the composite multi-sphere model [184, 185] and the continuous superquadric model [185, 186], and for detecting the contacts of non-spherical particles, big challenges still exist to efficiently and accurately handle particles involving the aspects of non-convex shapes, heterogeneous sizes and multiple contacts. The evidence on the validity of the multi-sphere model is limited. Kruggel-Emden et al. [184] and Höhner et al. [187] approximated a spherical particle by the multi-sphere model together with a roughness factor; and studied the particle-wall collision behavior. Markauskas and Kačianauskas [188] and Santos et al. [189] compared the discharge time, the angle of repose, and the coefficient of friction obtained from multi-sphere DEM simulations with experiments for rice grains.

Experiment data for highly angular, lowly spherical, irregular and even non-convex particles (similar to maltodextrin in Figure 4.2a) is very scarce. A particle is non-convex if there exist two points inside the particle such that the line segment connecting these two points does not lie entirely inside the particle [190]. Due to the complex behavior of such irregular particles after collision, the coefficient of restitution should be expected to be distributed depending on the geometry. Thus, experiments that enable to obtain the distributions of characteristics associated with collisions of non-spherical particles are essential for the comparison and the improvement of different non-spherical DEM algorithms.

The objective of this chapter is to evaluate the performance of the improved particle tracking velocimety (PTV) in tracking irregular particles with a characteristic size of 100 $\mu$m. Moreover, the distributions of COR and properties associated with particle-wall collision behavior, including the rotational speed after impacting and the difference of incidence angle and rebound angle, can be evaluated from individual particle trajectories. The measurement data can be further used to validate DEM simulations of the collisions between irregular particles and horizontal substrates.

The structure of this chapter is: Section 5.2 introduces the improvement of PTV for the COR of irregular particles. Section 5.3 briefly describes the multi-sphere (MS) model and the superquadric (SQ) model used in DEM simulations of non-spherical particles, together with the representation of irregular particles based on scanning electron microscope (SEM) images. Section 5.4 presents and discusses the measurement results about characteristics of particle-wall collisions, including distributions of total and normal coefficients of restitution, the rotation speed after collision, the absolute difference of incidence angle and rebound angle. In addition, detailed comparison of collision characteristics is performed with data from DEM simulations using two models of representation.

## 5.2 Tracking of non-spherical particles

### 5.2.1 Iterative thresholding

Based on the setup of measurements given in Section 4.1, the PTV method described in Chapter 2 was improved to reconstruct trajectories of irregular particles.

The raw image acquired by the high-speed camera is a gray level image, the intensity $I$ of which ranges from 0 to $2^{10}$. Provided that an image contains target particles and the background occupying different average intensity (gray) levels, the histogram-based iterative thresholding provides a simple and effective technique to automatically select the optimal threshold $T_{opt}$ to target particles [191], expressed as

$$T_{opt} = \lim_{n \to \infty} \frac{w_b(T_n) + w_p(T_n)}{2}. \tag{5.1}$$

The histogram was used to estimate the probability mass function (PMF) $p(I)$ of the raw image. With a threshold intensity $T$, the probability mass functions of the target particle and the background are $p_p(I)$, $T + 1 < I < I_{max}$ and $p_b(I)$, $I_{min} < I < T$, respectively. According to Eq. (5.1), a new threshold $T_n$ is calculated by the average of weighted mean of the background $w_b(T_n)$ and the target particle $w_p(T_n)$ for each iteration $n$ [192]. The weighted mean of the background $w_b(T_n)$ and the target particle $w_p(T_n)$ can be, respectively, calculated by

$$w_b(T_n) = \sum_{I=0}^{T_n} I \cdot p_b(I), \tag{5.2}$$

$$w_p(T_n) = \sum_{I=T_n+1}^{I_{max}} I \cdot p_p(I). \tag{5.3}$$

The initial threshold is $T_0 = (I_{max} - I_{min})/2$; and the termination criterion for the iteration is $|T_{n+1} - T_n|/T_n < 0.05$. After the iterative thresholding process, the raw image was transformed into a binary image, i.e. regions of particles and the background were assigned values of unity and zero, respectively. The method of image moment was then used to get the centroid $\boldsymbol{r}$, orientation $\theta_o$, aspect ratio $L_{minor}/L_{major}$ and area $A_I$ of each individual irregular particle (from Eq. (2.3) to Eq. (2.9)). The minimum displacement algorithm was used to reconstruct the trajectory of each individual irregular particle (Eq. (2.11)).

If the irregularly shaped particle experiences a translational motion in the out-of-plane direction, the area $A_I$ of the particle obviously varies due to the small depth of the field of view (approximately 0.1 mm). If the irregularly shaped particle experiences rotations around axis x and axis y (space-fixed), the aspect ratio $R_A = L_{minor}/L_{major}$ can vary depending on the detailed particle geometry. Hence, the coefficients of variation $c_v$ of area and aspect ratio of the tracked particles were used to filter particles with out-of-plane motion and rotations around axis x and axis y. Only if $c_v(A_{I,i}) < 10\%$ and

$c_v(R_{A,i}) < 10\%$, the particle was considered as qualified for the analysis of coefficient of restitution and other collision properties. The total number of variables in the data sets of $A_I$ and $R_A$ was determined by the length of the individual particle trajectory. In order to avoid the influence of rotation of particles before collision, only the particles without rotation before collision are considered in the post-processing.

### 5.2.2   Particle-wall collision behavior

The trajectory obtained from PTV was used to analyze the particle-wall collision behavior for each individual particle. As shown in Figure 4.1b, the total coefficient of restitution $e$ for particle-wall collisions is defined from the impact velocity $v_1$ and rebound velocity $v_2$, expressed by

$$COR = e = \frac{|v_2|}{|v_1|}. \tag{5.4}$$

The normal and tangential coefficients of restitution can be further evaluated using the normal and tangential components of impact and rebound velocities, respectively, as

$$COR_n = e_n = \frac{|v_{n,2}|}{|v_{n,1}|}, COR_t = e_t = \frac{|v_{t,2}|}{|v_{t,1}|}. \tag{5.5}$$

Assuming that the variation of orientations in two subsequent frames is not larger than $\pi/2$, the angular velocity of the particle around the $z$ axis (in space-fixed system) can be obtained by

$$\omega = \frac{\min(\pi - |\theta_{o,2} - \theta_{o,1}|, |\theta_{o,2} - \theta_{o,1}|)}{\Delta t}, \tag{5.6}$$

in which the subscripts 1 and 2 stand for the subsequent frames. The numerator is the shortest difference of two angles, as $\theta_o \in [-\pi/2, \pi/2]$. Furthermore, the incidence angle $\theta_1$ and the rebound angle $\theta_2$ are defined as the angles between velocity vectors and the vertical axis,

$$\theta_1 = \arctan\left(\left|\frac{v_{1,t}}{v_{1,n}}\right|\right), \theta_2 = \arctan\left(\left|\frac{v_{2,t}}{v_{2,n}}\right|\right). \tag{5.7}$$

These two angles are in the range of 0 to 90°. The absolute difference of the two angles $\Delta\theta$ equals to $|\theta_2 - \theta_1|$.

## 5.3   DEM simulation of non-spherical particles

### 5.3.1   Equation of motion

In order to handle the rotational motion of irregularly shaped particles, two coordinate systems, i.e. the space-fixed (or laboratory, global) system $S^s$ and the body-fixed (local) system $S^b$, must be clearly defined. The space-fixed coordinate system is not moving with the particle but fixed in the global space. Newton's equations of motion are formulated in the space-fixed system. Therefore, it is the native system of

the DEM simulation; and other coordinates and other variables describing the state of particles must be finally expressed in this system. However, in the space-fixed system, the moment of inertia tensor $I_i$ contains off-diagonal elements which change with the orientation of irregularly shaped particles. This problem is solved by introducing the body-fixed system that has the centroid of an individual particle as its origin and axes which are coinciding with the principle axes of inertia of this particle. Note that any physical parameter can be transformed from the space-fixed axes $\Phi^s$ into the body-fixed axes $\Phi^b$ and vice versa by the transformation matrix $\Lambda_i$, as follows:

$$\Phi^b = \Lambda_i^{-1} \cdot \Phi^s, \ \Phi^s = \Lambda_i \cdot \Phi^b. \tag{5.8}$$

The translational motion governed by Newton's second law of motion in the space-fixed system, is expressed by

$$m_i \frac{d\boldsymbol{G}_i^2}{d^2 t} = \boldsymbol{F}_{sum}, \tag{5.9}$$

in which $m_i$ and $\boldsymbol{G}_i$ are the total mass and the coordinates of the centroid of gravity of the non-spherical particle $i$, respectively. The term $\boldsymbol{F}_{sum}$ is the sum of forces acting on particle $i$ in the space-fixed system, including normal and tangential particle-particle contact forces and other external forces. The Hertzian spring-dashpot (HSD) model was used to calculate the contact force and detailed equations are given in Section 3.4.

The rotational motion is affected by the particle shape, which can be obtained from the Euler equations in the body-fixed frame. It follows:

$$\hat{I}_i \frac{d\boldsymbol{W}_i}{dt} + \boldsymbol{W}_i \times \left( \hat{I}_i \boldsymbol{W}_i \right) = \Lambda_i^{-1} \boldsymbol{T}_{sum}, \boldsymbol{W}_i = \frac{d\boldsymbol{\theta}_i}{dt}, \tag{5.10}$$

where $\boldsymbol{W}_i$ is the angular velocity in the body-fixed system, $\boldsymbol{T}_{sum}$ is the sum of all torques acting on the particle $i$ in the space-fixed frame; and the $\hat{I}_i$ is the principal moment of inertia calculated by the principal axis transformation from inertia tensor $I_i$ in the space-fixed system. Accordingly, the transformation is required to convert the moments $\boldsymbol{T}_{sum}$ from the space-fixed frame to the body-fixed frame, via the transformation matrix $\Lambda_i$. Different algorithms can be used to deal with the problems caused by the orientation of irregularly shaped particles, depending on different approaches to represent irregular particle shapes [103, 183].

## 5.3.2 Representation of irregular shapes of particles

As shown in Figure 5.1, the multi-sphere model and the superquadric model were used to represent the irregularly shaped maltodextrin particles according to the scanning electron microscope (SEM) measurements.

*Multi-sphere model*

In the composite multi-sphere model, the irregularly shaped particle can be approximated by a certain number of rigidly connected primary spheres with different sizes.

Table 5.1: Summary of equations used in the multi-sphere model and the superquadric model.

*Multi-sphere (MS) model*

$$m_i = \sum_{k=1}^{N_s} m_{i,k}$$ 

(5.11)

$$\boldsymbol{G}_i = \sum_{k=1}^{N_s} (\boldsymbol{G}_{i,k} m_{i,k})/m_i$$ 

(5.12)

$$I_i = \begin{bmatrix} \sum I_{i,k} + \sum m_{i,k}(G_{y,k}^2 + G_{z,k}^2) & -\sum m_{i,k} G_{x,k} G_{y,k} & -\sum m_{i,k} G_{x,k} G_{z,k} \\ -\sum m_{i,k} G_{x,k} G_{y,k} & \sum I_{i,k} + \sum m_{i,k}(G_{x,k}^2 + G_{z,k}^2) & -\sum m_{i,k} G_{y,k} G_{z,k} \\ -\sum m_{i,k} G_{x,k} G_{z,k} & -\sum m_{i,k} G_{y,k} G_{z,k} & \sum I_{i,k} + \sum m_{i,k}(G_{x,k}^2 + G_{y,k}^2) \end{bmatrix}$$ 

(5.13)

$$I_i = \Lambda_i \cdot \hat{I}_i \cdot \Lambda_i^{-1}$$ 

(5.14)

*Superquadric (SQ) model*

$$\boldsymbol{q} = (q_0, q_1, q_2, q_3) = \cos(\theta_e/2) + e^b \sin(\theta_e/2);$$ 

(5.15)

$$\Lambda_i = \begin{pmatrix} 1 - 2(q_2^2 + q_3^2) & 2(q_1 q_2 - q_0 q_3) & 2(q_1 q_3 + q_0 q_2) \\ 2(q_1 q_2 + q_0 q_3) & 1 - 2(q_1^2 + q_3^2) & 2(q_2 q_3 - q_0 q_1) \\ 2(q_1 q_3 - q_0 q_2) & 2(q_2 q_3 + q_0 q_1) & 1 - 2(q_1^2 + q_2^2) \end{pmatrix}$$ 

(5.16)
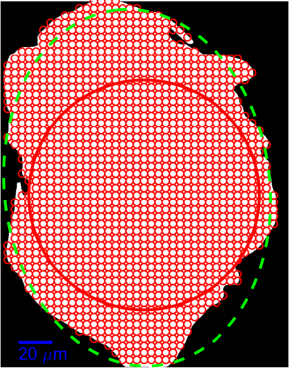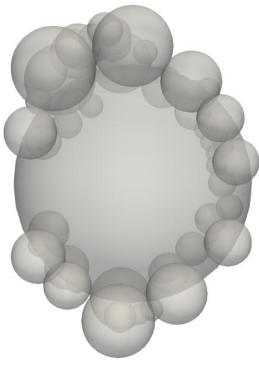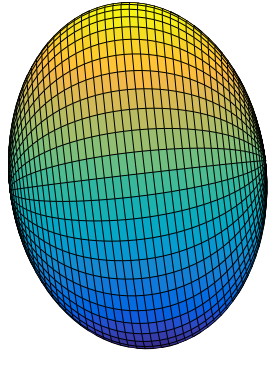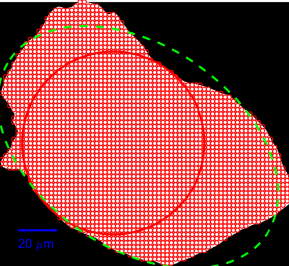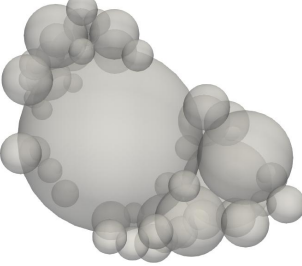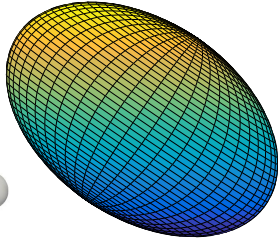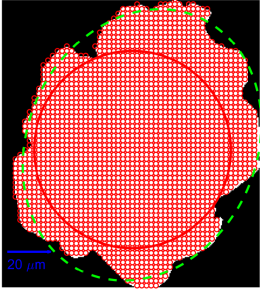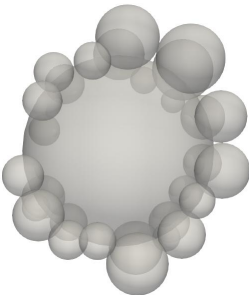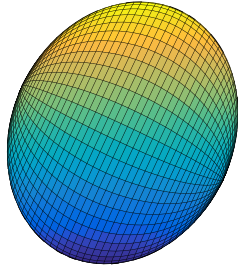
| Parameter | Binary image from SEM | MSM | Superquadric (ellipsoid) |
|---|---|---|---|
| **DE 6-P1**<br>Major axis: 199 $\mu$m<br>Minor axis: 148 $\mu$m<br>Aspect ratio: 1.35<br>Porosity in MS: 0.395<br>Sphericity: 0.75<br>Nr. of spheres: 51 | | | |
| **DE 6-P2**<br>Major axis: 150 $\mu$m<br>Minor axis: 98 $\mu$m<br>Aspect ratio: 1.53<br>Porosity in MS: 0.398<br>Sphericity : 0.82<br>Nr. of spheres: 48 | | | |
| **DE 6-P3**<br>Major axis: 119 $\mu$m<br>Minor axis: 98 $\mu$m<br>Aspect ratio: 1.22<br>Porosity in MS: 0.396<br>Sphericity : 0.77<br>Nr. of spheres: 33 | | | |

Figure 5.1: Representations of irregular and non-convex maltodextrin (DE 6) particles by means of the multi-sphere model and the superquadric model based on scanning electron microscope (SEM) images.

During the DEM simulation, the relative distances between spheres will remain fixed. The contact force between multi-sphere particles is calculated from primary spheres using the sphere-sphere contact detection model and the HSD contact force model. Then, the forces and torques acting on all primary spheres are accumulated to the center of mass of the multi-sphere particle. Specifically, for an irregular particle $i$ assembled from spheres with the same density, the total mass $m_i$, the coordinate of the centroid of gravity $\boldsymbol{G}_i$, and the inertia tensor $I_i$ can be calculated by Eq. (5.11), Eq. (5.12), and Eq. (5.13), respectively, in Table 5.1. $N_s$ is the number of spheres in the multi-sphere particle $i$; $m_{i,k}$ and $I_{i,k}$ are the mass and moment of inertia of the individual sphere $k$,

respectively, and $G_{x,k}$, $G_{y,k}$ and $G_{z,k}$ are the distances from the principal axes of the multi-sphere particle $i$ to the centroid of sphere $k$.

The detailed multi-sphere representation is achieved by the clustering method [193] according to the 2D geometry of individual particles from SEM. As indicated in Figure 5.1, the steps of the clustering method include:

1 Obtain the surface of an irregular particle from a SEM image. The original SEM image was first binarized by the iterative thresholding method (Section 5.2.1). Then, it is easy to generate primary circles inside the boundary of the 2D irregular particle.

2 Expand all primary circles to the boundary of the 2D particle; the one with the largest diameter is recorded as $S_1$. The centroid of $S_1$ locates at $(x_{s,1}, y_{s,1})$, and the diameter of $S_1$ is $d_{s,1}$.

3 Expand the 2D surface in the third direction with a depth of $d_{s,1}$ to generate the 3D structure of the irregular particle. The centroid of $S_1$ is adjusted to $(x_{s,1}, y_{s,1}, d_{s,1}/2)$.

4 Generate primary spheres inside the boundary of the 3D particle and remove the primary spheres the centroids of which are located inside the boundary of $S_1$. The boundary of $S_1$ is considered to constrain the expansion of other primary spheres.

5 Expand the remaining primary spheres to the boundaries of the 3D particle and $S_1$, and record the one with the largest diameter as $S_2$. Remove the primary spheres the centroids of which are located inside the boundary of $S_2$. The boundary of $S_2$ is added as a new constraint.

6 Repeat step 5 to find the sphere $S_n$. The termination criterion used in this work is $\epsilon = \sum^n V_{s,i}/V_P \leq (\rho_p/\rho_{solid})$.

7 Generate the 3D multi-sphere irregular particle according to the centroids and the diameters of $S_1$ to $S_n$.

The entire clustering representation is accomplished by a self-developed algorithm in MATLAB. Figure 5.1 shows three typical multi-sphere maltodextrin particles generated by this method. The aspect ratios of $P3$, $P1$, $P2$ are 1.22, 1.35 and 1.53, which, receptively, corresponds to the $R_{A,10}$, $R_{A,50}$ and $R_{A,90}$ measured by the Camsizer. The ratios of smallest to largest sphere diameter of $P1$, $P2$, $P3$ are 0.092, 0.117 and 0.154; and the numbers of spheres of $P1$, $P2$, $P3$ are 51, 48, 33, respectively. The density of each sphere is the solid density of maltodextrin $\rho_{solid}$. By this presentation method, the relative differences between the centroid of gravity $\boldsymbol{G}_i$ (Eq. (5.12)) and the centroid of $S_1$ are less than 5 %. Moreover, the non-convex feature of the particles can be partly preserved. Obviously, the shape of particles can be better represented with increasing number of spheres, but the simulation expenses are also significantly increased.

In case of 3D geometries of irregular particles obtained from X-ray tomography [157, 194], the clustering method can start from step 4. Notably, the multi-sphere model can be further modified into the bonded-particle model [195] to formulate clusters with arbitrary shapes; in which the bonds between particles are possible to deform and break.

*Superquadric model*

The superquadric model is a continuous functional approach to smoothly represent non-spherical particles, given as follows

$$f_{super}(\boldsymbol{X}) = \left( \left| \frac{x}{a} \right|^{n_2} + \left| \frac{y}{b} \right|^{n_2} \right)^{n_1/n_2} + \left| \frac{z}{c} \right|^{n_2} - 1 = 0, \qquad (5.17)$$

where $a$, $b$, $c$ are the half-lengths of the particle along its principal axes, and $n_1$ and $n_2$ are blockiness parameters. The contact detection of superquadric model can be achieved by analytically or iteratively resolving the interactions between functions of different particles, or by the discrete function representation [183]. Equation (5.17) defines the surface of superquadric particles in the body-fixed coordinate system. If a certain $\boldsymbol{X}$ makes $f_{super} < 0$, then the point $\boldsymbol{X}$ is located inside the superquadic particle. If $f_{super} > 0$, the point $\boldsymbol{X}$ is outside the particle. If $f_{super} = 0$, the point $\boldsymbol{X}$ lies on the surface of the particle. In the superquadric model, the transformation matrix can be calculated by the method of quaternions. A rotation by angle $\theta_e$ around the unit axis of rotation $\boldsymbol{e}^b$ can be represented by a rotation quaternion with the help of an extension of Euler's formula (Eq. (5.15)). The quaternions must satisfy the constraint of $q_0^2 + q_1^2 + q_2^2 + q_3^2 = 1$. Then, the rotation matrix $\Lambda = \Lambda(\boldsymbol{q})$ can be constructed from the quaternion components according to Eq. (5.16). The analytical expressions for the volume and inertia tensor of superquadric particle follow the work of Jaklic et al. [196]; and the detailed particle-particle and particle-wall contact detection algorithms have been described in the paper of Podlozhnyuk et al. [186].

Supposing that the shape of irregular particles can be represented by a 3D ellipsoid (as shown in Figure 5.1), the blockiness parameters $n_1$ and $n_2$ in Eq. (5.17) are both set to 2 and the parameters $a$ and $b$ representing half the lengths of the principal axes are set to be equal. Then, the values of $a$, $b$, $c$ are measured from the SEM image by evaluation of image moments (Eq. (2.8) and Eq. (2.9)), i.e. $a = b = L_{minor}/2$ and $c = L_{major}/2$. By the SQ method, all non-convex features of maltodextrin particles are lost and particle surfaces are smooth.

For impacts between maltodextrin particles (DE 6) and the maltodextrin tablet substrate, the DEM simulations were performed using the built-in multi-sphere model or the superquadric model in the DEM package LIGGGHTS [197]. For each approach of the shape representation, 1000 irregular particles with random initial orientations were dropped onto the substrate from different heights to finally achieve the normal distributions of normal and tangential impact velocities. The required means and standard deviations were evaluated from PTV measurements (Table 5.2). The initial rotational speed of all particles was set to zero. As listed in Table 4.1, the Young's modulus and Poisson ratio of maltodextrin particles were obtained from published experimental data

[198]. The mean value of the COR from measurements was used as the input parameter of the HSD contact model. A simple inclined plane experiment was used to estimate the particle-wall sliding friction coefficient. Maltodextrin particles were placed on a maltodextrin tablet and the tablet was then gradually tilted. The angle at which the maltodextrin particles started to slide down was recorded by the high-speed imaging system and was used to calculate sliding friction coefficient. The measurement was repeated 10 times and the average sliding friction coefficient was about 0.5.

## 5.4    Results and discussion

### 5.4.1    Analysis for sample particle

Figure 5.2a shows the trajectory of a sample maltodextrin (DE 6) particle before and after impacting on the maltodextrin (DE 6) tablet. Due to the complex contact geometry of the irregular particle, the trajectories of the sample particle before and after the
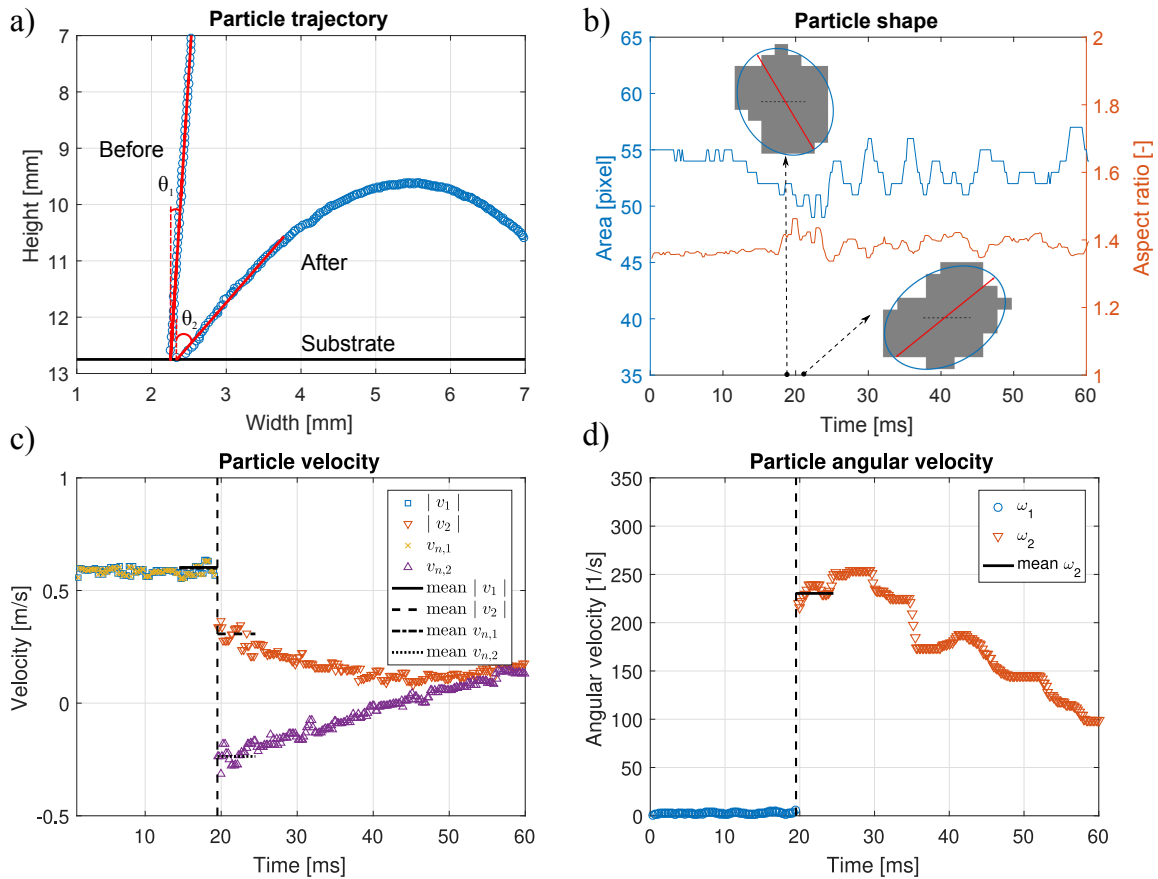


Figure 5.2: Analysis for sample particle: a) particle trajectory (with incidence angle $\theta_1$ and rebound angle $\theta_2$), b) area $A_I$ and aspect ratio $R_A$, c) translational velocities $v_1$ and $v_2$, and d) rotational speeds $\omega_1$ and $\omega_2$.

collision with the substrate are both located at the right-hand side of the vertical axis. The rebound angle is larger than the incidence angle, resulting in an absolute difference of two angles of 25.5 degrees.

Considering the entire trajectory of the sample particle (320 time steps), the mean value of the area $A_I$ is 53.07 with a CV of 3.16%; and the mean value of the aspect ratio $R_A$ is 1.38 with a CV of 1.78%, as shown in Figure 5.2b. Thus, the sample particle is a qualified particle, in which the effects of the motion in $z$ direction and the rotations around $x$, $y$ axes on the particle tracking are very small.

Figure 5.2c shows both the total velocities and the normal velocities before and after the collision with the tablet. Before the collision, the total velocity has reached a relatively constant value and the normal velocity almost coincides with the total velocity. Whereas the motion after the collision is a process of gradual deceleration due to the effect of aerodynamic and gravity forces. The difference of absolute values of total velocity and normal velocity implies an increased tangential velocity. Moreover, there are some fluctuations of velocity, especially in the range near the contact point, which are caused by big variations of particle orientation. In order to reduce the negative influence of velocity fluctuations and constrain the effect of aerodynamic forces and gravity, the means of total and normal velocities in the time span of 25 time steps (5 ms) before and after the collision were used to evaluate the respective coefficients of restitution. A similar method was used in the experiments of Sutkar et al. [24] and Crüger et al. [173]. For this sample particle, $e = 0.512$ and $e_n = 0.421$. However, the tangential coefficient of restitution of this sample particle attains a value larger than 100 due to the small incidence angle and the large absolute difference of incidence angle and rebound angle. It is predictable that the tangential coefficient of restitution will be distributed in a very wide range due to the irregular shape of particles. Therefore, the analysis of tangential coefficient of restitution will not be included in the following results, but could be performed in general.

Figure 5.2d shows the rotational speeds of the particle before and after the collision with the tablet. Different from the unit rad/s for angular velocity (angular frequency), the unit of rotation in the results is the ordinary frequency $\omega/2\pi$ (1/s, revolutions per second). The rotational speed before the collision is nearly zero, whereas it is rapidly increased to the peak value of approximately 250 1/s after the collision. The very low but finite value of rotational speed before the collision does not result from real particle rotation; indeed, it comes from the slight variations of orientation in the particle segmentation process. The rotational speed after the collision was averaged by the same method as the translational velocity.

The measured trajectories of all irregular particles before and after collision in a time period of 100 ms are shown in Figure A.1.

## 5.4.2 Measurement data of the COR

The described analysis was applied to evaluate each particle-wall collision, including total and normal coefficients of restitution, rotational speed after collision, and the

incidence and rebound angles. In total, the number of qualified particles for the maltodextrin tablet and the glass slide substrate are 808 and 395, respectively. For the current experimental configuration, the mean impact velocity is approximately 0.65 m/s with a low CV, as listed in Table 5.2. In this range, the dependence of the coefficient of restitution on the impact velocity, i.e. the $v_1^{-1/4}$ dependence, is very weak according to the theoretical model of Johnson [199] and the simulation results of Wu et al. [200]. Moreover, the thickness of the glass substrate and the maltodextrin tablet used in this work is large enough to eliminate the effect of plate support on the coefficient of restitution, as proposed by Sondergaard et al. [182].

For each set of data, the mean (average), the coefficient of variation (CV), the median ($x_{50}$), and the span ($(x_{90} - x_{10})/x_{50}$) are reported to describe both the central point and the relative width of distribution (Table 5.2). In terms of means and medians, the total and normal coefficients of restitution on the DE 6 tablet are smaller than those on the glass substrate, while the rotational speed after collision and the absolute angle difference of the DE 6 tablet are larger than those of the glass substrate. The observation that a more elastic substrate (larger Young's modulus) has a larger mean coefficient of

Table 5.2: Measurement data of maltodextrin (DE 6) particles impacting on maltodextrin tablets or on glass substrate.

| Parameter | Maltodextrin (DE 6) tablet | | | | Glass substrate | | | |
|---|---|---|---|---|---|---|---|---|
| | mean | CV [%] | $x_{50}$ | $\frac{x_{90}-x_{10}}{x_{50}}$ | mean | CV [%] | $x_{50}$ | $\frac{x_{90}-x_{10}}{x_{50}}$ |
| $e$ [-] | 0.536 | 15.71 | 0.523 | 0.382 | 0.651 | 14.77 | 0.633 | 0.356 |
| $e_n$ [-] | 0.386 | 39.44 | 0.382 | 1.023 | 0.487 | 35.98 | 0.479 | 0.837 |
| $\omega_2/2\pi$ [1/s] | 261 | 55.23 | 233 | 1.657 | 237 | 49.12 | 214 | 40.66 |
| $\Delta\theta$ [°] | 20.56 | 71.97 | 18.28 | 2.143 | 18.73 | 63.75 | 17.69 | 2.079 |
| $v_1$ [m/s] | 0.64 | 3.21 | - | - | 0.66 | 2.79 | - | - |
| $v_{1,n}$ [m/s] | 0.635 | 3.33 | - | - | 0.656 | 2.83 | - | - |
| $v_{1,t}$ [m/s] | 0.078 | 1.25 | - | - | 0.071 | 1.08 | - | - |

Table 5.3: Supplementary measurement data.

| Material | $d_{50}$ [$\mu$m] | Sphericity [-] | $\bar{v}_1$ [m/s] | $\bar{e}$ [-] | CV [%] | $\bar{e}_n$ [-] | CV [%] |
|---|---|---|---|---|---|---|---|
| DE 47 | 155 | 0.82 | 0.66 | 0.64 | 26.7 | 0.49 | 29.3 |
| Glass | 227 | 0.93 | 1.12 | 0.74 | 16.7 | 0.71 | 18.9 |
| MCC | 314 | 0.87 | 1.36 | 0.69 | 11.2 | 0.61 | 17.5 |
| $\gamma$-Alumina | 604 | 0.97 | 1.61 | 0.79 | 8.3 | 0.78 | 9.1 |
| Rapeseed | 2140 | 0.94 | 1.79 | 0.68 | 10.3 | 0.65 | 13.6 |
| ABS | 6012 | 0.99 | 1.66 | 0.57 | 4.8 | 0.57 | 5.0 |

[1] DE 47: dried glucose syrup; MCC: microcrystalline cellulose; ABS: acrylonitrile butadiene styrene.

[2] The data of particle size and sphericity were measured by the Camsizer (Retsch GmbH).

restitution is in accordance with the measurement studies by Bharadwaj et al. [164] and Gibson et al. [175]. Due to the irregular shapes of particles and irregular contact geometries, all measured properties related to the macroscopic particle-wall collisions are scattered. According to the coefficients of variation and spans, the measured data on the DE 6 tablet are scattered more than those on the glass substrate. For each substrate, the mean and the median of the normal coefficient of restitution are smaller than those of the total coefficient of restitution; and the data of normal coefficient of restitution is more spreading. The difference between normal and total coefficients of restitution resulted from the tangential velocity of the particle after collision, which is largely affected by the rebound angle and the rotational speed.

The experimental method and the PTV algorithms used in this work are flexible enough to measure irregular or spherical particles with characteristic lengths ranging from 100 $\mu$m to several mm. The measurement results of 6 different particles are summarized in Table 5.3. Some of these results will be used in Chapter 6 and Chapter 7 to study the granular flow in fluidized beds.

### 5.4.3 Comparison with DEM simulations

*COR of irregular particles*

Figure 5.3 shows the comparison of distributions of total and normal coefficients of restitution from measurements and non-spherical DEM simulations with the multisphere model and the superquadric model. The medians, spans, means and coefficients of variation of all distributions shown in Figure 5.3 are given in Table 5.4. The MS model predicts the global distribution of the coefficient of restitution $e$ better than the SQ model, even though the mean and the median of the SQ model are closer to the measurement data. In particular, the profiles of the measurement and the MS model almost coincide when the coefficient of restitution is less than 0.5; and the deviation increases only slightly as the coefficient of restitution increases from 0.5 to 0.7. Contrary, the width of the distribution of the coefficient of restitution predicted by the SQ model is much narrower compared with the measurement data. Referring to the span and the coefficient of variation, the distribution of the SQ model is too concentrated. The influence of particle shape on the distribution of the coefficient of restitution is nearly negligible for both the MS and the SQ models.

Compared with the measurement data of normal coefficient of restitution, the MS model slightly underestimates the mean and the median normal coefficient of restitution; inversely, the SQ model overestimates those value. The discrepancies in the coefficient of variation and the span of the MS model are much lower than those of the SQ model. Some deviation between measurement and the MS model is observed at cumulative frequency higher than 0.5. The normal coefficient of restitution is sensitive to the shape of irregular particles; and the influence of aspect ratio is more pronounced for the SQ method. With increasing aspect ratio, the means and medians predicted by $P3$, $P1$, and $P2$ decrease and the corresponding coefficients of variation and the spans increase.
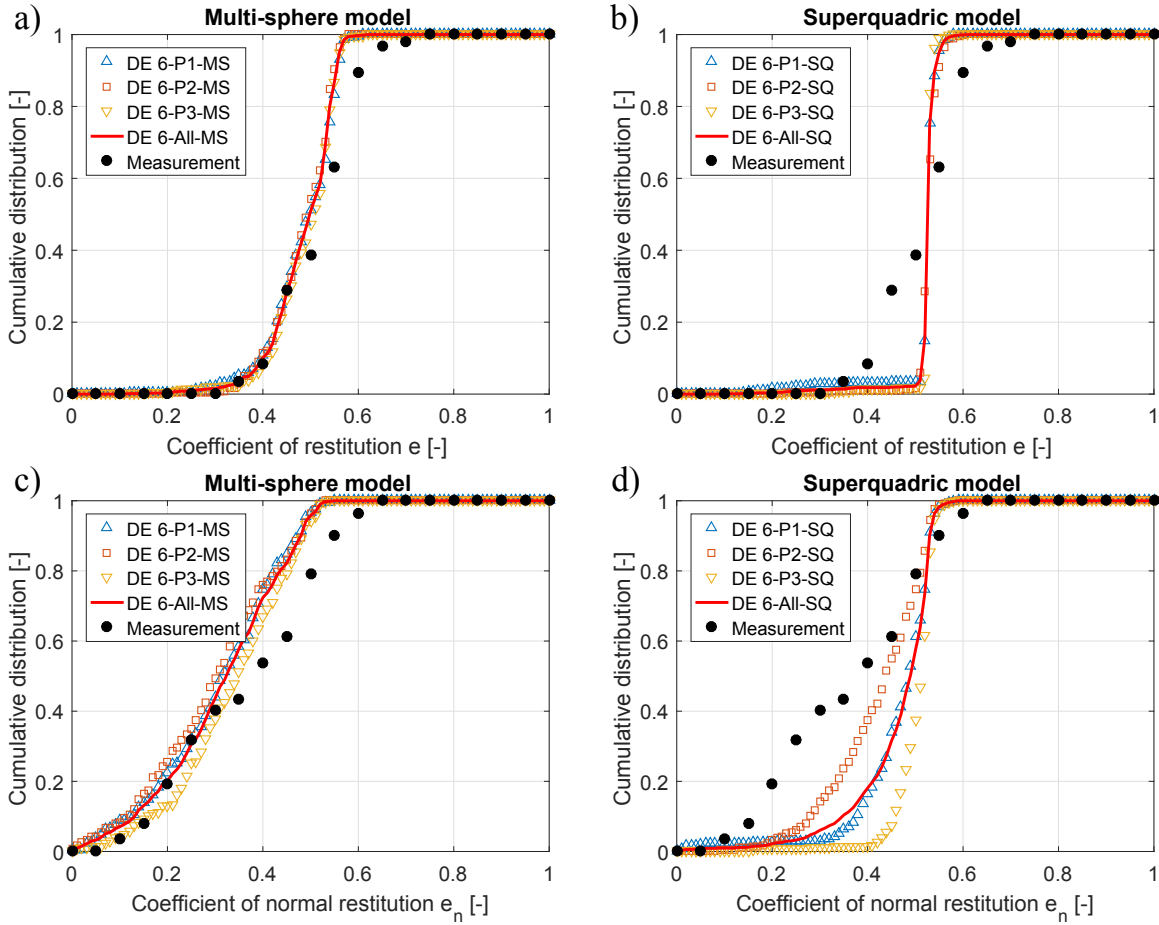
Figure 5.3: Comparison of distributions of total and normal coefficients of restitution: a), b) $e$ from measurements, the multi-sphere simulations and the superquadric simulations, and c), d) $e_n$ from measurements, the multi-sphere simulations and the superquadric simulations.

Nevertheless, all distributions of the normal coefficient of restitution obtained by the SQ model quite strongly differ from the measurement data.

For the MS model, there is no clear dependency of the coefficients of restitution on the aspect ratio. This is because the influence of irregular shape on particle-wall collisions is more complex and not limited to the aspect ratio. In addition to the geometry properties like the number of sub-spheres $N_S$, the aspect ratio $R_A$ and the ratio of smallest sphere diameter to largest sphere diameter $d_{s,min}/d_{s,max}$, the contact properties including the number of spheres involved in the individual contact and the corresponding radii of involved spheres $r_{s,c}$, are also important to measure the influence of irregular particle shape, as listed in Table 5.5. The means and coefficients of variation of $N_{s,c}$ are close for the three investigated particles, which may explain the relatively compact arrangement of distribution curves in Figure 5.3. The average $r_{s,c}$ of $P1$ is much larger than that of $P2$ and $P3$, due to the larger size of sphere $S_1$, the smaller $d_{s,min}/d_{s,max}$, and the

Table 5.4: Total and normal coefficients of restitution of maltodextrin (DE 6) particles impacting on maltodextrin tablets.

| Parameter | Exp. | Multi-sphere (MS) model | | | | Superquadric (SQ) model | | | |
|---|---|---|---|---|---|---|---|---|---|
| | | P1 | P2 | P3 | All | P1 | P2 | P3 | All |
| $e$ | | | | | | | | | |
| $e_{50}$ | 0.523 | 0.496 | 0.492 | 0.506 | 0.498 | 0.525 | 0.526 | 0.525 | 0.526 |
| $\frac{e_{90}-e_{10}}{e_{50}}$ | 0.382 | 0.323 | 0.316 | 0.280 | 0.309 | 0.051 | 0.072 | 0.027 | 0.048 |
| mean | 0.536 | 0.488 | 0.487 | 0.493 | 0.489 | 0.523 | 0.531 | 0.529 | 0.529 |
| CV | 15.71 | 14.79 | 12.62 | 13.47 | 13.61 | 11.01 | 5.48 | 4.56 | 7.39 |
| $e_n$ | | | | | | | | | |
| $e_{n,50}$ | 0.382 | 0.315 | 0.303 | 0.346 | 0.323 | 0.485 | 0.437 | 0.512 | 0.489 |
| $\frac{e_{n,90}-e_{n,10}}{e_{n,50}}$ | 1.023 | 1.116 | 1.208 | 0.936 | 1.079 | 0.313 | 0.563 | 0.154 | 0.373 |
| mean | 0.386 | 0.311 | 0.300 | 0.339 | 0.317 | 0.466 | 0.423 | 0.504 | 0.465 |
| CV | 39.44 | 41.44 | 44.58 | 35.32 | 40.51 | 19.54 | 23.09 | 9.72 | 18.91 |

Table 5.5: Contact properties and geometry properties of multi-sphere particles.

| Parameter | Multi-sphere (MS) model | | | |
|---|---|---|---|---|
| | P1 | P2 | P3 | All |
| Contact property | | | | |
| mean $N_{s,c}$ [-] | 1.506 | 1.489 | 1.522 | 1.515 |
| CV [%] | 35.3 | 29.5 | 31.6 | 33.8 |
| mean $r_{s,c}$ [$\mu$m] | 21.6 | 11.8 | 11.5 | 18.3 |
| CV [%] | 71.8 | 52.5 | 19.3 | 75.5 |
| Geometry property | | | | |
| $N_s$ [-] | 51 | 48 | 33 | |
| $d_{s,min}/d_{s,max}$ [-] | 0.092 | 0.117 | 0.154 | |
| $R_A$ [-] | 1.35 | 1.53 | 1.22 | |

higher probability of $S_1$ to collide with the substrate. The coefficient of variation of $r_{s,c}$ is mainly affected by the ratio of smallest sphere diameter and largest sphere diameter involved in individual multiple contacts. Kruggel-Emden et al. [184] found that artificial multiple contacts may lead to large deviations from the experimental results when attempting to approximate smooth spherical particles in the DEM. The increase in number of spheres to form smooth particles had no direct effects on improving the accuracy of the numerical predictions [184, 188]. Whereas the MS model approximates the irregular shape of non-convex particles, multiple contacts in individual collision may be essential to represent the non-convex features. Unfortunately, the microscopic particle contact geometry cannot be measured by the current experimental configuration. Further increase in the spatial resolution of the imaging system would require to combine an additional long distance microscope with the high-speed camera.

Generally, the total and normal coefficients of restitution numerically obtained by the MS model are in good agreement with the experimental data. The performance of the MS model is better than that of the SQ model due to the capability to represent the non-convex features.

*Rotational speed after collision $\omega_2$*

In the post-processing of measurement data, particles with rotation before collision were manually filtered. The initial rotational speed was set to zero for all particles in DEM simulations. Thereby, only the rotational speed after collision was used as a characteristic of particle-wall collision behavior. For particles with irregular shape, the rotational motion after collision is generated at the contact point, mainly resulting from plastic–elastic deformation, frictional effects and irregular contact geometries. Figure 5.4 shows the comparison of distributions of the rotational speed after collision from measurements and DEM simulations with the multi-sphere model and the superquadric model. The medians, spans, means and coefficients of variation of all distributions in Figure 5.4 are given in Table 5.6. The prediction by the MS model was more accurate than that by the SQ model, which severely underestimated the rotational speed after collision. The simulations with the SQ model are very sensitive on the aspect ratio, i.e. the mean and median of rotational speed after collision increase as the aspect ratio grows. There is no clear dependence of $\omega_2$ on contact properties, but the rotational speed after collision increases with decreasing $N_s$ and increasing $d_{s,min}/d_{s,max}$ (by referring to Table 5.5).

Figure 5.5 shows the relationships between total and normal coefficients of restitution and the rotational speed after collision, in terms of mean values and error bars. For measurement data, the relationship between mean normal coefficient of restitution and the rotational speed after collision can be fitted by a simple linear equation $e_n = k_1 \omega_2 + k_2$, in which $k_1 = -7.2 \times 10^{-4}$ s and $k_2 = 0.581$. The coefficient of determination (R-square) of the fitting is about 0.966. The linearly decreasing trend can also be found in simulations by both the MS and SQ models. Strong scattering was observed in both measurements and simulations, which is expectable due to the irregular shape of particles. The results of total coefficient of restitution exhibit no regular dependence on the rotational speed after collision. The total coefficient of restitution in both measurements and simulations fluctuates around the approximate mean values listed in Table 5.4.

*Absolute angle difference $\Delta\theta$*

Although the tangential velocity of most qualified particles before collisions is relatively small compared to the normal velocity, its contribution to the incidence angle cannot be neglected. Hence, the absolute difference of incidence angle and rebound angle was evaluated as another measure of particle-wall collision behavior. Figure 5.6 shows comparisons of distributions of the absolute difference of incidence angle and rebound angle from measurements and DEM simulations with the multi-sphere model and the superquadric model. The medians, spans, means and coefficients of variation of all distributions in Figure 5.6 are given in Table 5.6. Deviations of cumulative distributions are observed for both the MS model and the SQ model. The MS model overestimates the

value of $\Delta\theta$ and the SQ model underestimates the value of $\Delta\theta$. Again the simulations with the SQ model are heavily dependent on the aspect ratio; accordingly, the mean and the median of $\Delta\theta$ increase with increasing aspect ratio. For the MS model, there
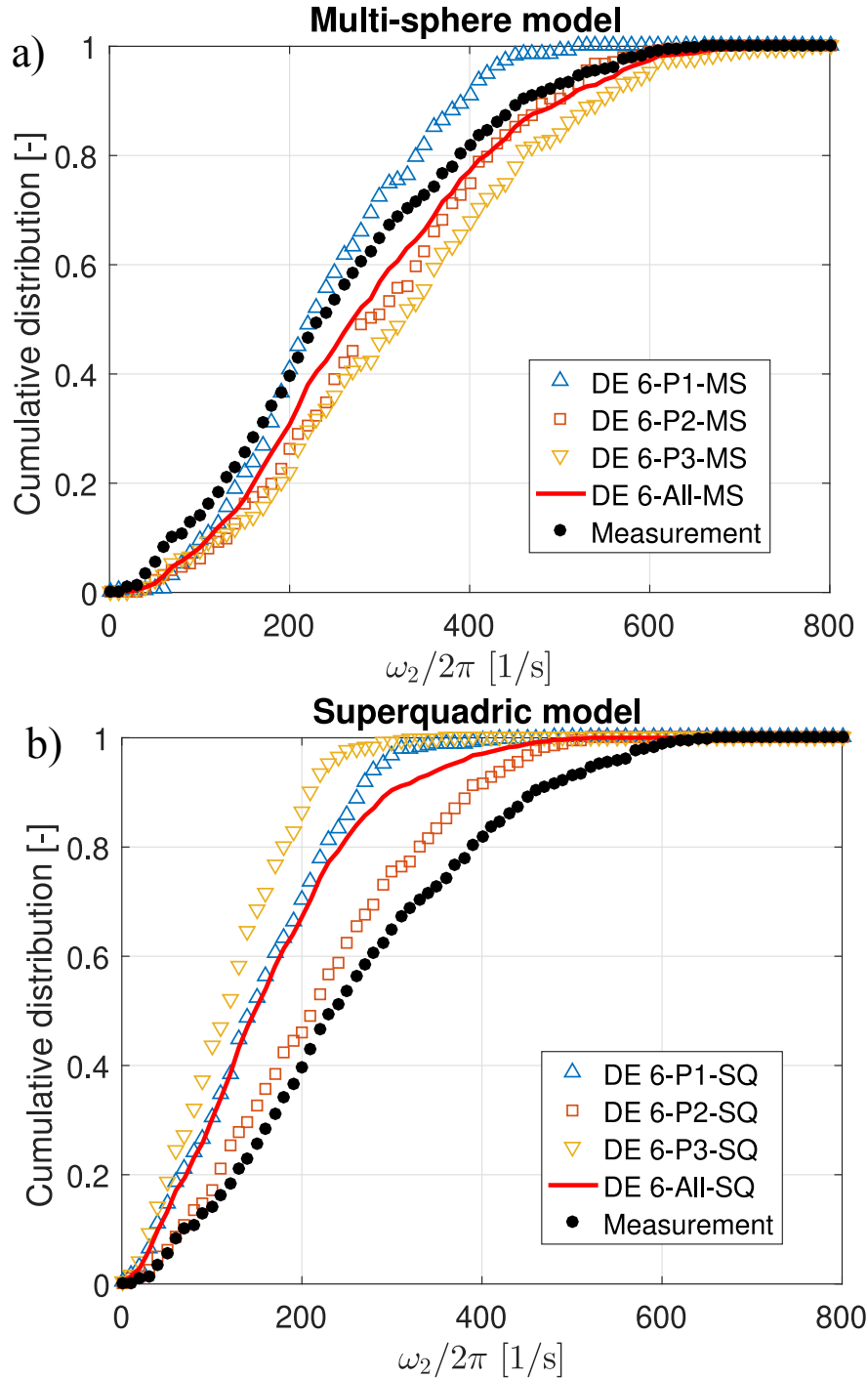


Figure 5.4: Comparison of rotational speed after collision $\omega_2$: a) measurements and the multi-sphere simulations, and b) measurements and the superquadric simulations.

is a weak increase of the mean and the median of $\Delta\theta$ with increasing aspect ratio; in
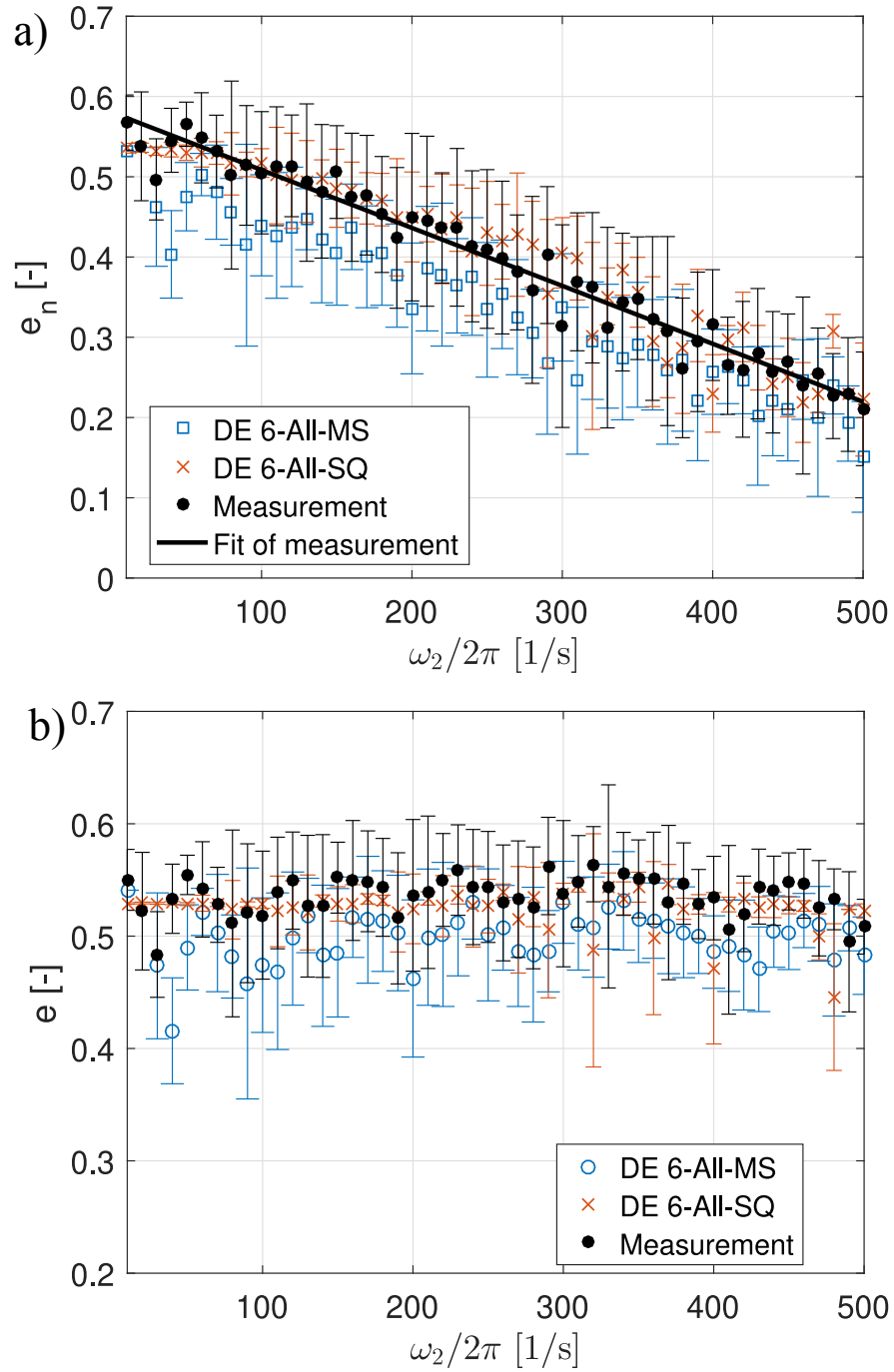


Figure 5.5: Comparison between measurements and simulations: a) normal coefficient of restitution and b) coefficient of restitution, as a function of the rotational speed after collision $\omega_2$.

contrast, the mean and the median of $\Delta\theta$ increase when the mean number of spheres involved in individual contact is decreased (by referring to Table 5.5).

Figure 5.7 shows the relationships between total and normal coefficients of restitution and the absolute angle difference, in terms of mean values and error bars. The measured relationship between normal coefficients of restitution and the absolute angle difference can be fitted by a simple linear equation $e_n = k_1 \Delta\theta_2 + k_2$, where $k_1 = -9.8 \times 10^{-3}$ 1/deg and $k_2 = 0.620$. The coefficient of determination ($R$-square) of the fitting is about 0.975. A decrease in normal coefficient of restitution with increasing $\Delta\theta$ was also observed in the experiment of Hastie [174] for irregular particles. No clear relation can be obtained for the total coefficients of restitution. For both normal and total coefficients of restitution, strong scatter is found in all data sets due to the irregular shape of particles. It is noticeable that there are several outliers in the data of the SQ simulations as the absolute angle difference exceeds 40°, which occurred when the corner points (the ends of principal axes) of the 3D ellipsoid were the impact points and the angles between the impact velocity and the principal axes were exactly 0° and 90° as also reported by Podlozhnyuk et al. [186].

The computational efficiency of the multi-sphere model depended on both the number of spheres for a single irregular particle and the radius of the smallest sphere. The number of spheres mainly affected the search of neighbor particles and potential contacts, while the radius of sphere influenced the largest time step allowed for accurately modeling the particle contacts. The computational efficiency of the superquadric model is influenced by the aspect ratio. Furthermore, the blockiness parameters $n_1$ and $n_2$ do not affect the computational time significantly, however, numerical stability decreases with increasing particle blockiness and particle aspect ratios deviating from unity [186]. The relative CPU time $\tau_{rel}$ is defined as the ratio of the time spent by the multi-sphere model to the time spent by the superquadric model for the same number of irregular

Table 5.6: Rotational speed after collision and absolute difference of incidence angle and rebound angle for maltodextrin (DE 6) particles impacting on maltodextrin tablets.

| Parameter | Exp | Multi-sphere (MS) model | | | | Superquadric (SQ) model | | | |
|---|---|---|---|---|---|---|---|---|---|
| | | P1 | P2 | P3 | All | P1 | P2 | P3 | All |
| $\omega_2$ | | | | | | | | | |
| $\omega_{2,50}/2\pi$ | 233 | 223 | 288 | 324 | 213 | 143 | 270 | 116 | 147 |
| $\frac{\omega_{2,90}-\omega_{2,10}}{\omega_{2,50}}$ | 1.657 | 1.293 | 1.239 | 1.319 | 1.498 | 1.577 | 1.449 | 1.538 | 1.734 |
| mean | 261 | 343 | 305 | 331 | 223 | 154 | 295 | 123 | 168 |
| CV | 55.23 | 42.98 | 44.44 | 47.25 | 53.11 | 54.74 | 49.73 | 54.53 | 60.58 |
| $\Delta\theta = \theta_2 - \theta_1$ | | | | | | | | | |
| $\Delta\theta_{50}$ | 18.28 | 29.38 | 31.28 | 28.09 | 29.40 | 8.59 | 14.70 | 4.18 | 7.77 |
| $\frac{\Delta\theta_{90}-\Delta\theta_{10}}{\Delta\theta_{50}}$ | 2.143 | 1.182 | 1.166 | 1.209 | 1.177 | 2.554 | 2.017 | 2.974 | 3.019 |
| mean | 20.56 | 29.96 | 30.87 | 27.05 | 29.23 | 10.88 | 15.84 | 6.05 | 10.82 |
| CV | 71.97 | 42.36 | 43.91 | 46.45 | 44.66 | 86.76 | 67.75 | 89.95 | 89.23 |

particles and same number of contacts. The relative CPU times $\tau_{rel}$ of the three different shapes $(P1, P2, P3)$ were, respectively, 10.81, 8.96 and 5.45. The $\tau_{rel}$ is reduced
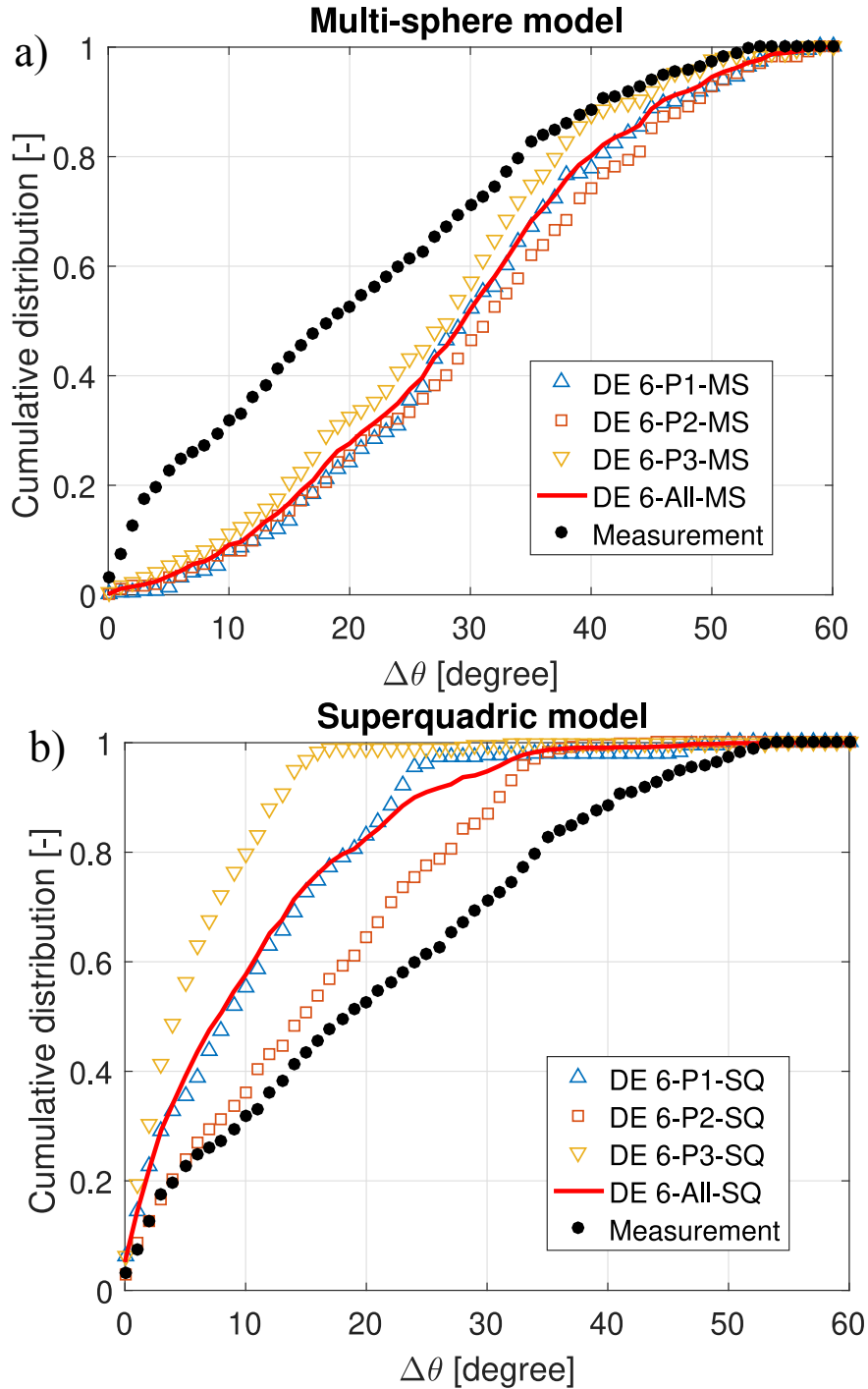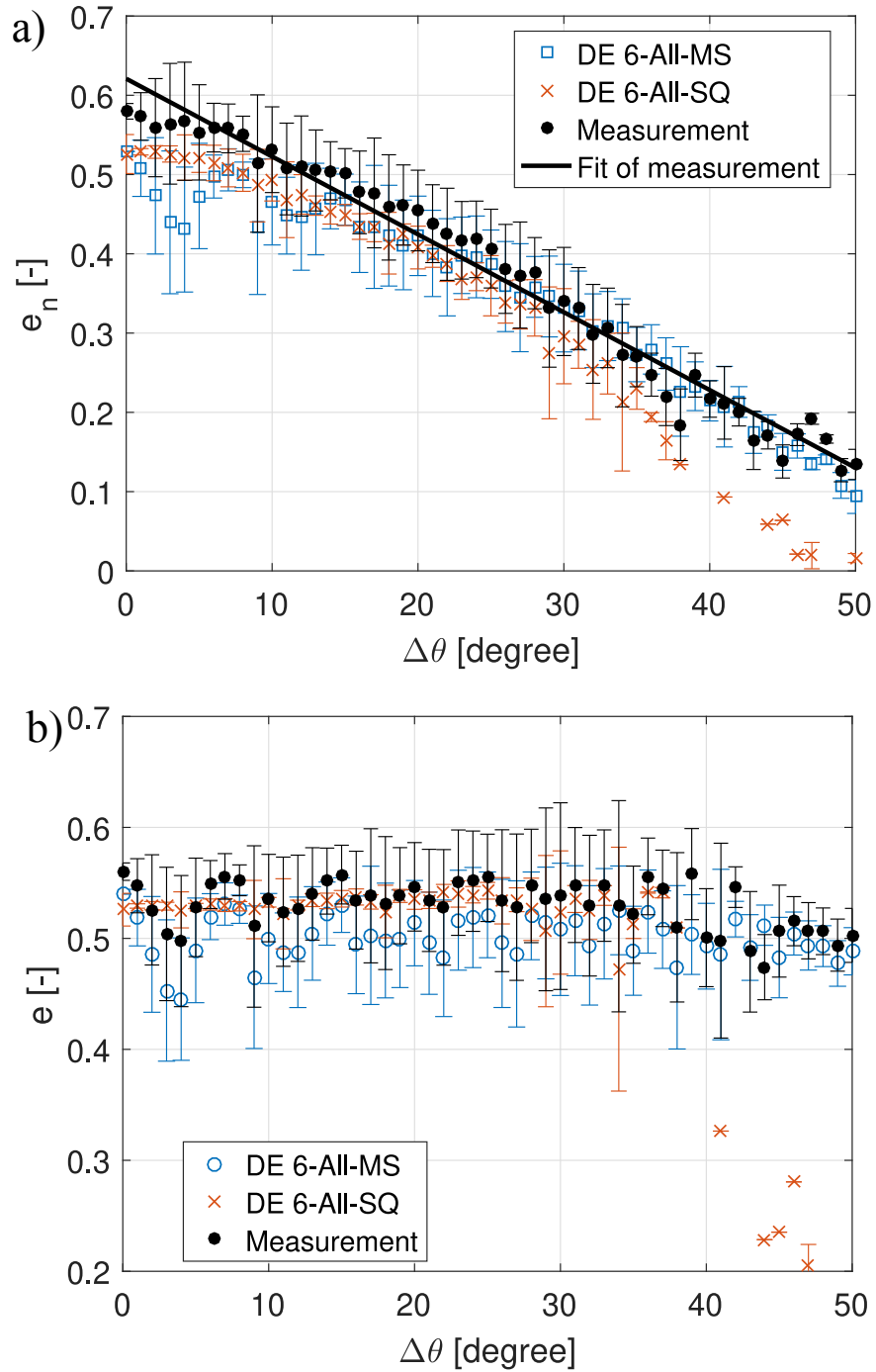


Figure 5.6: Comparison of the absolute difference of incidence angle and rebound angle $\Delta\theta = |\theta_2 - \theta_1|$: a) measurements and the multi-sphere simulations, and b) measurements and the superquadric simulations.

with decreasing number of spheres in the non-spherical particle. In the case with 51 spheres ($P1$), the CPU time necessary to perform the multi-sphere simulations is about



Figure 5.7: Comparison between measurements and simulations: a) normal coefficient of restitution and b) coefficient of restitution, as a function of the absolute difference of incidence angle and rebound angle $\Delta\theta = |\theta_2 - \theta_1|$.

one order of magnitude higher than that required to perform the superquadric simulations. Thus, the computational cost (requirements of CPU and memory resource), especially for modeling industrial scale problems, must be reckoned when selecting either the multi-sphere model or the superquadric model. When using the multi-sphere model, a reasonable number of spheres and minimum sphere size should be chosen as a compromise between acceptable accuracy and computational cost.

# Chapter 6

# PTV measurements and CFD-DEM simulations of particle dynamics in mono-disperse particle systems

*Parts of this chapter are based on Jiang et al. [104].*

## 6.1 Particle collision dynamics

Fluidized bed spray granulation, coating and agglomeration are widely utilized in the industry to produce, for example, food, pharmaceuticals, fertilizers, powder catalysts and cosmetics, as a result of excellent heat and mass transfer between solid particles and fluid phase [3, 4]. In typical applications, particles are fluidized by hot gas through the bottom distributor, which mainly controls the global circulation and particle formulation process. Meanwhile, a spray zone containing solid material is formed by the atomization process, and particles are wetted in the spray zone. The shape and location of the spray zone depend on the specific sub-process and the apparatus configuration. Obviously, in a fluidized bed, the motion of particles is not only influenced by aerodynamic transport and turbulent effects, but is also significantly affected by particle-particle interactions [1]. In agglomeration processes, for instance, primary particles randomly collide and may stick at wet spots due to the formation of liquid bridges that are subsequently solidified by evaporation, whereas the global motion of all particles is governed by the macroscopic aerodynamic transport effect. Since the wet granulation process is highly complex, it is often operated inefficiently in industrial applications. The enhanced understanding of underlying mesoscale particle dynamics is required to improve the efficiency of processes and to achieve high product quality [15, 19].

As a well-established macroscopic approach to describe product quality, population balance models (PBM) are usually used to investigate particle formation processes in industrial scale [201]. Additionally, the Monte-Carlo method is another useful approach to model particle formation based on mesoscale events and processes [19, 202]. Nevertheless, the accuracy of both approaches relies on model parameters associated with

mesoscale particle dynamics and collision dynamics, such as the residence time, the impact velocity and the collision frequency. For example, the so-called viscous Stokes number $St_v$ [203], strongly depending on the impact velocity, can be used as the coalescence criterion and provides the critical condition for the dissipation of kinetic energy by a given thickness of viscous layer [154, 204]. The particle collision frequency, a main parameter in the aggregation kernel of the population balance models, dominates the agglomeration process [205, 206]. Therefore, a sound understanding of mesoscale particle dynamics and collision dynamics in gas-solid fluidized beds is important in order to design and scale-up new equipment, as well as to control the product quality.

Due to the industrial significance and experimental difficulty of mesoscale particle dynamics and collision dynamics of both mono- and poly-disperse systems, the accurate measurement of these quantities has been the objective of many experimental studies of particulate flows in different configurations. Based on elaborate particle segmentation and particle tracking algorithms, the PTV technique can be utilized to simultaneously track a large number of particles for a relatively short period, and hence has the potential to evaluate particle collision characteristics in complex granular flows [42]. However, the PTV technique is limited to pseudo-2D fluidized beds [43].

Compared with the general measurement of particle dynamics, the measurement of collision dynamics requires much higher spatial and temporal resolution, and much higher sensitivity of the measurement techniques. Thus, the experimental investigations about collision dynamics in different configurations are very limited. Buffière and Moletta [207] measured the collision frequency and the particle pressure with a flush-mounted hydrophone in a three-phase fluidized bed and proposed an empirical relation between collision frequency, superficial gas velocity $U$ and local solid volume fraction $\epsilon_s$. This empirical correlation was applied to macroscopic modeling by Terrazas-Velarde et al. [154] and Hussain et al. [206]. You et al. [41] used PTV measurements to estimate particle collision rate $\dot{n}_c$ in a vertical duct, which was further compared with that obtained from theoretical collision models. However, the manual count of particle collision number $N_c$ restricted the estimation in a very dilute flow region. The first improvement for measuring collision dynamics is to develop a new algorithm in PTV to automatically count particle collisions using individual particle trajectories obtained. The new PTV can analyze particle collision dynamics at different heights of the fluidized bed under various operation conditions.

Many theoretical collision models have been developed in the past decades to improve the understanding of the underlying physics of particle collision behavior. Generally, there exist two limiting boundaries for investigations of particle-particle collisions characterized by the Stokes number $St$, which is defined as the ratio of the particle response time to the characteristic time scale of the turbulence. The lower limit corresponds to small particles perfectly following the turbulence ($St \rightarrow 0$) [208] and the upper limit corresponds to large particles moving almost without response to the turbulence ($St \rightarrow \infty$) [209]. Highly massive particles encountered in gas-solid fluidized beds have large particle response time and belong to the latter case [1]. Detailed critical reviews on the theoretical collision models are given by Wang et al. [210] and Meyer and Deglon

[211]. Based on the kinetic theory of granular flow (KTGF), Gidaspow [60] proposed a particle collision model in fluidized beds, which is associated with the solid volume fraction and the granular temperature. As an extension of classical kinetic theory of dense gases, the KTGF is commonly used as the constitutive or closure relation for the solid phase and momentum exchange between phases in two-fluid computational fluid dynamics (CFD) simulations of multiphase granular flows.

As an important quantity in KTGF, the granular temperature is defined as the mean of the squares of the instantaneous particle velocity fluctuation, which is a measure of the random particle kinetic energy per unit mass. The granular temperature provides the relative velocity of particles that drives the collision of particles (collision mechanism), and the diffusive mixing of particles (streaming mechanism) [212]. Note that the fluctuation velocity refers to the difference between the instantaneous particle velocity and the mean particle velocity. In the theoretical analysis, the ensemble average is used to calculate average particle velocity [60], which is not possible in real experimental measurements. Thus, Jung et al. [213] identified two kinds of granular temperatures: i) particle granular temperature, and ii) bubble granular temperature, which are based on different definitions of average velocity and the corresponding fluctuation velocity. For the particle granular temperature, the mean particle velocity is an instantaneous spatial-averaged velocity and the fluctuation velocity represents the oscillations in small regions for a short time period. For the bubble granular temperature, the mean particle velocity is a time-averaged velocity for certain particles and the fluctuation velocity is caused by the formation and traveling of bubbles. As pointed out by Tang et al. [214], both definitions of granular temperature are reasonable, depending on different measurement techniques and investigation objectives using the granular temperature. If the investigation of instantaneous particle collision dynamics is the target, the particle granular temperature is more meaningful. Due to the effect of traveling bubbles on particle motion in fluidized beds, the value of bubble granular temperature is usually higher than particle granular temperature [213]. Most of the published techniques involving the granular temperature actually measure the bubble granular temperature, or a granular temperature reflecting the coupling of bubbles and particles, such as PEPT, MPT as well as magnetic resonance (MR) [215–217]. In terms of particle granular temperature representing particle collision dynamics, Hagemeier et al. [42] evaluated the particle granular temperature based on the instantaneous particle velocity of all individual particles. According to the cross-covariance and assumption of Gaussian distribution of particle velocity, Dijkhuizen et al. [218] extended the standard particle imaging velocimetry (PIV) method to calculate particle granular temperature using the standard deviation of the correlation peak attributed to the particle velocity distribution.

Despite the importance of the collision model in KTGF, there exist very few prior studies on experimental validation, especially for high solid volume fraction regions. Therefore, taking full advantages of PTV measurements, experimental collision dynamics can be compared with the theoretical collision model by directly measuring the relationship between the particle collision frequency, the particle granular temperature and the solid

volume fraction. In addition, experimental data on impact velocity, particle granular temperature and collision frequency measured systematically at different locations can be used to validate the corresponding CFD-DEM simulation in the same fluidized bed and operation condition.

Section 6.2 illustrates improvements of PTV for particle dynamics, including the intensity calibration and the determination of collision events. In addition, the fundamentals of particle granular temperature and theoretical collision models are briefly introduced. Section 6.3 presents and discusses the experimental results on particle granular temperature, particle collision frequency and impact velocity, as well as the comparisons with the CFD-DEM simulation and the theoretical collision model. Section 6.4 offers a summary of experiments and simulations.

## 6.2   Method to track particle collisions

### 6.2.1   Intensity calibration

The PTV experiments and CFD-DEM simulations in the pseudo-2D fluidized bed with a mono-disperse particle system are conducted according to Section 4.2. The scale factor
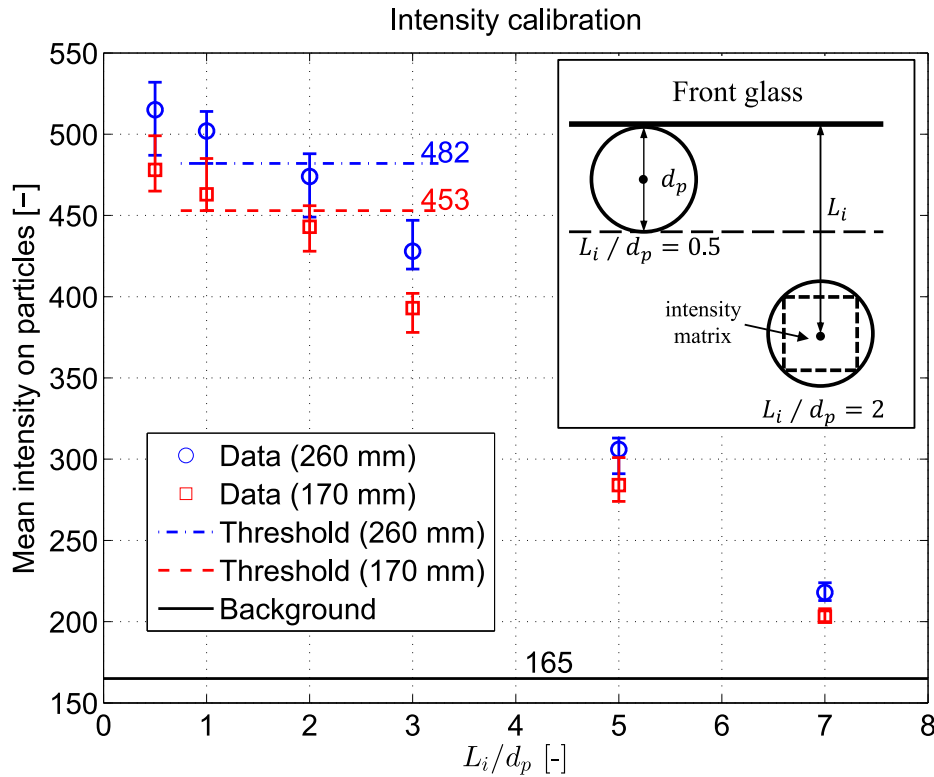


Figure 6.1: The intensity calibration for particles with different distances to the front glass wall (insert figure: a schematic of particle arrangements and single particle intensity matrix).

Table 6.1: Parameters used in particle segmentation and particle tracking algorithms.

| Parameters | Value | Unit |
|---|---|---|
| *Segmentation method* | | |
| sample matrix size | $\sqrt{2}d_p \cdot S_f/2$ | pixel |
| mean intensity threshold | 482 ("high-level") | – |
| | 453 ("low-level") | – |
| *Voronoi method* | | |
| maximum displacement filter | $U \cdot S_f \cdot \Delta t$ | pixel |
| *Probability relaxation method* | | |
| maximum displacement radius $T_m$ | $U \cdot S_f \cdot \Delta t$ | pixel |
| neighboring radius $T_n$ | $1.5 \cdot U \cdot S_f \cdot \Delta t$ | pixel |
| quasi-rigidity radius $T_q$ | $0.2 \cdot U \cdot S_f \cdot \Delta t$ | pixel |
| constant A | 0.3 | – |
| constant B | 4.0 | – |
| iteration steps | 50 | – |
| threshold matching probability $P_{ij(i)}$ | 0.95 | – |

$\Delta t$ is 1 ms according to the frame rate of the imaging system.

from the geometry calibration gives an accurate ratio of real size to pixel size in the focus plane, which is assumed to have a depth of one particle diameter from the front wall. When particles move out of the focus plane towards the third direction, which happens especially in dilute regions, the scale factor and intensity of particles in the image will decrease with the distance to the focus plane. The measured velocity of such particles that have significantly departed from the first layer region is inaccurate. In addition, the accuracy of evaluation of quantities involving investigation volume, such as solid volume fraction and collision frequency, will be influenced by the out-of-plane motions. Therefore, an intensity calibration is needed for filtering these particles.

The particle-mask correlation method (discussed in Section 2.1) was used in this chapter. The detailed parameters are listed in Table 6.1. As an enhancement of the particle segmentation process relying on the intensity distribution, the targets of this intensity value calibration process are particles with completely visible contour (without any overlap with other particles in front), which can be recognized by the particle segmentation process even when they have moved away from the focus plane.

The intensity calibration was conducted for static particles. On a substrate, six particles were fixed with different distances to the front edge of the substrate. Then, the front edge of the substrate was fitted at 20 evenly distributed locations of the internal side of the front glass at heights 170 mm and 260 mm, which are the center heights of the "high-level" and "low-level". Keeping the same illumination condition and parameters of camera system as in the real fluidization measurements, the intensity of six particles at different locations was measured to calibrate the relationship between the mean intensity of particles and the distance to the focus plane. As shown in Figure 6.1, $L_i$

is the distance from the particle center to the front glass. The ratios of distance $L_i$ to particle diameter $d_p$ of the six particles are 0.5, 1, 2, 3, 5, 7, respectively.

When a superficial gas velocity of $3.0U_{mf}$ was used in the measurements, some particles could move by more than 2.0 pixels during one exposure (1/10 000 s). The pixel intensities along the periphery of the particle are then influenced by the negative effect of motion blur. Therefore, only the square matrix with edge size equal to $\sqrt{2}d_p \cdot S_f/2$ pixel was considered as the effective region for the intensity calibration and the particle segmentation process. Most of pixels affected by the motion blur can be excluded by this method. Then, the mean intensity of each single particle was calculated based on all pixel intensities in the effective region, and the mean intensity of particles at each height was calculated using the mean intensities of 20 different particles.

It is important to note that the mean intensity of particles in the fluidization measurements was influenced by factors such as the shade effect of neighboring particles and the non-uniform intensity distribution of illumination:

- The intensity of particles was inevitably influenced by the shade effect of other particles in fluidization measurements by our configuration of illumination. Compared to the intensity calibration, the mean intensity of particles decreased due to shade effects.

- As shown in Figure 6.1, red squares and blue circles refer to the mean intensity of particles at height 170 mm and 260 mm, respectively. The maximum and minimum intensities of a single particle are also given for each ratio $L_i/d_p$. The differences of mean intensity and relatively large scatter at the center heights of the two levels imply a non-uniform intensity distribution of illuminating; due to two halogen lamps illuminating the bed from positions higher than the camera positions.

For each level, only a single threshold value was used to filter the out-of-focus particles that were identified based on the template particle intensity distribution. Thus, relatively relaxed threshold values should be applied to consider all relevant factors. To this end, the minimum mean intensity of particles with the ratio $L_i/d_p = 1$ was chosen as the threshold value. In this study, the threshold intensity was set as 482 and 453 for the "high-level" and the "low-level", respectively.

## 6.2.2   Determination of collision events

Measurement of particle collision dynamics requires a high temporal resolution, due to very short collision duration depending on material properties and impacting velocity. Buffière and Moletta [207] mentioned a maximum duration of 50 to 60 $\mu$s for their measurements. Based on Hookean model [219] or Hertzian model [161], the estimated contact duration was in the range from 10 to 50 $\mu$s in our measurement conditions. In the frame of our measurements, additional experiments with an imaging frame rate of
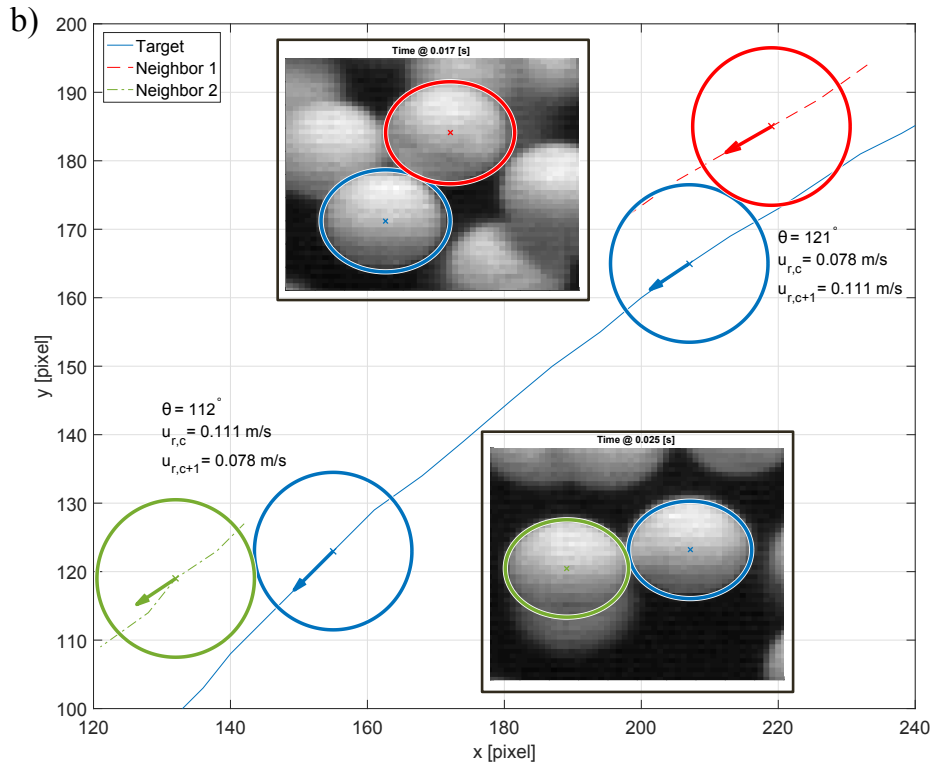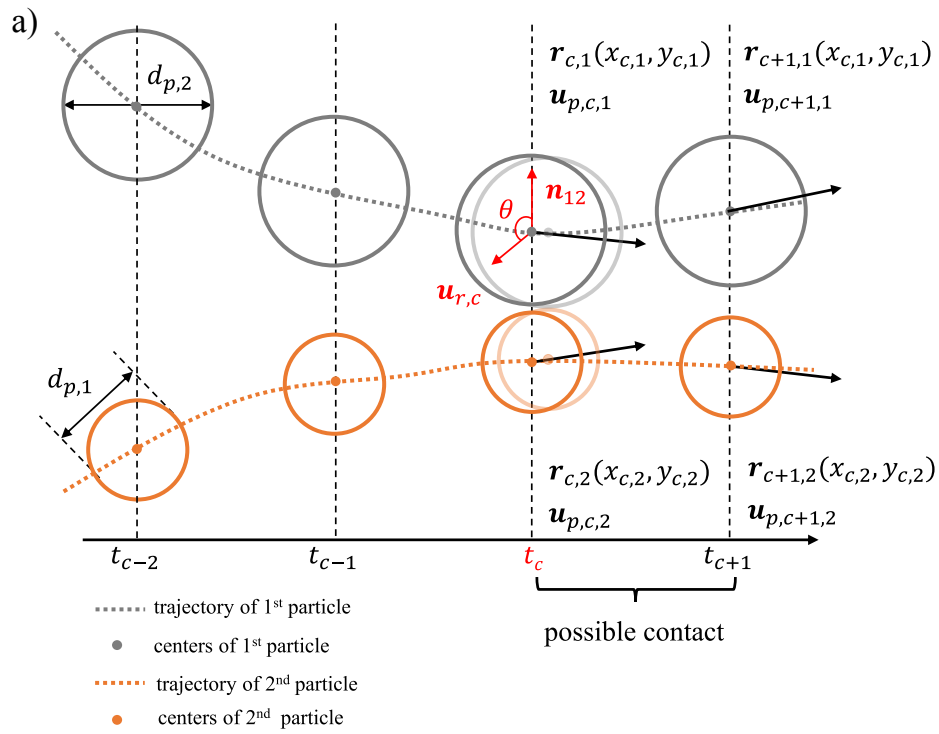
Figure 6.2: Determination of particle-particle collisions based on individual particle trajectories reconstructed by PTV.

10 000 fps were conducted to estimate the collision duration and time interval between two collisions. Due to the high frame rate, the size of FOV decreases to $128 \times 128$ pixels. It was found that the collision duration is smaller than 100 $\mu$s, but most of the time intervals between two particle-particle interactions are larger than 1 ms. Therefore, the occurrence of particle collision events can be captured depending on the geometric variation of individual particle trajectories, as shown in Figure 6.2a.

After particle segmentation, the pairing of identical particles can be achieved by the integrated particle tracking method (Section 2.2). The detailed parameters related to PTV are listed in Table 6.1. For the 2-D case, the location vectors of two particles are $\boldsymbol{r}_1 = (x_{c,1}, y_{c,1})$ and $\boldsymbol{r}_2 = (x_{c,2}, y_{c,2})$, subscripts 1 and 2 refer to different particles. $L_c$ is the distance between the two particle centers at the "imaginary" contact moment $t_c$, which can be expressed as

$$L_c = |\boldsymbol{r}_1 - \boldsymbol{r}_2| = \sqrt{(x_{c,1} - x_{c,2})^2 + (y_{c,1} - y_{c,2})^2}. \tag{6.1}$$

The corresponding normal unit vector $\boldsymbol{n}_{12}$ is defined as $\boldsymbol{n}_{12} = (\boldsymbol{r}_1 - \boldsymbol{r}_2)/|\boldsymbol{r}_1 - \boldsymbol{r}_2|$. The location vectors of individual particles can be obtained by the particle-mask correlation method (Section 2.1).

The term "imaginary" means that even when no collision happens at exactly this moment, there could be a collision within the next time step ($\Delta t = 1$ ms). The particle size is uniform in the measurements. Consequently, a threshold value $\delta = 2$ pixel, about 10% of $d_p \cdot S_f$, is defined for the difference between $L_c$ and $d_p$, as the criterion for a possible particle-particle collision event

$$|L_c - d_p| \leqslant \delta. \tag{6.2}$$

In case $|L_c - d_p| = 0$, a collision takes place at the imaginary contact moment. In the case $0 < |L_c - d_p| < \delta$, the relative velocity of the two particles at $t_c$, reconstructed by the integrated tracking method (Section 2.2), should be estimated to decide if it is possible to finish a collision before the end of the next time step, i.e. until time $t_{c+1}$. Firstly, the angle $\theta$ between the relative velocity vector $\boldsymbol{u}_{r,c} = \boldsymbol{u}_{p,c,1} - \boldsymbol{u}_{p,c,2}$ and the normal unit vector $\boldsymbol{n}_{12}$ is used to check if the two particles have an approaching tendency, calculated as

$$\theta = arccos\left(\frac{\boldsymbol{u}_{r,c} \cdot \boldsymbol{n}_{12}}{|\boldsymbol{u}_{r,c}| \cdot |\boldsymbol{n}_{12}|}\right). \tag{6.3}$$

If the angle is larger than 90 degree, the two particles move towards each other. Then, if $|\boldsymbol{u}_{r,c}cos(\pi - \theta)| \cdot \Delta t > (L_c - d_p)$, the two particles are considered to really collide in the time between $t_c$ and $t_{c+1}$. The relative velocity of the two particles $\boldsymbol{u}_{r,c}$ is considered as their impact velocity.

From the viewpoint of physics, collision and contact do not differ significantly. Collision is essentially a contact with a very short time duration. In this study, the evaluation of collision duration is out of the scope due to limitations of the measurement technique. Instead, the relative velocity at the end of the time step after contact detection ($\boldsymbol{u}_{r,c+1} = \boldsymbol{u}_{p,c+1,1} - \boldsymbol{u}_{p,c+1,2}$) is analyzed to distinguish contact from real collision.

- Particle contact means $|\boldsymbol{u}_{r,c+1}| = 0$. This may occur for static conditions when particles are not fluidized or for instance when two particles keep pace with each other for a long time.

- Particle collision is characterized by a subsequent relative motion of the contact partners, hence $|\boldsymbol{u}_{r,c+1}| \neq 0$.

Note the focus is on real particle collisions only. The number of particle collisions $N_c$ is used to evaluate the experimental particle collision frequency $f_c$.

In image post-processing, only particle trajectories longer than 3 ms were analyzed by this approach, because most of the short particle trajectories are generated by motions out of plane. This filter operation may lead to a minor under-prediction of collision number but ensured that only true collisions are detected. Figure 6.2b shows examples of collisions between a target particle and two neighboring particles determined by the variations of particle trajectories.

### 6.2.3   Granular temperature

The granular temperature is perhaps one of the dominant quantities to understand the behavior of granular flows with strong particle-particle collisions [212]. Note that the granular temperature measured here is the particle granular temperature representing instantaneous relative motion between particles according to the definition by Jung et al. [213], which is usually applied in KTGF and CFD-DEM simulations. Although PTV can be used to evaluate the macroscopic movement of bubbles, the estimation of the bubble granular temperature is beyond the scope of this study.

The particle velocity $\boldsymbol{u_p}$ can be decomposed into a local mean particle velocity and an instantaneous fluctuation velocity $\boldsymbol{u_f}$. Accounting for independence of velocity components, $\Theta_{3D}$ can be defined as one-third of the mean square of $\boldsymbol{u_f}$ for a three-dimensional space [60]

$$\Theta_{3D} = \frac{1}{3}\langle \boldsymbol{u_f u_f}\rangle, \tag{6.4}$$

where the bracket denotes instantaneous local spatial average. Based on the individual particle velocity from PTV measurements, the granular temperature for a two-dimensional space $\Theta_{2D}$ can be calculated as

$$\Theta_{2D} = (\Theta_x + \Theta_y)/2; \tag{6.5}$$

$$\Theta_j = \frac{1}{N_p}\sum_{i=1}^{N_p}(u_{p,j}(i,t) - \langle u_{p,j}(t)\rangle)^2, j = x, y; \tag{6.6}$$

$$\langle u_{p,j}(t)\rangle = \frac{1}{N_p}\sum_{i=1}^{N_p}u_{p,j}(i,t). \tag{6.7}$$

$N_p$ is the number of particles in the interrogation region used for calculating the spatial average; $u_{p,j}(i,t)$ is component $j$ of the instantaneous velocity of individual particle $i$ and $\langle u_{p,j}(t) \rangle$ is the instantaneous spatial average velocity in direction $j$. The value and distribution of granular temperature are strongly affected by the choice of interrogation region size, which actually determines the level of the influence of macroscopic bubble motion on the local microscopic particle velocity distribution. However, too small interrogation region size may introduce large statistical errors from the measurements [214].

### 6.2.4   Particle collision frequency

Before proceeding, several quantities concerning particle collisions need to be defined clearly. In any dispersed particulate system, the collision rate $\dot{n}_c$ is defined as the total number of particle-particle collisions per unit time per unit volume, and the collision frequency $f_c$ is related to the number of collisions for one single particle per unit time. The relation between them is given by

$$f_c = \frac{\dot{n}_c}{2n}, \tag{6.8}$$

where $n$ is the particle number density that refers to the number of particles per unit volume. The factor $1/2$ corrects the double counting issue in most theoretical collision models, which ensures that each collision pair is counted only once and the calculated collision frequency $f_c$ is rigorous according to the definition [60, 207].

The solid volume fraction $\epsilon_s$ is defined as the ratio of the volume of solid particles $V_p$ and the total volume $V_{total}$ in the investigation region. In a mono-disperse system, it can be expressed as

$$\epsilon_s = \frac{V_p}{V_{total}} = \frac{N_p \cdot \frac{1}{6}\pi d_p^3}{V_{total}}. \tag{6.9}$$

Since particle number density $n$ is the number of particles by the total volume, this relation can be rearranged to give

$$n = \frac{6\epsilon_s}{\pi d_p^3}. \tag{6.10}$$

Recalling the theoretical collision model proposed by [60] in the KTGF, the collision rate $\dot{n}_c$ can be written as

$$\dot{n}_c = 4n_1 n_2 d_{12}^2 g_0 \sqrt{\pi\Theta}, \tag{6.11}$$

where the subscripts 1 and 2 refer to colliding particles from different size classes, $d_{12}$ is the distance of the mass centers of the collision partners and $g_0$ is a radial distribution function. The role of this function in KTGF is to correct the probability of collision for the effect of the volume occupied by particles. Assuming that the bed is quasi-isotropic, the radial distribution function only depends on $\epsilon_s$ and $g_0$ can be written as

$$g_0 = \frac{3}{5}\left(1 - \left(\frac{\epsilon_s}{\epsilon_{s,max}}\right)^{\frac{1}{3}}\right)^{-1}, \tag{6.12}$$

where $\epsilon_{s,max}$ is the maximum solid fraction for a random packing [220].

The equation for $\dot{n}_c$ simplifies in the case of particle collisions in a 2D mono-dispersed system to

$$\dot{n}_c = 4n^2 d_p^2 g_0 \sqrt{\pi \Theta_{2D}}. \tag{6.13}$$

Then, the corresponding collision frequency $f_c$ can be expressed as

$$f_c = 2n d_p^2 g_0 \sqrt{\pi \Theta_{2D}}. \tag{6.14}$$

Taking into account Eq. (6.10) and Eq. (6.12), this equation can be rewritten as

$$f_c = \frac{36}{5\sqrt{\pi} d_p} \cdot \frac{\epsilon_s \sqrt{\Theta_{2D}}}{\left(1 - (\epsilon_s/\epsilon_{s,max})^{1/3}\right)}. \tag{6.15}$$

Note that, when solid volume fraction approaches $\epsilon_{s,max}$, the value of radial distribution function tends to infinity and granular temperature approaches to zero, leaving the collision frequency undefined at this point.

Based on the definition of the collision rate $\dot{n}_c$, the experimental collision rate $\dot{n}_{c,e}$ of the investigation region in a certain time interval $\Delta t$ is given as

$$\dot{n}_{c,e} = \frac{N_c}{A_i \cdot d_p \cdot \Delta t}, \tag{6.16}$$

where $A_i$ is the area of investigation region. For the solid volume fraction, Eq. (6.9) can be rearranged as

$$\epsilon_s = \frac{N_p \cdot \frac{1}{6}\pi d_p^3}{A_i \cdot d_p}. \tag{6.17}$$

The particle density $n$ can be calculated by

$$n = \frac{N_p}{A_i \cdot d_p}. \tag{6.18}$$

As a result, the experimental collision frequency $f_c$ is obtained as

$$f_c = \frac{\dot{n}_{c,e}}{n} = \frac{N_c}{N_p \cdot \Delta t}. \tag{6.19}$$

Different from the collision ratio $\dot{n}_c$ in theoretical collision models, the two colliding particles are distinguished when measuring the particle collision number $N_c$ in the determination of collision events, i.e. $\dot{n}_{c,e} = \dot{n}_c/2$. The scale factor $1/2$ is not needed in Eq. (6.19) to correct the double counting.

It is important to note that although the 3-dimensional velocities can be obtained from the CFD-DEM simualtion, only x and y components are used in all evaluations of collision dynamics to better compare with the 2-dimensional PTV measurements.
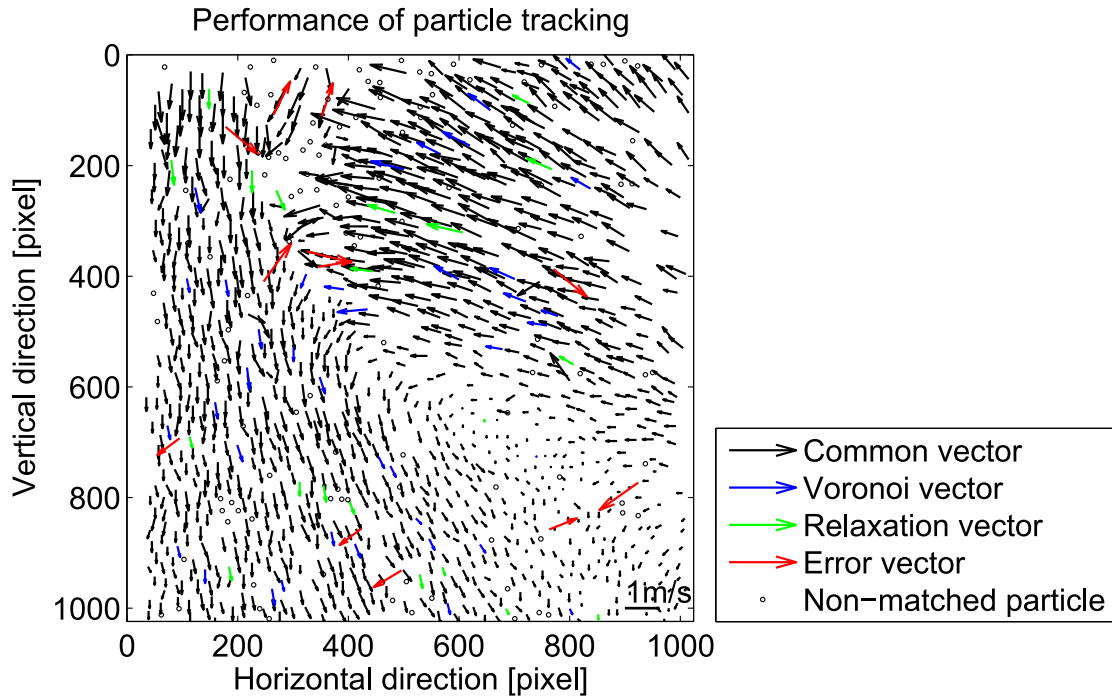
Figure 6.3: Comparison of tracking performance of the Voronoi method and the probability relaxation method (for $3.0 \cdot U_{mf} = 1.68$ m/s at the "left" location of the "low-level" height).

## 6.3   Results and discussion

Results from PTV measurements are presented in form of instantaneous particle velocity, time-averaged volumetric flux of particles, granular temperature, particle collision frequency and impact velocity. The PTV measurements will be compared with CFD-DEM simulations in terms of time-averaged volumetric flux of particles, granular temperature, impact velocity and collision frequency.

For particles in the group D of the Geldart classification that were used in measurements, bubbling regime begins as soon as the superficial gas velocity exceeds the minimum fluidization velocity. Based on visual observations of particle motion in the whole bed using the high speed camera, the flow regime of all three superficial gas velocities (2.0, 2.5, 3.0 times $U_{mf}$) was identified as the slugging regime, in which separated slugs (bullet-shaped voids) and bubbles filled the entire cross-section of the pseudo-2D bed. The turbulent fluidization flow regime was not observed even at the highest gas velocity. This is because the transition from slugging regime to turbulent fluidization regime is very gradual for group D particles due to intermittent periods of slug-like and turbulent characteristics [221]. Although 24 measurements from 8 different locations under 3 operation conditions were evaluated in the study, only the results for $3.0 \cdot U_{mf} = 1.68$ m/s from the "left" region of "low-level" (sample case) are given in detail. Nevertheless, all granular temperatures and main indices of particle collision dynamics are summarized

in Table A.2, Table A.3 and Table A.4. The CFD-DEM simulation was only performed for $3.0 \cdot U_{mf} = 1.68$ m/s.

## 6.3.1 Instantaneous velocity

The primary result from PTV measurements is the instantaneous velocity of all individual particles in each time step. Figure 6.3 shows an example time step for $3.0 \cdot U_{mf} = 1.68$ m/s, in which black vectors are vectors that matched by both methods, while blue and green vectors refer to particular vectors that only matched by either the Voronoi method or the probability relaxation method, respectively. Black circles represent particles detected by the segmentation algorithm but not successfully matched in two consecutive frames. The number of identified particles is 1258 in this time step, corresponding to approximate solid volume fraction of 0.33. Figure 6.3 represents a group of particles that slides down along the left side wall, which interacts with another group of particles driven by traveling bubbles or slugs from the right side. Due to the integration of Voronoi and probability relaxation tracking method, the time-averaged recovery ratio $\langle R_r \rangle$ of the sample case is 89.2 % with a coefficient of variation (CV) 7.1 % in the 5 s measurement time. The error ratio is less than 1 %. Further, instantaneous velocities of the same particle in consecutive time steps can be connected to construct the particle's trajectory. The recorded lifetime $\tau_p$ of an individual particle results from the sum of the time steps of this particle's visible trajectory. If the particle moves out of the focus plane, it cannot be recognized by the particle segmentation process anymore, and the trajectory of this particle is considered as terminated. The average lifetime of particles $\langle \tau_p \rangle$ in the sample case is 11.5 ms with a CV of 91.3 %.

Average recovery ratios $\langle R_r \rangle$ and average lifetimes $\langle \tau_p \rangle$ for all cases are listed in Table A.2. The minimum average recovery ratio is 86.1 % and the average lifetime is about 10 ms, while particles have longer lifetime in the dense regions (the "low-level" or close to side walls). The large coefficient of variation of lifetime implies a wide distribution caused by the open boundaries of the FOVs and the intentional restriction to study particles only in the first layer by the intensity calibration and particle segmentation algorithm. Compared to the preliminary studies by a single algorithm in Figure 6.3 (Voronoi or probability relaxation), PTV measurements coupling the Voronoi method and the probability relaxation method demonstrate very good performance, which can be effectively applied to analyze granular temperature and particle collision dynamics.

More results of the instantaneous velocities obtained using integrated tracking method can be found in Figure A.3 for the low-level left at 1.68 m/s (with an interval of 20 ms). In the investigation region (c) (as shown in Figure 4.3), the average velocity field, similar to PIV results, and the solid volume fraction can be evaluated, which are depicted, respectively, in Figure A.4 and Figure A.6.

## 6.3.2 Global circulation

In spite of the superior ability of PTV measurement to reveal instantaneous particle information, a representation of global particle circulation patterns may also be desirable
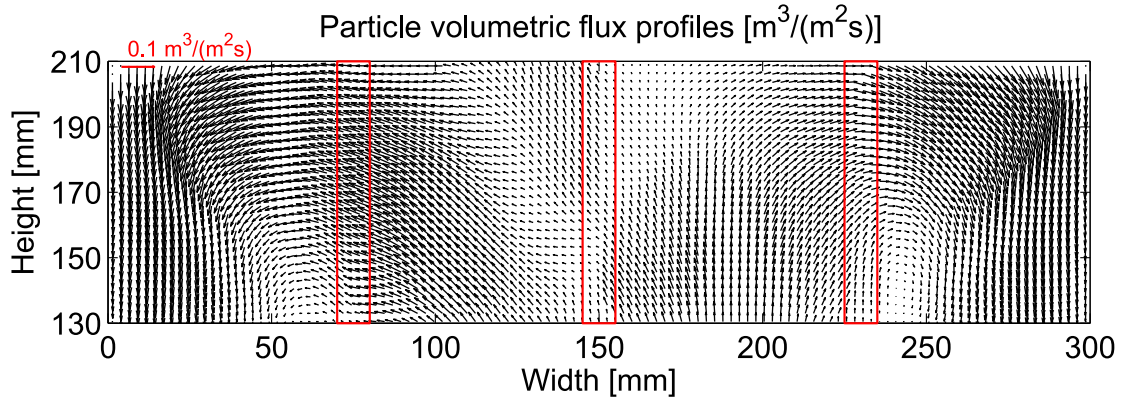
Figure 6.4: Profiles of volumetric flux of particles for 1.68 m/s at the "low-level" height (overlaps between different measurement locations are indicated by red rectangles; the vectorial scale is plotted on the top left).

in order to show the 'big picture' of particle motion in the slugging fluidization flow regime. To study time-averaged particle circulation patterns based on instantaneous velocity of individual particles, the field of view was divided into small investigation regions [42], similarly to the approach used in standard PIV measurements. The details of different investigation regions used in the post-processing of measurement and simulation data have been depicted in Figure 4.3. The size of the small investigation region (named as region (c)) is about $6 \cdot d_p$ with a 75 % overlap to obtain better spatial resolution. For each time step, the spatial-averaged velocity in each such interrogation region is calculated by Eq. (6.7) and the corresponding solid volume fraction follows from Eq. (6.17). Then, a time-averaging was performed for a total of 5 s measurement time. Sometimes, however, the time-averaged particle velocity profiles can be spurious to describe particle circulation patterns, because the contribution of several particles with really high velocity to the global motion of particles is overestimated in the dilute region. For instance, the particles rain from the top surface of each slug or bubble. Therefore, the volumetric flux of particles $\Phi$, i.e. the volume flow rate of particles per unit area $(m^3/(m^2 \cdot s))$, is evaluated to accurately reveal particle circulation patterns. Based on PTV measurement data, the volumetric flux of particles can be calculated as the product of particle velocity and solid volume fraction.

As shown in Figure 6.4, two symmetric vortices can be observed for the sample case gas velocity 1.68 m/s at the "low-level" bed height, although the data from different measurement locations were obtained at different times. In other words, 5 s measurement time is enough to investigate the circulation motions in this pseudo-2D fluidized bed. There are still little deviations, especially in the overlapping regions indicated by red rectangles. The center of the left vortex is located at a bed height of about 130 mm, and that of the right vortex is at about 145 mm. The top boundaries of the two vortices start to form at a height of about 200 mm, which is the height of stable dense bed surface. Bubbles or slugs erupt after exceeding the dense bed surface, resulting in hori-
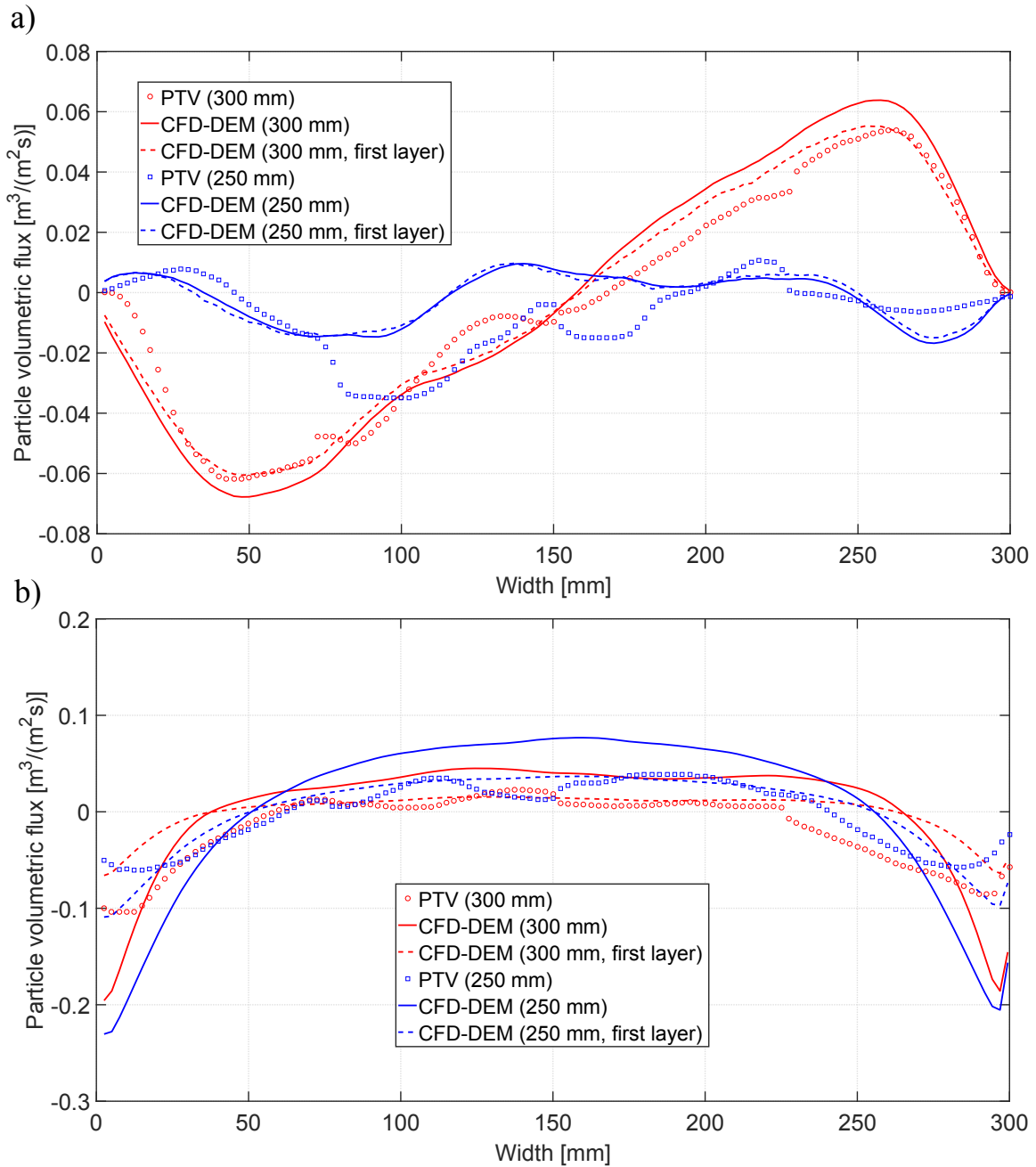
a)



b)

Figure 6.5: Comparison of time-averaged particle volumetric flux of particles at height ranges of 240 to 250 mm and 290 to 300 mm for 1.68 m/s from PTV measurements and CFD-DEM simulations: a) horizontal direction and b) vertical direction.

zontal transport by accelerating particles into the freeboard and towards the side walls. In the global circulation pattern, particles are transported upwards in the center of the bed and slide downwards close to the side walls, which is associated with the inception, coalescence and eruption of traveling bubbles or slugs at different heights of the flu-

idized bed. This result of particle circulation pattern corresponds well to the published observations using PIV measurements [43, 158, 214]. However, it is important to note that instantaneous pattern may differ significantly from the time-averaged circulation pattern. At lower superficial gas velocity ($U = 2.0U_{mf}$ or $U = 2.5U_{mf}$), the circulation patterns were not so pronounced, and the centers of the vortices disappeared from the field of view. The average volumetric flux of particles and the average particle velocity from all measurement cases, calculated by means of region (c), are listed in Table A.2.

Figure 6.5 shows comparison of time-averaged particle volumetric flux of particles in both vertical and horizontal directions over 5 s. The data points of "250 mm" and "300 mm" are averaged from investigation regions in height ranges of 240 to 250 mm and 290 to 300 mm, respectively. For the simulation results, the "first layer" in legends means that the depth of the investigation regions for post-processing CFD-DEM data is one particle diameter. Generally, the CFD-DEM simulation can well predict the time-averaged particle volumetric flux in these two height ranges according to the PTV measurement data. The simulation results obtained in the first layer are closer to the 2D PTV measurements in both horizontal and vertical directions.

### 6.3.3   Particle granular temperature

Approaching the particle granular temperature, the size of investigation region was firstly selected as the full field of view (about $45 \cdot d_p$, named as region (a)) to investigate the granular temperature of the slugging flow regime on the macroscopic scale. Figure 6.6 shows the square root of 2D granular temperature by the investigation region (a) over measurement time, including components in $x$ and $y$ directions. The cases of "left" and "left-center" are compared here to represent the effect of spatial location on the granular temperature. The calculation of $\Theta_{2D}$ and $\Theta_j$ follows Eq. (6.5) and Eq. (6.6), respectively. In both fields, the square root of granular temperature $\Theta_{2D}$, $\Theta_x$ and $\Theta_y$ fluctuates with the measurement time in the range from 0.05 to 0.65 m/s. Generally, the fluctuations of granular temperature are caused by the motion of bubbles or slugs in the investigation region. When a bubble (slug) or part of a bubble (slug) enters the investigation region with a velocity different from the local mean velocity of particles, the granular temperature increases due to the random addition of particle kinetic energy. By ongoing particle-particle collisions and diffusive mixing of particles, this kinetic energy is dissipated and granular temperature gradually decreases until the appearance of new bubbles (slugs). It is interesting to observe that granular temperature is anisotropic (directionally dependent) in both the "left" and the "left-center" locations on the macroscopic scale. And, obviously, the peaks of the square root of the axial granular temperature $\sqrt{\Theta_y}$ in Figure 6.6b can reach higher positions compared to those in Figure 6.6a, representing the heterogeneous (spatially dependent) feature of granular temperature. The ratio of $\sqrt{\Theta_y}/\sqrt{\Theta_x}$ can be applied as a measure of the anisotropy of the granular temperature. The averaged value of $\sqrt{\Theta_y}/\sqrt{\Theta_x}$ is about 1.30 with a CV of 38.5 % for the "left" case, while it is about 1.45 with a CV of 43.2 % for the "left-center" case. But the ratio $\sqrt{\Theta_y}/\sqrt{\Theta_x}$ is not larger than unity in every time step,
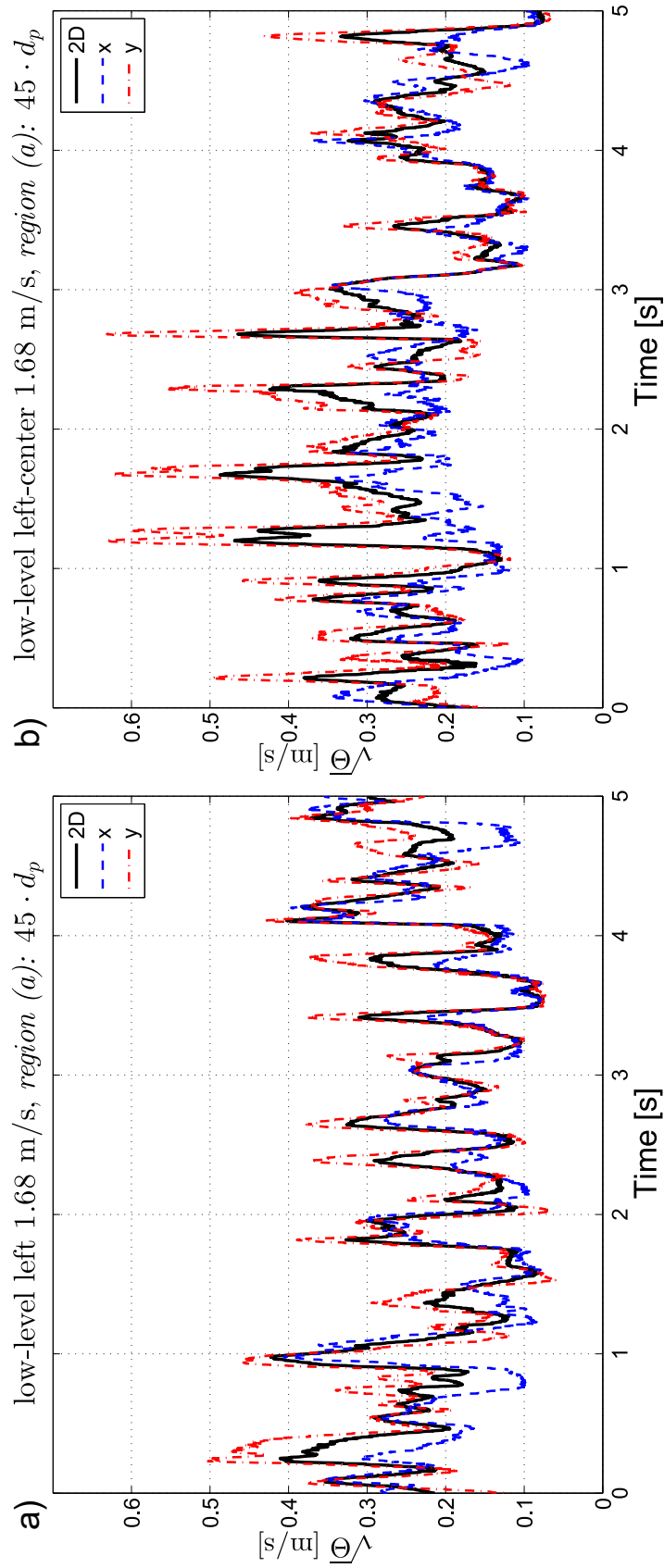
Figure 6.6: Square root of granular temperature using the investigation region (a) over measurement time, together with components in $x$- and $y$- directions (plot a: 1.68 m/s, "low-level left"; plot b: 1.68 m/s, "low-level left-center").

which implies that relatively large fluculation velocities can also appear in the horizontal direction. From the view of macroscopic motion of particles, the axial fluctuation velocity of particles in the " left " case is relatively small due to the manner of sliding motion of particles in the relatively dense region. On the other hand, large number of bubbles (slugs) are vertically accelerated and transported through the center region of the bed, together with coalescence and eruptions, which can provide large axial fluctuation velocity of particles in the "left-center" case. The observations of the anisotropy of granular temperature on the macroscopic scale arising from the motion of bubbles (slugs) are in accordance with the measurement studies by Tang et al. [214], Müller et al. [216], Holland et al. [217].

As addressed above, the size of the investigation region influences the evaluation of the granular temperature. Actually, the granular temperature is usually used to characterize the fluctuation velocity of particles on the microscopic (particle) scale in real applications, for example in the KTGF. Thus, sizes of $15 \cdot d_p$ (region (b)) and $6 \cdot d_p$ (region (c)) were further used to analyze the micro-scale characteristics of the granular temperature. The smallest region (c) with size $6 \cdot d_p$ is, on the one hand, small enough to expose particle scale information in the granular temperature and, on the other hand, sufficiently large to base the evaluation on enough particles, avoiding large statistical measurement errors. Figure 6.7a shows the influence of region size on the granular temperature $\Theta_{2D}$ and Figure 6.7b indicates the influence on the anisotropy of the granular temperature, both for the sample case "low-level left" 1.68 m/s. For each time step, the average value calculated from all individual investigation regions is plotted. Notably, the granular temperatures from different sizes of investigation region fluctuate with similar frequency, but the amplitudes of fluctuations depend strongly on the size of the investigation region. Data concerning granular temperature are listed in Table A.3. In the sample case, the mean value of the square root of granular temperature $\langle\sqrt{\Theta_{2D}}\rangle$ decreases by more than 50 % from 0.219 to 0.092 m/s, when the size of region varies from $45 \cdot d_p$ to $6 \cdot d_p$. The large CV of 86.7 % in region (c) implies that the granular temperature calculated in regions of size (c) becomes more chaotic and is distributed in a wider range. Meanwhile, the anisotropy of the granular temperature gradually disappears, as a result of the reduction of the influence from macroscopic bubble motion. The average ratio $\langle\sqrt{\Theta_y}/\sqrt{\Theta_x}\rangle$ decreases with decreasing investigation region size to 1.05 for the sample case, which means the granular temperature is almost isotropic on the particle scale.

Figure 6.8 shows the comparison of the square root of granular temperature for "low-level left" and "low-level left-center" at 1.68 m/s using region (c). As shown in Figure 6.8a and Figure 6.8b, results from the CFD-DEM simulation fluctuate in comparable frequencies with the PTV measurements for both "low-level left" and "low-level left-center". But the amplitudes of fluctuations evaluated from the CFD-DEM simulation are wider than those from PTV measurements, especially for the case of "low-level left-center". Comparing results of the CFD-DEM using different regions for post-processing, the general fluctuations of granular temperature are similar; but, in some time steps, particles in the "first layer" can reach much higher square root of granular temperature
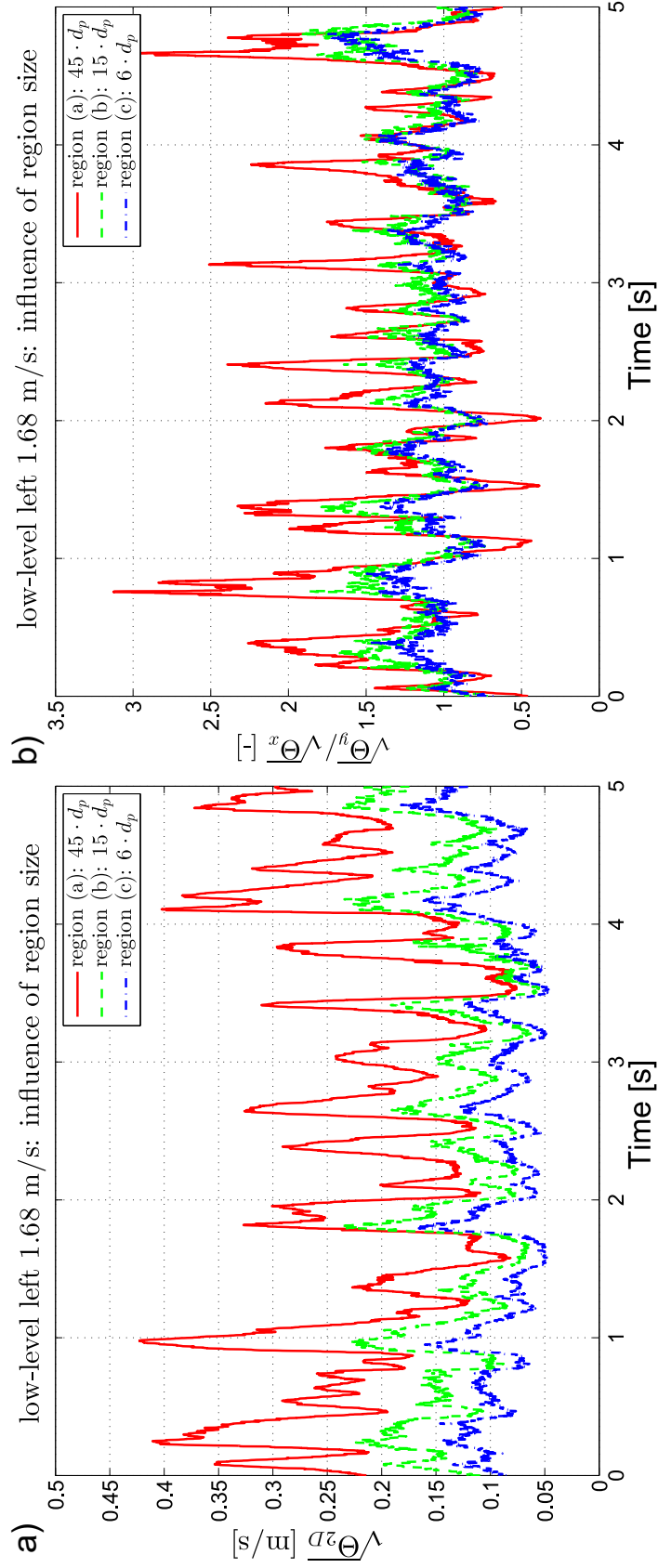
Figure 6.7: Influences of a) the size of the investigation region on the square root and b) on the anisotropy of granular temperature (1.68 m/s, "low-level left"; region (a): $45 \cdot d_p$, region (b): $15 \cdot d_p$, region (c): $6 \cdot d_p$).
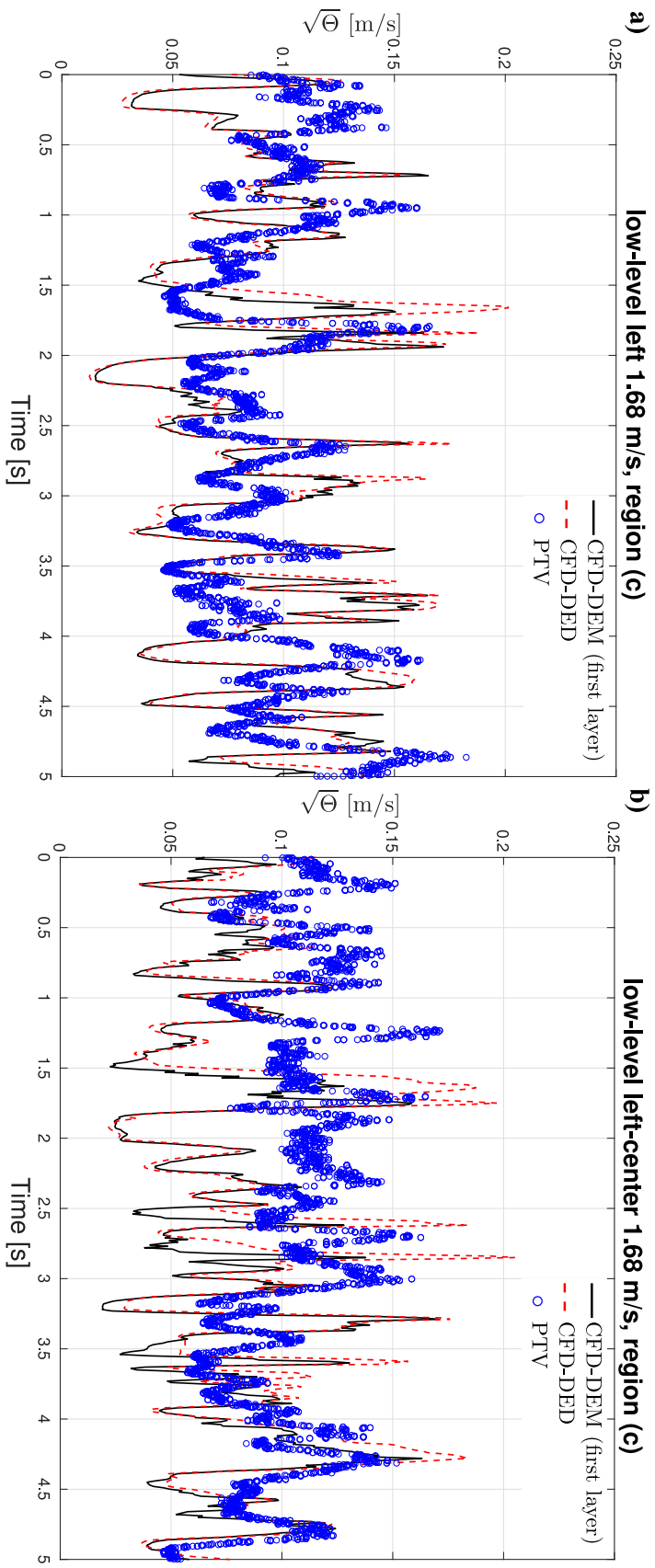
Figure 6.8: Comparison of the square root of granular temperature at different locations obtained from PTV and CFD-DEM (1.68 m/s; region (c)).
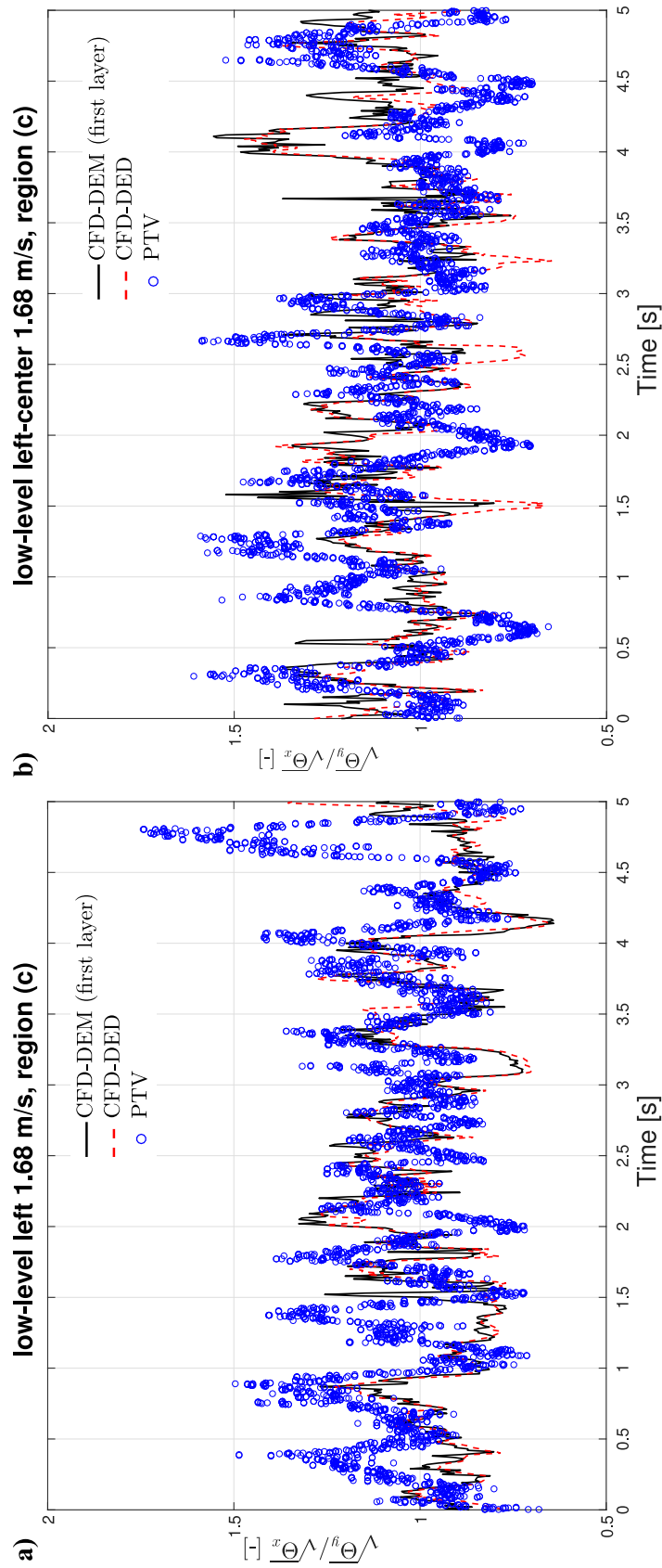
Figure 6.9: Comparison of the anisotropy of granular temperature at different locations obtained from PTV and CFD-DEM (1.68 m/s; region (c)).

than the particles in the entire bed. The mean values of granular temperature predicted by CFD-DEM simulations using different regions for post-processing are about 30 % larger than that measured by the PTV measurement for the case of "low-level left-center".

Figure 6.9a and Figure 6.9b show that the CFD-DEM simulation can well predict the anisotropy of granular temperature for both "low-level left" and "low-level left-center". For results of the CFD-DEM simulation, the variations of anisotropy of granular temperature are similar using different depths for post-processing. The average ratios $\langle\sqrt{\Theta_y}/\sqrt{\Theta_x}\rangle$ obtained from CFD-DEM simulations in the "first layer" and the entire bed are close to unity for both cases, which implies that the granular temperature is isotropic on the particle scale.

These observations from both measurements and simulations agree with the assumption that velocities of particles are isotropically and independently distributed, and the further deduced Maxwellian velocity distributions in the KTGF [60].
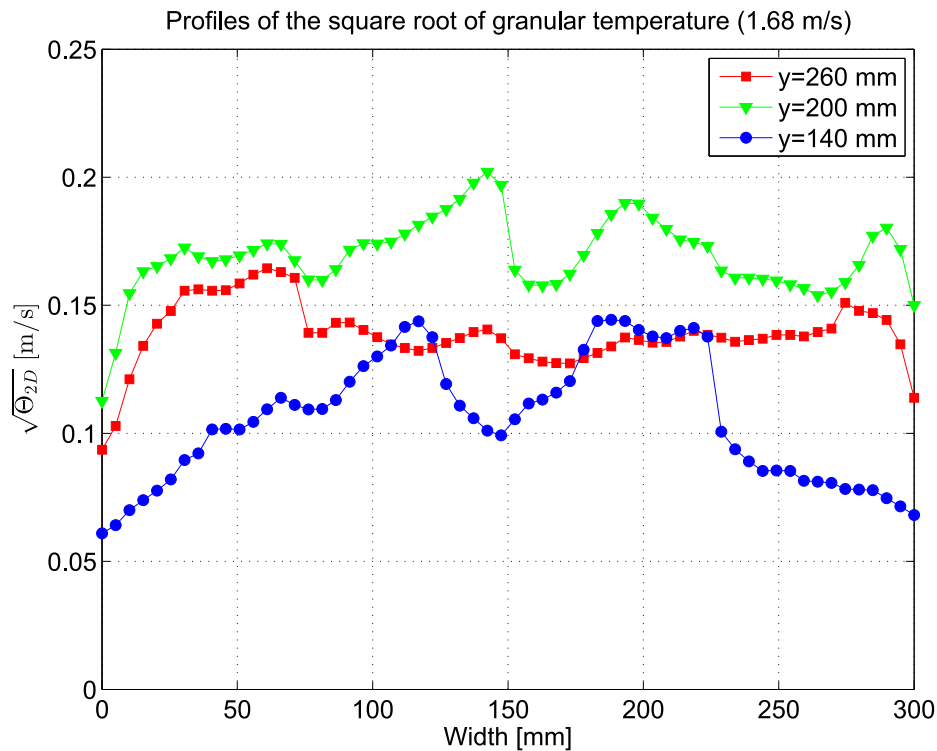


Figure 6.10: Profiles of the square root of granular temperature at different heights of the fluidized bed (1.68 m/s; $y = 260, 200, 140$ mm; region (c)).

Figure 6.10 depicts profiles of the square root of granular temperature $\Theta_{2D}$ at different bed heights, based on the investigation region (c). The average square root of granular temperature first increases with bed height, then reaches a maximum, and finally decreases again. The maximum appears near the height of the dense bed surface

(200 mm), where particles are expelled into the freebroad by the eruptions of bubbles. At each bed height, granular temperature close to the side walls is smaller than in the center region, due to the sliding motion of particles along the side walls.

In addition, some general tendencies of the variation of the granular temperature can be drawn from the detailed measurement data listed in Table A.3:

1. The average granular temperature increases for all investigation region sizes used and in all measurement locations when the superficial gas velocity increases. In other words, the increase of the time-averaged fluctuation velocity of particles by more intensive fluidization is independent of the spatial location, on both the macroscopic and the microscopic scale. However, the value of granular temperature does depend on the spatial location, and is larger near the dense bed surface.

2. When the investigation region varies from the macroscopic to the particle scale, the anisotropy of granular temperature is significantly decreased due to the reduction of the influence of bubble or slug motion at all measurement locations.

3. The large CV of the average of the square root of granular temperature indicates the wide distribution of granular temperature at single particle scale.

### 6.3.4 Particle-particle collision frequency

Based on the number of collision events $N_c$ obtained from the analysis of individual particle trajectories, the experimental particle collision frequency can be calculated by Eq. (6.19). Figure 6.11 shows the experimental collision frequency with respect to the measurement time for the sample case "low-level left" 1.68 m/s. Similarly to Figure 6.7, the average collision frequency of investigation regions with different sizes, regions (a), (b), (c), is plotted for each time step. The experimental collision frequency varies in the range from about 100 to 500 1/s. In clear contrast to variations of granular temperature, the collision frequency is rather independent of the size of the investigation region, which may be a consequence of the combined effect of granular temperature and local solid volume fraction on the particle collision frequency. The fluctuations in the collision frequency can be further analyzed based on the Fourier transformation, as a useful tool to study the period $t_{p,fit}$ of variations with time or space. Fourier transformation with 3 terms was able to fit well the frequency of the fluctuation of the collision frequency, which gives a period $t_{p,fit}$ of approximately 0.77 s. The specific data about average collision frequency, average solid volume fraction and fitted period $t_{p,fit}$ are listed in Table A.4. The average collision frequency at the "high-level" height is much smaller compared with that at the "low-level" height, due to significantly smaller average solid volume fraction. In some time steps, even no particle exists in the FOVs at "high-level" height under low superficial gas velocity. However, the collision frequency and solid volume fraction in individual investigation regions in some time steps can reach high values, which corresponds to large CVs obtained for both collision frequency and solid volume fraction at the "high-level". In other words, there existed large fluctuations

in the region exceeding the stable dense bed surface. At the "low-level" height and gas velocity 1.68 m/s, at least 5 entire periods are completed in the 5 s of measurement time, leading to the pronounced symmetric flow pattern of particles shown in Figure 6.4 and Figure 6.5. Inversely, the periods at "high-level" height or low gas velocity are longer, depending on relative position between the stable dense bed surface and the measurement location during the experiments.

From another point of view, experimental collision frequencies acquired in individual investigation regions can be commonly represented with respect to the corresponding solid volume fraction to enable comparison with the theoretical collision model. Because data from particle scale are more meaningful for comparison with KTGF, we focus on the analysis based on the investigation region of size (c) in the following study. Figure 6.12 shows the particle collision frequency with respect to solid volume fraction for the four measurement locations at "low-level" height under 1.68 m/s gas velocity. Individual black squares represent the experimental collision frequencies measured in each investigation region (c) volume and each time step. Compared with Figure 6.11, the collision frequency is distributed in a wider range from 0 to 700 1/s. Only 10 % of the randomly selected data are plotted for better visualization (total number of discrete data points is more than 5 millions). Comparing collision frequency at solid volume
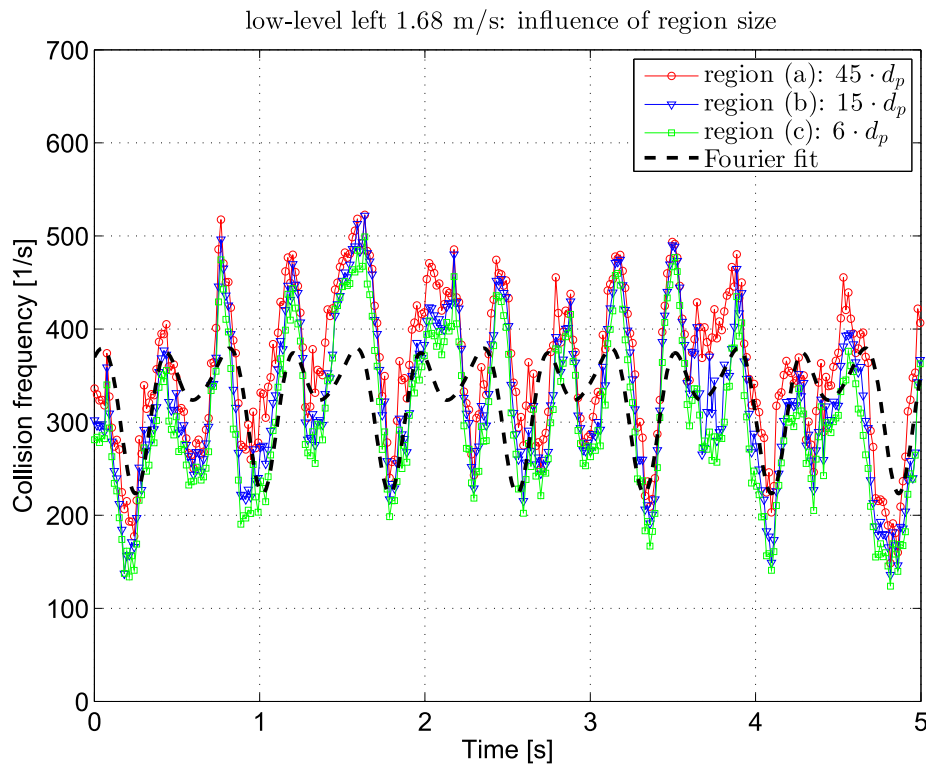


Figure 6.11: Particle collision frequency (evaluated for regions (a), (b), (c)) over measurement time for 1.68 m/s at the "low-level left", together with three-term Fourier fit (the period approximately equals to 0.77 s).

Figure 6.12: Particle collision frequency over solid volume fraction for the four "low-level" measurement locations at 1.68 m/s gas velocity: a) left, b) left-center, c) right-center, d) right (only 10% randomly selected data are plotted for better visualization in each sub-figure; red solid lines are obtained from Eq. (6.15) with a constant $\langle\sqrt{\Theta_{2D}}\rangle_{(c)}$ calculated from PTV measurements; blue dashed lines fitted from all individual collision frequency data from region (c) are also based on Eq. (6.15)).
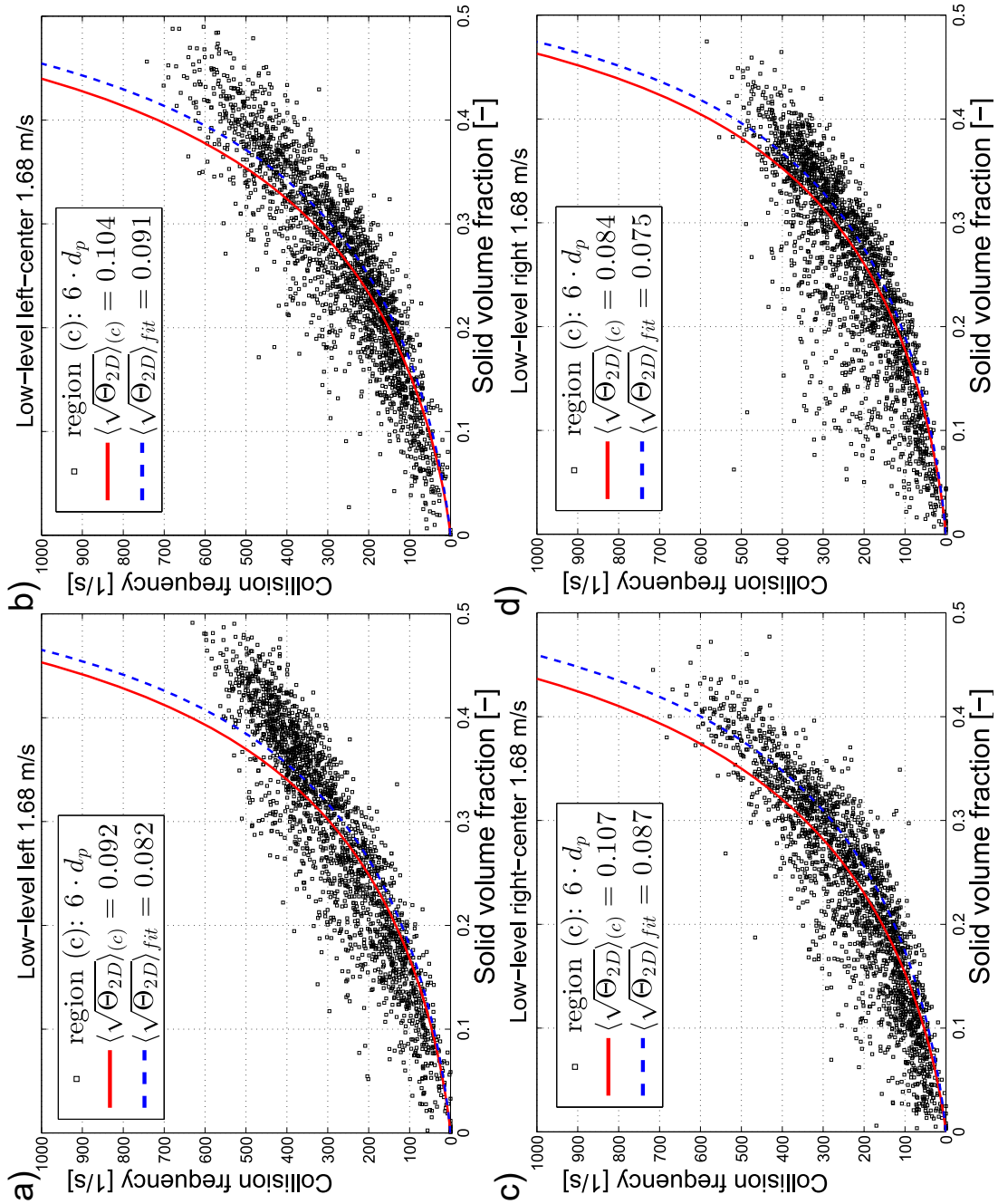
fraction 0.4 for all locations, the maximum value of the collision frequency can reach about 700 1/s in the center locations, but only 500 1/s for the side locations. If the large granular temperature in the center locations is taken into account, this observation is reasonable according to the collision model.

For each measurement location, the theoretical collision frequency is plotted based on Eq. (6.15) with a constant square root of granular temperature, which equals to the average square root of granular temperature $\langle\sqrt{\Theta_{2D}}\rangle_{(c)}$ from PTV measurement (red solid line). Using the experimental collision frequency in all individual investigation regions and all time steps, an average square root of granular temperature $\langle\sqrt{\Theta_{2D}}\rangle_{fit}$ can be fitted from Eq. (6.15) (blue dash line). Generally, $\langle\sqrt{\Theta_{2D}}\rangle_{(c)}$ is only slightly larger than $\langle\sqrt{\Theta_{2D}}\rangle_{fit}$, meaning that the collision model can predict the overall features of the experimentally observed collision frequency relatively well. However, a significant difference is observed in the dense region (at approximately, $\epsilon_s > 0.3$) for all locations, in which the collision model overestimates the collision frequency. From the model view point, the value of the radial distribution function $g_0$ (Eq. (6.12)) will rapidly increase when the solid volume fraction approaches $\epsilon_{s,max}$, which might yield the overestimation. More accurate analysis would require use of the corresponding granular temperature in the dense region. From the experimental perspective, many particle-particle interactions did not show a clear rebound behavior, due to the serious decrease of the mean free path of particles in dense regions. This part of particle-particle interactions is not considered as real collisions in our algorithm (Section 6.2.2). The $\langle\sqrt{\Theta_{2D}}\rangle_{fit}$ values obtained for all cases are listed in Table A.4. Referring to $\langle\sqrt{\Theta_{2D}}\rangle_{(c)}$ in Table A.3, all values of $\langle\sqrt{\Theta_{2D}}\rangle_{fit}$ are smaller than the corresponding values of $\langle\sqrt{\Theta_{2D}}\rangle_{(c)}$, and the relative difference ranges from 3 to 23 %, depending on operation conditions and measurement location. The largest differences in collision frequency between measurements and model occur in dense regions for all cases.

Clearly, particle collision frequency is influenced by the combined effect of solid volume fraction and granular temperature. Both these variables can be evaluated from PTV measurements in each investigation region and each time step. To further compare with the Gidaspow collision model, a new variable $\chi$ with unit [1/s] is defined from Eq. (6.15):

$$\chi = \frac{\epsilon_s\sqrt{\Theta_{2D}}}{\left(1 - (\epsilon_s/\epsilon_{s,max})^{1/3}\right)\cdot d_p}.$$
(6.20)

Then, Eq. (6.15) can be rearranged to a linear form

$$f_c = \frac{36}{5\sqrt{\pi}}\chi,$$
(6.21)

in which the collision frequency increases directly proportionally with the model variable $\chi$ and the slope is a constant $36/(5\sqrt{\pi})$. Due to the huge number of experimental data, the average values of collision frequency and granular temperature corresponding to a certain solid volume fraction range are meaningful for model comparison by Eq. (6.21). Specifically, solid volume fraction from 0 to 0.5 is divided into 50 intervals. For each

solid volume fraction interval $k$, the average collision frequency $\langle f_c \rangle$ is calculated by averaging the collision frequency $f_c(k)$ from each individual investigation region (c) with the corresponding solid volume fraction located in the interval $k$. The same approach is used to calculate the average square root of 2D granular temperature $\langle \sqrt{\Theta_{2D}} \rangle$. Then, the average $\langle \chi \rangle$ can be calculated together with the median value of each solid volume fraction interval.

Figure 6.13 represents the average collision frequency $\langle f_c \rangle$ with respect to the average model parameter $\langle \chi \rangle$ for all cases, compared to the Gidaspow collision model. Each sub-figure contains four measurement locations at one bed height for one gas velocity. Similarly to the analysis according to Figure 6.12, the Gidaspow collision model overestimates the collision frequency at $\langle \chi \rangle > 130$ for the "low-level" and at $\langle \chi \rangle > 100$ for the "high-level". The approximate critical solid volume fraction is also labeled in each plot. After the critical solid volume fraction, collision frequencies from the black solid line (model predicted collision frequency) will be always larger than the experimental data. When the value of the average model variable $\langle \chi \rangle$ increases beyond 130 or 100, the experimental average collision frequency reaches a relatively constant value or even shows a decreasing tendency in some cases. This may be due to the opposing contributions of increasing solid volume fraction, which facilitates the particle-particle interactions, and decreasing of the granular temperature.

The critical solid volume fraction of the "high-level" is smaller than that of the "low-level". This shift in different heights may arise from the different bubble or slug motion at the "low-level" and at the "high-level", especially for the gas velocities 1.40 and 1.12 m/s. Most bubbles or slugs have erupted and the particles are not able to obtain new random kinetic energy from the irregular motion of bubbles or slugs at the "high-level", resulting in a strong reduction of granular temperature. Whereas, the "low-level" is still well below the dense bed surface, so that active bubble or slug motion in both horizontal and vertical directions generates a relatively large granular temperature compared to the same particle density at the "high-level". Interestingly, the experimental average collision frequency $\langle f_c \rangle$ displays a large increase with $\langle \chi \rangle$ in the range $0 < \langle \chi \rangle < 25$ compared to the Gidaspow collision model for almost all cases. This can also be observed in Figure 6.12. Note that the first data point corresponds to the solid volume interval 0 to 0.01, where the average collision frequency $\langle f_c \rangle$ is not equal to zero. The average model parameter $\langle \chi \rangle = 25$ corresponds to a solid volume fraction of about 0.1. Moreover, the experimental average collision frequency $\langle f_c \rangle$ once again exceeds the model predicted value in, approximately, the range of $50 < \langle \chi \rangle < 130$ in Figure 6.13a and Figure 6.13b.

When the collision frequency was evaluated from the CFD-DEM simulations, the number of collisions between two particles $N_c$ was directly calculated by the DEM data for individual collision events (as depicted in Figure B.1), instead of using the algorithm based on the trajectories of particles (Section 6.2.2). The calculation of model parameter $\langle \chi \rangle$ is the same as when evaluating PTV measurement data. For the cases of "low-level" and "high-level" at 1.68 m/s, Figure 6.14 shows the average collision frequency $\langle f_c \rangle$ with respect to the average model parameter $\langle \chi \rangle$ from the CFD-DEM simulations in
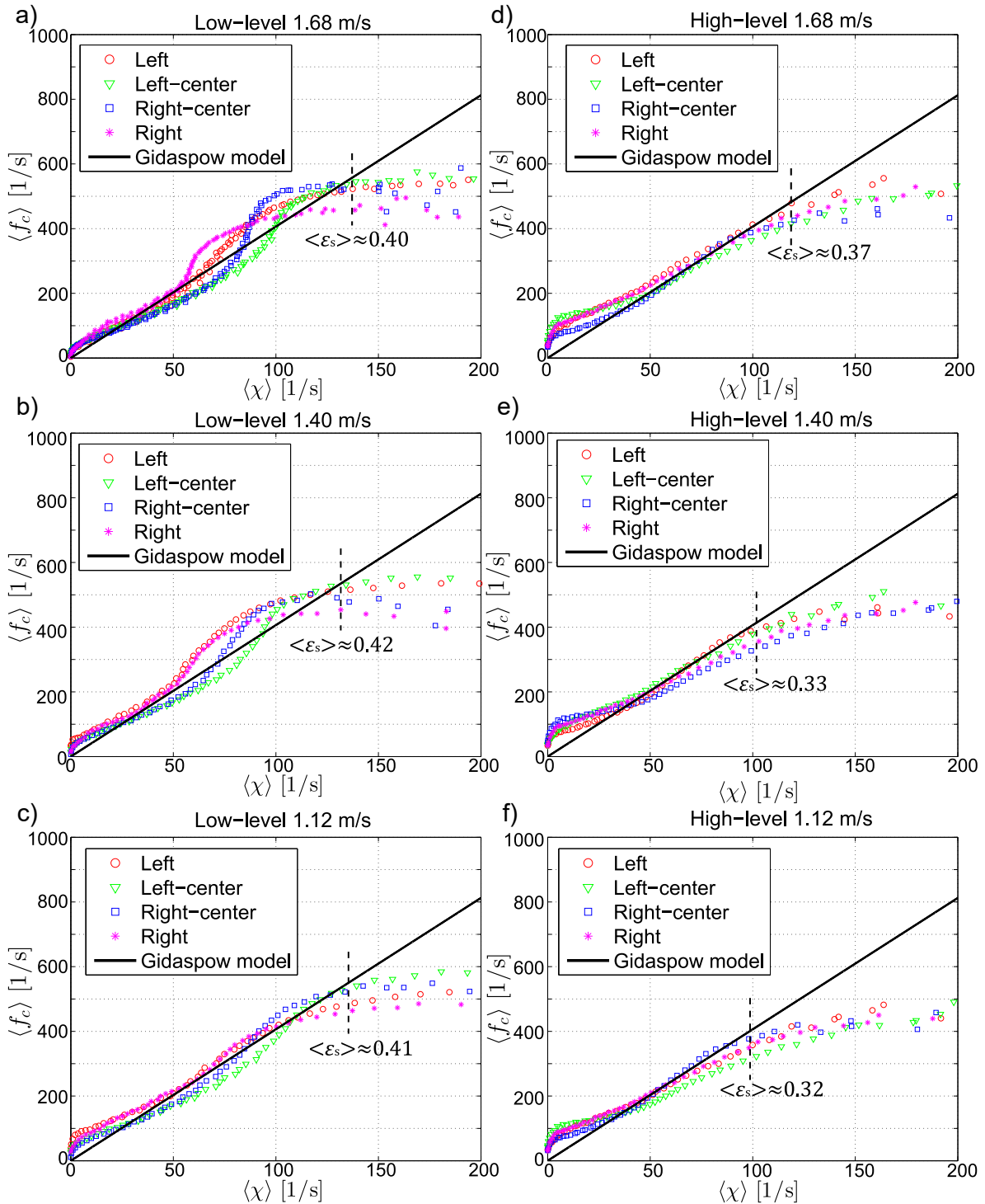
Figure 6.13: Comparison of average collision frequency from PTV measurements and the Gidaspow collision model for different locations under different superficial gas velocities: left side for the "low-level" and right side for the "high-level" (theoretical lines are plotted based on Eq. (6.21)).

the "first layer", compared to the Gidaspow collision model. In the approximate range
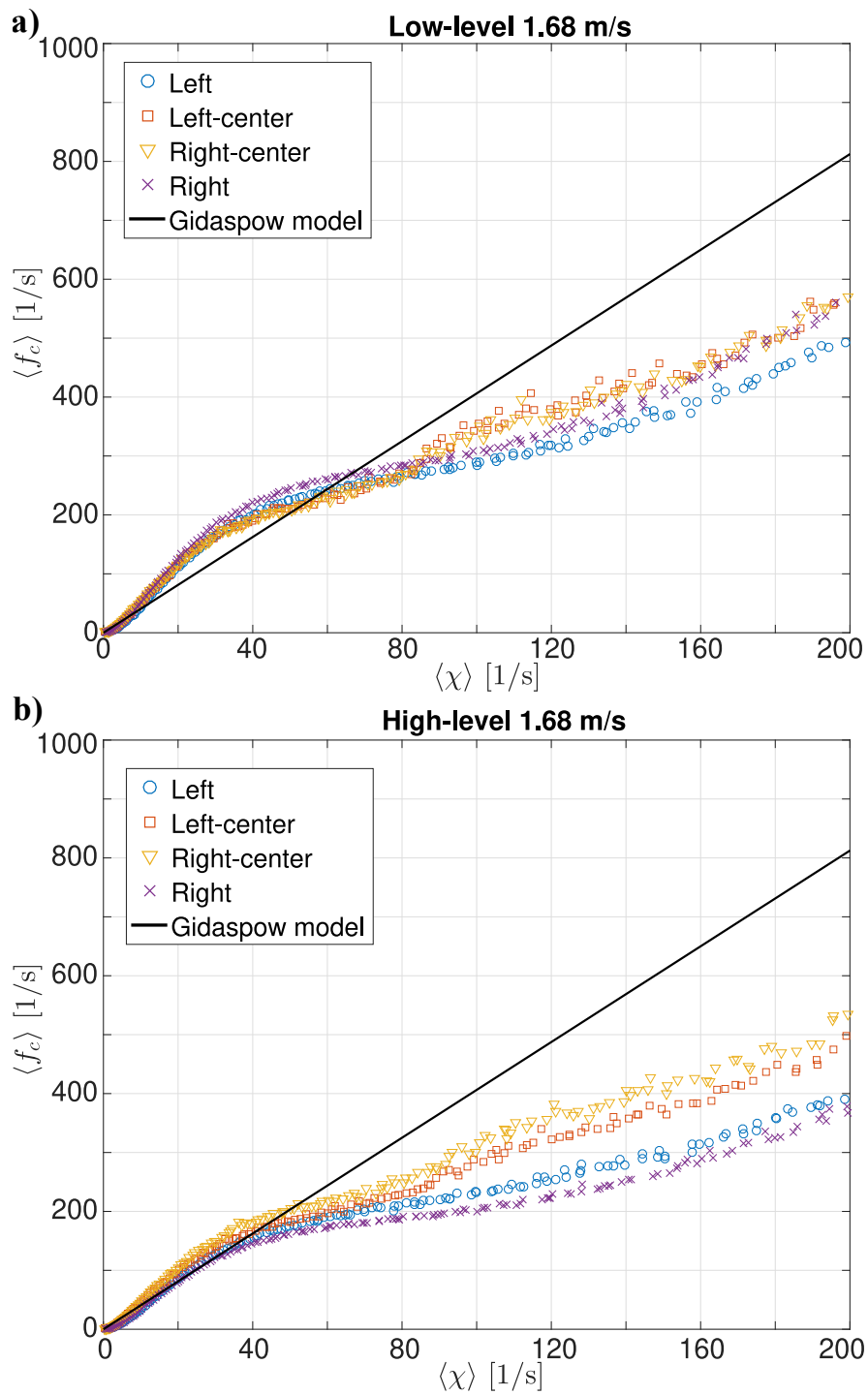


Figure 6.14: Comparison of average collision frequency from CFD-DEM simulations in "first layer" and the Gidaspow collision model for different locations at gas velocity of 1.68 m/s (theoretical lines are plotted based on Eq. (6.21)).

of $50 < \langle \chi \rangle < 130$, the average collision frequency $\langle f_c \rangle$ predicted by the CFD-DEM simulation is obviously lower than that measured by the PTV method. The increase of average collision frequencies $\langle f_c \rangle$ predicted by the CFD-DEM simulation is faster than that measured by the PTV method when $\langle \chi \rangle$ is larger than 130. Consequently, the maximum average frequencies $\langle f_c \rangle$ from simulations and measurements are comparable. The values for "low-level" and "high-level" are about 600 and 550, respectively. The tendency of staying relatively constant or even decreasing with increasing $\langle \chi \rangle$ is not observed from the CFD-DEM simulations.

### 6.3.5   Particle-particle collision velocity

In measurements, the particle-particle collision velocity $\boldsymbol{u}_{r,c}$ of all individual particle-particle interactions can be acquired during the determination of the collision events. The average magnitude of impact velocity $\langle |\boldsymbol{u}_{r,c}| \rangle$ has been calculated based on the data from 5 s measurement time, and is listed in Table A.4 together with corresponding CV. The average magnitude of impact velocity $\langle |\boldsymbol{u}_{r,c}| \rangle$ differs with operation conditions and spatial location. The maximum detected value of magnitude of impact velocity for an individual collision was about 0.6 m/s. In spray fluidized beds, the magnitude of impact velocity $|\boldsymbol{u}_{r,c}|$ significantly affects the coalescence of particles. Based on Ennis et al. [203], the collision of two particles will result in coalescence if the viscous Stokes number $St_v$ is less than the critical viscous Stokes number. Indeed, the viscous Stokes number $St_v$ is the ratio of kinetic energy of two approaching particles to the viscous dissipation by the liquid film. Taking typical conditions (liquid viscosity of 10 mPa $\cdot$ s and a ratio between liquid thickness and the characteristic height of surface asperities of 10) from investigations of spray agglomeration [154, 154], the critical magnitude of impact velocity $|\boldsymbol{u}_{r,c}|$ for coalescence is 0.124 m/s for the used particles with 1.8 mm diameter. Therefore, the particle formation process associated with the coalescence of particles needs to be accurately controlled by adjustment of operation gas velocity and arrangement of the spray zones.

The experimental measurement of impact velocity is actually even more difficult than the measurement of granular temperature. Figure 6.15 reveals the relationship between the average square root of 2D granular temperature and the average magnitude of impact velocity at the "low-level left" and the "high-level left" under different gas velocities. In each investigation region (c), an average magnitude of impact velocity $\langle |\boldsymbol{u}_{r,c}| \rangle$ and a square root of 2D granular temperature $\sqrt{\Theta_{2D}}$ can be calculated for particle collisions that happen in this region. Then, the magnitude of impact velocity is divided to intervals of 0.001 m/s and the corresponding square roots of 2D granular temperature located in each such interval are averaged to get the average square root of 2D granular temperature $\langle \sqrt{\Theta_{2D}} \rangle$. Large gas velocity increases the granular temperature and leads to a large impact velocity, but it does not appear to act in another way than via $\langle \sqrt{\Theta_{2D}} \rangle$. This holds for both heights, though the data are more scattered at the "high-level". The experimental data can be fitted by a simple linear equation $f(x) = p_1 x + p_2$; the values of $p_1$ and $p_2$ for different measurement locations are given in Table A.4. The coefficients of determination for all locations at the "low-level" are close to about 0.9, and about 0.7
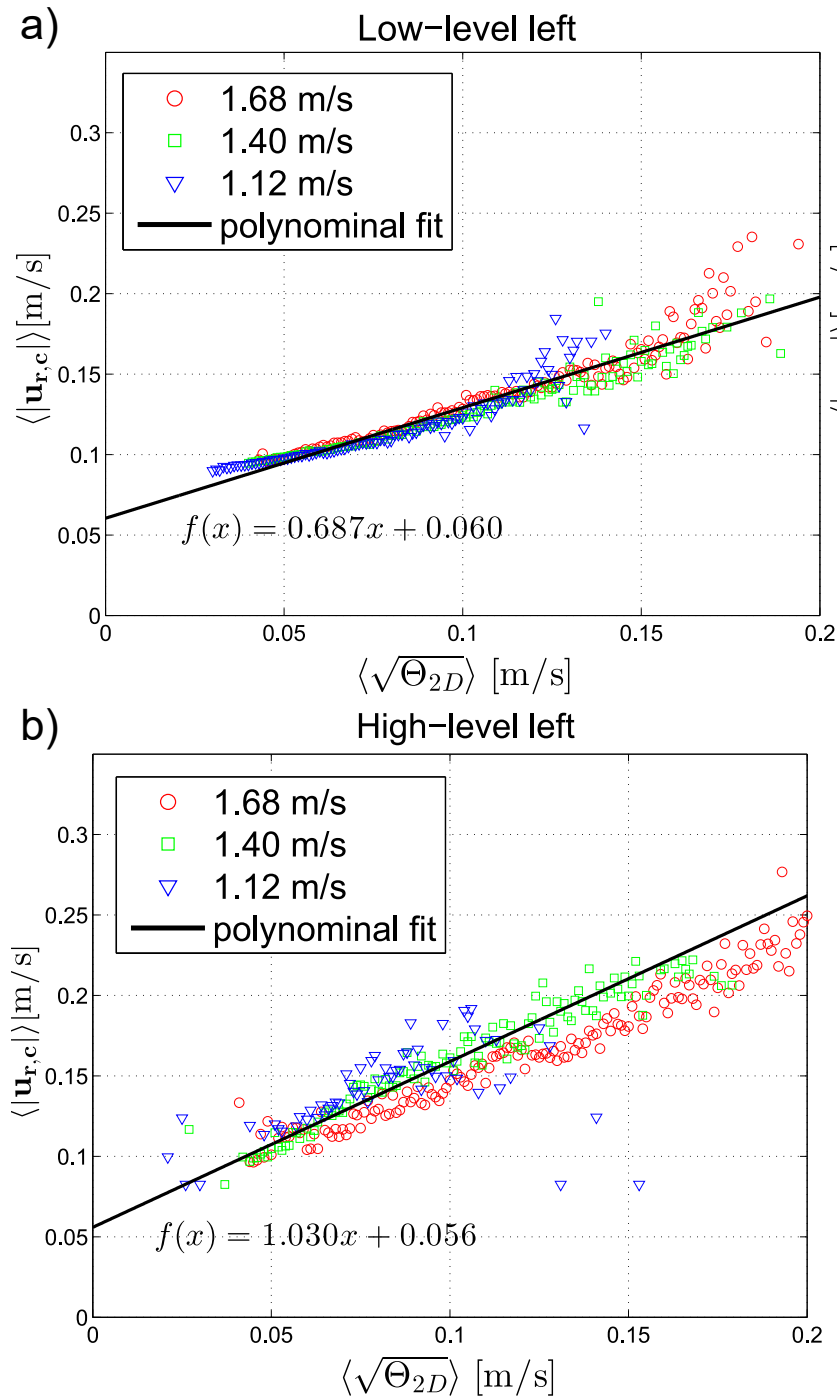
Figure 6.15: Correlations between average square root of 2D granular temperature and average magnitude of impact velocity: a) "low-level left" and b) "high-level left". Curve fits are based on the linear equation: $f(x) = p_1 x + p_2$; and superficial gas velocity does not play a separate role.

for the "high-level". The y-intercepts are very similar for all locations, but the slopes
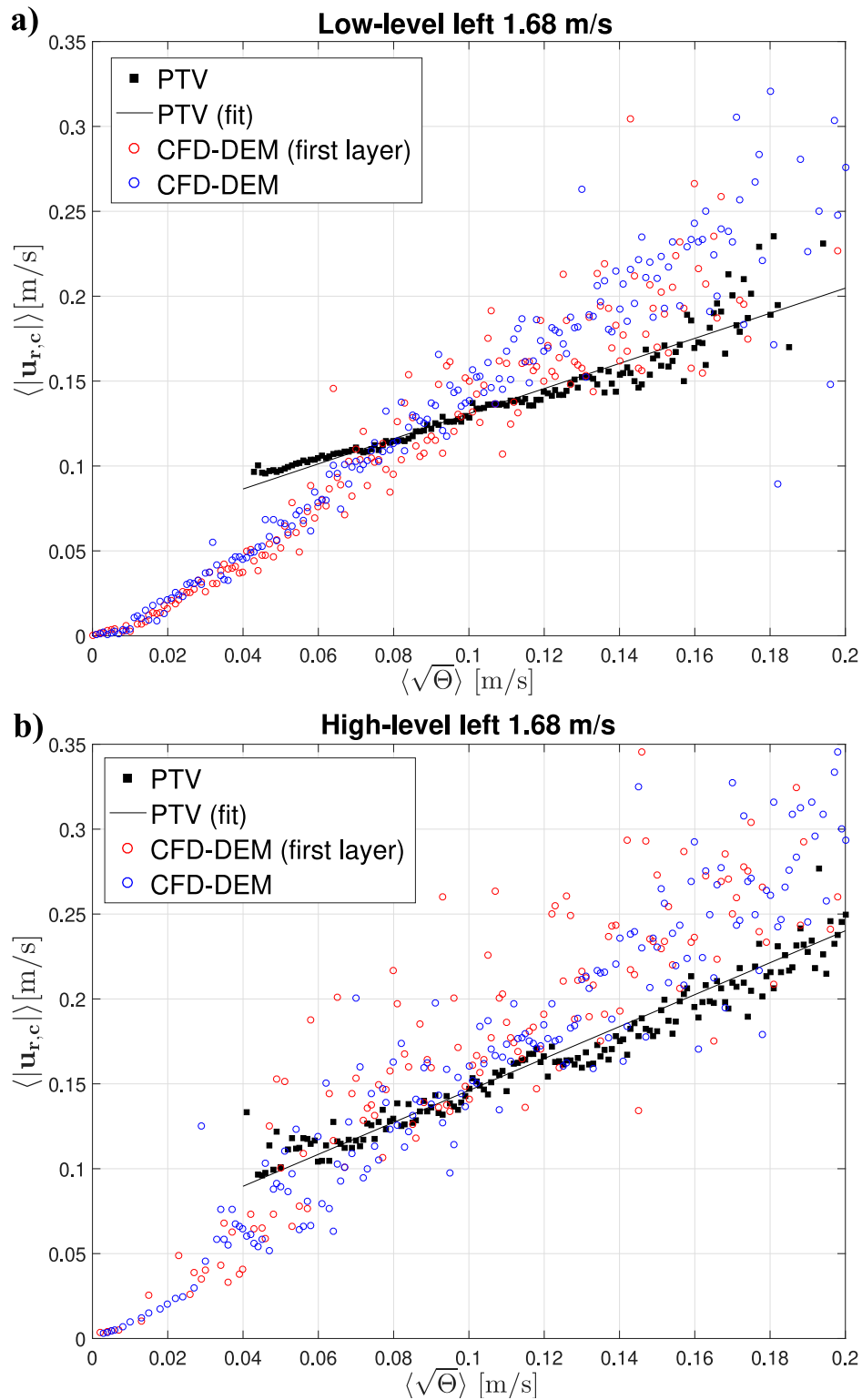
Figure 6.16: Comparison of correlations between average square root of granular temperature and average magnitude of impact velocity obtained from PTV and CFD-DEM.

of the linear fitting for the "low-level" are smaller than those for the "high-level", which can be explained by the fact that particles at the "high-level" have larger mean free paths to achieve stronger particle-particle interactions compared with particles at the "low-level" with the same granular temperature. The fitting parameters can be used to estimate the impact velocity based on the granular temperature.

From the side of CFD-DEM simulations, the impact velocity $\boldsymbol{u}_{r,c}$ equals to the relative velocity of two particles at the first contact instant (as depicted in Figure B.1). Figure 6.16 shows the comparison of relationships between the average square root of 2D granular temperature and the average magnitude of impact velocity obtained from PTV and CFD-DEM (for the "low-level left" and the "high-level left" at 1.68 m/s). Note that the minimum velocity of particles measured by PTV was affected by the scale factor and frame rate of imaging system, resulting in the corresponding shifts of impact velocity and granular temperature from zero. However, these shifts are not existent in results of the CFD-DEM simulation. Generally, the relationships evaluated using the CFD-DEM data in the "first layer" and in the entire bed depth are very similar when only the x and y components of velocity are considered. The simulation data are roughly in accordance with the linear increase observed from the measurement data, but more scattered. The increase of the impact velocity with the granular temperature that is predicted by the CFD-DEM simulations is faster than that measured by the PTV measurements, even though the range of $\langle\sqrt{\Theta_{2D}}\rangle < 0.04$ is not considered. The increase rate of the "high-level left" is faster than that of the "low-level left".

Note that proper scaling-up of experimental data from the laboratory to industrial scales is still challenging due to the inherent scale dependence of many of the essential operating and design parameters. Generally, the scale-up methodology is based on matching dimensionless groups in terms of combinations of the physical properties (such, as particle size and density, fluid density, and fluid viscosity), in order to achieve hydrodynamic similarity when the geometry and the operation conditions are varied in different processes [222]. However, inter-particle forces other than mechanical forces are neglected in the scaling-up. As pointed out by Efhaima and Al-Dahhan [223], the method of matching dimensionless groups is not sufficient to maintain similarity in the local hydrodynamics and particle dynamics according to non-invasive measurement results obtained by radioactive particle tracking and gamma-ray computed tomography. Hence, the scaling-up of the collision frequency and the impact velocity, which are dominated by particle-scale interactions, needs a reliable method, not only considering the similarity of global hydrodynamics, but also identifying key parameters that indicate the similarity of local particle dynamics such as the solid volume fraction and granular temperature.

## 6.4   Summary

In a pseudo-2D fluidized bed, the granular temperature, the collision frequency and the impact velocity were investigated using an optimized PTV method and CFD-DEM. Together with the filter process based on the intensity calibration, the combination

of Voronoi and probability relaxation tracking can simultaneously track thousands of particles with a high average recovery ratio. On the basis of the variations of related particle trajectories, the particle-particle collision events were recognized by a self-developed algorithm. The relative velocity of the pair of involved particles was evaluated to identify real collisions. Key conclusions are:

1. The global particle circulation pattern of slugging flow regime, two reversely symmetric vortices, could be well represented by PTV measurements. The negative effect of large particle velocity in the dilute regions (freeboard, bubbles and slugs) on the evaluation of global motion was avoided using the time-averaged volume flux of particles instead of time-averaged particle velocity. The CFD-DEM simulation can well predict the time-averaged flux of particles.

2. The magnitude and anisotropy of the granular temperature were significantly reduced as the size of investigation region decreased from $45 \cdot d_p$ to $6 \cdot d_p$. Since, the size of investigation region actually reflected the level of influence of macroscopic motions on the particle scale relative velocity. The magnitude and anisotropy of the granular temperature predicted by the CFD-DEM simulation agree with PTV using investigation region (c).

3. Within the range of studied experimental conditions, the average granular temperature increased with the increase in superficial gas velocity at any measurement location regardless of the investigation region size. Hence, the time-averaged fluctuation velocity of particles on both the macroscopic and microscopic scale is essentially dependent on energy input. Moreover, the magnitude of granular temperature depends on the local flow regime, and was larger close to the dense bed surface.

4. Compared with the Gidaspow collision model, there was a significant difference of collision frequency in dense regions for all experimental cases. The experimental average collision frequency tended to be constant or even decrease after exceeding a critical solid volume fraction. It can be postulated that the contribution of increasing of solid volume fraction to facilitate particle-particle interactions is overrated by the restraint of decreasing granular temperature. Critical solid volume fractions depend on the global bubble or slug motion. The average collision frequency evaluated from the CFD-DEM simulation data is lower than that from PTV measurements.

5. The measured average impact velocity could be correlated with the average square root of granular temperature by a simple linear equation. The relationships predicted by CFD-DEM are roughly in accordance with measurement data. The intercept of the correlation was nearly the same for all experimental cases, but the slope increased with increasing distance from the distributor plate, meaning that particles had larger mean free paths.

# Chapter 7

# Color-PTV measurements and CFD-DEM simulations of particle dynamics in poly-disperse particle systems

*This chapter is based on Jiang et al. [45].*

## 7.1 Mixing of poly-disperse system

In Chapter 6, the dynamics of the mono-disperse particle system were investigated by PTV measurment and CFD-DEM simulations. However, poly-disperse systems (with particles of different sizes, different densities, or both different sizes and densities) are commonly encountered in practical applications. As an important phenomenon in poly-disperse fluidization, the segregation of particles strongly influences particle formation processes; for instance, it is essential to guarantee that smaller drug particles can be uniformly blended into larger granules in fluidized bed granulation [224]. Due to their industrial importance, the segregation and the mixing behavior have been experimentally studied using various techniques, such as digital image analysis (DIA) [225, 226], and frozen bed sieving [227, 228]. On the one hand, the segregation state is determined by several competing factors associated with particle dynamics and hydrodynamics, including drag force, turbulence of gas-phase, particle granular temperature and particle collisions [228]. On the other hand, particle dynamics and hydrodynamics are strongly affected by the size-ratio and the density-ratio of different particles. However, published experimental studies on particle dynamics in poly-disperse systems are lacking due to inherent difficulties in measurement, especially in tracking individual particles with different sizes in fluidized beds.

The CFD-DEM approach can capture the majority of macro-scale and micro-scale characteristics of multi-phase flow, simultaneously providing an insight into underlying physics at particle-scale. As mentioned, some aspects that are difficult to be captured in the traditional continuum description of the solid phase by the two-fluid method closed by the kinetic theory of granular flow [60, 140], such as poly-dispersity,

cohesion and non-spherical particles, can be readily incorporated in DEM. With the help of the CFD-DEM approach, the segregation and the mixing behavior in fluidized beds, characterized by the mixing index that indicates the overall segregation state of mixture [225, 229], have been numerically studied and compared with measurements [230–233]. It was found that the drag model for poly-disperse systems is important for the accuracy of predictions of the mixing degree. Beetstra et al. [232] proposed a correction factor, integrated diameter ratio and porosity, based on lattice-Boltzmann simulations, which gives a significant improvement over drag models for mono-disperse systems. Notably, the comparison of mixing index is not enough for the comprehensive validation of CFD-DEM simulations of poly-disperse systems, since particle dynamics are not directly included in the mixing index.

As a well established macroscopic approach to predict particle formation processes, the population balance modeling (PBM) has been widely used in investigations at industrial scale [201, 234, 235]. When mesoscale particle dynamics from CFD-DEM simulations are further integrated with the population balance modeling, a multi-scale model can be created to predict wet particle granulation processes, leading to a better understanding of the effects of process parameters and particle properties on critical quality attributes [236–238]. The performance of the multi-scale coupling approach depends on the accuracy of CFD-DEM simulations of poly-disperse particle systems, which have to be validated not only with regard to segregation (or mixing) behavior, but also to detailed particle dynamics.

The objective of this chapter is to use color-PTV method to study particle dynamics and mixing behavior of poly-disperse systems in a pseudo-2D fluidized bed. The structure is: Section 7.2 illustrates the color classification algorithm. Section 7.3 presents and discusses the color-PTV measurement results of one binary mixture case and one ternary mixture case. Furthermore, detailed comparisons are performed with CFD-DEM simulations using drag models with or without the correction of poly-disperse effect.

## 7.2   Color classification in PTV

The color-PTV experiments and CFD-DEM simulations in the pseudo-2D fluidized bed with poly-disperse particle systems are conducted according to Section 4.3.

Based on the study of Olaofe et al. [226], classification of colored particles in the hue-saturation-value (HSV) space is easier and more accurate compared with classification in the RGB space, because the HSV representation rearranges the geometry of RGB (Cartesian) space to cylindrical-coordinate space in an attempt to be more intuitive and perceptual. Thus, raw images in the RGB space were firstly transformed into the HSV space based on standard function in MATLAB. After space transformation, the intensity in each channel of the HSV space ranged from 0 to unity.

To find the characteristic of each color, statistical analysis of the three HSV channels was conducted in sampling regions with only particles of a single color (red, green or
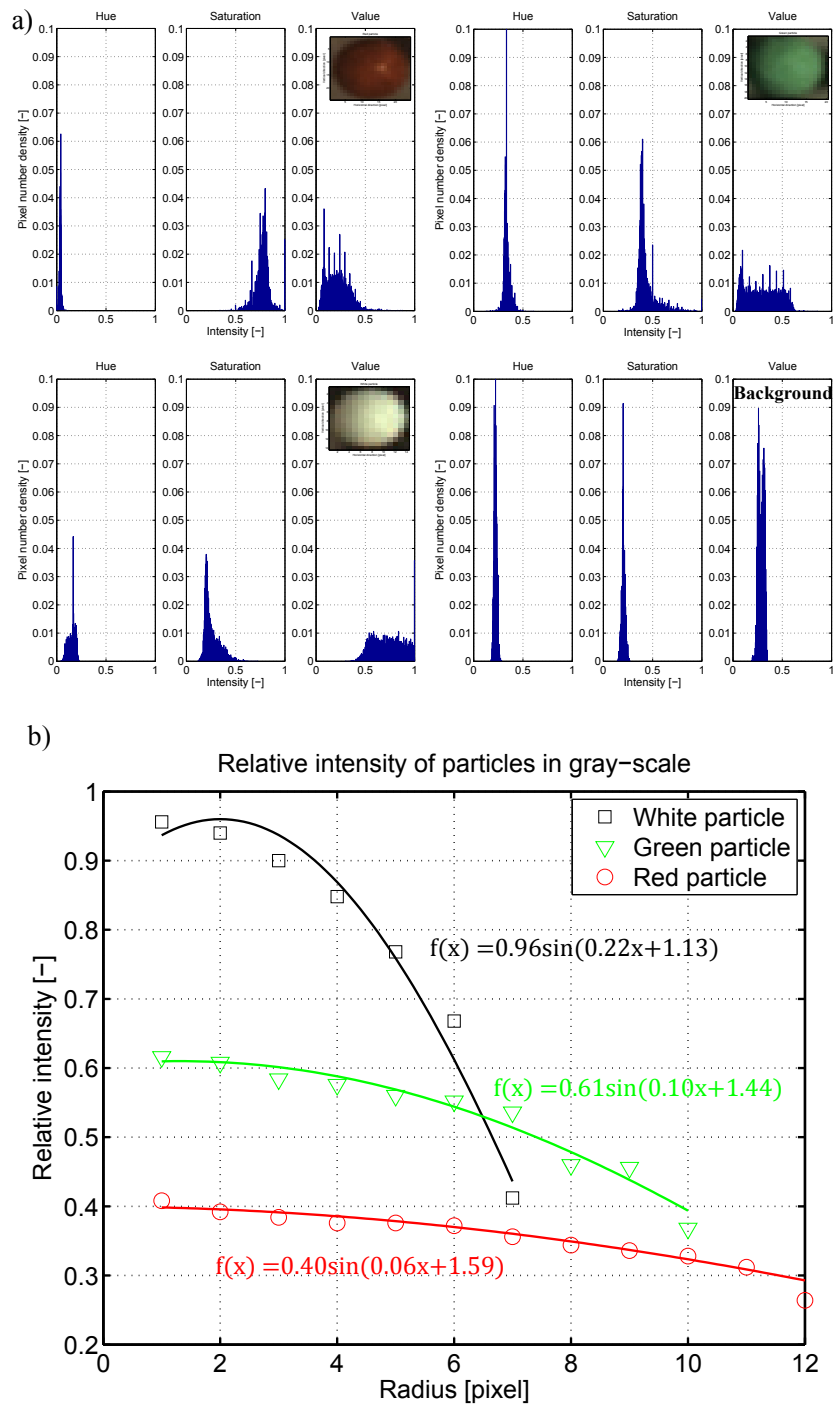
Figure 7.1: The image properties of colored particles: a) histograms of HSV channels for particles of different colors and the background; b) mean intensity distributions in gray-scale space along radii of different color particles (Curve fits are based on the sine equation: $f(x) = a \cdot sin(bx + c)$).

white). In this study, the size of sampling region was $100 \times 100$ pixels, and 10 different sampling regions were manually selected for each color from raw images. A similar approach was applied for the color of the background. Figure 7.1a shows histograms of the three channels of the HSV space for different colors. In each histogram, the vertical axis relates to pixel number density and the horizontal axis is pixel intensity. It can be seen that the intensity peaks of different colors are separated. The criteria of color classification (range of thresholds) used in this chapter are listed in Table 7.1. The color red can be obviously distinguished by the saturation channel (S); whereas the colors green and white can be distinguished by the hue channel (H). Further, the information in the value channel (V) was mainly applied to distinguish the background color. After the color classification, a label matrix was generated to store flags representing four colors for each pixel of a raw image. The label matrix is important to accurately and quickly extract intensity information for different colors in the particle segmentation and tracking process.
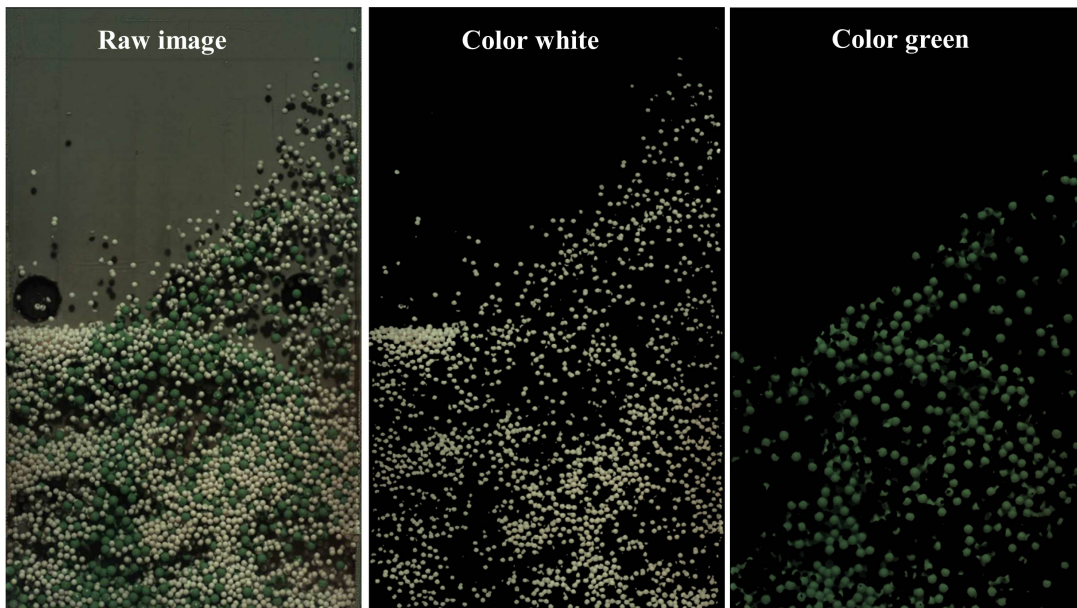


Figure 7.2: Typical example of color classification (*Case 1*), including colors of white, green and background.

Figure 7.2 shows an example for the classification of three relatively similar colors (green, white and background) from *Case 1*, in which pixels belonging to white particles and green particles were respectively extracted from the raw image using the label matrix. Obviously, different colors are successfully distinguished and shapes of particles are completely retained based on the criteria spans, which is favorable to the segmentation process using particle-mask correlation method (Section 2.1). After particle segmentation, the pairing of identical particles can be achieved by the integrated

particle tracking method (Section 2.2). The detailed parameters related to PTV are listed in Table 7.1.

Table 7.1: Main parameters used in Color-PTV method.

| Parameter | Value | Unit |
|---|---|---|
| *Color classification method* | | |
| *Thresholds of pixel intensity in three channels (H: hue, S: saturation, V: value)* | | |
| Red | $H \in (0, 0.1), S \in (0.5, 1), V \in (0, 0.5)$ | — |
| Green | $H \in (0.25, 0.5), S \in (0.2, 0.5), V \in (0, 0.6)$ | — |
| White | $H \in (0, 0.2), S \in (0.2, 0.5), V \in (0.5, 1)$ | — |
| Background | $H \in (0.1, 0.25), S \in (0.1, 0.25), V \in (0.1, 0.3)$ | — |
| *Particle segmentation method* | | |
| Template particle size | $\sqrt{2} \cdot d_p \cdot S_f / 2$ | pixel |
| *Voronoi tracking method* | | |
| Maximum displacement radius | $U_g/2 \cdot S_f \cdot \Delta t$ | pixel |
| *Relaxation probability method* | | |
| Maximum displacement radius | $U_g/2 \cdot S_f \cdot \Delta t$ | pixel |
| Neighboring radius | $0.5 \cdot U_g \cdot S_f \cdot \Delta t$ | pixel |
| Quasi-rigidity radius | $0.1 \cdot U_g \cdot S_f \cdot \Delta t$ | pixel |
| constant A | 0.3 | — |
| constant B | 4.0 | — |
| iteration steps | 50 | — |
| Threshold matching probability | 0.95 | — |

$\Delta t$ is 1 ms according to the frame rate of the imaging system.

## 7.3 Results and discussion

We will present results from color-PTV measurements of *Case 1* (binary mixture) and *Case 2* (ternary mixture), in form of the time-averaged particle volumetric flux, distributions of individual particle velocity, distributions of particle granular temperature and the mixing index. In addition, comparisons with CFD-DEM simulations using two drag models: 1) poly-disperse Beetstra drag model (PBVK) with the correction for poly-dispersity (Eq. (3.37)), and 2) mono-disperse Beetstra drag model (MBVK) without correction (Eq. (3.33)), will be conducted.

It is noted that only particles in the first layer were extracted from simulation data to be close to pseudo-2D conditions of measurements. Specifically, the normal distances from the centers of particles to the front wall were smaller than 3 mm. On the basis of visual observations, the flow in both investigated cases can be assigned to the slugging regime, with separated slugs (bullet-shaped voids) and bubbles filling the entire cross-section of the pseudo-2D fluidized bed. Turbulent fluidization flow regime was not observed in either of the two cases.

## 7.3.1    Particle volumetric flux

As discussed in Chapter 6, the time-averaged particle velocity profiles can be spurious to describe particle circulation pattern, because the contribution of few particles with really high velocity to the global motion of particles is overestimated in the dilute region. Therefore, the volumetric flux of particles, i.e. the volume flow rate per unit area $m^3/(m^2 \cdot s)$, was evaluated to accurately reveal the global particle circulation motion. With regard to PTV measurements, the volumetric flux of particles was calculated by the product of solid volume fraction and average particle velocity in each investigation region. The size and arrangement of investigation regions is the same as in the verification study.

The size of CFD grid may affect the mapping and evaluation of solid volume fraction field and the numerical solution of turbulent gas flow with solid particles. Clearly, grid independence needs to be established, before one can conduct the qualitative or quantitative analysis of CFD-DEM simulations in confidence.

The study of grid independence was performed using the drag model with correction for size dispersity in *Case 1*. Figure 7.3a shows the time-averaged particle volumetic flux profiles over 5 s from the measurement and simulations with three sets of CFD grid. The data points are averaged from investigation regions in a height range of 450 to 525 pixels and are assigned to the right boundary of the investigation region in the $x$ axis. The simulations with three different grid sizes predict almost the same profiles of volumetric particle flux in both the vertical and the horizontal direction. Therefore, the CFD grid with size ratio $d_{cell}/d_{32}$ of 2.3 was used together with the "divided" void-fraction approach in this study.

Figure 7.3c shows the results of time-averaged particle circulation for *Case 1*, and the vector for time-averaged particle volumetric flux is assigned to the bottom right corner of each investigation region. Obviously, two nearly symmetric vortices can be observed in the results of both the experiment and the simulation (using Eq. (3.37)), which implies that 5 s time is enough to investigate the circulation motion in this pseudo-2D fluidized bed. Only minor difference exists between the heights of the centers of the two vortices obtained from the experiment and the simulation. The center of the left hand-side vortex is located at a height of about 240 pixels, and the center of the right hand-side vortex is located at about 220 pixels. The top boundary of the two vortices starts to form at a height of about 450 pixels, which is also the stably fluctuating height of the dense bed surface. Bubbles or slugs erupt at this surface, accelerating particles into the freeboard and resulting in horizontal transport towards the side walls. Globally, particles are transported upwards in the center of bed and slide downwards close the side walls, which is associated with the inception, coalescence and eruption of traveling bubbles or slugs at different heights of the fluidized bed. However, it is important to note that instantaneous flow patterns may differ significantly from the time-averaged circulation pattern due to the strongly chaotic motion of bubbles and particles. This result for particle circulation is very similar to published observations for mono-disperse systems using PIV and PTV measurements [104, 158, 214] and results in Chapter 6.
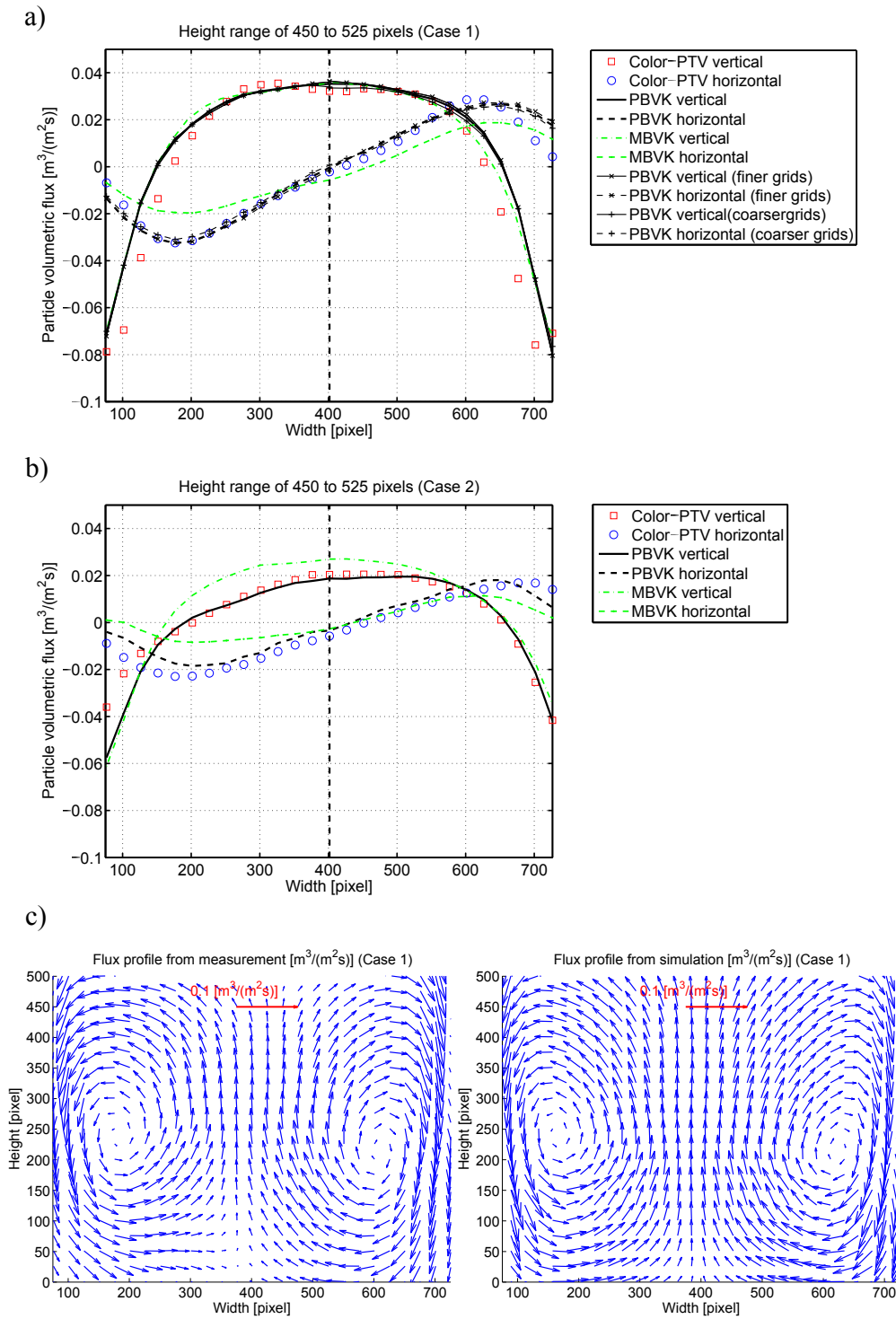
Figure 7.3: Time-averaged particle volumetric flux: a) profiles in vertical and horizontal directions for *Case 1* at a height range of 450 to 525 pixels, together with the results of grid independence study for three CFD grids, b) profiles for *Case 2* at a height range of 450 to 525 pixels and c) global circulation patterns for *Case 1* from the experiment and the simulation (Eq. (3.37)).

The global particle circulation for *Case 2* also shows two nearly symmetric vortices, but their centers were located lower compared to *Case 1* (not shown in the figure).

The results from PBVK and MBVK in Figure 7.3a show that the accuracy of simulation is improved by correction for size poly-dispersity, especially in the horizontal direction. Obviously, the simulation using MBVK underestimates the horizontal transport of particles due to eruptions of bubbles or slugs near the dense bed surface. In this context, it should be noted that the height range of 450 to 525 pixels was somewhat higher than the upper surface of the fluidized bed. The variation trend in the horizontal direction of all methods indicates the approximate reflection symmetry of the two vortices. However, the simulation with MBVK underestimates the motion of particles sliding downwards the side walls. As shown in Figure 7.3b, the general shapes of profiles are similar with *Case 1*. The decrease of particle volumetric fluxes in both horizontal and vertical directions was caused by the reduction of height of the two vortices.

## 7.3.2   Distributions of velocity and granular temperature

The superiority of color-PTV measurement lies in its ability to reconstruct instantaneous velocities of particles with different sizes. Hence, comparisons of density distributions of the individual velocities of particles with different sizes were performed in both vertical and horizontal directions, as shown in Figure 7.4. The density distributions were evaluated by particles appearing at heights ranging from 450 to 525 pixels at all time steps. The total number of time steps is 5000 for both experiments and simulations. From the measurement results, the transport of all particles in the vertical direction is stronger than that in the horizontal direction at this bed height. The density distributions are approximately symmetric with respect to the vertical center line. In this height range, the velocities of small particles are slightly larger than those of large particles in the vertical direction; and, inversely, the velocities of small particles are slightly lower in horizontal direction. The differences of particle velocities in both vertical and horizontal directions are relatively small at this height range, compared with the profiles of volumetric flux in Figure 7.3a and Figure 7.3b. Most of results from simulations using PBVK are more conform to the measurement results, compared with the drag model without correction for the effect of size poly-dispersity. This correction improved the agreement with measurement results by avoiding the over-estimation of drag force for small particles and the under-estimation of drag force for large particles.

On the basis of Eqs. (6.5) to (6.7) the color-PTV measurement can also provide distinguishable information about particle granular temperature for particles with different sizes. The particle granular temperature corresponds to the relative velocity of particles that may drive diffusive mixing and particle collisions. Figure 7.5a shows the comparison of cumulative distributions of the square root of particle granular temperature of different particles for *Case 1*. Different to Figure 7.4, the cumulative distributions were obtained from all investigation regions in the field of view at all time steps. According to the color-PTV measurement, the granular temperature of small particles is higher than that of large particles. Compared to the result from MBVK, the correction for size
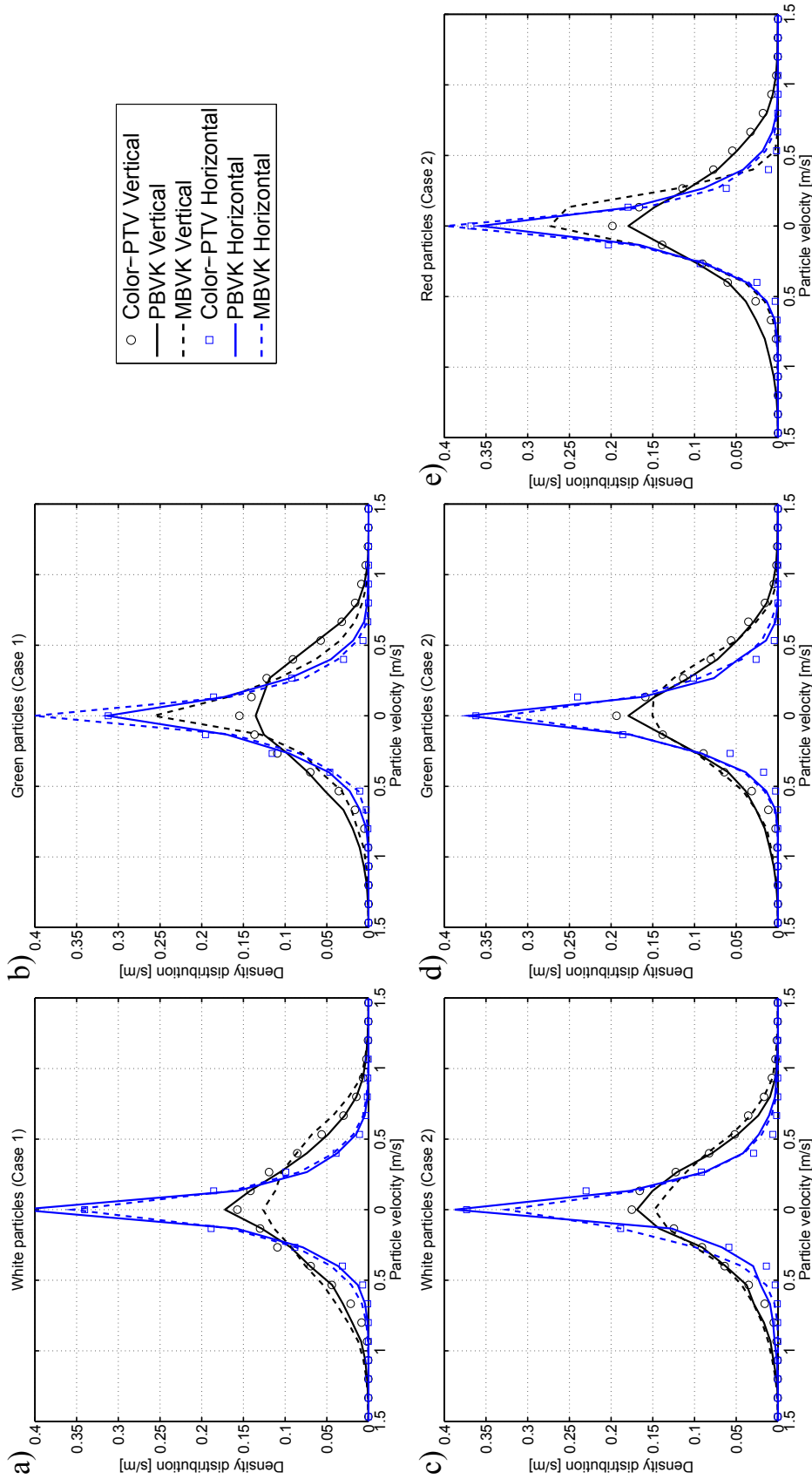
Figure 7.4: Comparisons of density distributions of the individual particle velocity (including vertical and horizontal directions) at a height range of 450 to 525 pixels: a) white particles of *Case 1*, b) green particles of *Case 1*; c) white particles of *Case 2*, d) green particles of *Case 2* and e) red particles of *Case 2*.
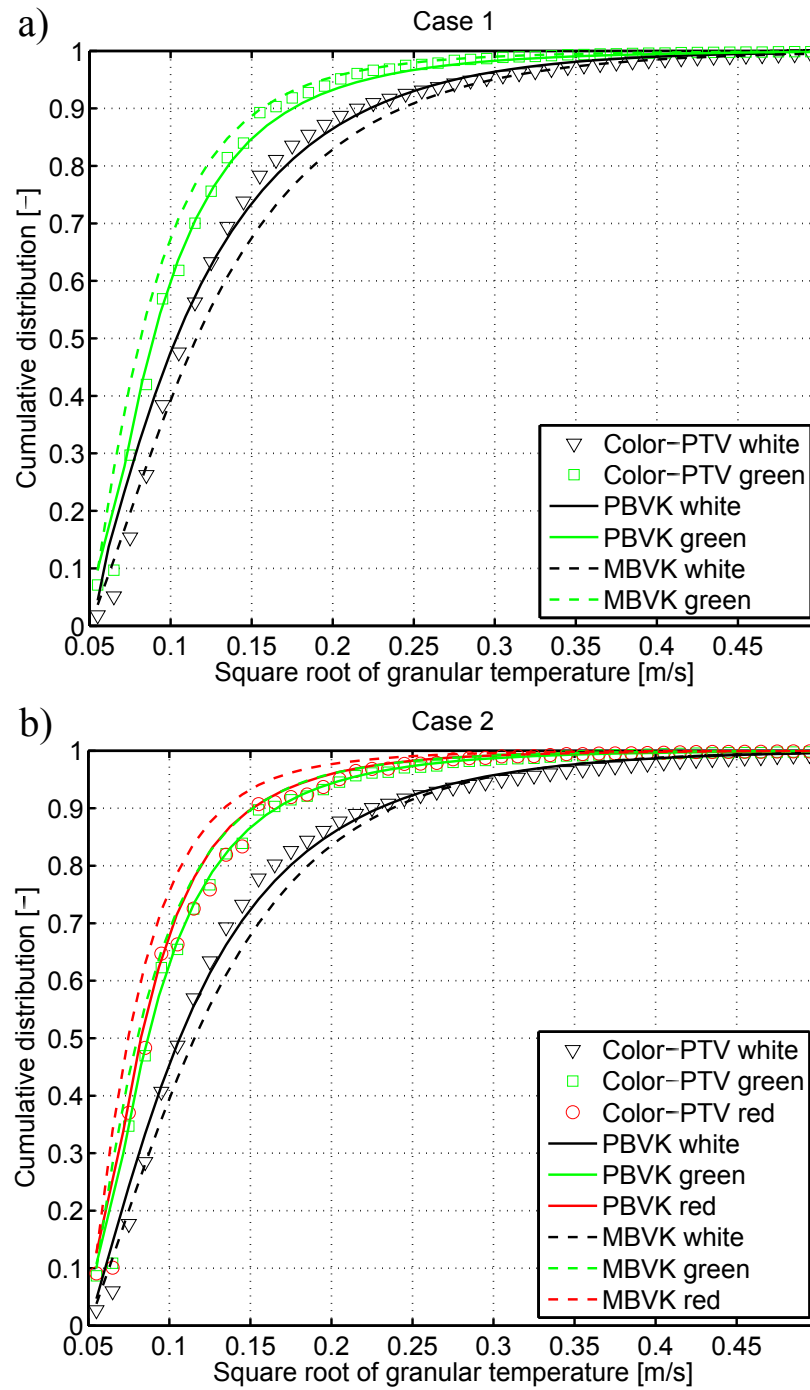
Figure 7.5: Comparisons of cumulative distributions of the square root of granular temperature for different classes of particles in the entire field of view: a) white and green particles for *Case 1* and b) white, green and red particles for *Case 2*.

dispersity reduces the difference between the curves for small and large particles, which is in good accordance with measurement data. Figure 7.5b shows the results for *Case 2*. The experimental data for red and green particles almost coincide. The prediction using PBVK is, again, better than that with MBVK.

### 7.3.3 Mixing behavior

In this chapter, the mixing degree of particles was investigated by the improved Lacey index that was proposed by Feng et al. [231]. This index is based on the statistical analysis of variances of volume fraction of different particles in different samples, which can be given as

$$M = \frac{S_0^2 - S^2}{S_0^2 - S_r^2}, \tag{7.1}$$

where $S^2$ is the actual variance; $S_0^2 = P_s(1 - P_s)$ and $S_r^2 = P_s(1 - P_s)/N_e$, respectively, represented the variances for the completely segregated state (maximum) and the well mixed state (minimum). The variable $P_s$ is the global volume fraction of the smallest particles in a mixture. The original index was used for mono-disperse systems [229]. In the poly-disperse system, the concept of the equivalent number $N_e$ is used. To keep the same total particle volume in the sample, the equivalent number $N_e$ can be evaluated based on the number of particles in each size class and the corresponding ratio of the volume of single particle in this size class to the volume of single smallest particle. The size of the sample is fixed, while the contribution of the sample to the variance $S^2$ is weighted according to the equivalent number of particles. If $c_i$ is defined as the volume fraction of the smallest particles in each sample $i$ and $N_s$ is the number of samples, the variance $S^2$ can be expressed as

$$S^2 = \frac{1}{k_t} \sum_{i=1}^{N_s} k_{s,i} \cdot (c_i - P_s)^2, \tag{7.2}$$

$$k_t = \sum_{i=1}^{N_s} k_{s,i} \tag{7.3}$$

where $k_{s,i}$ is the weighting factor in the sample $i$ and $k_t$ is the total weighting factor. $k_{s,i}$ can be calculated as the ratio of the equivalent number of particles in the sample $i$ to the maximum equivalent number of particles for all samples at each time step ($N_{e,i}/N_{e,max}$). The mixing index obtained from Equation (7.1) is by definition zero for a completely segregated mixture and increases to unity for a fully random mixture.

Based on a sensitivity study, sample size was set equal to the size of the investigation region, which can satisfy the conditions that the mixing index should be close to one for the well-mixed state and close to zero for the fully segregated state. However, due to interlaced arrangements in the interface of different layers of particles, the mixing indices in the initial states of both the measurement and the simulation are slightly larger than zero in the results, as shown in Figure 7.6. The maximum mixing index is
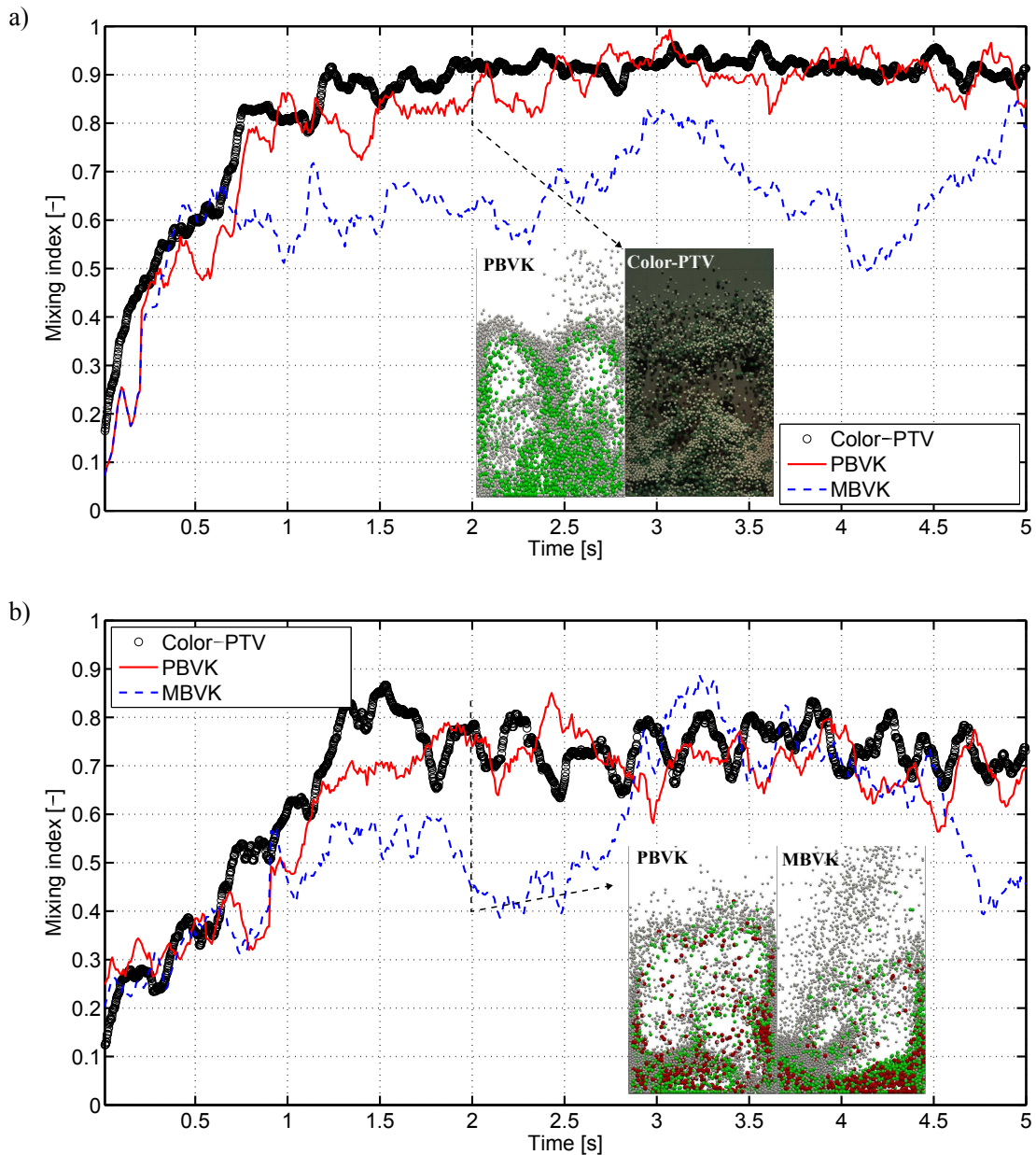
a)



b)



Figure 7.6: Comparisons of mixing index: a) *Case 1*, and b) *Case 2* (snapshots at 2 s are included to visualize characteristic results of the different methods).

lower than unity, meaning that the perfect mixing state cannot be reached under the measurement conditions.

Figure 7.6a shows comparisons of mixing index for *Case 1* in the time period from zero to 5 s. According to the color-PTV measurement, the mixing index gradually increases from 0.15 to an equilibrium state with a mean value of approximately 0.9. The duration of the increasing stage of mixing index is approximately 1.5 s. After that, the maximum

fluctuation of mixing index remains within 0.1. The simulation using PBVK predicts qualitatively and quantitative comparable results with the color-PTV experiment. The inserted snapshots from color-PTV and CFD-DEM with PBVK at time 2 s show the particle distributions at the corresponding mixing indices. The simulation using MBVK gives relatively large deviations of both, the mean value and the fluctuations of mixing index, especially after the increasing mixedness stage. Compared with the cumulative distribution of the square root of particle granular temperature (Figure 7.5a), the large difference of particle granular temperature between small and large particles by MBVK implied strong relative motions between particles of different sizes, resulting in the decrease and the fluctuation of mixing index.

For *Case 2*, red particles and green particles were considered as one component when calculating the volume fraction of white particles in the mixture. As shown in Figure 7.6b, the final mixing state for *Case 2* is much different from that of *Case 1*, although they have very similar initial bed height, Sauter mean diameter, bed mass, and the same superficial gas velocity. According to the color-PTV measurement, the mean value of mixing index after 1.5 s is approximately 0.75; and the maximum spread is larger than 0.2. The final mixing index is, thus, affected by the initial packing state. The ternary system is more difficult to be brought and kept at a relatively stable equilibrium than the binary system under the same fluidization conditions. The simulation using PBVK still shows better performance than that based on MBVK. As shown in the snapshot for MBVK, it is difficult for small particles to enter into and stay in the void space between large particles in the corresponding CFD-DEM, leading to the under-estimation and the large fluctuation of the mixing index.

**Chapter 8**

# CFD-DEM study of the particle behavior in a Wurster fluidized bed

*This chapter is based on Jiang et al. [120].*

## 8.1 Wurster fluidized bed

Particle coating is widely applied in the pharmaceutical, food, cosmetic, and fertilizer industry. As an efficient device for film coating of particles, the Wurster coater has been commonly used as a batch or continuous fluidized bed to precisely coat pellets and tablets (deposit drug substances or functional films on particles) in pharmaceutical industries [6, 165, 239].

During a typical coating process in batch Wurster fluidized beds, coating material is atomized into droplets by a two-fluid nozzle located on the distributor plate under the bottom of the Wurster tube. Particles are wetted by the droplets in the spray zone and dried when subsequently passing the Wurster tube, fountain zone, down bed and horizontal zone (as illustrated in Figure 8.1). Single circulation is accomplished when particles enter to the spray zone again through the partition gap, which is repeated until the desirable total amount of coating material has been deposited on the particles. Indeed, the individual particle spends its time in various regions with different solid volume fraction, moisture content and temperature, which are influenced by the combined effects of the motion of gas and the spray of coating material. Moreover, particle-particle or particle-wall collisions sometimes generate non-ideal circulations (recirculation) in the Wurster tube, which considerably affect the individual particle residence time and cycle time.

The mass of coating material received by an individual particle in each cycle plays a critical role in achieving a stable particle formation process and the required coating thickness, which is closely associated with the residence time of the particle in the spray zone [29, 240]. While particles pass through the spray zone, the distance to the spray nozzle and the particle-to-particle sheltering effect are also considered to influence the mass of coating per cycle [29, 241]. In addition, the cycle time of the

particle determines the total amount of obtained coating material, but contributes less to the coating uniformity compared with the mass of coating per cycle [240, 242]. From another point of view, the agglomeration of particles should be avoided in the coating process to achieve high product quality.

Due to the industrial significance of particle circulation behavior and spray characteristics in coating processes, there have been some experimental investigations of these quantities in different configurations. Shelukar et al. [240] and Cheng and Turton [242] applied magnetic particle tracking (MPT) to measure particle circle time in Wurster coaters. Further, Shelukar et al. [240] measured the coating per cycle by a dye tracing technique. Depypere et al. [243] used positron emission particle tracking (PEPT) to visualize the circulating motion of particles in a Wurster coater. With the same technique, Li et al. [27] studied the cycle time and the residence time of poly-disperse particles in a laboratory-scale Wurster coater. Note that only a single tracer particle is used in the MPT and PEPT measurements [244]. Thus, it is essential to benefit from the principle of ergodicity in the probability theory for processing the particle residence time distribution (RTD) and the particle cycle time distribution (CTD), which is required for Monte Carlo modeling [29] or population balance modeling [6, 245] of the Wurster coating process. Börner et al. [28] used conductivity probes to map the boundaries of the spray zone in top-spray fluidized beds. The cycle time and residence time distributions in different zones were estimated combining particle imaging velocimetry and digital image analysis technologies.

Nevertheless, it is very difficult to directly measure the spray characteristics and residence time distributions in different processing zones. Conversely, the CFD-DEM simulation approach has great potential to evaluate residence time and even the particle collision dynamics in different zones. Fries et al. [91] investigated particle collision dynamics in different processing zones of a top-spray fluidized bed, Wurster coater and spouted bed using CFD-DEM simulations. Hilton et al. [99] developed an approach to model particle motion and gas flow by CFD-DEM simulation, and mapped Stokesian solid-like droplets on individual particles based on the spherical harmonic formulation, which can be used to predict the coating quality at the intra-particle level. Li et al. [93] used CFD-DEM simulation to estimate the cycle time and residence time distributions in a Wurster coater corresponding to the PEPT experiments [27].

The main objective of this chapter is to evaluate the particle residence time distribution, the particle cycle time distribution, and the particle collision velocity in a binary (two different particle sizes) Wurster coater by the CFD-DEM simulation. In order to validate the simulation, the geometry of the Wurster coater and operation conditions follow the experimental work of Li et al. [27]. The details of simulation setup are given in Section 4.4.1. Different from the simulations of Li et al. [93], solid-like droplets are included in the simulation to directly investigate the droplet deposition rate in the spray zone, which implies the coating-per-cycle characteristic. Moreover, the ideal and the non-ideal cycles are distinguished to analyze the particle circulating time distribution. Accurate results from the CFD-DEM simulation will help optimiza-

tion of macroscopic modeling, including drying, and provide a more reliable prediction of the particle formation process in Wurster coaters.

## 8.2 Results and discussion

### 8.2.1 Cycle time and residence time distribution

As shown in Figure 8.1, the global circulating flow in the Wurster coater is that particles move upwards into the tube from the spray zone, lose momentum in the fountain zone, fall downwards into the external annulus (down bed), are transported in the horizontal zone in plug flow manner, and re-enter the spray zone through the partition gap at the bottom of the internal annulus. Note that droplets only exist in the predefined spray zone in the simulation. In other words, particles can only receive coating material in
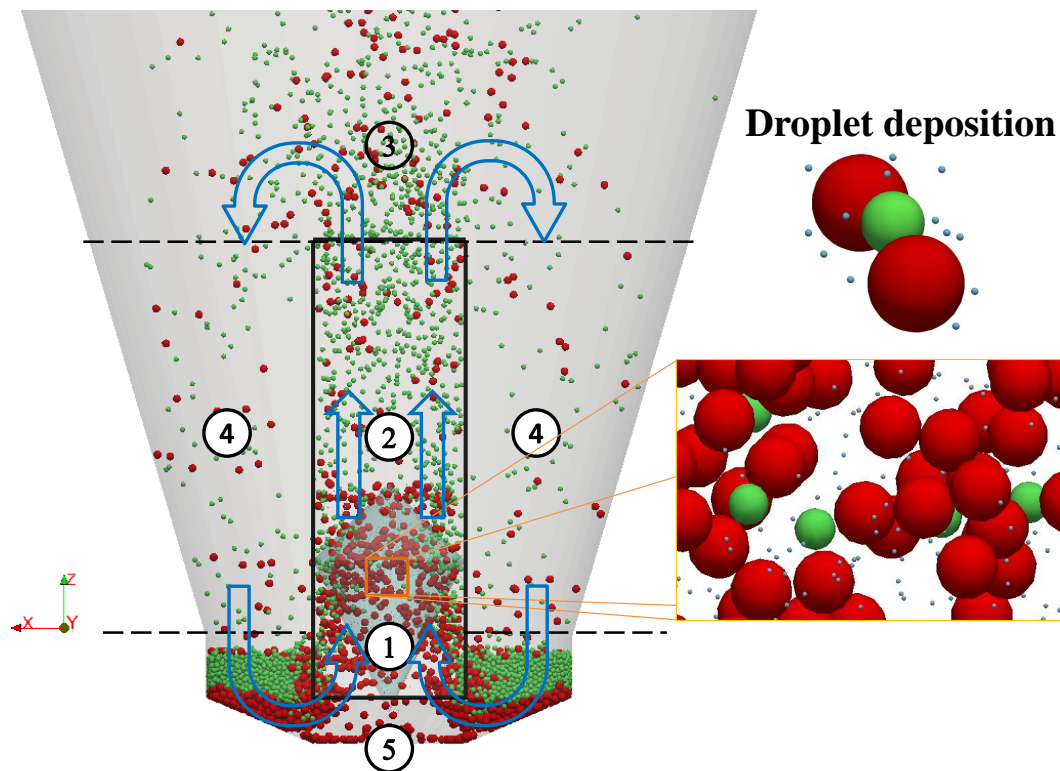


Figure 8.1: Snapshot representing the global circulating flow of particles (large particles colored by red and small particles colored by green) in the Wurster coater, which is divided into (1) Spray zone; (2) Wurster tube; (3) Fountain zone (only part of fountain zone depicted for a better visualization); (4) Down bed; and (5) Horizontal zone. The droplets (colored by blue) are injected into the pre-defined spray zone for the evaluation of droplet deposition characteristics.

the spray zone. However, recirculation of particles may occur when particles recirculate within the Wurster tube without having passed through the down bed zone. When a cycle does not have any recirculation, it is defined as an ideal cycle by Li et al. [27]; otherwise it is a non-ideal cycle.

The trajectory of a sample particle from the CFD-DEM simulation is illustrated in Figure 8.2a. On the one hand, when blue crosses are higher than the tube height, particles move into the fountain zone. On the other hand, when red circles are lower than the tube radius, particles travel into the Wurster tube. In order to distinguish ideal and non-ideal cycles, the location of each particle in each time step of 0.01 s was labeled with a zone number (as shown in Figure 8.1) in the post-processing of CFD-DEM simulation data. The identification of an ideal cycle is relatively simple, in which the particles travel through zone 1 to zone 5 in this order without any recirculation, as shown in the left side of Figure 8.2b. To identify non-ideal cycles, three types of recirculation in the Wurster tube must be first clearly defined: a) the particle falls to the Wurster tube from the fountain zone (zone 3 to zone 2 in the trajectory); b) the particle re-enters into the spray zone from the Wurster tube (zone 2 to zone 1 in the trajectory); c) the particle moves backward to the horizontal transport zone from the spray zone (zone 1 to zone 5 in the trajectory). As an example, the right-hand side of Figure 8.2b represents the recirculation type b). Apparently, the appearance of the recirculation increases the risk of particle agglomeration and gives a broader film thickness distribution. Compared to the PEPT measurements without the spray zone [27], the two definitions of recirculation are not exactly the same but comparable. In a non-ideal cycle of this study, the particle experiences one or more recirculations before completing an entire circulation that includes all five zones. Further, the cycle times and the residence times in different zones can be evaluated based on the numbers of zone labels. The cycle times of ideal and non-ideal cycles are denoted by $t_{ic}$ and $t_{nc}$, respectively. The overall cycle time (including both ideal and non-ideal cycles) is denoted by $t_c$. In the ideal cycle of Figure 8.2b, the sample particle slides continually along the Wurster tube in the horizontal zone and enters the spray zone from the lower edge of the tube, which leads to a short cycle time. Sometimes, however, particles slide along the chamber wall and spend a longer time in the horizontal transport zone, which obviously results in a longer cycle time. Therefore, the cycle time distribution is considerably influenced by the ratio of ideal and non-ideal cycles and the detailed flow behavior in each cycle.

Based on the analysis of ideal cycles of all 32400 particles from 5 s to 30 s, the cumulative distribution of ideal cycle time $t_{ic}$ has been obtained for both large and small particles, as depicted in Figure 8.3. From the cumulative distribution curve, the median ideal cycle time of large particles is 2.95 s, shorter than 3.31 s of small particles. The relative spans of the ideal cycle time $((t_{ic,90} - t_{ic,10})/t_{ic,50})$ are 0.94 and 0.91 for large and small particles, respectively. In the experimental work of Li et al. [27], the mean value and the coefficient of variation (CV) were used to represent the characteristics of ideal cycle time distribution and overall cycle time distribution. The comparison of results for mean ideal cycle time $\bar{t}_{ic}$ and mean overall cycle time $\bar{t}_c$, together with the corresponding
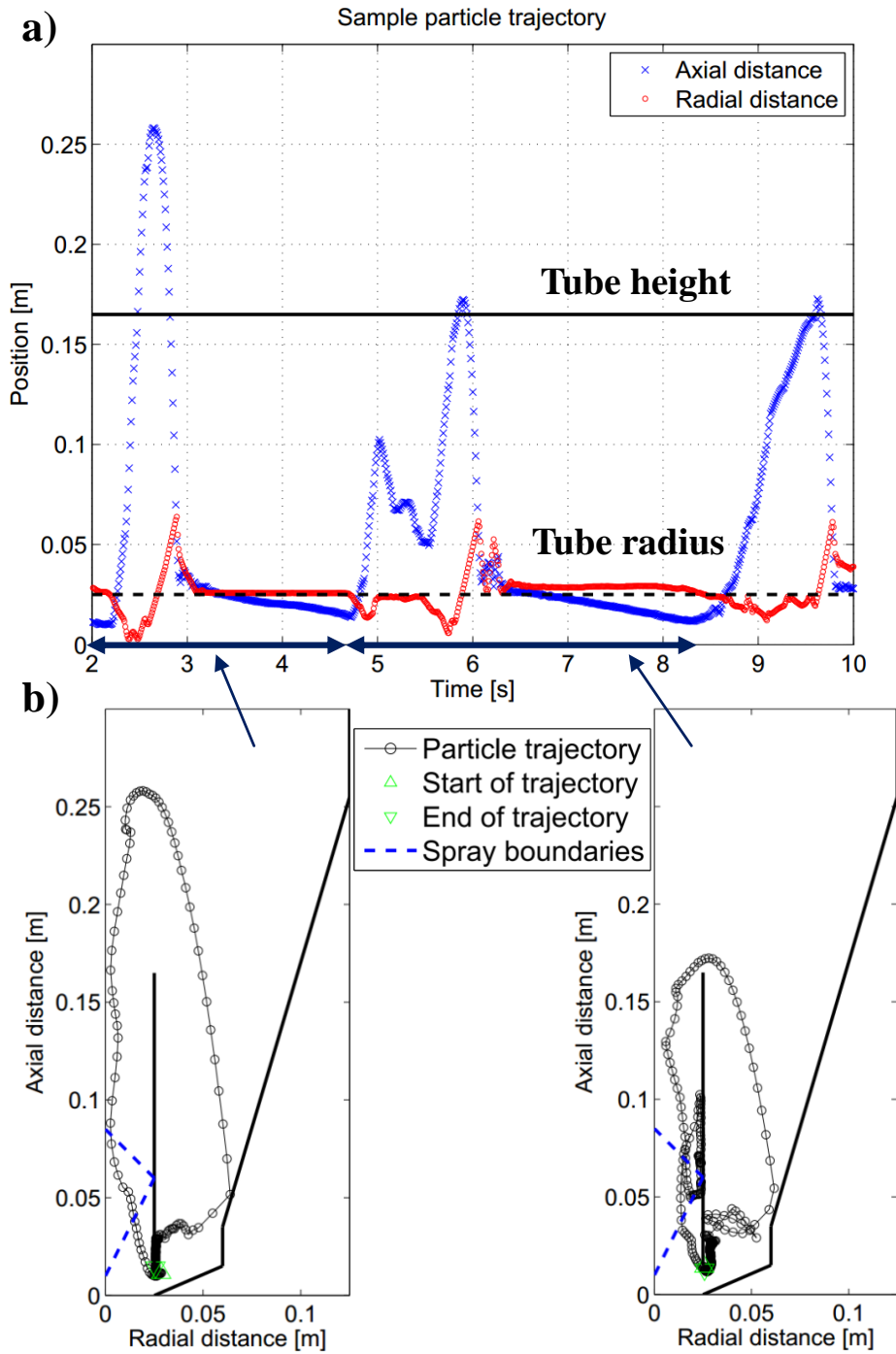
Figure 8.2: Sample particle trajectory: a) axial distance (blue crosses) and radial distance (red circles) with respect to time; b) ideal cycle (left) and non-ideal cycle (right) in subsequent time ranges (the spray zone is located inside the blue dashed lines).
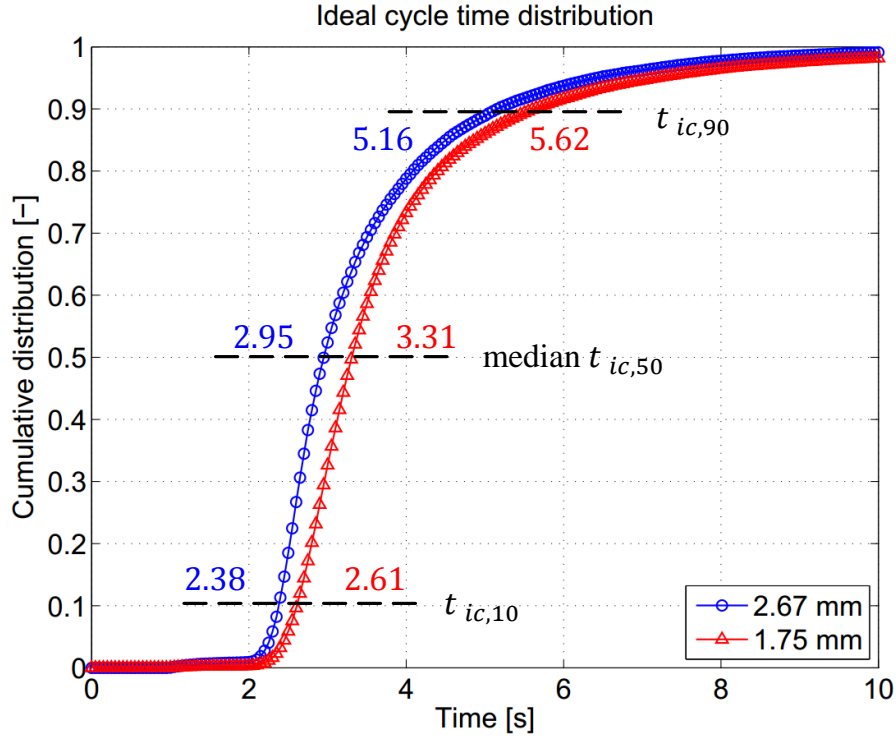
Figure 8.3: Cumulative distributions of ideal cycle time for large and small particles.

Table 8.1: Comparison of ideal cycle time and overall cycle time distributions.

| Variable | CFD-DEM | | PEPT [27] | |
|---|---|---|---|---|
| | small | large | small | large |
| $\bar{t}_{ic}$ [s] | 3.46 | 3.09 | 3.22 | 2.74 |
| $CV(t_{ic})$ [%] | 38.9 | 44.8 | 50.5 | 44.3 |
| $\bar{t}_c$ [s] | 4.32 | 5.18 | 4.95 | 5.95 |
| $CV(t_c)$ [%] | 62.2 | 83.1 | 73.0 | 96.3 |
| $r_n$ [%] | 72.3 | 53.1 | 46.9 | 33.1 |

$\bar{t}_{ic} = \sum_j^{N_{ic}} t_{ic,j}/N_{ic}$, $N_{ic}$ is total number of ideal cycles, $t_{ic,j}$ is time of each ideal cycle.

$\bar{t}_c = \sum_j^{N_c} t_{c,j}/N_c$, $N_c$ is total number of cycles, $t_{ic,j}$ is time of each cycle.

CVs are listed in Table 8.1. There is a good agreement with the PEPT measurements in terms of mean ideal cycle time and the corresponding coefficient of variation for both sizes. However, some discrepancies in the number ratio of ideal cycles to total cycles $r_n$ exist. Obviously, the CFD-DEM simulation underestimates the number of non-ideal cycles for both large and small particles. Further research on the possible reasons requires more information about particle-particle and particle-wall interactions from both CFD-DEM simulation and PEPT measurements. Nevertheless, the number ratio $r_n$ for small particles is higher than that for large particles in both simulation and

experiment, which results in a longer mean cycle time of large particles. Meanwhile, the high coefficients of variation of overall cycle time imply broad distributions of cycle time, which are undesirable to reach uniformity in the coating product.

Based on the length of trajectory (number of zone labels) within the spray zone and the Wurster tube zone of each cycle, the residence time distributions can be evaluated and compared to the PEPT measurements and the simulations of Li et al. [93]; the results are listed in Table 8.2. Our simulation predicts well the mean residence time in the Wurster tube $\bar{t}_{r,t}$ for both small and large particles. Note that the residence time in the Wurster tube also has a large coefficient of variation, due to the influence of the recirculation. In terms of the residence time in the spray zone, the mean values of $\bar{t}_{r,s}$ for both small and large particles are shorter than those of Li et al. [93], in other words, the mean particle velocities in the spray zone of our simulation are somewhat higher.

Table 8.2: Comparison of residence time distributions in the spray zone and the Wurster tube.

| Variable | CFD-DEM | | PEPT Li et al. [27] | | Simulation Li et al. [93] | |
|---|---|---|---|---|---|---|
| | small | large | small | large | small | large |
| $\bar{t}_{r,t}$ [s] | 0.89 | 0.97 | 0.93 | 1.02 | 0.99 | 1.13 |
| $CV(t_{r,t})$ [%] | 32.7 | 41.2 | - | - | - | - |
| $\bar{t}_{r,s}$ [s] | 0.09 | 0.12 | - | - | 0.11 | 0.17 |
| $CV(t_{r,s})$ [%] | 18.5 | 24.1 | - | - | - | - |
| $\varphi$ [%] | 2.1 | 2.3 | - | - | - | - |

$\bar{t}_{r,t} = \sum_j^{N_c} t_{r,t,j}/N_c$, $t_{r,t,j}$ is residence time in the Wurster tube in each cycle.
$\bar{t}_{r,s} = \sum_j^{N_c} t_{r,s,j}/N_c$, $t_{r,s,j}$ is residence time in the spray zone in each cycle.
$\varphi = \bar{t}_{r,t}/\bar{t}_c$.

To model the particle growth by the two-zone population balance model approach [6, 246], the ratio of the volume of the spray zone to the volume of the process chamber $\varphi$ is an important model parameter relating to process stability [7]. The model parameter $\varphi$ can be evaluated by setting the volume ratio equal to the ratio of average residence times $\bar{t}_{r,s}/\bar{t}_c$, which, respectively, gives values of 2.1 % and 2.3 % for small and large particles. From the view of geometry of process apparatus, the model parameter $\varphi$ can also be calculated using the expression for the Wurster coater proposed by Bück et al. [7], given as

$$\varphi = \left(\frac{D_t}{D_{eq}}\right)^2 \frac{1}{L}. \tag{8.1}$$

Where $D_t$ is diameter of Wurster tube, $D_{eq}$ is the effective diameter of the Wurster coater, and $L$ is the ratio of fluidized bed height to the length of the spray zone. In this work, $D_{eq}$ equals to 161 mm and $L$ equals to 4.53. Then, $\varphi$ equals to 2.1 %, which is in good accordance to the value obtained from the mean residence time in the spray zone and the mean cycle time. In addition, CFD-DEM simulation provides

further features of particle dynamics, which are important to design a stable particle coating process, such as the solid volume fraction, particle velocity, and the distance of particles from the spray nozzle. Based on the locations of individual particles, the solid volume fraction can be calculated by the ratio of total volume of particles in a certain zone to the volume of this zone. The mean solid volume fraction in the Wurster tube is 0.0148, which means that particle motion in the tube belongs to the pneumatic conveying flow region. This value is similar to the mean value of 0.0143 evaluated from the corresponding CFD cells, which implies that solid volume fraction is well computed during the coupled CFD-DEM simulation, which is important to accurately evaluate the momentum exchange coefficient $\beta_{pf}$. The mean values of particle velocity magnitude in the Wurster tube are 0.53 m/s and 0.45 m/s for large and small particles, with coefficients of variation 67.0 % and 67.8 %, respectively. However, the widths of the distributions of velocity are relatively large due to the effects of particle-particle interactions and particle-wall interactions in the Wurster tube. Moreover, a shorter distance of the particle to the spray nozzle represents a higher probability to receive more coating material. The mean distance of large particles to the spray nozzle is 46.2 mm and shorter than that of small particles, which experience a mean distance of 48.3 mm.

## 8.2.2   Droplet deposition rate

The droplet deposition rate is referred to the total mass of coating droplets deposited on the surface of a particle per unit time, which is normally related to spray rate, residence time in the spray zone, and the proximity of particles to the spray nozzle in the coating equipment. In this study, with the injection of mono-disperse solid-like droplets in the spray zone, it is possible to directly evaluate the droplet deposition rate based on the number of particle-droplet interactions $N_{d,j}$ in each cycle and the residence time in the spray zone $t_{r,s,j}$. The droplet deposition rate $R_{d,j}$ in a cycle $j$ can be defined as

$$R_{d,j} = \frac{N_{d,j} \cdot m_d}{t_{r,s,j}}, \tag{8.2}$$

where $m_d$ is the mass of single droplet ($5.24 \times 10^{-4}$ mg). On the basis of all cycles experienced by small or large particles in the time period 5 s and 30 s, the cumulative distributions of droplet deposition rate can be obtained and represented as in Figure 8.4. The median deposition rates of large and small particles are 0.125 mg/s and 0.103 mg/s, respectively. The larger particles with a larger cross-sectional area and a shorter average distance to the spray nozzle had a higher possibility to come in contact with droplets. Due to the high fraction of non-ideal cycles of large particles, the droplet deposition rate of large particles is distributed in a relatively wider range with relative span 1.09 (small particles with relative span 0.78), which finally affects the distribution of coating thickness. Considering only droplet deposition rates and particle sizes, coating thicknesses can be calculated. The resulting ratio of the median coating thickness between large and small particles is 0.52.
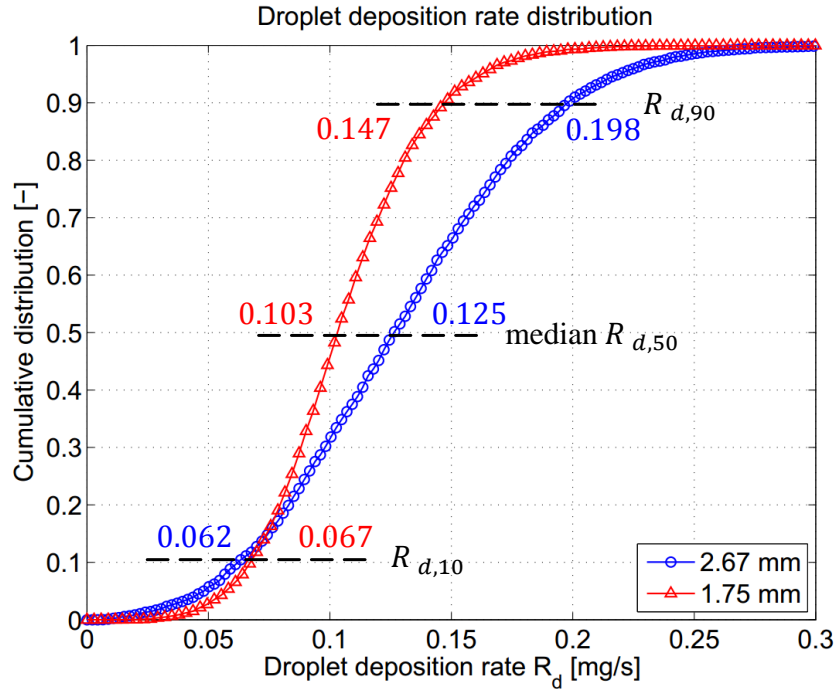
Figure 8.4: Cumulative distributions of droplet deposition rate for large and small particles (relative span refers to $(R_{d,90} - R_{d,10})/R_{d,50}$).

### 8.2.3 Particle collision velocity

The collision velocity significantly affects the probability of coalescence of two colliding particles, based on the work of Ennis et al. [20]. The collision of two particles will result in coalescence if the viscous Stokes number is less than a critical value. Actually, the viscous Stokes number, determined by the collision velocity, is the ratio of kinetic energy of the two approaching particles to viscous dissipation by the liquid film. In the DEM simulation, the collision velocity can be modeled by the contact model and the cumulative distribution of collision velocity in each zone was estimated on the basis of all individual collision events in the zone in the time range of 5 s to 30 s (as shown in Figure 8.5). According to the definition, only the relative velocity of two particles at the first contact moment was considered as collision velocity. The median collision velocities in the spray zone, the Wurster tube and the horizontal zone are 0.212 m/s, 0.192 m/s and 0.054 m/s, with relative spans of 1.63, 1.92 and 2.72, respectively. As an illustration, the critical magnitude of collision velocity for two small particles would be 0.18 m/s, assuming typical conditions used in the investigations of spray fluidized bed agglomeration (liquid viscosity of 25 mPa·s and a ratio of thickness of the liquid layer to the characteristic height of surface asperities of value 10) [154]. Clearly, the relatively high collision velocity in the spray would prevent the appearance of particle agglomeration in the Wurster coater process, despite of high moisture content in this zone. The low fluidization gas velocity and high solid volume fraction in the horizontal zone lead to relative low collision velocities, which would mean agglomeration between
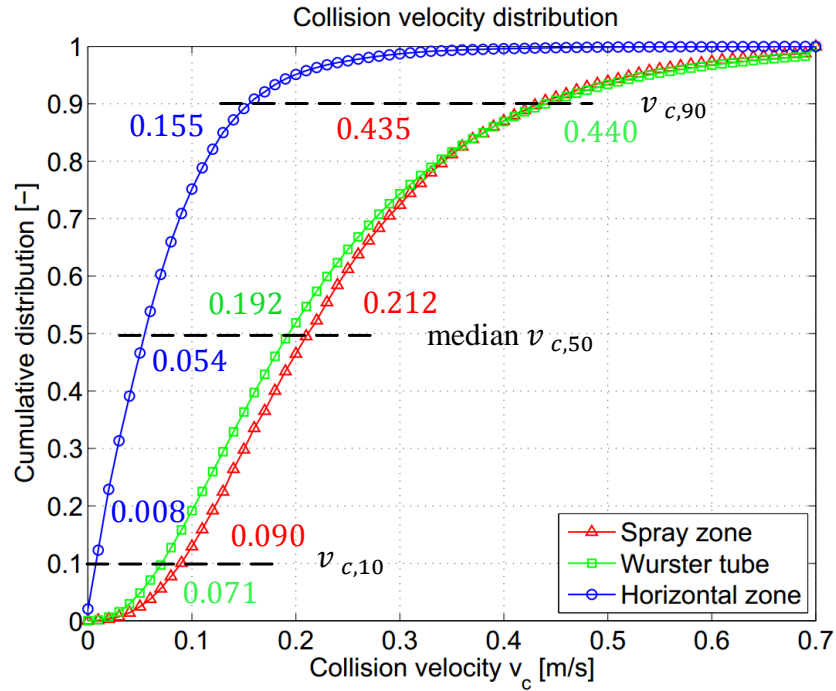
Figure 8.5: Cumulative distributions of collision velocity in spray zone, Wurster tube and horizontal zone (relative span refers to $(v_{c,90} - v_{c,10})/v_{c,50}$).

wet particles in this zone. It is therefore important to provide enough drying capacity of the fluidization gas, so that particles are dry in the horizontal zone. Note that a maximum collision velocity of 1.32 m/s appeared in the spray zone, which is smaller than the 1.5 m/s used in Equation 10 to estimate the DEM time step.

# Chapter 9

# Modeling of inter- and intra-particle coating uniformity in a Wurster fluidized bed by a coupled CFD-DEM-Monte Carlo approach

*This chapter is based on Jiang et al. [121].*

## 9.1   Coating uniformity

In Chapter 8, motion of particles in the Wurster fluidized bed was simulated by CFD-DEM to investigate the residence time in different zones. In this chapter, the CFD-DEM will be coupled with a Monte Carlo method to directly predict the inter- and intra-particle coating uniformity.

Coating of particulate materials is widely applied in the pharmaceutical, food, cosmetic, and fertilizer industries. In pharmaceutical applications, polymer-based film coating is critical to control and prolong the release of active ingredients [247]. For instance, minimum thickness and the absence of cracks of the functional coating film are required to protect the active pharmaceutical ingredient (API) against the acid environment in the stomach. Besides, the amount of API is directly correlated to the coating layer thickness in the active coating process. In the food industries, potential applications of coating include the protection of ingredients from the environment, the stabilization of the core during processing, the improvement of flowability and compression properties, and many more [248].

Spray fluidized beds and rotating drum (perforated pan) coaters are mainly used to conduct particle coating [202]. The Wurster fluidized bed is an efficient device for film coating of particles, which has been widely used in batch or continuous mode to precisely coat pellets and pharmaceutical tablets [6–8, 249, 250]. The high gas velocity in the internal annulus generates pneumatic transport of particles in the Wurster tube, resulting in relatively narrow residence time distributions (RTDs) in the spray zone

and the Wurster tube, respectively. As discussed in Chapter 8, the particles move in Wurster fluidized beds by means of circulation in five different zones. In addition to imposing a circulation motion on the particles, the drying capacities of the gases in different regions can be adjusted to control the overall coating performance [4].

The uniformity of the coating layer among particles (*inter-particle*) and on a single particle (*intra-particle*), the integrity, and the porosity of the coating layer are important attributes of the final product quality, especially in the pharmaceutical coating process. The end point and (average) coating layer thickness can be estimated. As reviewed by Knop and Kleinebudde [251], experimental techniques to characterize coating attributes include visual imaging analysis, near infrared and Raman spectroscopy, terahertz pulsed imaging, and X-ray microtomography. Near-infrared and Raman spectroscopy rely on calibration models that require ongoing maintenance support. Sondej et al. [13, 194] investigated intra-particle coating layer morphology, the inter-particle coating thickness distribution and the porosity of coating layer by X-ray micro-computed tomography ($\mu$-CT). By means of the same technique, Rieck et al. [16] found a linear expression for the relationship between layer porosity and drying potential representing drying conditions in the fluidized bed. Laksmana et al. [252] quantified the pore size distribution using confocal laser scanning microscopy. Schmidt et al. [14] proposed a simple method to estimate layer porosity of particles coated with aqueous suspensions based on the size distribution (measured by a Camsizer, Retsch GmbH) and moisture content (measured by a drying oven) of particles before and after coating. Lin et al. [253] reported the in-line measurement of intra-particle coating uniformity and inter-particle coating thickness distribution (in the range of 20 $\mu$m to above 300 $\mu$m) using combined terahertz and optical coherence tomography.

Coupling computational fluid dynamics (CFD) with DEM can be used to simulate particle-fluid systems in fluidized beds, cyclones, pneumatic conveying and channels [123], involving non-spherical particles [103] and dense particulate system reactions [254]. So far, most of CFD-DEM or DEM studies about wet coating and granulation processes investigated the residence time distributions (RTDs) in different zones of different configurations [88, 93, 94, 120, 255, 256], which then can be used as the input parameters for macroscopic population balance modeling.

An essential part of wet particle formation processes is the generation of droplets by a nozzle (one or two-fluid), in which a liquid jet disintegrates into unstable sheets, then ligaments and finally droplets due to the combined effects of the turbulent (or cavitation) flow inside the nozzle, the high shear force induced by the interactions with the second fluid outside the nozzle, and the surface tension force and the viscosity force of the liquid [30, 257]. Owing to its great importance in environmental, chemical or medical applications and the inherently complex underlying physics, the modeling of the spraying and atomization process has always been at the leading edge of numerical simulations of multiphase flow [258, 259]. Nevertheless, there is still no efficient numerical method to couple droplets into CFD-DEM accounting for the phenomena of, for instance, aggregation and breakage, the droplet deposition on particles, and drying and solidifying of droplets on particles or in the gas flow. As a common compromise, the

droplets are treated as a type of solid discrete elements in CFD-DEM simulations, with the assumption that droplets are spherical, no aggregation and breakage occur, and certain simplified droplet coalescence and death criteria apply [94, 99, 120, 247, 255, 260]. Hilton et al. [99] developed a method to map Stokesian solid-like droplets on individual particles based on the spherical harmonic formulation, which can predict the coating coverage and deposition volume at both intra-particle and inter-particle levels. The intra-particle coating variability of differently shaped particles was investigated by DEM simulations coupled with a graphical processing unit (GPU) based image analysis method in horizontal rotating pans [261, 262]. Specifically, as the particle appears in the predefined spray zone, the pixels in the image that are rendering the corresponding areas of the particles are considered to be coated. Askarishahi et al. [70] used scalar transport equations to model the interaction between droplets and particles, and evaporation from the droplet in both, the spray and on the particle surface using an Euler-Lagrange approach. Moreover, the Monte-Carlo approach can be used to model particulate processes in which a sequence of discrete events, e.g., droplet deposition, aggregation of particles, and breakage of particles, are applied to the particle population [153–155, 263–269].

In this chapter, a coupled CFD-DEM-Monte Carlo approach was developed to study the inter- and intra-particle coating coverage and layer thickness distributions in a Wurster fluidized bed. The deterministic CFD-DEM method was used to predict the circulation motion of particles in different processing zones. Based on the particle positions and particle velocities obtained from CFD-DEM simulations, the stochastic Monte Carlo approach was used to model the deposition, the splashing and the drying of droplets on the surface of each individual particle. Then, variations of particle size due to deposition and drying were given back to the CFD-DEM solver. The outline of this contribution is as follows. Section 9.2 gives a detailed description of the Monte Carlo approach for microscopic processes and events on individual particles. Section 9.3 presents and discusses simulation results of one case with cohesion forces in the DEM and one case without cohesion forces. Furthermore, detailed comparisons in terms of the residence time distribution, coating coverage and coating layer thickness are performed with experiment data and analytic models.

## 9.2 Monte Carlo methodology

An overview of the integration of the Monte Carlo with CFD-DEM is given in Figure 9.1. The details of simulation setup are given in Section 4.4.1. In each Monte Carlo time step $\Delta t_m$, one event of droplet deposition is guaranteed to occur on the single particle in the Monte Carlo domain. Particle dynamics in the CFD-DEM simulation are used in the stochastic Monte Carlo approach to model microscopic processes including deposition and splashing of droplets and drying of droplets, as shown in Figure 9.2. The time step
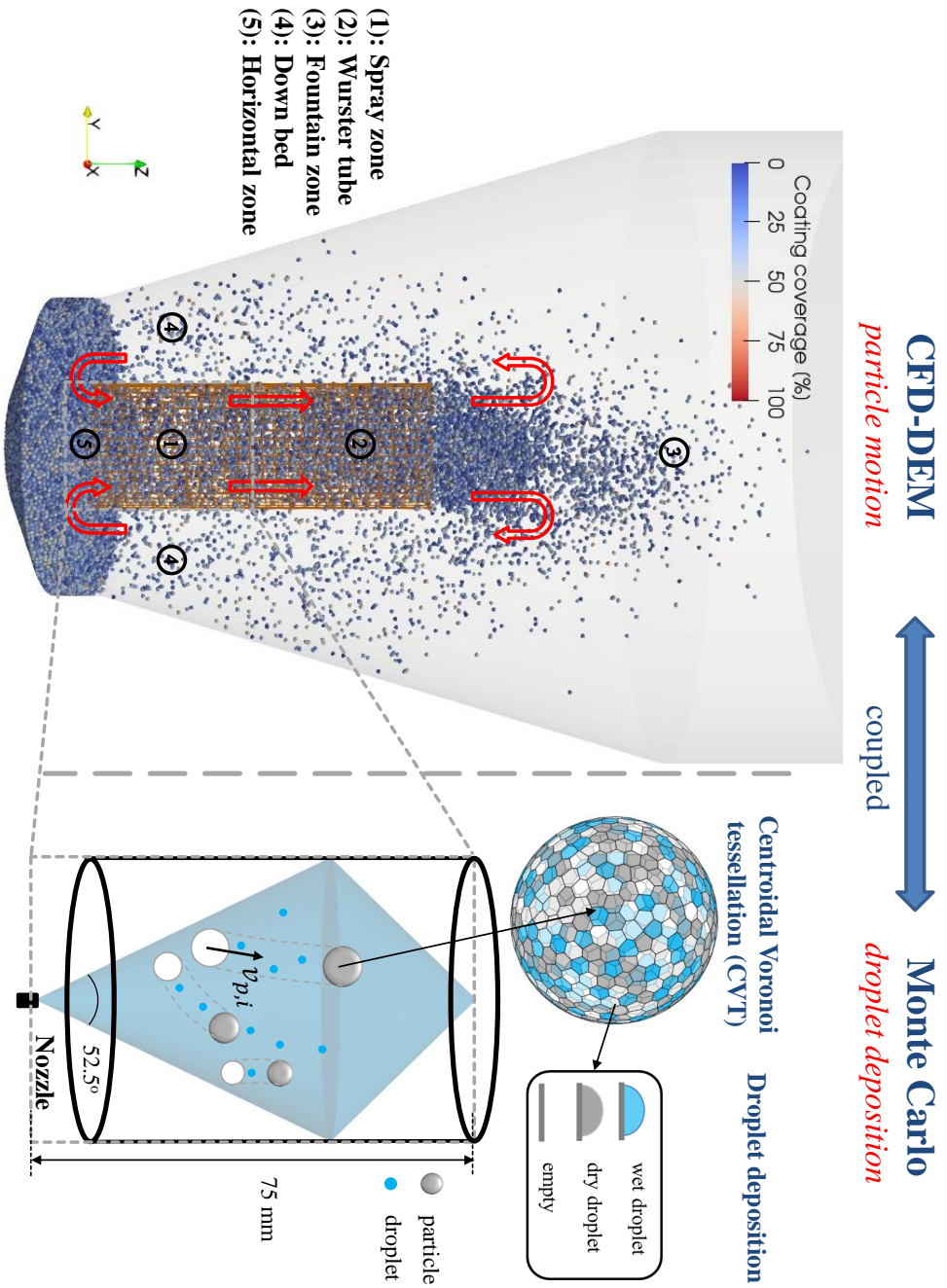
Figure 9.1: Schematic of the coupled CFD-DEM-Monte Carlo approach for predicting coating of particles in the Wurster fluidized bed, including the macroscopic particle circulation motion in different zones and microscopic droplet deposition on the surface of individual particles in the spray zone.
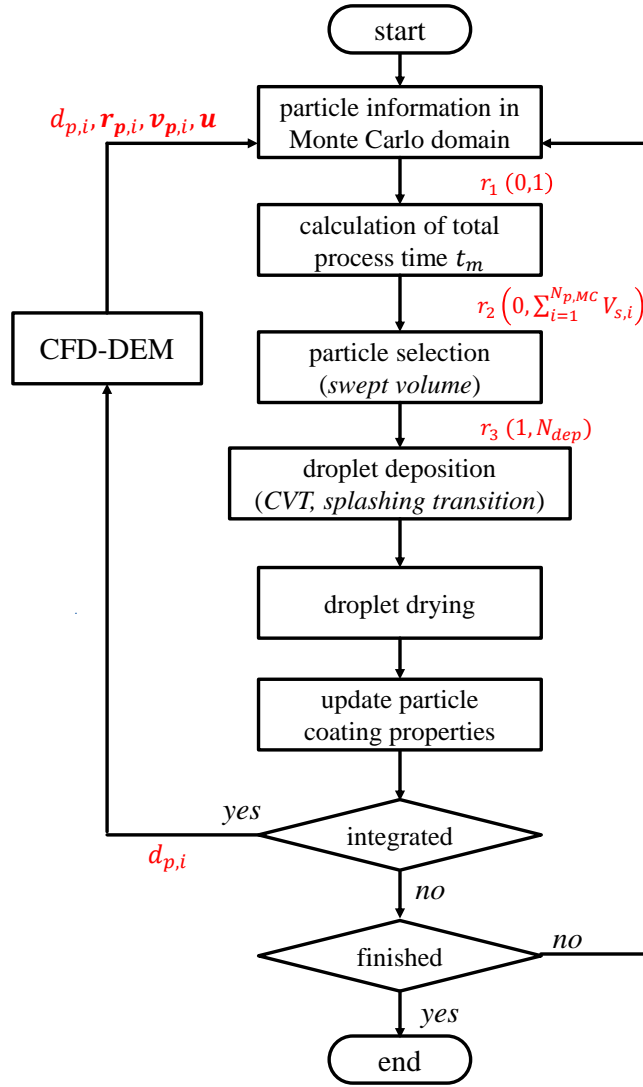
Figure 9.2: Flowchart of the coupled CFD-DEM-Monte Carlo approach.

$\Delta t_m$ can be calculated from the number flow rate of droplets sprayed into the spray zone, expressed by:

$$\Delta t_m = -\ln r_1 \left( \frac{6 \dot{M}_l}{\pi \rho_d d_d^3} \right)^{-1} \tag{9.1}$$

where $\dot{M}_l$ is the mass flow rate of solution and $r_1$ is a uniformly distributed random number from the interval $\in (0, 1)$. The initial diameter of droplets $d_d$ and mass density of droplets $\rho_d$ are constant in the model. Once total Monte Carlo process time $t_m$ has become larger than $\Delta t_{c,2}$ (Table 9.1), the new particle diameters $d_p$ are given back to the CFD-DEM solver; and the CFD-DEM simulation is conducted for another time period of duration $\Delta t_{c,2}$. Accordingly, the particles in the Monte Carlo domain are updated based on the new CFD-DEM data.

## 9.2.1   Particle selection and surface discretization

The Monte Carlo domain was set according to the geometry of the spray zone, as shown in Figure 9.1. The number of particles in the Monte Carlo domain, $N_{p,MC}$, was evaluated from the positions of individual particles in CFD-DEM simulations.

The probability of particle $i$ to receive liquid droplets was related to the volume swept by this moving particle in the spray zone, which can be calculated by $V_{s,i} = \pi(d_{p,i}/2 + d_d/2)^2 v_{p,i}\Delta t_m$. In other words, the particles were weighted by the swept volumes and the probability of each particle to be selected was determined by its relative weight. Figure 9.3 shows a straightforward algorithm: 1) calculate the cumulative sum of weights for each particle $s(i) = \sum_i V_{s,i}$ (particles are arranged in a sequence of 1 to $N_{p,MC}$), 2) select a random number $r_2$ from the interval $(0, \sum_{i=1}^{N_{p,MC}} V_{s,i})$, and 3) find the particle $i$ that has a sum of weight larger than $r_2$, i.e. $s(i) - r_2 > 0$.
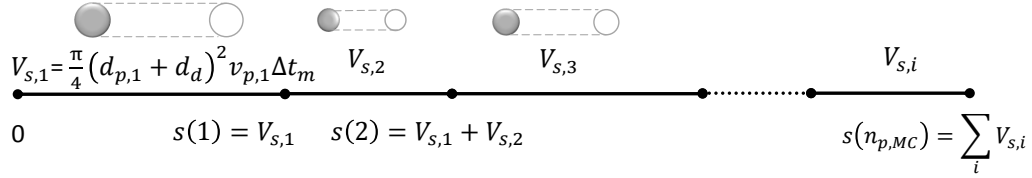


Figure 9.3: The weighted random selection of particles based on the volumes swept by the moving particles.

The surface of each individual particle was divided into labeled panels with the same area that can be used to receive droplets. Supposed that droplets do not overlap, the number of panels per particle $N_{dep}$ was calculated based on the surface area of each primary particle $A_p$ and the mean contact area of single droplet deposition $A_{contact}$; formed as

$$N_{dep,i} = \frac{A_{p,i}}{A_{contact}}, \quad i = 1, ..., N_{p,MC}. \tag{9.2}$$

The calculated number of panels per particle was then rounded to the next integer value. If the shape of deposited droplet is approximated as a truncated spherical cap and the ratio of particle diameter and droplet diameter is large enough, the diameter of contact area is given by [31, 270]

$$d_{contact} = 2d_d \left[ \frac{\sin^3 \theta}{2(1 - \cos\theta)(2 - \cos\theta - \cos^2\theta)} \right]^{1/3}, \tag{9.3}$$

in which $\theta$ is the contact angle between the liquid droplet and the solid particle. For the sake of simplicity, variations of contact angle depending on the surface wettability [270] in the spreading period were not considered and a constant contact angle was used in the model.

By spherical centroidal Voronoi tessellation (CVT) [271], a set of $N_{dep}$ points (centroids of panels) can be uniformly distributed on the surface of individual spherical particle.
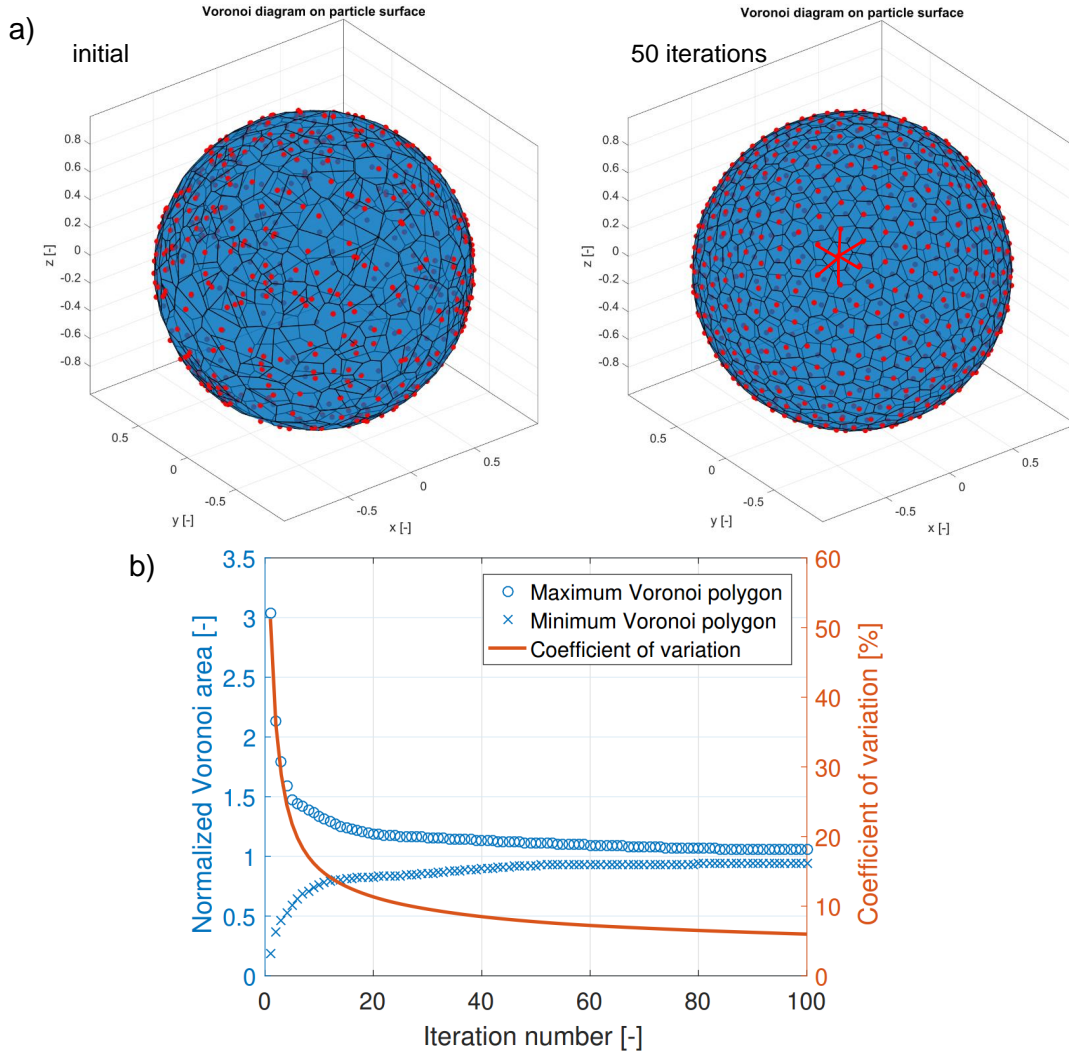
Figure 9.4: Centroidal Voronoi tessellation of a spherical particle: a) the set of 500 points (red points) generated via the proposed approach and corresponding Voronoi diagrams (at initial condition and after 50 iteration steps), and b) the normalized maximum and minimum areas of Voronoi tessellations (normalized by $\pi d_{contact}^2/4$) and the coefficient of variation of areas with respect to the number of iterations. The Voronoi first star structure is also depicted using the red lines.

This problem is of great importance in many scientific and engineering applications [272]. The main idea of centroidal Voronoi tessellation is that the points used as generators of Voronoi regions coincide with the mass centroids of those regions. In this work, the construction of spherical centroidal Voronoi tessellation was conducted by Lloyd iteration [273], as follows:

Step 1: Select a set of $N_{dep}$ points $\boldsymbol{r}_{cvt,i}^{(0)}$ on the surface of a unit sphere based on the standard normal distribution.

Step 2: Construct the Voronoi diagrams associated to the set of points $\boldsymbol{r}_{cvt,i}$, as shown in Figure 9.4a. The Voronoi regions $V_i$ of $\mathbb{R}^N$ corresponding to the generators $\boldsymbol{r}_{cvt,i}$ are defined by

$$V_i = \left\{ \boldsymbol{x} \in \mathbb{R}^N, \, |\boldsymbol{x} - \boldsymbol{r}_{cvt,i}| < |\boldsymbol{x} - \boldsymbol{r}_{cvt,j}|, \, j = 1, ..., k, j \neq i \right\}, \tag{9.4}$$

in which $|\cdot|$ denotes the Euclidean norm.

Step 3: Determine the mass centroids of all Voronoi polygonal regions $\boldsymbol{r}_{cvt,i}^*$. Given a constant probability density function $g(\boldsymbol{x})$ in Voronoi regions $V_i$, the mass centroids are calculated by

$$\boldsymbol{r}_{cvt,i}^* = \frac{\int_{V_i} g(\boldsymbol{x}) d\boldsymbol{x}}{\int_{V_i} \boldsymbol{x} d\boldsymbol{x}}. \tag{9.5}$$

Then, these centroids $\boldsymbol{r}_{cvt,i}^*$ are used to form the new set of points $\boldsymbol{r}_{cvt,i}$ and the corresponding Voronoi regions $V_i$.

Step 4: Check the coefficient of variation of areas of Voronoi polygonal regions, as depicted in Figure 9.4b. If the Voronoi polygonal regions $V_i$ generated by $\boldsymbol{r}_{cvt,i}$ meet criterion that the coefficient of variation of areas is less than 10%, the iteration is terminated; otherwise, return to step 2.

After the spherical centroidal Voronoi tessellation, the centroids of the labeled panels are $\boldsymbol{r}_{cvt,i}$, and the area of every labeled panel is approximately $\pi d_{contact}^2/4$. Figure 9.4b shows that the discrepancy between the normalized maximum and minimum areas of Voronoi tessellations is very small when satisfying the termination criterion. Given that the probability for each panel to get the droplet is the same in this work, a random integer $r_3$ from the interval $(1, N_{dep})$ can be generated to select the deposition panel for each droplet. Moreover, all information about droplet deposition is stored in the labeled panels on each individual particle.

## 9.2.2   Droplet deposition

The droplet deposition on each individual panel is affected by both the impact energy of a single droplet and the wetting condition of each individual panel. According to the method used by Jiang et al. [120], solid-like droplets with a diameter of 40 $\mu$m and a coefficient of restitution of 0.1 were injected in the spray zone of the CFD-DEM simulation to estimate the impact velocity between the particle and the droplet. The computational cost of this simulation is very high due to the required small DEM time step and the large number of particles and solid-like droplets. Based on the results of about 2 s CFD-DEM simulation, the distribution of normal impact velocity $v_{rel}$ between the particle and the droplet was assumed as a normal distribution with a mean of 13.13 m/s and a standard deviation of 3.58 m/s in the Monte Carlo model.

The impact of droplets on the dry particle surface can exhibit very complex flow patterns, such as deposition, splash (radial ejection of secondary droplets due to breakup)

or rebounding (partly or fully), which is affected by the droplet size, the impact energy of droplet and the wettability and roughness of the surface [31, 274]. The Weber number and Reynolds number characterizing the droplet impact dynamics are

$$We = \frac{\rho_d d_d v_{rel}^2}{\gamma}, \tag{9.6a}$$

$$Re = \frac{\rho_d d_d v_{rel}}{\mu_d}; \tag{9.6b}$$

in which $\rho_d$ is the mass density of liquid droplet, $\gamma$ is the surface tension of droplet, $v_{rel}$ is the normal relative velocity between the particle surface and the droplet, $d_d$ is the diameter of droplet, and $\mu_d$ is the dynamic viscosity of droplet. Regardless of surface roughness, the well-known parameter $K_d = We^{1/2}Re^{1/4}$ was used in this work to characterize the transition from deposition to splashing with a threshold value of $K_{d,s} = 57.7$ [275].

If $K_d < K_{d,s}$, the impact was considered to result in normal deposition of the entire volume of the droplet on the deposition panel. If $K_d \geqslant K_{d,s}$, splashing of the droplet occurred. The prompt or corona splashing of suspension droplets on the particle surface and the influence of drying during the impact are very complex. Droplets will break up, redistribute and reshape on the particle surface, and eject small secondary droplets to the surrounding [274]. Therefore, the splashing of droplets was regarded as a source of non-uniformity of porosity in the coating layer. In this work, only half of the droplet was assumed to deposit on the considered position, according to the measurement of the number and size distribution of secondary droplets by Yarin and Weiss [276]. The contribution of fine secondary droplets generated by the splashing to the neighboring panels has been neglected.

### 9.2.3 Droplet drying

A relatively simple drying model has been used in this work, in which the drying rate $\dot{m}_{drying}$ (in $\text{kg} \cdot \text{m}^{-2} \cdot \text{s}^{-1}$) of the first drying period was applied to evaluate the total drying time. The drying rate during the first period is dependent only on the conditions of drying in the Wurster tube, formed as

$$\dot{m}_{drying} = \beta \rho_g \left( Y_{sat} - Y \right), \tag{9.7}$$

in which $Y_{sat}$ is the adiabatic saturation moisture content of the gas, and $Y$ is the moisture content of the bulk gas. Given that, at any time, the amount of evaporated water should be equal to the amount of sprayed water, $Y$ can be calculated by

$$Y = Y_{inlet} + \frac{\dot{M}_l}{\dot{M}_{g,dry}}, \tag{9.8}$$

in which $Y_{inlet}$ is the moisture content at the inlet, $\dot{M}_l$ is the mass flow rate of the spray liquid, and $\dot{M}_{g,dry}$ is the mass flow rate of the dry fluidization gas. As for a spherical

particle, the gas side mass transfer coefficient $\beta$ can be calculated by the correlation [277]:

$$\beta = \frac{Sh \cdot \delta}{d_d}, \tag{9.9}$$

$$Sh = 2 + \sqrt{Sh_1^2 + Sh_2^2}, \tag{9.10}$$

$$Sh_1 = 0.664 Re_d^{1/2} Sc^{1/3}, \tag{9.11}$$

$$Sh_2 = \frac{0.037 Re_d^{0.8} Sc}{1 + 2.443 Re_d^{-0.1} \left(Sc^{2/3} - 1\right)}. \tag{9.12}$$

Sherwood number $Sh$ represents the ratio of convective mass transfer to the rate of diffusive mass transport and $\delta$ is the binary diffusion coefficient of water in air. $Sc = \mu_f/(\rho_g \delta)$ denotes the Schmidt number, and the Reynolds number of the droplet is given by

$$Re_d = \frac{\epsilon_f \rho_f \left| \boldsymbol{u} - \boldsymbol{v}_i \right| d_d}{\mu_f}. \tag{9.13}$$

The magnitude of relative velocity between the gas and the particle that received the droplet $\left| \boldsymbol{u} - \boldsymbol{v}_i \right|$ and the volume fraction of gas $\epsilon_f$ obtained from the CFD-DEM simulation were used to calculate $Re_d$.

Then, the drying time $\Delta t_{drying}$ can be calculated using the drying rate $\dot{m}_{drying}$ and the liquid mass of a single deposited droplet $M_{drop,l}$ to

$$\Delta t_{drying} = \frac{M_{drop,l}}{A_{drop} \cdot \dot{m}_{drying}}, \tag{9.14}$$

where $A_{drop} = \pi d_{contact}^2/(2 + 2cos\theta)$ is the surface area of the deposited droplet in contact with the gas [278]. The drying of the liquid droplet was assumed to start after its deposition on the particle at the instant $t_{deposition}$. The following criterion determined whether a droplet on the deposition panel had been dried:

$$t_m \geq t_{deposition} + \Delta t_{drying}. \tag{9.15}$$

If the Monte Carlo simulation time $t_m$ was larger than the sum of the deposition time and the drying time of the droplet, the deposition panel was considered dry. In the current model, a droplet can only be deposited on dry or empty panels. Empty panels are either initial panels or new panels generated due to the increase of $d_{p,i}$. If a panel with a wet droplet was selected, a new one was chosen randomly until the surface of selected panel was dry or empty.

### 9.2.4   Intra-particle coating properties update

According to the method used by Rieck et al. [267], the layer thickness of the $i^{th}$ individual panel on the $j^{th}$ particle $h_{layer,i,j}$ can be evaluated from the volume of the

complete coating layer $V_{layer,i,j}$ assuming every droplet to possess the same solid mass $M_{drop,s,i,j}$. Hence,

$$V_{layer,i,j} = \frac{M_{drop,s,i,j}}{(1 - \epsilon_{layer,i,j})\rho_s} N_{dep,j}, \tag{9.16}$$

$$h_{layer,i,j} = \left( \frac{d_{core}^3}{8} + \frac{3}{4} \frac{V_{layer,i,j}}{\pi} \right)^{1/3} - \frac{d_{core}}{2}, \tag{9.17}$$

where $d_{core}$ is the diameter of the core particle. In the current work, the porosity of layer $\epsilon_{layer,i,j}$ for normal deposition was a constant model parameter according to the X-ray micro-computed tomography experiments ($\epsilon_{layer,i,j} = 0.3$, Table 9.1, Sondej et al. [194]). Splashing is not considered to affect layer thickness; instead, layer porosity increases compared with normal droplet deposition. Keeping the factor $M_{drop,s,i,j}/(1 - \epsilon_{layer,i,j})$ constant for both, normal and splashing deposition results in a higher porosity of $\epsilon_{layer,i,j}^* = 0.65$ for splashing deposition.

Moreover, the average layer thickness (intra-particle) and the diameter of each particle can be written as:

$$h_{m,j} = \frac{1}{N_{dep,j}} \left( \sum_{i}^{N_{dep,j}} h_{layer,i,j} \right), \tag{9.18}$$

$$d_{p,j} = d_{core} + 2h_{m,j}. \tag{9.19}$$

The diameter of each particle was given back to the DEM solver. The mean layer thickness in the particle population (inter-particle) was calculated by

$$h_m = \frac{1}{N_p} \left( \sum_{j}^{N_p} h_{m,j} \right). \tag{9.20}$$

To evaluate the coating coverage of each particle, the number of initial deposition panels $N_{dep,j}$ and the number of deposition panels that have received droplets (dry or wet) $N_{coat,j}$ were counted. Then, the following equation was used to calculate the coating coverage of each particle $\Psi_j$ in each time step:

$$\Psi_j = \frac{N_{coat,j}}{N_{dep,j}}. \tag{9.21}$$

If the coating coverage of the particle reaches 100 %, a full closed coating layer has formed around the particle. The average inter-particle coating coverage is

$$\Psi_m = \frac{1}{N_p} \left( \sum_{j}^{N_p} \Psi_j \right). \tag{9.22}$$

## 9.2.5    Monte Carlo setup

All models, boundary conditions, and numerical techniques used in CFD-DEM simulations had previously been published. The entire CFD-DEM method, including the governing equations for the solid particles and the gas phase [123], the drag model for the particle-fluid momentum exchange [136, 137], the Hertzian spring-dashpot contact model (soft-sphere) [143], the rolling model [144], and the cohesion model for capillary force [149], as given in Chapter 3.

CFD-DEM simulations of two cases were performed using four-way coupling by the code OpenFOAM and LIGGGHTS [128]. The first case without capillary forces between particles can be directly compared to the PEPT measurement at dry condition by Li et al. [27]. The second case with capillary forces was designed to investigate the influence of wetting and agglomeration in the Wurster tube on the residence time distribution. The liquid bridges were assumed to be formed by sodium benzoate (NaB) solution with a mass fraction of approximately 30 %. The surface tension of the liquid is $\gamma = 6.98 \times 10^2$ N/m, which was measured by the pendant drop method. As measured by Zhu et al. [279], the motion of particles in spouted beds was significantly influenced by the effects of cohesion as $\alpha_l$ exceeded $10^{-3}$. Therefore, the parameter $\alpha_l$ was set as 0.1% in order to investigate the effects of cohesion on particle circulation. In other words, the parameter $\alpha_l$ was purposely enlarged, compared with the value of $6 \times 10^{-6}$ calculated by the volume of a single droplet used in the Monte Carlo model (Table 9.1).

A relatively large $t_{c,2} = 0.005$ s, about 1/200 of the mean residence time in the tube and 1/30 of the residence time in the spray zone, was used to avoid excessively high computational cost because of too frequent communication between CFD-DEM code and Monte Carlo method.

Sondej et al. [13, 194] measured both the intra-particle and inter-particle distributions of coating layer thickness in a top-spray fluidized bed. In their experiment series A, the diameter of the core particles was 1.8 mm which is similar to the value of 1.75 mm used in the current simulations. In order to compare with their experiment, the mass flow rate of spray solution $\dot{M}_l$ used in the Monte Carlo model was scaled according to the numbers of primary particles in the different beds, which leads to similar values of the mean layer thickness and mean coating mass per particle. Although the coating performances of the top-spray fluidized bed and the Wurster fluidized bed are not exactly the same, the comparison of intra-particle layer thickness distribution is still meaningful when the mean coating mass received by individual particles is the same. The coating material is sodium benzoate, which has an antibacterial effect and is used as a preservative in the food industry. The mass fraction of sodium benzoate solution is about 30 %. The viscosity of the solution was measured by a Höppler viscosimeter; and the density of the liquid was measured by a density meter (DMA 58, Anton Paar). Other properties associated with the spray droplets and gas flow were set same as in the corresponding experiment series A [13]. Detailed parameters of the Monte Carlo model and the experiment are listed in Table 9.1.

Table 9.1: Monte Carlo simulation parameters.

| Parameter | Monte Carlo | Experiment |
|---|---|---|
| Configuration | Wurster bed | Top-spray bed |
| Particle material | MCC | $\gamma$-$Al_2O_3$ |
| Coating material | NaB | NaB |
| Initial bed mass [kg] | 0.2 | 0.4 |
| Initial particle diameter $d_{p,0}$ [mm] | 1.75 | 1.80 |
| Initial particle density [kg/m$^3$] | 1420 | 1040 |
| Number of particles [$-$] | 50000 | 125000 |
| Solid density of coating material $\rho_s$ [kg/m$^3$] | 1440 | 1440 |
| Mass flow rate of solution $\dot{M}_l$ [kg/h] | 0.048 | 0.12 |
| Droplet diameter $d_d$ [$\mu$m] | 40 | 40 |
| Viscosity of droplet $\mu_d$ [Pa $\cdot$ s] | $4.18 \times 10^{-3}$ | $4.18 \times 10^{-3}$ |
| Surface tension of droplet $\gamma$ [N/m] | $6.98 \times 10^{-2}$ | $6.98 \times 10^{-2}$ |
| Density of droplet $\rho_d$ [kg/m$^3$] | 1125 | 1125 |
| Contact angle $\theta$ [°] | 40 | 40 |
| Solid mass fraction of solution [%] | 30 | 30 |
| Porosity of the coating layer [%] | 30 | 30 |
| Inlet temperature of gas [°C] | 75 | 75 |
| Inlet moisture content of gas $Y_{inlet}$ [g/kg] | 1 | 1 |
| Mass flow rate of gas $\dot{M}_{g,dry}$ [kg/h] | 96 | 120 |

## 9.2.6   Recurrence of particle circulation

In this work, the CFD-DEM takes about 5 h to simulate 1 s real time (with 8 CPUs), while the Monte Carlo only needs about 0.05 h. If the simulation had to be performed, for example, for 1 h to predict a real coating process, it would take more than 750 days, which is not acceptable.

In the CFD-DEM-Monte Carlo model, the coating of particles is largely determined by the cycle time distribution and residence time distribution in the spray zone obtained from the CFD-DEM, with the details of droplets deposition, drying and solidifying being modeled by the Monte Carlo. It was found that the distributions of cycle time and residence times are almost constant after 60 s. As listed in Table 9.2, the deviations of mean cycle time, mean ideal cycle time, mean residence times in the tube and the spray zone, as well as the corresponding coefficients of variation are very small between 60 s and 180 s. Based on the circulation characteristics of particles, it is thus reasonable to use the database of particle dynamics obtained from a relative short duration to reconstruct the recurring motion of particles in a long-term period. In this work, a simple approach was used to recur the particle circulation motion, as follows:

First, a database of 50000 individual particles was generated using the full CFD-DEM-Monte Carlo simulation data in the duration of 180 s, including particle positions $\boldsymbol{r}_i$, particle velocities $\boldsymbol{v}_{p,i}$, relative velocities between particles and the fluid phase $\boldsymbol{u} - \boldsymbol{v}_{p,i}$,
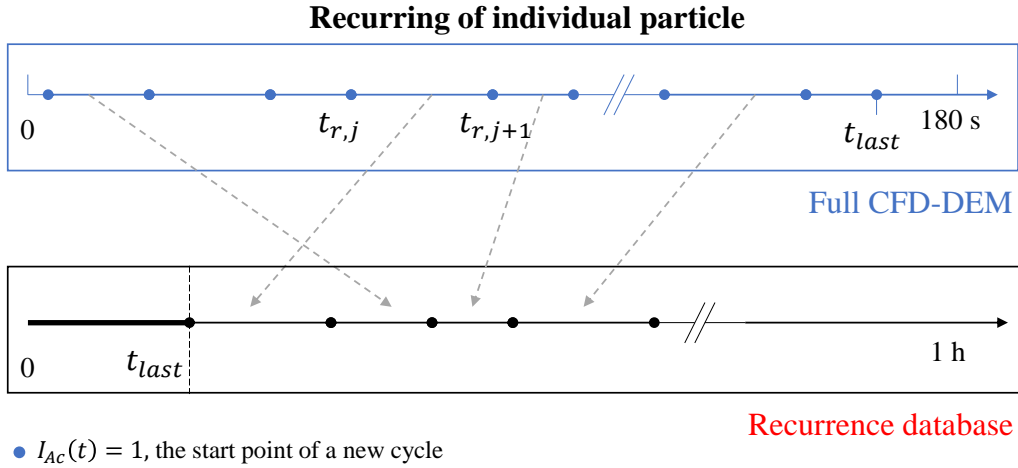
**Recurring of individual particle**



Figure 9.5: Recurrence algorithm for the circulation motion of individual particles in the Wurster fluidized bed.

particle diameter $d_{p,i}$ and the indicator $I_{A_c,i}$. Based on the trajectory of each individual particle, the indicator function was defined to indicate the occurrence of event $A_c$ that the particle entered into the spray zone through the partition gap at instant $t$, expressed as

$$I_{A_c}(t) = \begin{cases} 1, & if\ t \in A_c, \\ 0, & if\ t \notin A_c. \end{cases} \tag{9.23}$$

In other words, the instant $t$ corresponds to the start point of a new cycle as $I_{A_c}(t) = 1$.

Second, for each individual particle, the particle dynamics after the last instant $t_{last}$ satisfying $I_{A_c,i}(t) = 1$ in the full simulation can be recurred by repeatedly extrapolating the particle dynamics in the range of $(t_{r,j}, t_{r,j+1}]$ from the database. The instant $t_{r,j}$ was a randomly selected instant that corresponds to $I_{A_c}(t_{r,j}) = 1$; and $t_{r,j+1}$ was the next instant that made the indicator function equal to unity. As listed in Table 9.2, the relative deviations of mean cycle time, mean ideal cycle time, mean residence times in the tube and the spray zone as well as the corresponding coefficients of variation are all almost negligible (less than 1%) between the full simulation results of 180 s and recurring results of 1 h by this method.

It is emphasized that this simple approach to recur the particle circulation only reproduces the circulating motion. However, if the database obtained from the full simulations is large enough, this simple method is statistically reliable and can well predict the distributions of cycle time and residence times in the Wurster fluidized bed with negligible computation cost compared with the CFD-DEM. Therefore, the CFD-DEM simulation was terminated after 180 s in this work; subsequently, the particle dynamics required in the Monte-Carlo model were extrapolated from the database. It should be noted that the influence of increasing particle diameter $d_{p,i}$ on the particle dynamics

cannot be captured in this way. However, this influence is very limited for particles with very thin coating layers considered in this work.

## 9.3 Results and discussion

The results obtained from the coupled CFD-DEM-Monte Carlo method will be presented in form of the residence and cycle time distributions, and the intra-particle and inter-particle coating properties. Residence and cycle time distributions are compared with PEPT measurement data [27]; and the intra-particle coating layer thickness distribution is compared with experimental data gained by X-ray micro-computed tomography ($\mu$-CT) [13, 194].

### 9.3.1 Residence and cycle time distributions

The particle oriented features of the CFD-DEM simulation environment were advantageous to investigate the circulation of particles in the Wurster fluidized bed. As depicted in Figure 9.1, the chamber of the Wurster fluidized bed is divided into: (1) spray zone, (2) Wurster tube (without overlap with the spray zone), (3) fountain zone (only a part of the fountain zone is depicted for better visualization), (4) down bed, and (5) horizontal zone. In each ideal cycle, particles move upward into the tube from the spray zone, lose momentum in the fountain zone, fall down into the external annulus, are transported in the horizontal zone in plug flow manner, and re-enter the spray zone through the partition gap at the bottom of the internal annulus. Particles can recirculate within the Wurster tube without passing the partition gap, including the motion from zone 2 to zone 1 and from zone 3 to zone 2. The recirculation influences the distributions of cycle time and residence time in the spray zone and Wurster tube. In this work, ideal cycles and nonideal cycles were distinguished by the determination of the appearance of recirulation based on particle trajectories [120]. The cycle time of particles related to the number of passes through the spray zone and the residence time in the spray zone related to the amount of the obtained coating material per cycle are two significant parameters for the uniformity of the coating process.

Simulation results associated with distributions at different processing times are summarized in Table 9.2. Data for 10 s, 60 s and 180 s come from the full simulations, and data for 1 h was evaluated based on the recurrence of particle circulation, as discussed in Section 9.2.6. Comparing the data of 180 s and 1 h for dry condition without capillary forces in the DEM shows that the recurrence method well reconstructs the long-term circulation of particles in terms of mean values of cycle time $t_c$, ideal cycle time $t_{ic}$, residence time in the spray zone $t_{r,s}$ and residence time in the Wurster tube $t_{r,t}$ as well as the corresponding coefficients of variation. However, if the database is not big enough for the recurrence process (for instance after only 10 s), large deviations will be introduced into the recurring data and final coating properties. To apply the recurrence method for the Wurster fluidized bed, the full CFD-DEM simulation must be performed at least until stabilization of the mean cycle time of particles has been achieved.

Table 9.2: Comparison of ideal cycle time, overall cycle time, and residence times in the Wurster tube and the spray zone obtained from CFD-DEM simulations for dry conditions as well as with cohesion forces ($\alpha_l = 0.1\%$); and the PEPT measurement [27].

| Variable | CFD-DEM simulations | | | | | PEPT |
|---|---|---|---|---|---|---|
| | dry (10 s) | dry (60 s) | dry (180 s) | dry (1 h) | $\alpha_l = 0.1\%$ (1 h) | dry (1 h) |
| $\bar{t}_{ic}$ [s] | 4.76 | 4.97 | 4.98 | 4.98 | 4.75 | 4.84 |
| $C_v(t_{ic})$ [%] | 68.7 | 53.3 | 52.5 | 52.8 | 43.5 | 99.0 |
| $\bar{t}_c$ [s] | 5.63 | 5.80 | 5.83 | 5.82 | 6.02 | 6.14 |
| $C_v(t_c)$ [%] | 88.3 | 61.4 | 62.0 | 61.5 | 70.3 | 90.0 |
| $\bar{t}_{r,t}$ [s] | 0.891 | 0.958 | 0.965 | 0.963 | 0.925 | 1.00 |
| $C_v(t_{r,t})$ [%] | 51.6 | 33.0 | 34.3 | 33.7 | 54.6 | - |
| $\bar{t}_{r,s}$ [s] | 0.136 | 0.156 | 0.158 | 0.158 | 0.153 | - |
| $C_v(t_{r,s})$ [%] | 47.8 | 23.7 | 22.5 | 22.1 | 42.3 | - |
| $R_{ic}$ [%] | 69.3 | 77.3 | 78.4 | 78.3 | 60.2 | 55.3 |

[1] $\bar{t}_{ic} = \sum_j^{N_{ic}} t_{ic,j}/N_{ic}$, $N_{ic}$ is total number of ideal cycles, $t_{ic,j}$ is time of each ideal cycle.
[2] $\bar{t}_c = \sum_j^{N_c} t_{c,j}/N_c$, $N_c$ is total number of cycles, $t_{ic,j}$ is time of each cycle.
[3] $\bar{t}_{r,t} = \sum_j^{N_c} t_{r,t,j}/N_c$, $t_{r,t,j}$ is residence time in the Wurster tube in each cycle.
[4] $\bar{t}_{r,s} = \sum_j^{N_c} t_{r,s,j}/N_c$, $t_{r,s,j}$ is residence time in the spray zone in each cycle.
[5] $R_{ic} = N_{ic}/N_c$.
[6] $C_v$ is the coefficient of variation.

Comparing the data of simulation for dry condition with the PEPT measurement [27], the mean of ideal cycle time obtained from the simulation is found to be slightly higher; inversely, the mean of total cycle time is under-predicted, which is due largely to a high fraction of ideal cycles in the simulation. In the simulation, most of the non-ideal cycles were caused by intensive interactions with the Wurster tube wall and other particles. Further discussion on the possible reasons would require more information about particle-particle and particle-wall interactions from the PEPT measurements. Moreover, the distributions of total cycle time and ideal cycle time were found to be fairly broad for the PEPT measurement, the spreads predicted by the simulation being somewhat smaller. These observations are similar to those made on simulations for binary particle mixtures [120]. The mean residence times in the Wurster tube were found to be in good agreement with experimental data. The mean residence time in the spray zone is 0.158 s (about 1/6 $\bar{t}_{r,t}$) based on the geometry of the predefined spray zone. Note that only a single tracer particle was used in PEPT measurement. According to the concept of ergodicity, the distribution of circulations was evaluated by the motion of this tracer particle in a long tracking period of about 1 h.
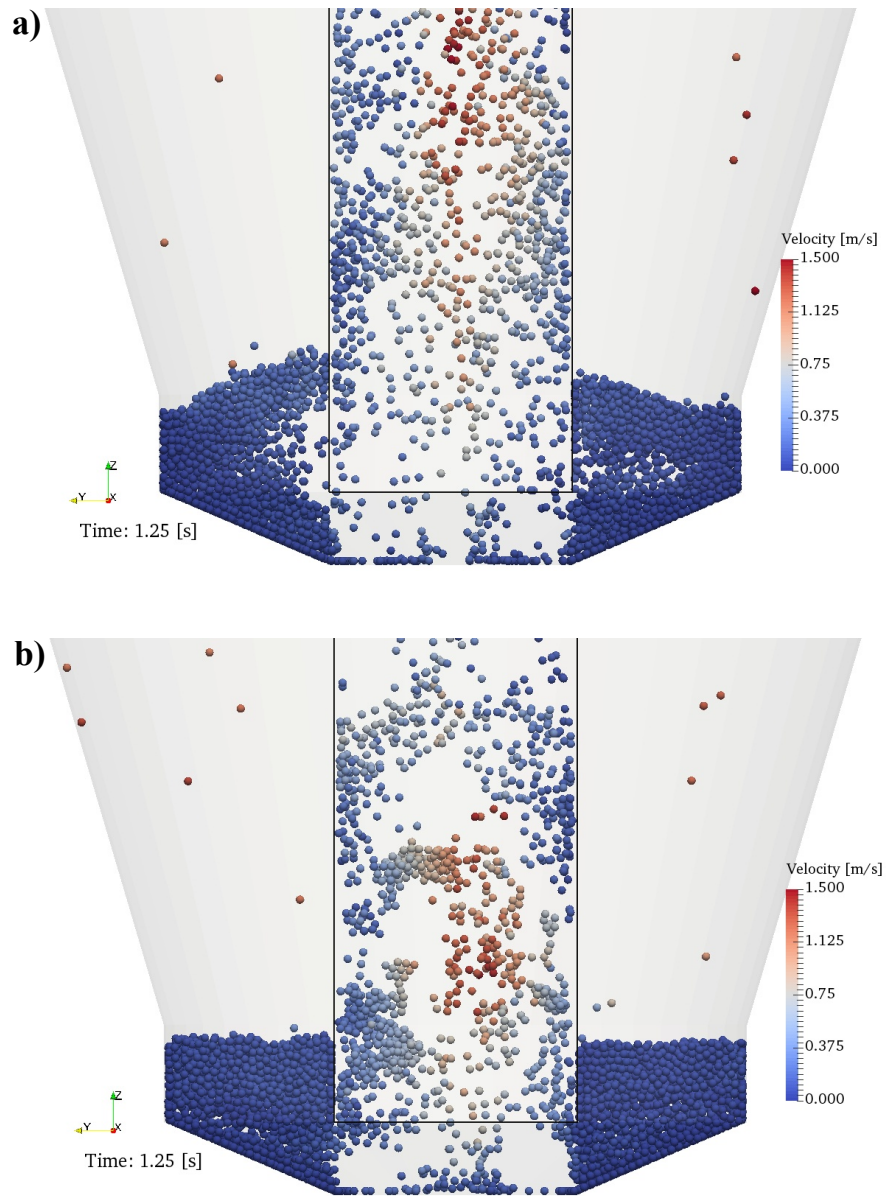
Figure 9.6: Snapshot of particle motion in the Wurster fluidized bed: a) without cohesion force, b) with cohesion force ($\alpha_l = 0.1\%$).

Additionally, the influence of capillary forces in the Wurster tube on the circulation motion was investigated by the cohesion DEM model. Figure 9.6 shows snapshots of particle motion for conditions with and without capillary force. The global circulation of particles with capillary forces ($\alpha_l = 0.1$ %) is very similar to that at dry condition; however, the particles tend to be agglomerated by liquid bridges when inter-particle distances are shorter than the rupture distance. Because no drying and solidification of liquid bridges were considered in CFD-DEM simulations, the agglomerates formed

by liquid bridges were not stable, and could break up as the relative distances between particles in the agglomerate varied due to collisions with the tube wall or other particles (or agglomerates). Comparing the simulation results of the two cases in Table 9.2, the capillary force decreases the mean ideal cycle time as well as the mean residence times in the Wurster tube and in the spray zone. Since agglomeration of particles increased the local solid volume fractions $\epsilon_s$ in Eq. (3.32), momentum exchange between particles and the gas in these regions and the mean velocities in vertical direction in the Wurster tube were increased. Nevertheless, the capillary force decreases the fraction of ideal cycles $R_{ic}$ due to more complex interactions between temporary agglomerates and the tube wall. As a consequence of this decrease, the capillary force further scatters the distributions of total cycle time, and residence times in the Wurster tube and the spray zone. This effect is more obvious in the Wurster tube. It is therefore important to provide enough drying capacity of the fluidization gas, so that particles are dry before re-entering the spray zone. The influence of the capillary force is expected to be more pronounced in coating of fine particles, and is subject of further investigations.

## 9.3.2 Coating properties of a sample particle

Figure 9.7 illustrates the coating properties of a random sample particle predicted by the simulation without capillary forces. The intra-particle coating coverage is an important property for functional coatings especially in pharmaceutical film coating applications. The variations of coating coverage from 20 s to 100 s are shown in Figure 9.7a. Droplets on the deposition panels can be dried (gray color) or wet (blue color) depending on Eq. (9.15). The coating coverage $\Psi$ increases from 9.24 % to 33.51 % in a duration of 80 s, which is affected by both the cycle time and residence time of this particle in the spray zone.

At process times of 500 s, 1500 s and 3000 s, the coating layer thickness and the splashing positions along a great-circle of the spherical particle are depicted in Figure 9.7b. The layer thickness on each panel on the single particle was calculated by Eq. (9.17). The information on layer thickness of each panel can be further used to evaluate the uniformity of coating by, for instance, the mean layer thickness $h_{m,j}$ (Eq. (9.18)), the standard deviation, the coefficient of variation and the arithmetic average roughness.

In the current Monte-Carlo model, the porosity of splashing panels was assumed to increase, due to lower volume of received droplets, changes in droplet shapes, as well as droplet drying and solidification during the impact. The splashing panel is drawn with a relatively light color, which implies a relatively high porosity. For an individual splashing position, the orthodromic distance to its nearest neighboring splashing position on the same layer was defined as $L_{min}$, which can be further normalized by the particle radius $r_p$. For the sample particle at 3000 s, the mean and the coefficient of variation of $L_{min}/r_p$ are 0.224 and 45.2 % in the 3D space, respectively. In addition, the size of individual high porosity regions $S_p$ was defined by the number of connected splashing positions. If several splashing positions with the same radial distance belonged to the same Voronoi star, these positions were considered as a connected high porosity region

**a)**

Time = 20.00 [s], Coverage = 9.24 [%]    Time = 50.00 [s], Coverage = 17.28 [%]    Time = 100.00 [s], Coverage = 33.51 [%]
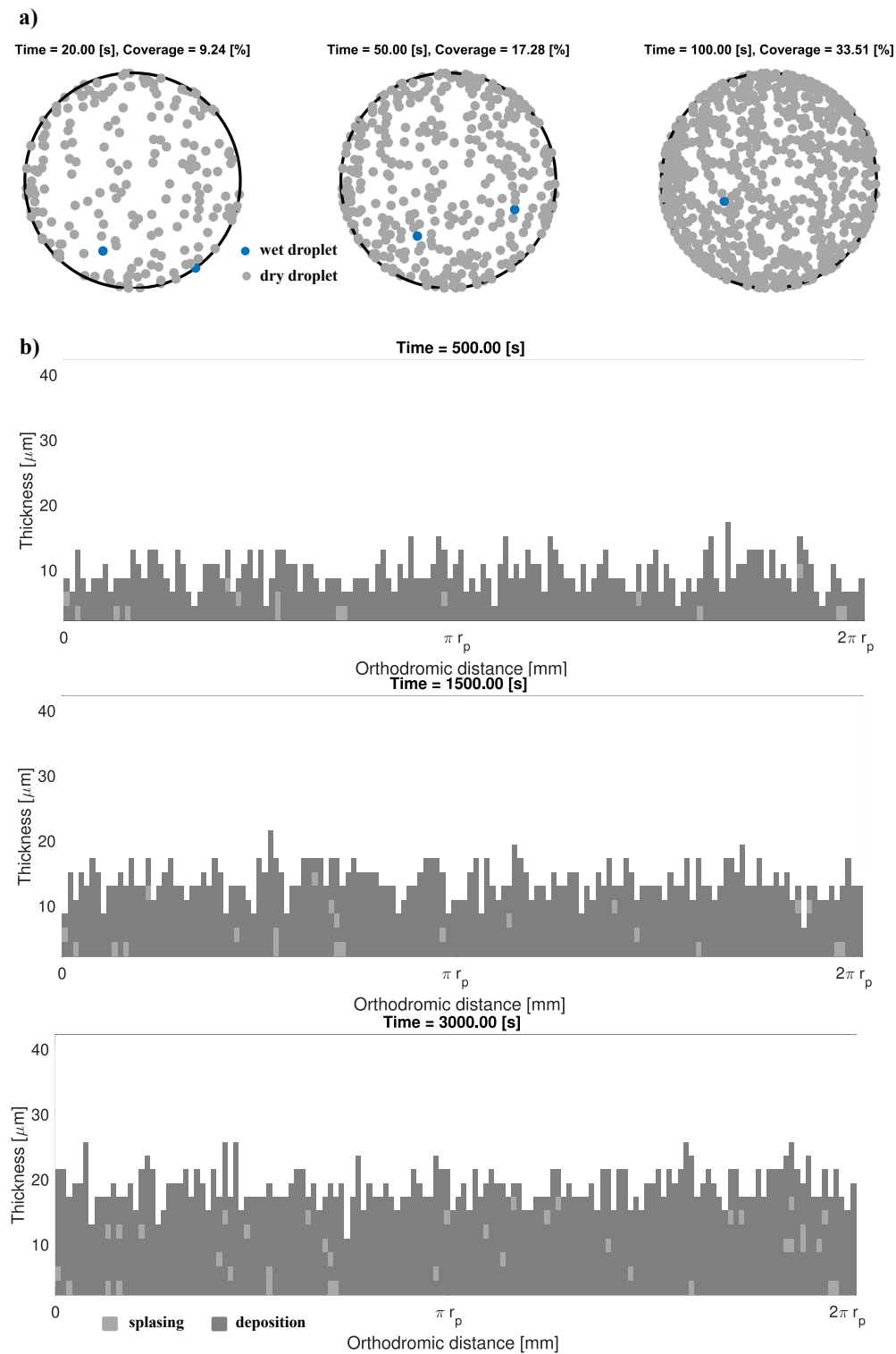


- wet droplet
- dry droplet

**b)**



Figure 9.7: Coating quality of single sample particle: a) coating coverage (2D front elevation), b) coating layer thicknesses and splashing positions along a great-circle of the spherical particle.

at this radial distance. The Voronoi star was assembled by the centroid (the center of star) and corresponding natural neighboring points (endpoints of the extremities of the star) in the Voronoi diagram [104], as shown in Figure 9.4. If several high porosity regions at different radial distances were overlapping, these high porosity regions were merged. For the sample particle at 3000 s, the mean and the coefficient of variation of $S_p$ are 1.21 and 42.8 % in the 3D space, respectively. Usually, the risk to form cracks and large pores in the coating layer increases with decreasing $L_{min}$ and increasing $S_p$.

At 500 s, all deposition panels along the chosen great-circle have been coated. However, this does not imply complete coating in all great-circles. Actually, the time to accomplish the 100% coating coverage $t_{cover,100}$ for this sample particle is about 880 s.

### 9.3.3 Coating layer thickness

Figure 9.8 shows intra-particle cumulative distributions of coating layer thickness. The individual particles correspond to 0.1, 0.5, and 0.9 of the property value in the population. Besides the plotted distributions, the mean values and coefficients of variation of intra-particle and inter-particle coating properties are listed in Table 9.3 to further characterize the distributions.

Table 9.3: Summary of intra-particle (10%, 50%, 90%) and inter-particle coating properties obtained from simulations without and with capillary force.

| Coating properties | without cohesion | | | | with cohesion $\alpha_l = 0.1\%$ | | | |
|---|---|---|---|---|---|---|---|---|
| | 10% | 50 % | 90 % | inter | 10% | 50% | 90% | inter |
| $mean(h)$ [$\mu$m] | 24.28 | 26.17 | 29.86 | 26.03 | 21.75 | 26.94 | 32.25 | 26.77 |
| $C_v(h)$ [%] | 26.8 | 27.0 | 27.1 | 7.7 | 27.3 | 26.5 | 26.0 | 12.4 |
| $mean(S_p)$ [%] | 1.13 | 1.34 | 1.58 | 1.36 | 1.13 | 1.36 | 1.62 | 1.39 |
| $C_v(S_p)$ [%] | 20.7 | 32.3 | 44.7 | 6.9 | 22.8 | 34.1 | 46.0 | 7.7 |
| $mean(L_{min}/r_p)$ [$-$] | 0.177 | 0.206 | 0.248 | 0.215 | 0.173 | 0.209 | 0.261 | 0.219 |
| $C_v(L_{min}/r_p)$ [%] | 40.7 | 47.4 | 55.7 | 12.9 | 41.0 | 47.3 | 54.6 | 15.5 |
| $mean(t_{cover,100})$ [s] | 898 | 1213 | 1621 | 1245 | 882 | 1284 | 1997 | 1258 |
| $C_v(t_{cover,100})$ [%] | - | - | - | 22.7 | - | - | - | 27.5 |

It can be seen that the predicted results of MC-50 for both conditions are close to the measurement data. The distance between the curves of MC-10 and MC-90 for the condition with capillary forces is much larger than that for simulation without capillary forces, corresponding to a wider distribution of residence time in the spray zone with comparable mean value (Table 9.2). Compared with the Monte Carlo modeling of [267] (Exp. 3), the deviations of mean layer thickness between different single particles are much larger, as a result of the non-uniformity of residence times and cycle time predicted by the CFD-DEM. However, the coefficients of variation of all single particles for both conditions are very close, since the probability for each panel to receive droplets was similar and only affected by the number $N_{dep}$ in the Monte-Carlo model. If layer thickness of the particle is 30 $\mu$m, then there will be about 6.9 % increase in $N_{dep}$ due to growth of a 1.75 mm core particle.
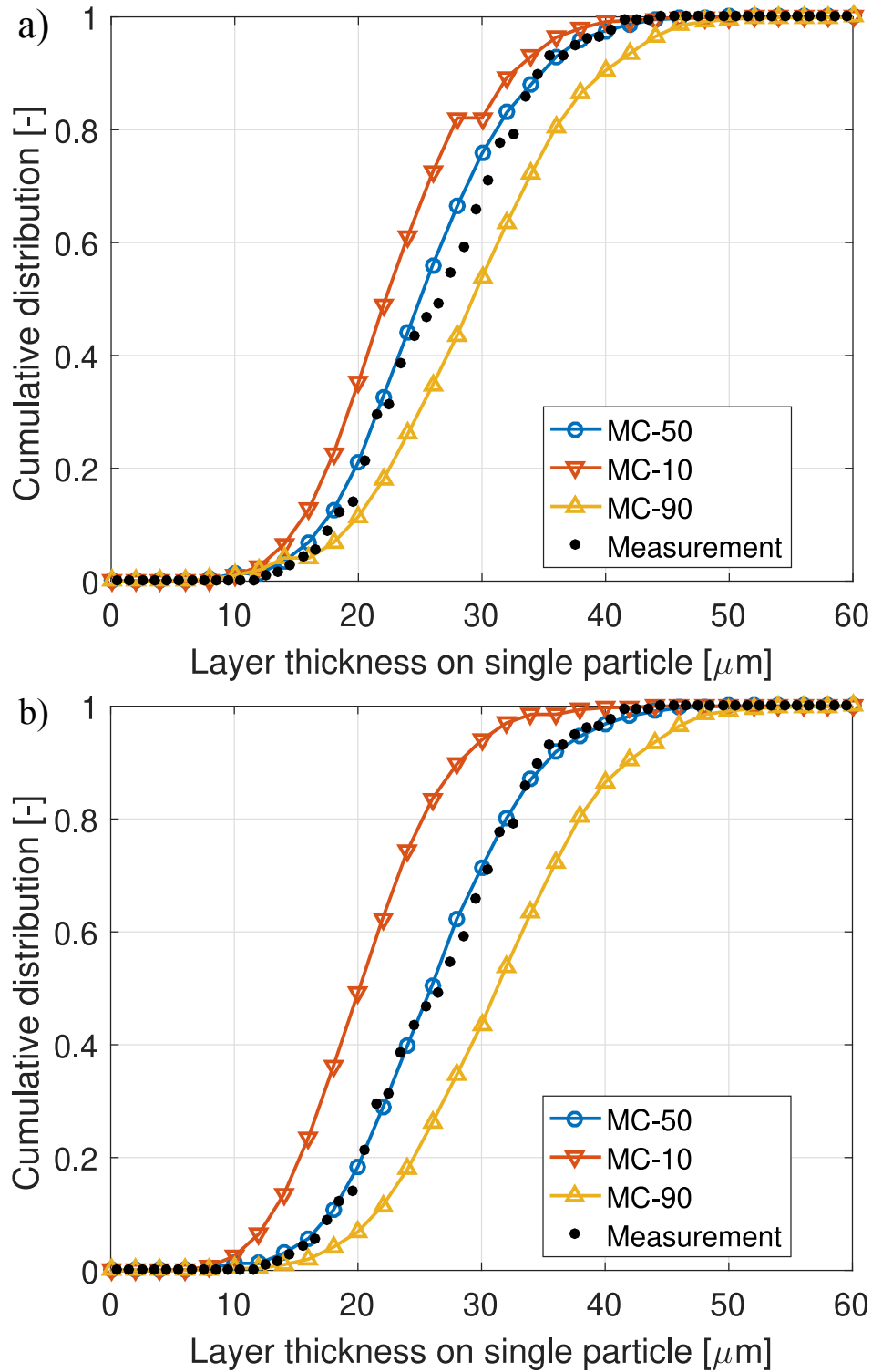
Figure 9.8: Comparison of cumulative distributions of layer thickness on single particles obtained from the measurement and the CFD-DEM-Monte Carlo simulations at 1 h processing time: a) without cohesion force, and b) with cohesion force ($\alpha_l = 0.1\%$).

In addition to the intra-particle scale, the distribution of mean layer thickness per single particle in the population (inter-particle) can also be extracted from the simulations (Table 9.3). It is interesting to observe that the coefficient of layer thickness variation in the particle population is much smaller than the values for the single particles (Table 9.3). The predicted value of 7.7 % is comparable to the value of 5.1 % for the particle population in the experimental data for top-spray coating of Sondej et al. [194]. Information about the RTDs in the coupled CFD-DEM-Monte Carlo approach can better represent the situation in experimental equipment under different operation conditions than the spatially concentrated, single compartment Monte Carlo approach by Rieck et al. [267].

### 9.3.4   Coefficient of variation of coating layer thickness

When the same amount of material is deposited on each particle for each pass through the spray zone, the coefficient of variation of the inter-particle coating mass distribution is given by [241]

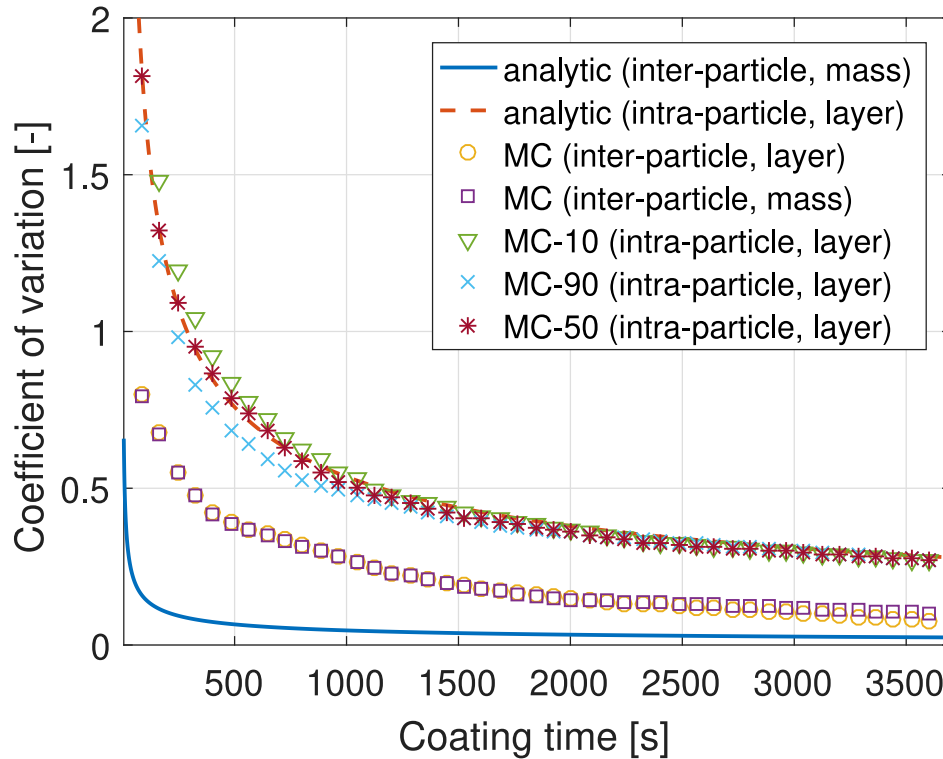$$C_{v,inter,m} = C_v(t_c)\sqrt{\frac{\bar{t}_c}{t_{coat}}}, \tag{9.24}$$



Figure 9.9: Comparison of the coefficients of variation of inter-particle and intra-particle layer thickness distributions obtained from the simulation without capillary forces, inter-particle analytic model of coating mass distribution [241], and intra-particle analytic model of layer thickness distribution [265].

in which $C_v(t_c)$ is the coefficient of variation of cycle time (Table 9.2), $\bar{t}_c$ is the mean cycle time and $t_{coat}$ is the total coating time. The coefficient of variation of the intra-particle layer thickness is proportional to the number of coating passes raised to the $-1/2$ power [265]. When every deposition panel has an equal opportunity of being coated and only one deposition panel can receive the droplet in each Monte Carlo time step, Eq. 28 in Freireich and Wassgren [265] can be rewritten as

$$C_{v,intra,l} = \sqrt{\frac{1}{N_{drop}}[N_{dep} + (N_{drop} - 1)] - 1},$$
(9.25)

where $N_{drop}$ is the number of droplets deposited on the certain particle.

According to simulation data, the coefficients of variation of intra-particle and inter-particle layer thickness distribution can be directly calculated based on Eq. (9.17) and Eq. (9.18), respectively. Figure 9.9 depicts the coefficients of variation from the simulation without capillary forces and from analytic models as functions of coating time. It can be seen that the coefficients of variation of intra-particle coating layer thickness predicted by the simulation (MC-10, MC-50 and MC-90) almost coincide with that of the analytic model after about 1500 s. In the simulation, the amount of material that is deposited on each particle in each pass is affected by the volume swept by the moving particle and residence time in the spray zone. As a result, the inter-particle coefficient of the coating mass distribution predicted by the simulation is larger than that of the analytic model. The inter-particle coefficient of the coating mass distribution predicted by the simulation is very similar to that of the coating layer thickness. However, the difference between the two curves gradually becomes distinct, since the distribution of $N_{dep}$ spreads with increasing coating time. Generally, the trend is that the coefficient of variation quickly decreases in the initial stage and then it gradually asymptotes to zero as time increases. The reduction of the value of the coefficient of variation on the inter-particle scale is faster than that on the intra-particle scale.

## 9.3.5 Coating coverage and uniformity

Figure 9.10 shows the changes of mean coating coverage $\Psi_m$ of all individual particles with coating time. It takes more than 1600 s to achieve a completely closed coating layer on every individual particle in both simulation cases. The rate of increase of coating coverage incrementally decreases as the coating time increases. The mean coating coverage of the simulation without capillary forces is slightly larger than that of the simulation with capillary forces, which can be traced back to the influence of the capillary force on the RTDs in the Wurster coater. Figure 9.11 shows the density distributions of coating coverage $\Psi_j$ obtained from the simulation without capillary forces for different processing times. The coating coverage can be seen to experience a highly peaked distribution at 50 s, flat distributions at 100 s and 200 s, and a highly skewed distribution towards 100 % at 500 s. Note that 100 % is the maximum value that can be achieved according to Eq. (9.21). The shape of the distribution of coating coverage was
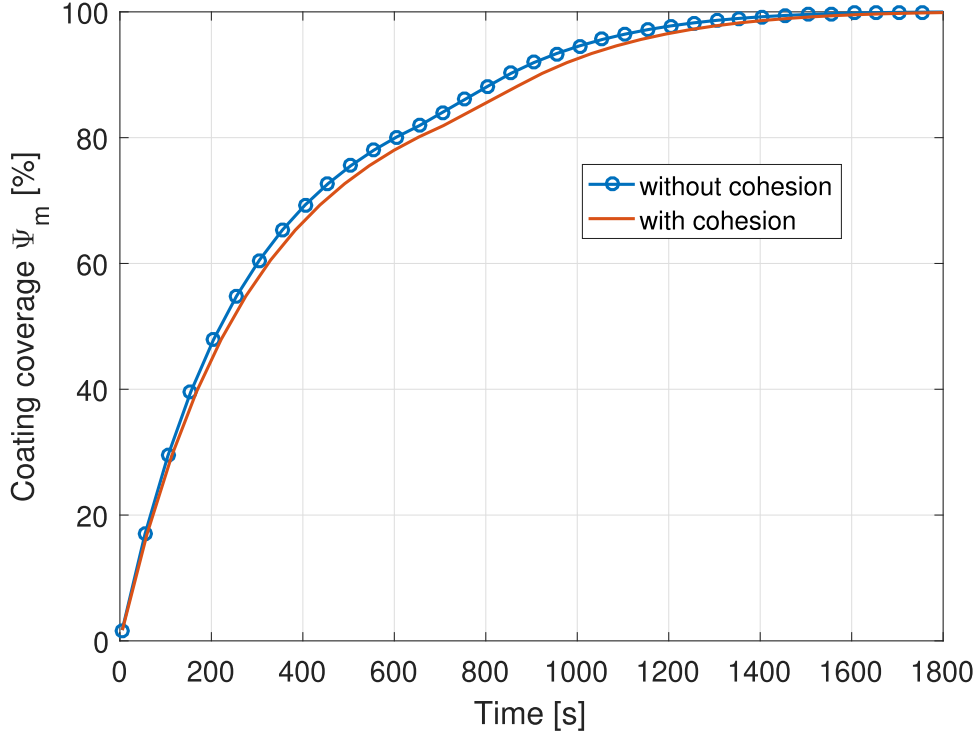
Figure 9.10: Mean coating coverage $\Psi_m$ obtained from simulations with ($\alpha_l = 0.1\%$) and without capillary forces with respect to coating time.

mainly affected by the RTDs in the bed. It is found that the distributions of coating coverage closely follow the Weibull distribution

$$
f_w(x) = \begin{cases} \dfrac{k_1}{k_2} \left(\dfrac{x}{k_2}\right)^{k_1-1} e^{-(x/k_2)^{k_1}}, & x \geq 0, \\ 0, & x < 0. \end{cases} \tag{9.26}
$$

The shape parameter $k_1$ and scale parameter $k_2$ are used to fit the simulation data given in Figure 9.11. Furthermore, information about the time to achieve 100 % coverage is also listed in Table 9.3. The difference of $t_{cover,100}$ at 90 % of the cumulative distribution with and without capillary force is longer than 6 minutes, due to the wider RTDs predicted by the simulation with capillary forces.

Figure 9.12 shows the cumulative distributions of $L_{min}/r_p$ and $S_p$ for the particle population. When capillary force is taken into account in the DEM, the spreads of distributions of $L_{min}/r_p$ and $S_p$ slightly increase due to the effect on RTDs. According to the related data listed in Table 9.3, the coefficients of variation are again much smaller than the values obtained for the single particles.
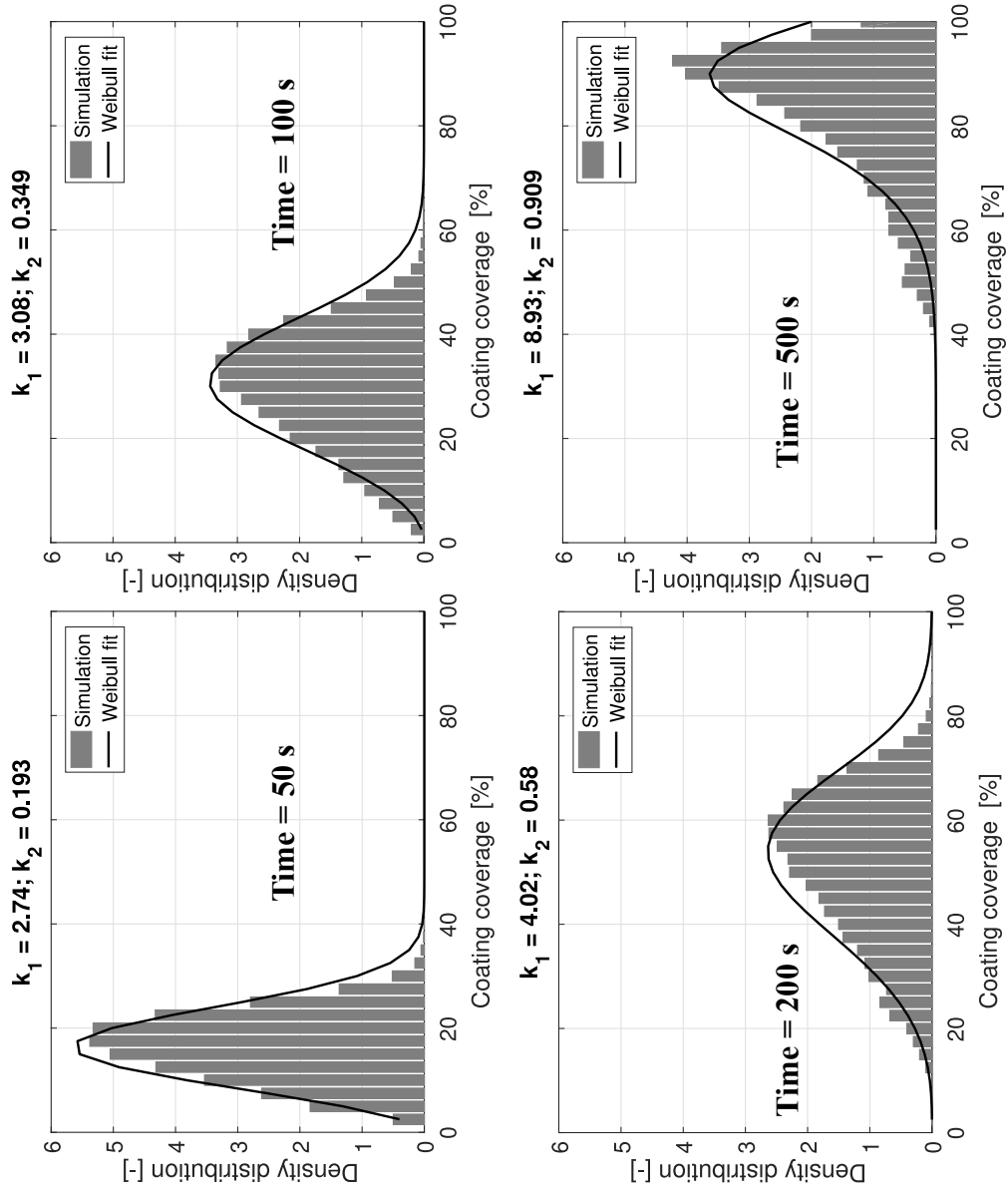
Figure 9.11: Simulation results (without capillary forces) of probability density distributions for coating coverage (grey histograms) of all individual particles at 50 s, 100 s, 200 s and 500 s, together with the fitted Weibull distributions (black lines).
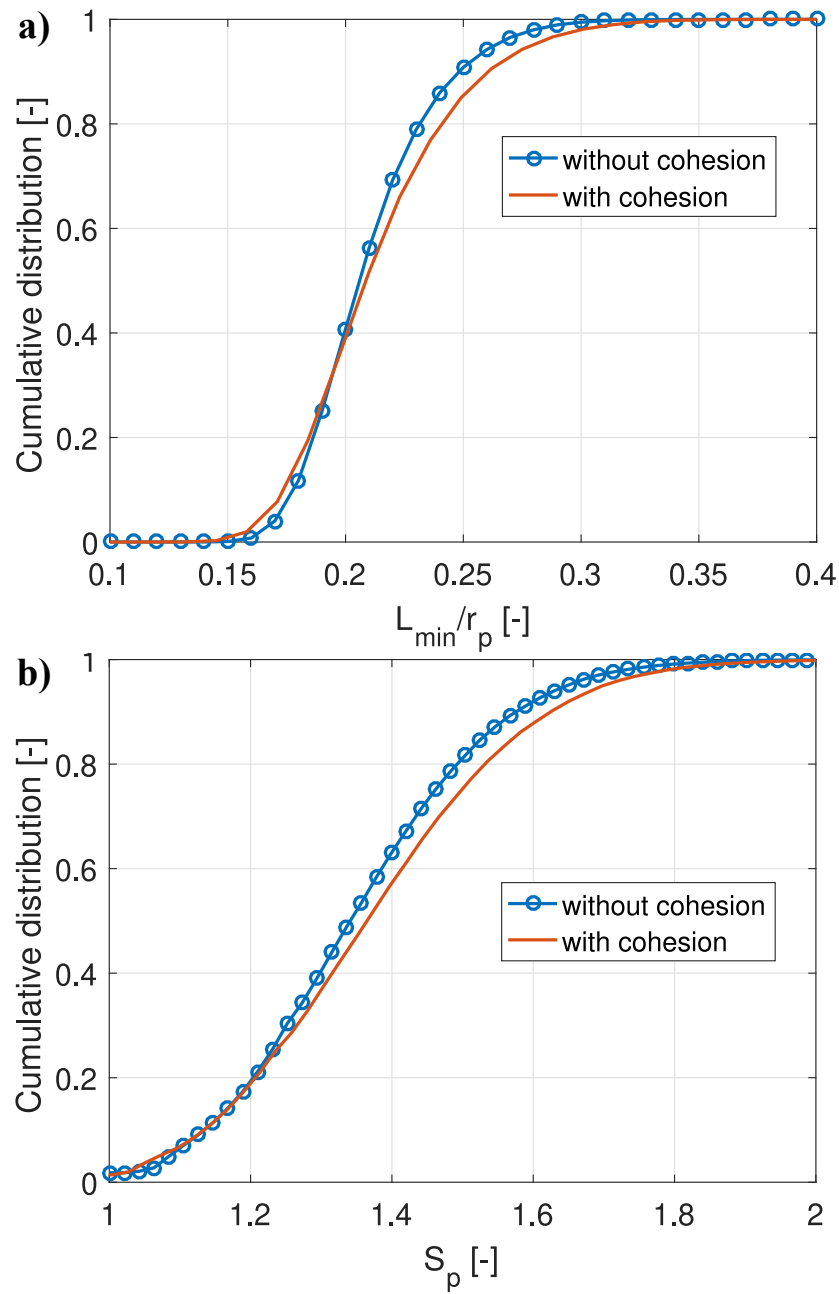
Figure 9.12: Cumulative distributions of inter-particle properties associated with high porosity regions induced by droplet splashing: a) $L_{min}/r_p$, and b) $S_p$ ($\alpha_l = 0.1\%$ in the capillary force model).

# Chapter 10

# Summary and outlook

## 10.1  Summary

The particle formation processes in spray fluidized beds produce various particulate products, which play a major role in many industries. An improved understanding of mesoscale phenomena between individual particles and the processing unit is critical to improve the efficiency of particle formation process and to achieve high product quality.

The methodologies associated with PTV measurements and CFD-DEM/DEM simulations used in this thesis were introduced in Chapter 2 and Chapter 3, respectively. On the basis of four quantitative criteria, the PTV methodology, including both particle segmentation algorithm and particle tracking algorithm, is comprehensively verified using synthetic images obtained from CFD-DEM simulations. All experimental and simulation setups related to the mesoscale phenomena in fluidized beds are systematically described in Chapter 4.

In Chapter 5, the COR of irregularly shaped maltodextrin particles impacting on horizontal substrates is measured by the PTV method. The behavior of collisions is further compared with non-spherical DEM simulations by means of the multi-sphere (MS) and superquadric (SQ) models. A decrease of the normal coefficient of restitution with increasing rotational speed after collision and increasing absolute difference of incidence angle and rebound angle is observed in all measurements and simulations. The predictions of irregular non-convex particles by the multi-sphere model are in better accordance with the measurement data, in terms of the distributions of total and normal coefficients of restitution, as well as of rotational speed after collision.

In Chapter 6, the granular temperature, collision frequency and impact velocity are investigated by the PTV method and CFD-DEM simulation in the mono-disperse system. The algorithms of intensity calibration and determination of collisions are implemented in the PTV method for evaluation of collision dynamics. The global particle circulation pattern of slugging flow regime, two reversely symmetric vortices, could be well represented by PTV measurements and the CFD-DEM simulation. The negative effect of large particle velocity in the dilute regions (freeboard, bubbles and slugs) on

the evaluation of global motion is successfully avoided by means of the time-averaged volume flux of particles instead of time-averaged particle velocity. The magnitude and anisotropy of the granular temperature are significantly reduced as the size of investigation region is decreased from $45 \cdot d_p$ to $6 \cdot d_p$. The magnitude and anisotropy of the granular temperature predicted by the CFD-DEM simulation agree well with PTV results using the small investigation region (c). Within the range of studied experimental conditions, the average granular temperature increased with the increase in superficial gas velocity at any measurement location regardless of the investigation region size. Hence, the time-averaged fluctuation velocity of particles on both the macroscopic and microscopic scale is essentially dependent on energy input. Moreover, the magnitude of granular temperature depends on the local flow regime, and was larger close to the dense bed surface. The experimental average collision frequency tended to be constant or even decrease after exceeding a critical solid volume fraction. It can be postulated that the contribution of increasing solid volume fraction to facilitate particle-particle interactions is overrated by the restraint of decreasing granular temperature. Critical solid volume fractions depend on the global bubble or slug motion. The average collision frequency evaluated from the CFD-DEM simulation data is lower than that from PTV measurements. The measured average impact velocity could be correlated with the average square root of granular temperature by a simple linear equation. The relationships predicted by CFD-DEM are roughly in accordance with measurement data.

Chapter 7 quantifies the dynamics of poly-disperse particle systems in a pseudo-2D fluidized bed by the PTV method and CFD-DEM simulations. The algorithm of color-classification is implemented in the PTV method. Similarly to observations in the mono-disperse system, two reversely turning but nearly symmetric vortices support the vertical and horizontal transport of particles. The change in mixing state, from the stage of increasing mixedness to quasi-equilibrium, can be quantitatively evaluated by the improved Lacey index for poly-disperse systems. The difference in granular temperature for particles of different sizes may lead to deviations of mixing index from unity and corresponding fluctuations. The final mixing state is influenced by the initial mixture conditions, even for cases with very similar Sauter mean diameter, bed height, bed mass; and with the same superficial gas velocity. CFD-DEM simulations with correction for the size dispersity effect agree better with the measurements in terms of time-averaged profiles of volumetric flux, density distributions of particle velocity, cumulative distributions of particle granular temperature and mixing index. Therefore, correction for the size dispersity effect in the drag model is essential to improve the accuracy of CFD-DEM simulations of poly-disperse particle systems in fluidized beds.

In Chapter 8, the cycle time distribution and residence time distributions in the spray zone and the Wurster tube obtained from post-processing of CFD-DEM simulation data are found to be in good agreement with PEPT measurement results for both small and large particles. However, the probability of appearance of non-ideal particle circulation cycles is underestimated for both particle sizes, which might be caused by the particle-particle and particle-wall interactions. The droplet deposition rate is evaluated based on particle-droplet collisions and the residence time in the spray zone. The median

deposition rate on large particles is relatively high, due to their large cross-section and short average distance from the spray nozzle. The high fraction of non-ideal cycles for both particle sizes resulted in broad distributions of droplet deposition rate. Note that relatively high collision velocities in the spray zone prevent the appearance of agglomeration in the Wurster coating process.

Chapter 9 presents a coupled CFD-DEM-Monte Carlo approach together with the spherical centroidal Voronoi tessellation (CVT) for predicting particle dynamics as well as the inter-particle and intra-particle morphology of coating layers. When the capillary force induced by liquid bridges between particles is included in the DEM, the spread of the RTDs in the spray zone and in the Wurster tube increases significantly. According to the circulation features in the Wurster fluidized bed, the cycle time distribution is used as the most important criterion in this work to recur the long-term circulation of individual particles using particle dynamics obtained from a relatively short duration of full CFD-DEM simulations. On the intra-particle scale, the layer thickness distributions are in accordance with available data on particles from coating experiments that had been characterized by X-ray micro-computed tomography ($\mu$-CT); the change of coefficient of variation with time is close to an existing analytic model. The value of the coefficient of variation of layer thickness over the particle population is much smaller than the values of individual particles. The capillary force makes the layer thickness distributions broader due to its influence on RTDs. The density distributions of coating coverage at different times are nearly Weibull. The required $t_{cover,100}$ to achieve a completely closed coating layer on every individual particle is much longer for the simulation with capillary force. With the postulate that splashing of droplets characterized by the dimensionless number $K_d = We^{1/2}Re^{1/4}$ would produce high porosity on deposition panels, the model can predict the uniformity of porosity in the coating layer in terms of distributions of the minimum orthodromic distance $L_{min}$ and the size of individual high porosity regions $S_p$. The simulation with capillary forces predicted slightly higher non-uniformity of high porosity regions for the particle population. In summary, it is important to reduce the negative effects of capillary forces on the coating process by providing enough drying capacity of the fluidization gas and by accurate control of the size distribution of spray droplets. The new numerical method allows to manipulate particles in the Wurster fluidized bed towards desired product properties.

## 10.2  Outlook

The further development of CFD-DEM simulation of solids-fluid flow without chemical reactions should focus on the aspects of non-spherical shape, heat and mass transfer and small particle size (cohesive forces). The non-spherical DEM/CFD-DEM modeling using the composite multi-sphere model and/or the continuous functional approach has a bright future as it provides a new way to upgrade the understanding of industrial processes with realistic non-spherical particle shapes in different configurations (fluidized beds, rotating drums and grinding mills), although there are still some issues related to model development that need to be improved: 1) accurately detect contacts and

evaluate contact forces and cohesive forces depending on complex particle shapes, 2) find appropriate shape factors to derive general correlation on drag coefficient, and 3) efficiently consider the effects of particle shape on heat transfer characteristics based on current thermal DEM for spherical particles [280].
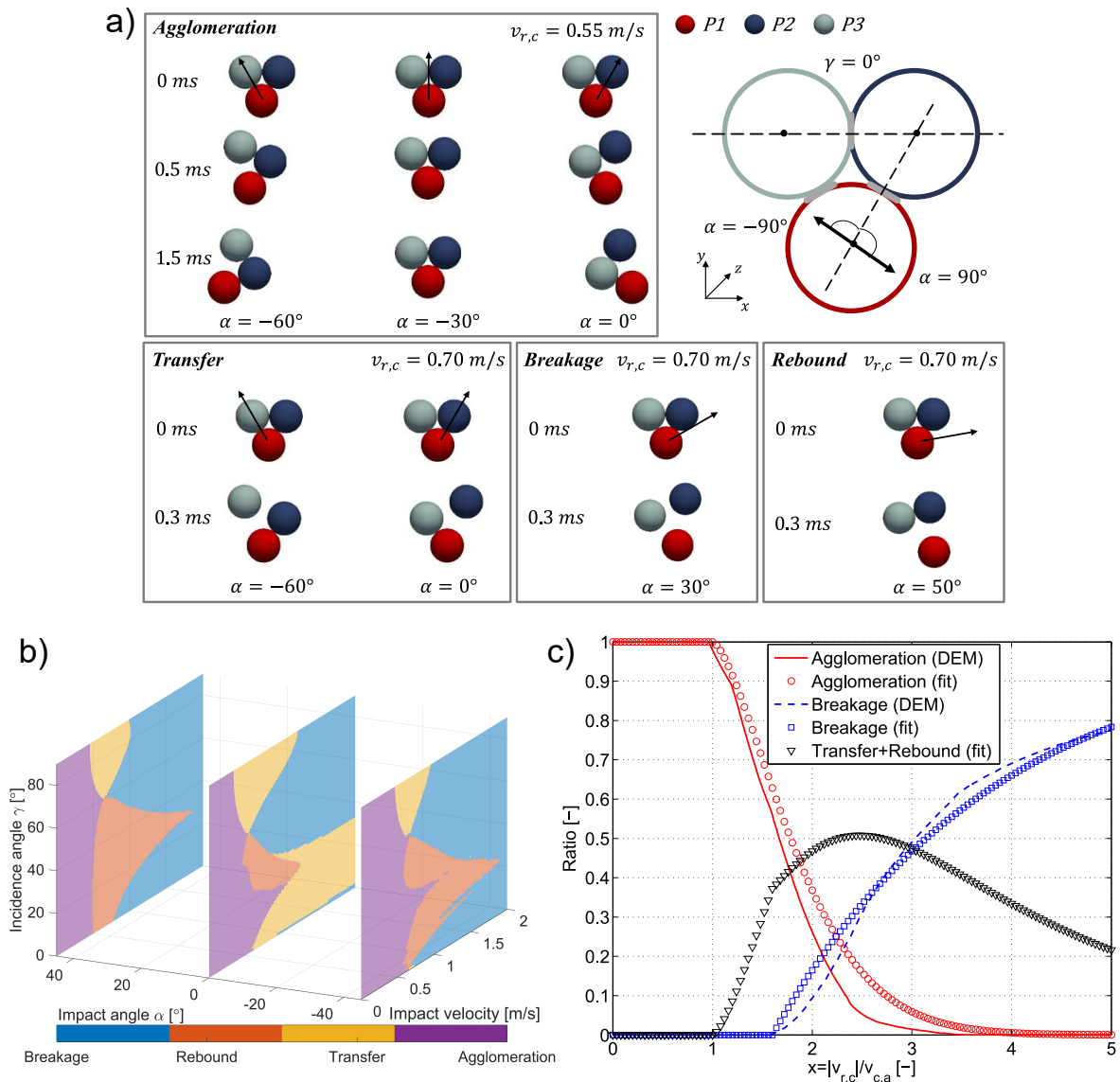


Figure 10.1: Dynamics of singlet-doublet collisions during agglomeration: a) four possible outcomes of singlet-doublet collisions: agglomeration, transfer, rebound and breakage, b) regime maps for different impact angles $\alpha$, and c) probabilities of different outcomes fitted from 3D regime map.

The mesoscale phenomena obtained from CFD-DEM simulations can support the macroscopic modeling approach for particle formation processes in spray fluidized beds. For instance, the ratios of collision outcome with respect to the impact velocity can be

implemented into the kernels of agglomeration and breakage used by McGuire et al. [269], Hussain et al. [281] in population balance modeling, and the breakage algorithm used by Rieck et al. [155] in Monte Carlo modeling.

Similarly to the pre-collision conditions of Liu et al. [26], the outcome of singlet-doublet collisions, including agglomeration, transfer, rebound and breakage, can be studied accounting for the capillary force and viscous force induced by liquid bridges with different wetting conditions, as shown in Figure 10.1a. The singlet-doublet collision pairs cover the pre-collision configurations: impact angle $\alpha \in (-90°, 90°)$ with an interval of 1°, incidence angle $\gamma \in [0, 90°]$ with an interval of 1°, and magnitude of impact velocity $v_{im} \in [0.005, 1]$ with an interval of 0.005 m/s. Figure 10.1b shows regime maps of different impact angles. By counting numbers of different outcome in all regime maps, the probabilities of a certain outcome can be evaluated with respect to the normalized impact velocity, as shown in Figure 10.1c. The ratio of agglomeration $R_a$ and the ratio of breakage $R_b$ can be fitted as:

$$R_a(x) = \begin{cases} 1, & 0 < x \leq \dfrac{v_{m,a}}{v_{c,a}}, \\ e^{-\left(x - \frac{v_{m,a}}{v_{c,a}}\right)^A}, & \dfrac{v_{m,a}}{v_{c,a}} < x \leq 5, \end{cases} \tag{10.1}$$

$$R_b(x) = \begin{cases} 0, & 0 < x \leq \dfrac{v_{m,b}}{v_{c,a}}, \\ 1 - e^{-B\left(x - \frac{v_{m,b}}{v_{c,a}}\right)}, & \dfrac{v_{m,b}}{v_{c,a}} < x \leq 5. \end{cases} \tag{10.2}$$

In the equations, $x$ is the ratio of relative collision velocity $v_{r,c}$ and the critical agglomeration velocity $v_{c,a}$ predicted using the Ennis model [20]; $v_{m,a}$ is the maximum velocity to retain completely agglomeration; $v_{m,b}$ is the minimum velocity to produce breakage. The values of $v_{m,a}$ and $v_{m,b}$ can be directly extracted from regime map. In the considered wetting conditions of liquid bridge, constant values of $A = 1.6$ and $B = 0.45$ have been obtained.

To reduce the computational effort, several coarse-grain models have been developed and validated in CFD-DEM to deal with mechanical particle-particle contact force and particle-fluid interaction force. However, a new coarse-grain model related to heat (mass) transfer is required to be developed for temperature sensitive granular flow systems. The mesh-free smoothed particle hydrodynamics (SPH) method has been used to study the droplet behavior (deposition, splashing and solidification) [282–284]. An SPH method coupled with DEM method [285] has the potential to investigate individual droplet-particle interactions in spray fluidized beds.

# References

[1] C.T. Crowe, J.D. Schwarzkopf, M. Sommerfeld, Y. Tsuji, Multiphase Flows with Droplets and Particles, Second Edition, CRC Press, Boca Raton, 2011.

[2] C.T. Crowe, Multiphase Flow Handbook, CRC Press, Boca Raton, 2005.

[3] L. Mörl, S. Heinrich, M. Peglow, Fluidized bed spray granulation, in: A.D. Salman, M. Hounslow, J.P. Seville (Eds.), Handbook of Powder Technology, vol. 11, Elsevier, Amsterdam, 21–188, 2007.

[4] M. Peglow, S. Antonyuk, M. Jacob, S. Palzer, S. Heinrich, E. Tsotsas, Particle Formulation in Spray Fluidized Beds, in: E. Tsotsas, A.S. Mujumdar (Eds.), Modern Drying Technology, WILEY-VCH Verlag GmbH & Co. KGaA, Weinheim, 295–378, 2011.

[5] M. Jacob, Granulation Equipment, in: A.D. Salman, M. Hounslow, J.P. Seville (Eds.), Handbook of Powder Technology, vol. 11, Elsevier, Amsterdam, 417–476, 2007.

[6] N. Hampel, A. Bück, M. Peglow, E. Tsotsas, Continuous pellet coating in a Wurster fluidized bed process, Chemical Engineering Science 86 (2013) 87–98.

[7] A. Bück, C. Neugebauer, K. Meyer, S. Palis, E. Diez, A. Kienle, S. Heinrich, E. Tsotsas, Influence of operation parameters on process stability in continuous fluidised bed layering with external product classification, Powder Technology 300 (2016) 37–45.

[8] D. Müller, A. Bück, E. Tsotsas, Influence of separation properties and processing strategies on product characteristics in continuous fluidized bed spray granulation, Powder Technology 342 (2019) 572 – 584.

[9] P. Bachmann, A. Bück, E. Tsotsas, Investigation of the residence time behavior of particulate products and correlation for the bodenstein number in horizontal fluidized beds, Powder Technology 301 (2016) 1067 – 1076.

[10] K. Chen, P. Bachmann, A. Bück, M. Jacob, E. Tsotsas, Experimental study and modeling of particle drying in a continuously-operated horizontal fluidized bed, Particuology 34 (2017) 134 – 146.

[11] A joint virtual special issue of Chemical Engineering Science, Powder Technology and Particuology, Towards engineering mesoscience, 2013.

[12] R.B. Bird, W.E. Stewart, E.N. Lightfoot, Transport Phenomena, Second Edition, John Wiley & Sons, Inc, New York, 2002.

[13] F. Sondej, A. Bück, E. Tsotsas, Comparative analysis of the coating thickness on single particles using X-ray micro-computed tomography and confocal laser-scanning microscopy, Powder Technology 287 (2016) 330–340.

[14] M. Schmidt, A. Bück, E. Tsotsas, Shell porosity in spray fluidized bed coating with suspensions, Advanced Powder Technology 28 (11) (2017) 2921–2928.

[15] E. Tsotsas, Influence of drying kinetics on particle formation: A personal perspective, Drying Technology 30 (11-12) (2012) 1167–1175.

[16] C. Rieck, T. Hoffmann, A. Bück, M. Peglow, E. Tsotsas, Influence of drying conditions on layer porosity in fluidized bed spray granulation, Powder Technology 272 (2015) 120–131.

[17] M. Schmidt, A. Bück, E. Tsotsas, Experimental investigation of process stability of continuous spray fluidized bed layering with internal separation, Chemical Engineering Science 126 (2015) 55–66.

[18] M. Schmidt, C. Rieck, A. Bück, E. Tsotsas, Experimental investigation of process stability of continuous spray fluidized bed layering with external product separation, Chemical Engineering Science 137 (2015) 466–475.

[19] E. Tsotsas, Multiscale approaches to processes that combine drying with particle formation, Drying Technology 33 (15-16) (2015) 1859–1871.

[20] B.J. Ennis, G. Tardos, R. Pfeffer, A microlevel-based characterization of granulation phenomena, Powder Technology 65 (1) (1991) 257–272.

[21] C. Thornton, Z.M. Ning, A theoretical model for the stick/bounce behaviour of adhesive, elastic-plastic spheres, Powder Technology 99 (2) (1998) 154–162.

[22] N.V. Brilliantov, N. Albers, F. Spahn, T. Pöschel, Collision dynamics of granular particles with adhesion, Physical Review E 76 (5) (2007) 051302.

[23] C.M. Donahue, W.M. Brewer, R.H. Davis, C.M. Hrenya, Agglomeration and de-agglomeration of rotating wet doublets, Journal of Fluid Mechanics 708 (2012) 128–148.

[24] V.S. Sutkar, N.G. Deen, J.T. Padding, J.A.M. Kuipers, V. Salikov, B. Crüger, S. Antonyuk, S. Heinrich, A novel approach to determine wet restitution coefficients through a unified correlation and energy analysis, AIChE Journal 61 (3) (2015) 769–779.

[25] C.M. Donahue, C.M. Hrenya, R.H. Davis, K.J. Nakagawa, A.P. Zelinskaya, G.G. Joseph, Stokes' cradle: Normal three-body collisions between wetted particles, Journal of Fluid Mechanics 650 (2010) 479–504.

[26] P. Liu, K.M. Kellogg, C.Q. LaMarche, C.M. Hrenya, Dynamics of singlet-doublet collisions of cohesive particles, Chemical Engineering Journal 324 (2017) 380–391.

[27] L. Li, A. Rasmuson, A. Ingram, M. Johansson, J. Remmelgas, C. von Corswant, S. Folestad, PEPT study of particle cycle and residence time distributions in a Wurster fluid bed, AIChE Journal 61 (3) (2015) 756–768.

[28] M. Börner, T. Hagemeier, G. Ganzer, M. Peglow, E. Tsotsas, Experimental spray zone characterization in top-spray fluidized bed granulation, Chemical Engineering Science 116 (2014) 317–330.

[29] K. KuShaari, P. Pandey, Y. Song, R. Turton, Monte Carlo simulations to determine coating uniformity in a Wurster fluidized bed coating process, Powder Technology 166 (2) (2006) 81–90.

[30] P.D. Hede, P. Bach, A.D. Jensen, Two-fluid spray atomisation and pneumatic nozzles for fluid bed coating/agglomeration purposes: A review, Chemical Engineering Science 63 (14) (2008) 3821–3842.

[31] A.L. Yarin, Drop impact dynamics: Splashing, spreading, receding, bouncing, Annual Review of Fluid Mechanics 38 (1) (2006) 159–192.

[32] A. Rozhkov, B. Prunet-Foch, M. Vignes-Adler, Impact of water drops on small targets, Physics of Fluids 14 (10) (2002) 3485–3501.

[33] S.K. Pawar, F. Henrikson, G. Finotello, J.T. Padding, N.G. Deen, A. Jongsma, F. Innings, J.A.M. Kuipers, An experimental study of droplet-particle collisions, Powder Technology 300 (2016) 157–163.

[34] S. Mitra, G.M. Evans, E. Doroodchi, V. Pareek, J.B. Joshi, Interactions in droplet and particle system of near unity size ratio, Chemical Engineering Science 170 (2017) 154–175.

[35] J. Westerweel, G.E. Elsinga, R.J. Adrian, Particle image velocimetry for complex and turbulent flows, Annual Review of Fluid Mechanics 45 (1) (2013) 409–436.

[36] J.M. Link, N.G. Deen, J.A.M. Kuipers, X. Fan, A. Ingram, D.J. Parker, J. Wood, J.P.K. Seville, PEPT and discrete particle simulation study of spout-fluid bed regimes, AIChE Journal 54 (5) (2008) 1189–1202.

[37] G. Mohs, O. Gryczka, S. Heinrich, L. Mörl, Magnetic monitoring of a single particle in a prismatic spouted bed, Chemical Engineering Science 64 (23) (2009) 4811–4825.

[38] L.F. Gladden, A.J. Sederman, Magnetic resonance imaging and velocity mapping in chemical engineering applications, Annual Review of Chemical and Biomolecular Engineering 8 (1) (2017) 227–247.

[39] T.J. Heindel, A review of X-ray flow visualization with applications to multiphase flows, Journal of Fluids Engineering 133 (7) (2011) 074001.

[40] H. Capart, D.L. Young, Y. Zech, Voronoï imaging methods for the measurement of granular flows, Experiments in Fluids 32 (1) (2002) 121–135.

[41] C. You, H. Zhao, Y. Cai, H. Qi, X. Xu, Experimental investigation of interparticle collision rate in particulate flow, International Journal of Multiphase Flow 30 (9) (2004) 1121–1138.

[42] T. Hagemeier, C. Roloff, A. Bück, E. Tsotsas, Estimation of particle dynamics in 2-D fluidized beds using particle tracking velocimetry, Particuology 22 (2014) 39–51.

[43] T. Hagemeier, M. Börner, A. Bück, E. Tsotsas, A comparative study on optical techniques for the estimation of granular flow velocities, Chemical Engineering Science 131 (2015) 63–75.

[44] K. Meyer, A. Bück, E. Tsotsas, Determination of particle exchange rates at overflow weirs in horizontal fluidised beds by particle tracking velocimetry, Particuology 32 (2017) 1–9.

[45] Z. Jiang, T. Hagemeier, A. Bück, E. Tsotsas, Color-PTV measurement and CFD-DEM simulation of the dynamics of poly-disperse particle systems in a pseudo-2D fluidized bed, Chemical Engineering Science 179 (2018) 115–132.

[46] M Stein, Y.L. Ding, J.P.K. Seville, D.J. Parker, Solids motion in bubbling gas fluidised beds, Chemical Engineering Science 55 (22) (2000) 5291–5300.

[47] S.H. Schaafsma, T. Marx, A.C. Hoffmann, Investigation of the particle flowpattern and segregation in tapered fluidized bed granulators, Chemical Engineering Science 61 (14) (2006) 4467–4475.

[48] D.J. Parker, X. Fan, Positron emission particle tracking—Application and labelling techniques, Particuology 6 (1) (2008) 16–23.

[49] C. Chan, J.P.K. Seville, D.J. Parker, J. Baeyens, Particle velocities and their residence time distribution in the riser of a CFB, Powder Technology 203 (2) (2010) 187–197.

[50] T.W. Leadbeater, D.J. Parker, J. Gargiuli, Positron imaging systems for studying particulate, granular and multiphase flows, Particuology 10 (2) (2012) 146–153.

[51] K.A. Buist, A.C. Gaag, N.G. Deen, J.A.M. Kuipers, Improved magnetic particle tracking technique in dense gas fluidized beds, AIChE Journal 60 (9) (2014) 3133–3142.

[52] L. Zhang, F. Weigler, V. Idakiev, Z. Jiang, L. Mörl, J. Mellmann, E. Tsotsas, Experimental study of the particle motion in flighted rotating drums by means of Magnetic Particle Tracking, Powder Technology 339 (2018) 817–826.

[53] D.J. Holland, C.R. Müller, J.S. Dennis, L.F. Gladden, A.J. Sederman, Spatially resolved measurement of anisotropic granular temperature in gas-fluidized beds, Powder Technology 182 (2) (2008) 171–181.

[54] C.R. Müller, D.J. Holland, A.J. Sederman, S.A. Scott, J.S. Dennis, L.F. Gladden, Granular temperature: Comparison of magnetic resonance measurements with discrete element model simulations, Powder Technology 184 (2) (2008) 241–253.

[55] C.M. Boyce, N.P. Rice, A. Ozel, J.F. Davidson, A.J. Sederman, L.F. Gladden, S. Sundaresan, J.S. Dennis, D.J. Holland, Magnetic resonance characterization of coupled gas and particle dynamics in a bubbling fluidized bed, Physical Review Fluids 1 (7) (2016) 074201.

[56] U. Kertzscher, A. Seeger, K. Affeld, L. Goubergrits, E. Wellnhofer, X-ray based particle tracking velocimetry–a measurement technique for multi-phase flows and flows without optical access, Flow Measurement and Instrumentation 15 (4) (2004) 199–206.

[57] D. Escudero, T.J. Heindel, Bed height and material density effects on fluidized bed hydrodynamics, Chemical Engineering Science 66 (16) (2011) 3648–3655.

[58] X. Chen, W. Zhong, T.J. Heindel, Using stereo XPTV to determine cylindrical particle distribution and velocity in a binary fluidized bed, AIChE Journal 65 (2) (2019) 520–535.

[59] K. Chen, P. Bachmann, A. Bück, M. Jacob, E. Tsotsas, CFD simulation of particle residence time distribution in industrial scale horizontal fluidized bed, Powder Technology 345 (2019) 129–139.

[60] D. Gidaspow, Multiphase Flow and Fluidization: Continuum and Kinetic Theory Descriptions, Academic Press, San Diego, 1994.

[61] S. Subramaniam, Lagrangian–Eulerian methods for multiphase flows, Progress in Energy and Combustion Science 39 (2-3) (2013) 215–245.

[62] O.O. Olaofe, A.V. Patil, N.G. Deen, M.A. van der Hoef, J.A.M. Kuipers, Simulation of particle mixing and segregation in bidisperse gas fluidized beds, Chemical Engineering Science 108 (2014) 258–269.

[63] T. Oschmann, J. Hold, H. Kruggel-Emden, Numerical investigation of mixing and orientation of non-spherical particles in a model type fluidized bed, Powder Technology 258 (2014) 304–323.

[64] S.L.L. Seah, E.W.C. Lim, Density segregation of dry and wet granular mixtures in gas fluidized beds, AIChE Journal 61 (12) (2015) 4069–4086.

[65] K. Vollmari, T. Oschmann, H. Kruggel-Emden, Mixing quality in mono- and bidisperse systems under the influence of particle shape: A numerical and experimental study, Powder Technology 308 (2017) 101–113.

[66] L. Lu, Y. Xu, T. Li, S. Benyahia, Assessment of different coarse graining strategies to simulate polydisperse gas-solids flow, Chemical Engineering Science 179 (2018) 53–63.

[67] N.G. Deen, E.A.J.F. Peters, J.T. Padding, J.A.M. Kuipers, Review of direct numerical simulation of fluid–particle mass, momentum and heat transfer in dense gas–solid flows, Chemical Engineering Science 116 (2014) 710–724.

[68] F. Sudbrock, H. Kruggel-Emden, S. Wirtz, V. Scherer, Convective drying of agitated silica gel and beech wood particle beds: Experiments and transient DEM-CFD simulations, Drying Technology 33 (15-16) (2015) 1808–1820.

[69] A.V. Patil, E.A.J.F. Peters, J.A.M. Kuipers, Comparison of CFD–DEM heat transfer simulations with infrared/visual measurements, Chemical Engineering Journal 277 (2015) 388–401.

[70] M. Askarishahi, M.S. Salehi, S. Radl, Full-physics simulations of spray-particle interaction in a bubbling fluidized bed, AIChE Journal 63 (7) (2017) 2569–2587.

[71] J. Azmir, Q. Hou, A.B. Yu, Discrete particle simulation of food grain drying in a fluidised bed, Powder Technology 323 (2018) 238–249.

[72] J.E. Hilton, L.R. Mason, P.W. Cleary, Dynamics of gas–solid fluidised beds with non-spherical particle geometry, Chemical Engineering Science 65 (5) (2010) 1584–1596.

[73] Z.Y. Zhou, D. Pinson, R.P. Zou, A.B. Yu, Discrete particle simulation of gas fluidization of ellipsoidal particles, Chemical Engineering Science 66 (23) (2011) 6128–6145.

[74] B. Ren, W. Zhong, Y. Chen, X. Chen, B. Jin, Z. Yuan, Y. Lu, CFD-DEM simulation of spouting of corn-shaped particles, Particuology 10 (5) (2012) 562–572.

[75] K. Vollmari, R. Jasevičius, H. Kruggel-Emden, Experimental and numerical study of fluidization and pressure drop of spherical and non-spherical particles in a model scale fluidized bed, Powder Technology 291 (2016) 506–521.

[76] V.V. Mahajan, T.M.J. Nijssen, J.A.M. Kuipers, J.T. Padding, Non-spherical particles in a pseudo-2D fluidised bed: Modelling study, Chemical Engineering Science 192 (2018) 1105–1123.

[77] M. Sakai, M. Abe, Y. Shigeto, S. Mizutani, H. Takahashi, A. Viré, J.R. Percival, J. Xiang, C.C. Pain, Verification and validation of a coarse grain model of the DEM in a bubbling fluidized bed, Chemical Engineering Journal 244 (2014) 33–43.

[78] A. Ozel, J. Kolehmainen, S. Radl, S. Sundaresan, Fluid and particle coarsening of drag force for discrete-parcel approach, Chemical Engineering Science 155 (2016) 258–267.

[79] V. Verma, T. Li, J. De Wilde, Coarse-grained discrete particle simulations of particle segregation in rotating fluidized beds in vortex chambers, Powder Technology 318 (2017) 282–292.

[80] K. Takabatake, Y. Mori, J.G. Khinast, M. Sakai, Numerical investigation of a coarse-grain discrete element method in solid mixing in a spouted bed, Chemical Engineering Journal 346 (2018) 416–426.

[81] J.E. Galvin, S. Benyahia, The effect of cohesive forces on the fluidization of aeratable powders, AIChE Journal 60 (2) (2014) 473–484.

[82] Y. Gu, A. Ozel, S. Sundaresan, A modified cohesion model for CFD–DEM simulations of fluidization, Powder Technology 296 (2016) 17–28.

[83] M. Girardi, S. Radl, S. Sundaresan, Simulating wet gas–solid fluidized beds using coarse-grid CFD-DEM, Chemical Engineering Science 144 (2016) 224–238.

[84] D. Liu, B.G.M. van Wachem, R.F. Mudde, X. Chen, J.R. van Ommen, An adhesive CFD-DEM model for simulating nanoparticle agglomerate fluidization, AIChE Journal 62 (7) (2016) 2259–2270.

[85] H. Xu, W. Zhong, Z. Yuan, A.B. Yu, CFD-DEM study on cohesive particles in a spouted bed, Powder Technology 314 (2017) 377–386.

[86] A. Di Renzo, F. Cello, F.P. Di Maio, Simulation of the layer inversion phenomenon in binary liquid–fluidized beds by DEM–CFD with a drag law for polydisperse systems, Chemical Engineering Science 66 (13) (2011) 2945–2958.

[87] S. Wang, Z. Sun, X. Li, J. Gao, X. Lan, Q. Dong, Simulation of flow behavior of particles in liquid–solid fluidized bed with uniform magnetic field, Powder Technology 237 (2013) 314–325.

[88] K. Kerst, C. Roloff, L.G. Medeiros de S., A. Bartz, A. Seidel-Morgenstern, D. Thévenin, G. Janiga, CFD-DEM simulations of a fluidized bed crystallizer, Chemical Engineering Science 165 (2017) 1–13.

[89] H. Zbib, M. Ebrahimi, F. Ein-Mozaffari, A. Lohi, Comprehensive analysis of fluid-particle and particle-particle interactions in a liquid-solid fluidized bed via CFD-DEM coupling and tomography, Powder Technology 340 (2018) 116–130.

[90] E. Abbaszadeh Molaei, A.B. Yu, Z.Y. Zhou, Particle scale modelling of solid flow characteristics in liquid fluidizations of ellipsoidal particles, Powder Technology 338 (2018) 677–691.

[91] L. Fries, S. Antonyuk, S. Heinrich, D. Dopfer, S. Palzer, Collision dynamics in fluidised bed granulators: A DEM-CFD study, Chemical Engineering Science 86 (2013) 108–123.

[92] S. Yang, K. Luo, J. Fan, K. Cen, Particle-scale investigation of the solid dispersion and residence properties in a 3-D spout-fluid bed, AIChE Journal 60 (8) (2014) 2788–2804.

[93] L. Li, J. Remmelgas, B.G.M. van Wachem, C. von Corswant, M. Johansson, S. Folestad, A. Rasmuson, Residence time distributions of different size particles in the spray zone of a Wurster fluid bed studied using DEM-CFD, Powder Technology 280 (2015) 124–134.

[94] M. Börner, A. Bück, E. Tsotsas, DEM-CFD investigation of particle residence time distribution in top-spray fluidised bed granulation, Chemical Engineering Science 161 (2017) 187–197.

[95] K. Vollmari, H. Kruggel-Emden, Numerical and experimental analysis of particle residence times in a continuously operated dual-chamber fluidized bed, Powder Technology 338 (2018) 625–637.

[96] D. Jajcevic, E. Siegmann, C. Radeke, J.G. Khinast, Large-scale CFD–DEM simulations of fluidized granular systems, Chemical Engineering Science 98 (2013) 298–310.

[97] T. Lichtenegger, E.A.J.F. Peters, J.A.M. Kuipers, S. Pirker, A recurrence CFD study of heat transfer in a fluidized bed, Chemical Engineering Science 172 (2017) 310–322.

[98] V.S. Sutkar, N.G. Deen, A.V. Patil, V. Salikov, S. Antonyuk, S. Heinrich, J.A.M. Kuipers, CFD–DEM model for coupled heat and mass transfer in a spout fluidized bed with liquid injection, Chemical Engineering Journal 288 (2016) 185–197.

[99] J.E. Hilton, D.Y. Ying, P.W. Cleary, Modelling spray coating using a combined CFD–DEM and spherical harmonic formulation, Chemical Engineering Science 99 (2013) 141–160.

[100] R. Sun, H. Xiao, Diffusion-based coarse graining in hybrid continuum–discrete solvers: Theoretical formulation and a priori tests, International Journal of Multiphase Flow 77 (2015) 142–157.

[101] J.Q. Gan, Z.Y. Zhou, A.B. Yu, A GPU-based DEM approach for modelling of particulate systems, Powder Technology 301 (2016) 1172–1182.

[102] G. Kotalczyk, J. Devi, F.E. Kruis, A time-driven constant-number Monte Carlo method for the GPU-simulation of particle breakage based on weighted simulation particles, Powder Technology 317 (2017) 417–429.

[103] W. Zhong, A. Yu, X. Liu, Z. Tong, H. Zhang, DEM/CFD-DEM modelling of non-spherical particulate systems: Theoretical developments and applications, Powder Technology 302 (2016) 108–152.

[104] Z. Jiang, T. Hagemeier, A. Bück, E. Tsotsas, Experimental measurements of particle collision dynamics in a pseudo-2D gas-solid fluidized bed, Chemical Engineering Science 167 (2017) 297–316.

[105] Z. Jiang, J. Du, C. Rieck, A. Bück, E. Tsotsas, PTV experiments and non-spherical DEM simulations of the coefficient of restitution for irregular particles impacting on horizontal substrates, Powder Technology 360 (2020) 352–365.

[106] C. Cierpka, B. Lütke, C.J. Kähler, Higher order multi-frame particle tracking velocimetry, Experiments in Fluids 54 (5) (2013) 1–12.

[107] K. Takehara, T. Etoh, A study on particle identification in ptv particle mask correlation method, Journal of Visualization 1 (3) (1998) 313–323.

[108] K. Ohmi, H. Li, Particle-tracking velocimetry with new algorithms, Measurement Science and Technology 11 (6) (2000) 603–616.

[109] F. Meyer, Topographic distance and watershed lines, Signal Processing 38 (1) (1994) 113–125.

[110] M.K. Hu, Visual pattern recognition by moment invariants, IRE Transactions on Information Theory 8 (2) (1962) 179–187.

[111] M.R. Teague, Image analysis via the general theory of moments, Journal of the Optical Society of America 70 (8) (1980) 920–930.

[112] S.J. Baek, S.J. Lee, A new two-frame particle tracking algorithm using match probability, Experiments in Fluids 22 (1) (1996) 23–32.

[113] F. Pereira, H. Stüer, E.C. Graff, M. Gharib, Two-frame 3D particle tracking, Measurement Science and Technology 17 (7) (2006) 1680–1692.

[114] W. Brevis, Y. Niño, G.H. Jirka, Integrating cross-correlation and relaxation algorithms for particle tracking velocimetry, Experiments in Fluids 50 (1) (2010) 135–147.

[115] S.T. Barnard, W.B. Thompson, Disparity analysis of images, IEEE Transactions on Pattern Analysis and Machine Intelligence PAMI-2 (4) (1980) 333–340.

[116] Y.A. Hassan, T.K. Blanchat, C.H. Seeley Jr, PIV flow visualisation using particle tracking techniques, Measurement Science and Technology 3 (7) (1992) 633.

[117] K. Okamoto, S. Nishio, T. Saga, T. Kobayashi, Standard images for particle-image velocimetry, Measurement Science and Technology 11 (6) (2000) 685.

[118] B. Lecordier, D. Demare, L. M. J. Vervisch, J. Réveillon, M. Trinité, Estimation of the accuracy of PIV treatments for turbulent flow studies by direct numerical simulation of multi-phase flow, Measurement Science and Technology 12 (9) (2001) 1382.

[119] J.F. de Jong, S.O. Odu, M.S. van Buijtenen, N.G. Deen, M. van Sint Annaland, J.A.M. Kuipers, Development and validation of a novel Digital Image Analysis method for fluidized bed Particle Image Velocimetry, Powder Technology 230 (2012) 193–202.

[120] Z. Jiang, A. Bück, E. Tsotsas, CFD–DEM study of residence time, droplet deposition, and collision velocity for a binary particle mixture in a Wurster fluidized bed coater, Drying Technology 36 (6) (2018) 638–650.

[121] Z. Jiang, C. Rieck, A. Bück, E. Tsotsas, Modeling of inter- and intra-particle coating uniformity in a Wurster fluidized bed by a coupled CFD-DEM-Monte Carlo approach, Chemical Engineering Science 211 (2020) 115289.

[122] T.B. Anderson, R. Jackson, Fluid mechanical description of fluidized beds: Equations of motion, Industrial & Engineering Chemistry Fundamentals 6 (4) (1967) 527–539.

[123] Z.Y. Zhou, S.B. Kuang, K.W. Chu, A.B. Yu, Discrete particle simulation of particle–fluid flow: Model formulations and their applicability, Journal of Fluid Mechanics 661 (2010) 482–510.

[124] J. Ding, D. Gidaspow, A bubbling fluidization model using kinetic theory of granular flow, AIChE Journal 36 (4) (1990) 523–538.

[125] P.A. Cundall, O.D.L. Strack, A discrete numerical model for granular assemblies, Géotechnique 29 (1) (1979) 47–65.

[126] H.P. Zhu, Z.Y. Zhou, R.Y. Yang, A.B. Yu, Discrete particle simulation of particulate systems: Theoretical developments, Chemical Engineering Science 62 (13) (2007) 3378–3396.

[127] Y. Tsuji, T. Kawaguchi, T. Tanaka, Discrete particle simulation of two-dimensional fluidized bed, Powder Technology 77 (1) (1993) 79–87.

[128] C. Goniva, C. Kloss, N.G. Deen, J.A.M. Kuipers, S. Pirker, Influence of rolling friction on single spout fluidized bed simulation, Particuology 10 (5) (2012) 582–591.

[129] R. Di Felice, Hydrodynamics of liquid fluidisation, Chemical Engineering Science 50 (8) (1995) 1213–1245.

[130] D.L. Koch, R.J. Hill, Inertial effects in suspension and porous-media flows, Annual Review of Fluid Mechanics 33 (1) (2001) 619–647.

[131] A. Hölzer, M. Sommerfeld, New simple correlation formula for the drag coefficient of non-spherical particles, Powder Technology 184 (3) (2008) 361–365.

[132] M. Zastawny, G. Mallouppas, F. Zhao, B. van Wachem, Derivation of drag and lift force and torque coefficients for non-spherical particles in flows, International Journal of Multiphase Flow 39 (2012) 227–239.

[133] S. Ergun, Fluid flow through packed columns, Chemical Engineering Process 48 (1952) 89–94.

[134] C.Y. Wen, Y.H. Yu, A generalized method for predicting the minimum fluidization velocity, AIChE Journal 12 (3) (1966) 610–612.

[135] M.A. van der Hoef, R. Beetstra, J.A.M. Kuipers, Lattice-Boltzmann simulations of low-Reynolds-number flow past mono- and bidisperse arrays of spheres: Results for the permeability and drag force, Journal of Fluid Mechanics 528 (2005) 233–254.

[136] R. Beetstra, M.A. van der Hoef, J.A.M. Kuipers, Numerical study of segregation using a new drag force correlation for polydisperse systems derived from lattice-Boltzmann simulations, Chemical Engineering Science 62 (1-2) (2007) 246–255.

[137] R. Beetstra, M.A. van der Hoef, J.A.M. Kuipers, Drag force of intermediate Reynolds number flow past mono- and bidisperse arrays of spheres, AIChE Journal 53 (2) (2007) 489–501.

[138] Y. Tang, E.A.J.F. Peters, J.A.M. Kuipers, S.H.L. Kriebitzsch, M.A. van der Hoef, A new drag correlation from fully resolved simulations of flow past monodisperse static arrays of spheres, AIChE Journal 61 (2) (2015) 688–698.

[139] J.M. Link, L.A. Cuypers, N.G. Deen, J.A.M. Kuipers, Flow regimes in a spout–fluid bed: A combined experimental and simulation study, Chemical Engineering Science 60 (13) (2005) 3425–3442.

[140] N.G. Deen, M. van Sint Annaland, M.A. van der Hoef, J.A.M. Kuipers, Review of discrete particle modeling of fluidized beds, Chemical Engineering Science 62 (1-2) (2007) 28–44.

[141] S. Luding, Cohesive, frictional powders: Contact models for tension, Granular Matter 10 (4) (2008) 235.

[142] Y. Tsuji, T. Tanaka, T. Ishida, Lagrangian numerical simulation of plug flow of cohesionless particles in a horizontal pipe, Powder Technology 71 (3) (1992) 239–250.

[143] D. Antypov, J.A. Elliott, On an analytical solution for the damped Hertzian spring, EPL 94 (5) (2011) 50004.

[144] J. Ai, J. Chen, J.M. Rotter, J.Y. Ooi, Assessment of rolling resistance models in discrete element simulations, Powder Technology 206 (3) (2011) 269–282.

[145] Y. Guo, J.S. Curtis, Discrete element method simulations for complex granular flows, Annual Review of Fluid Mechanics 47 (1) (2015) 21–46.

[146] J.N. Israelachvili, Adhesion and Wetting Phenomena, in: J.N. Israelachvili (Ed.), Intermolecular and Surface Forces (Third Edition), Academic Press, San Diego, 415–467, 2011.

[147] G. Lian, C. Thornton, M.J. Adams, A theoretical study of the liquid bridge forces between two rigid spherical bodies, Journal of Colloid and Interface Science 161 (1) (1993) 138–147.

[148] S.T. Nase, W.L. Vargas, A.A. Abatan, J.J. McCarthy, Discrete characterization tools for cohesive granular material, Powder Technology 116 (2–3) (2001) 214–223.

[149] F. Soulié, F. Cherblanc, M.S. El Youssoufi, C. Saix, Influence of liquid bridges on the mechanical behaviour of polydisperse granular materials, International Journal for Numerical and Analytical Methods in Geomechanics 30 (3) (2006) 213–228.

[150] W.C. Swope, H.C. Andersen, P.H. Berens, K.R. Wilson, A computer simulation method for the calculation of equilibrium constants for the formation of physical clusters of molecules: Application to small water clusters, The Journal of Chemical Physics 76 (1) (1982) 637–649.

[151] T. Pöschel, T. Schwager, Computational Granular Dynamics: Models and Algorithms, Springer-Verlag, Berlin Heidelberg, 2005.

[152] S.M. Iveson, J.D. Litster, K. Hapgood, B.J. Ennis, Nucleation, growth and breakage phenomena in agitated wet granulation processes: A review, Powder Technology 117 (1–2) (2001) 3–39.

[153] K. Terrazas-Velarde, M. Peglow, E. Tsotsas, Kinetics of fluidized bed spray agglomeration for compact and porous particles, Chemical Engineering Science 66 (9) (2011) 1866–1878.

[154] K. Terrazas-Velarde, M. Peglow, E. Tsotsas, Investigation of the kinetics of fluidized bed spray agglomeration based on stochastic methods, AIChE Journal 57 (11) (2011) 3012–3026.

[155] C. Rieck, M. Schmidt, A. Bück, E. Tsotsas, Monte Carlo modeling of binder-less spray agglomeration in fluidized beds, AIChE Journal 64 (10) (2018) 3582–3594.

[156] T. Schwager, T. Pöschel, Coefficient of restitution and linear–dashpot model revisited, Granular Matter 9 (6) (2007) 465–469.

[157] R. Pashminehazar, S.J. Ahmed, A. Kharaghani, E. Tsotsas, Spatial morphology of maltodextrin agglomerates from X-ray microtomographic data: Real structure evaluation vs. spherical primary particle model, Powder Technology 331 (2018) 204–217.

[158] J.A. Laverman, I. Roghair, M.V.S. Annaland, H. Kuipers, Investigation into the hydrodynamics of gas–solid fluidized beds using particle image velocimetry coupled with digital image analysis, The Canadian Journal of Chemical Engineering 86 (3) (2008) 523–535.

[159] G.Q. Liu, S.Q. Li, X.L. Zhao, Q. Yao, Experimental studies of particle flow dynamics in a two-dimensional spouted bed, Chemical Engineering Science 63 (4) (2008) 1131–1141.

[160] P. Müller, M. Seeger, J. Tomas, Compression and breakage behavior of $\gamma\text{-}Al_2O_3$ granules, Powder Technology 237 (2013) 125–133.

[161] T. Kobayashi, T. Tanaka, N. Shimada, T. Kawaguchi, DEM–CFD analysis of fluidization behavior of Geldart Group A particles using a dynamic adhesion force model, Powder Technology 248 (2013) 143–152.

[162] Z. Peng, E. Doroodchi, C. Luo, B. Moghtaderi, Influence of void fraction calculation on fidelity of CFD-DEM simulation of gas-solid bubbling fluidized beds, AIChE Journal 60 (6) (2014) 2000–2018.

[163] R.J. Roberts, R.C. Rowe, P. York, The Poisson's ratio of microcrystalline cellulose, International Journal of Pharmaceutics 105 (2) (1994) 177–180.

[164] R. Bharadwaj, C. Smith, B.C. Hancock, The coefficient of restitution of some pharmaceutical tablets/compacts, International Journal of Pharmaceutics 402 (1) (2010) 50–56.

[165] B. Guignon, A. Duquenoy, E.D. Dumoulin, Fluid bed encapsulation of particles: Principles and practice, Drying Technology 20 (2) (2002) 419–447.

[166] R.J. Roberts, R.C. Rowe, P. York, The Poisson's ratio of microcrystalline cellulose, International Journal of Pharmaceutics 105 (2) (1994) 177–180.

[167] J. Wang, M.A. van der Hoef, J.A.M. Kuipers, The role of scale resolution versus inter-particle cohesive forces in two-fluid modeling of bubbling fluidization of Geldart A particles, Chemical Engineering Science 66 (18) (2011) 4229–4240.

[168] S. Antonyuk, M. Khanal, J. Tomas, S. Heinrich, L. Mörl, Impact breakage of spherical granules: Experimental study and DEM simulation, Chemical Engineering and Processing: Process Intensification 45 (10) (2006) 838–856.

[169] N.F.A. Bakar, R. Anzai, M. Horio, Direct measurement of particle–particle interaction using micro particle interaction analyzer (MPIA), Advanced Powder Technology 20 (5) (2009) 455–463.

[170] D.A. Gorham, A.H. Kharaz, The measurement of particle rebound characteristics, Powder Technology 112 (3) (2000) 193–202.

[171] P. Müller, R. Böttcher, A. Russell, M. Trüe, J. Tomas, A novel approach to evaluate the elastic impact of spheres on thin plates, Chemical Engineering Science 138 (2015) 689–697.

[172] J. Ma, D. Liu, X. Chen, Normal and oblique impacts between smooth spheres and liquid layers: Liquid bridge and restitution coefficient, Powder Technology 301 (2016) 747–759.

[173] B. Crüger, S. Heinrich, S. Antonyuk, N.G. Deen, J.A.M. Kuipers, Experimental study of oblique impact of particles on wet surfaces, Chemical Engineering Research and Design 110 (2016) 209–219.

[174] D.B. Hastie, Experimental measurement of the coefficient of restitution of irregular shaped particles impacting on horizontal surfaces, Chemical Engineering Science 101 (2013) 828–836.

[175] L.M. Gibson, B. Gopalan, S.V. Pisupati, L.J. Shadle, Image analysis measurements of particle coefficient of restitution for coal gasification applications, Powder Technology 247 (2013) 30–43.

[176] J. Grau-Bove, C. Mangwandi, G. Walker, D. Ring, K. Cronin, Studies into the effect of temperature on the impact of model particles in co-melt granulation, Powder Technology 294 (2016) 411–420.

[177] L. Wang, W. Zhou, Z. Ding, X. Li, C. Zhang, Experimental determination of parameter effects on the coefficient of restitution of differently shaped maize in three-dimensions, Powder Technology 284 (Supplement C) (2015) 187–194.

[178] L. Wang, B. Wu, Z. Wu, R. Li, X. Feng, Experimental determination of the coefficient of restitution of particle-particle collision for frozen maize grains, Powder Technology 338 (2018) 263–273.

[179] L. Labous, A.D. Rosato, R.N. Dave, Measurements of collisional properties of spheres using high-speed video analysis, Physical Review E 56 (5) (1997) 5717–5725.

[180] B. Crüger, V. Salikov, S. Heinrich, S. Antonyuk, V.S. Sutkar, N.G. Deen, J.A.M. Kuipers, Coefficient of restitution for particles impacting on wet surfaces: An improved experimental approach, Particuology 25 (2016) 1–9.

[181] M. Montaine, M. Heckel, C. Kruelle, T. Schwager, T. Pöschel, Coefficient of restitution as a fluctuating quantity, Physical Review E 84 (4) (2011) 041306.

[182] R. Sondergaard, K. Chaney, C.E. Brennen, Measurements of solid spheres bouncing off flat plates, Journal of Applied Mechanics 57 (3) (1990) 694–699.

[183] G. Lu, J.R. Third, C.R. Müller, Discrete element models for non-spherical particle systems: From theoretical developments to applications, Chemical Engineering Science 127 (2015) 425–465.

[184] H. Kruggel-Emden, S. Rickelt, S. Wirtz, V. Scherer, A study on the validity of the multi-sphere Discrete Element Method, Powder Technology 188 (2) (2008) 153–165.

[185] B. Soltanbeigi, A. Podlozhnyuk, S. Papanicolopulos, C. Kloss, S. Pirker, J.Y. Ooi, DEM study of mechanical characteristics of multi-spherical and superquadric particles at micro and macro scales, Powder Technology 329 (2018) 288–303.

[186] A. Podlozhnyuk, S. Pirker, C. Kloss, Efficient implementation of superquadric particles in Discrete Element Method within an open-source framework, Computational Particle Mechanics 4 (1) (2017) 101–118.

[187] D. Höhner, S. Wirtz, H. Kruggel-Emden, V. Scherer, Comparison of the multi-sphere and polyhedral approach to simulate non-spherical particles within the discrete element method: Influence on temporal force evolution for multiple contacts, Powder Technology 208 (3) (2011) 643–656.

[188] D. Markauskas, R. Kačianauskas, Investigation of rice grain flow by multi-sphere particle model with rolling resistance, Granular Matter 13 (2) (2011) 143–148.

[189] D.A. Santos, M.A.S. Barrozo, C.R. Duarte, F. Weigler, J. Mellmann, Investigation of particle dynamics in a rotary drum by means of experiments and numerical simulations using DEM, Advanced Powder Technology 27 (2) (2016) 692–703.

[190] C. Avendaño, F.A. Escobedo, Packing, entropic patchiness, and self-assembly of non-convex colloidal particles: A simulation perspective, Current Opinion in Colloid & Interface Science 30 (2017) 62–69.

[191] B. Sankur, Survey over image thresholding techniques and quantitative performance evaluation, Journal of Electronic Imaging 13 (1) (2004) 146.

[192] T.W. Ridler, S. Calvard, Picture thresholding using an iterative selection method, IEEE Transactions on Systems, Man, and Cybernetics 8 (8) (1978) 630–632.

[193] L. Wang, J. Park, Y. Fu, Representation of real particles for DEM simulation using X-ray tomography, Construction and Building Materials 21 (2) (2007) 338–346.

[194] F. Sondej, A. Bück, K. Koslowsky, P. Bachmann, M. Jacob, E. Tsotsas, Investigation of coating layer morphology by micro-computed X-ray tomography, Powder Technology 273 (2015) 165–175.

[195] Y. Guo, C. Wassgren, B. Hancock, W. Ketterhagen, J. Curtis, Computational study of granular shear flows of dry flexible fibres using the discrete element method, Journal of Fluid Mechanics 775 (2015) 24–52.

[196] A. Jaklic, A. Leonardis, F. Solina, Segmentation and Recovery of Superquadrics, Springer Netherlands, 2000.

[197] C. Kloss, C. Goniva, A. Hager, S. Amberger, S. Pirker, Models, algorithms and validation for opensource DEM and CFD–DEM, Progress in Computational Fluid Dynamics 12 (2-3) (2012) 140–152.

[198] A. Ramírez, M. Moya, F. Ayuga, Determination of the mechanical properties of powdered agricultural products and sugar, Particle & Particle Systems Characterization 26 (4) (2009) 220–230.

[199] K.L. Johnson, Contact Mechanics, Cambridge University Press, Cambridge, 1987.

[200] C.-Y. Wu, L.-Y. Li, C. Thornton, Rebound behaviour of spheres for plastic impacts, International Journal of Impact Engineering 28 (9) (2003) 929–946.

[201] D. Ramkrishna, Population Balances: Theory and Applications to Particulate Systems in Engineering, Academic Press, San Diego, 2000.

[202] R. Turton, Challenges in the modeling and prediction of coating of pharmaceutical dosage forms, Powder Technology 181 (2) (2008) 186–194.

[203] B.J. Ennis, G. Tardos, R. Pfeffer, Microlevel-based characterization of granulation phenomena, Powder Technology 65 (1) (1991) 257–272.

[204] S.M. Iveson, J.D. Litster, K. Hapgood, B.J. Ennis, Nucleation, growth and breakage phenomena in agitated wet granulation processes: A review, Powder Technology 117 (1–2) (2001) 3–39.

[205] M. Hussain, J. Kumar, M. Peglow, E. Tsotsas, Modeling spray fluidized bed aggregation kinetics on the basis of Monte-Carlo simulation results, Chemical Engineering Science 101 (2013) 35–45.

[206] M. Hussain, J. Kumar, E. Tsotsas, A new framework for population balance modeling of spray fluidized bed agglomeration, Particuology 19 (2015) 141–154.

[207] P. Buffière, R. Moletta, Collision frequency and collisional particle pressure in three-phase fluidized beds, Chemical Engineering Science 55 (22) (2000) 5555–5563.

[208] P.G. Saffman, J.S. Turner, On the collision of drops in turbulent clouds, Journal of Fluid Mechanics 1 (1) (1956) 16–30.

[209] J. Abrahamson, Collision rates of small particles in a vigorously turbulent fluid, Chemical Engineering Science 30 (11) (1975) 1371–1379.

[210] L.P. Wang, A.S. Wexler, Y. Zhou, Statistical mechanical description and modelling of turbulent collision of inertial particles, Journal of Fluid Mechanics 415 (2000) 117–153.

[211] C.J. Meyer, D.A. Deglon, Particle collision modeling: A review, Minerals Engineering 24 (8) (2011) 719–730.

[212] C.S. Campbell, Granular material flows: An overview, Powder Technology 162 (3) (2006) 208–229.

[213] J. Jung, D. Gidaspow, I.K. Gamwo, Measurement of two kinds of granular temperatures, stresses, and dispersion in bubbling beds, Industrial & Engineering Chemistry Research 44 (5) (2005) 1329–1341.

[214] Y. Tang, Y.M. Lau, N.G. Deen, E. Peters, J.A.M. Kuipers, Direct numerical simulations and experiments of a pseudo-2D gas-fluidized bed, Chemical Engineering Science 143 (2016) 166–180.

[215] R.D. Wildman, J.M. Huntley, D.J. Parker, Granular temperature profiles in three-dimensional vibrofluidized granular beds, Physical Review E 63 (6) (2001) 061311.

[216] C.R. Müller, D.J. Holland, A.J. Sederman, S.A. Scott, J.S. Dennis, L.F. Gladden, Granular temperature: Comparison of magnetic resonance measurements with discrete element model simulations, Powder Technology 184 (2) (2008) 241–253.

[217] D.J. Holland, C.R. Müller, J.S. Dennis, L.F. Gladden, A.J. Sederman, Spatially resolved measurement of anisotropic granular temperature in gas-fluidized beds, Powder Technology 182 (2) (2008) 171–181.

[218] W. Dijkhuizen, G.A. Bokkers, N.G. Deen, M. van Sint Annaland, J.A.M. Kuipers, Extension of PIV for measuring granular temperature field in dense fluidized beds, AIChE Journal 53 (1) (2007) 108–118.

[219] L.E. Silbert, D. Ertaş, G.S. Grest, T.C. Halsey, D. Levine, S.J. Plimpton, Granular flow down an inclined plane: Bagnold scaling and rheology, Physical Review E 64 (5) (2001) 051302.

[220] J. Ding, D. Gidaspow, A bubbling fluidization model using kinetic theory of granular flow, AIChE Journal 36 (4) (1990) 523–538.

[221] H.T. Bi, N. Ellis, I.A. Abba, J.R. Grace, A state-of-the-art review of gas–solid turbulent fluidization, Chemical Engineering Science 55 (21) (2000) 4789–4825.

[222] M. Rüdisüli, T.J. Schildhauer, S.M.A. Biollaz, J.R. van Ommen, Scale-up of bubbling fluidized bed reactors — A review, Powder Technology 217 (2012) 21–38.

[223] A. Efhaima, M.H. Al-Dahhan, Assessment of scale-up dimensionless groups methodology of gas-solid fluidized beds using advanced non-invasive measurement techniques (CT and RPT), The Canadian Journal of Chemical Engineering 95 (4) (2017) 656–669.

[224] F.J. Muzzio, T. Shinbrot, B.J. Glasser, Powder technology in the pharmaceutical industry: The need to catch up fast, Powder Technology 124 (1–2) (2002) 1–7.

[225] M.J.V. Goldschmidt, J.M. Link, S. Mellema, J.A.M. Kuipers, Digital image analysis measurements of bed expansion and segregation dynamics in dense gas-fluidised beds, Powder Technology 138 (2-3) (2003) 135–159.

[226] O.O. Olaofe, K.A. Buist, N.G. Deen, M.A. van der Hoef, J.A.M. Kuipers, Improved digital image analysis technique for the evaluation of segregation in pseudo-2D beds, Powder Technology 244 (2013) 61–74.

[227] H. Lu, Y. He, D. Gidaspow, L. Yang, Y. Qin, Size segregation of binary mixture of solids in bubbling fluidized beds, Powder Technology 134 (1) (2003) 86–97.

[228] G.G. Joseph, J. Leboreiro, C.M. Hrenya, A.R. Stevens, Experimental segregation profiles in bubbling gas-fluidized beds, AIChE Journal 53 (11) (2007) 2804–2813.

[229] P.M.C. Lacey, Developments in the theory of particle mixing, Journal of Applied Chemistry 4 (5) (1954) 257–268.

[230] G.A. Bokkers, M. van Sint Annaland, J.A.M. Kuipers, Mixing and segregation in a bidisperse gas–solid fluidised bed: A numerical and experimental study, Powder Technology 140 (3) (2004) 176–186.

[231] Y.Q. Feng, B.H. Xu, S. J. Zhang, A.B. Yu, P. Zulli, Discrete particle simulation of gas fluidization of particle mixtures, AIChE Journal 50 (8) (2004) 1713–1728.

[232] R. Beetstra, M.A. van der Hoef, J.A.M. Kuipers, Numerical study of segregation using a new drag force correlation for polydisperse systems derived from lattice-Boltzmann simulations, Chemical Engineering Science 62 (1-2) (2007) 246–255.

[233] O.O. Olaofe, A.V. Patil, N.G. Deen, M.A. van der Hoef, J.A.M. Kuipers, Simulation of particle mixing and segregation in bidisperse gas fluidized beds, Chemical Engineering Science 108 (2014) 258–269.

[234] C.D. Immanuel, F.J. Doyle, Solution technique for a multi-dimensional population balance model describing granulation processes, Powder Technology 156 (2) (2005) 213–225.

[235] A. Bück, S. Palis, E. Tsotsas, Model-based control of particle properties in fluidised bed spray granulation, Powder Technology 270 (2015) 575–583.

[236] M.J.V. Goldschmidt, G.G.C. Weijers, R. Boerefijn, J.A.M. Kuipers, Discrete element modelling of fluidised bed spray granulation, Powder Technology 138 (1) (2003) 39–45.

[237] B. Freireich, J. Li, J. Litster, C. Wassgren, Incorporating particle flow information from discrete element simulations in population balance models of mixer-coaters, Chemical Engineering Science 66 (16) (2011) 3592–3604.

[238] D. Barrasso, R. Ramachandran, Multi-scale modeling of granulation processes: Bi-directional coupling of PBM with DEM via collision frequencies, Chemical Engineering Research and Design 93 (2015) 304–317.

[239] E. Teunou, D. Poncelet, Batch and continuous fluid bed coating – review and state of the art, Journal of Food Engineering 53 (4) (2002) 325–340.

[240] S. Shelukar, J. Ho, J. Zega, E. Roland, N. Yeh, D. Quiram, A. Nole, A. Katdare, S. Reynolds, Identification and characterization of factors controlling tablet coating uniformity in a Wurster coating process, Powder Technology 110 (1–2) (2000) 29–36.

[241] X.X. Cheng, R. Turton, The prediction of variability occurring in fluidized bed coating equipment I: The measurement of particle circulation rates in a bottom-spray fluidized bed coater, Pharmaceutical Development and Technology 5 (3) (2000) 311–322.

[242] X.X. Cheng, R. Turton, The prediction of variability occurring in fluidized bed coating equipment II: The role of nonuniform particle coverage as particles pass through the spray zone, Pharmaceutical Development and Technology 5 (3) (2000) 323–332.

[243] F. Depypere, J.G. Pieters, K. Dewettinck, PEPT visualisation of particle motion in a tapered fluidised bed coater, Journal of Food Engineering 93 (3) (2009) 324–336.

[244] M. Aghbashlo, R. Sotudeh-Gharebagh, R. Zarghami, A.S. Mujumdar, N. Mostoufi, Measurement techniques to monitor and control fluidization quality in fluidized bed dryers: A review, Drying Technology 32 (9) (2014) 1005–1051.

[245] M. Börner, M. Peglow, E. Tsotsas, Derivation of parameters for a two compartment population balance model of Wurster fluidised bed granulation, Powder Technology 238 (2013) 122–131.

[246] T. Hoffmann, C. Rieck, M. Schmidt, A. Bück, M. Peglow, E. Tsotsas, Prediction of shell porosities in continuous fluidized bed spray layering, Drying Technology 33 (13) (2015) 1662–1670.

[247] D. Suzzi, S. Radl, J.G. Khinast, Local analysis of the tablet coating process: Impact of operation conditions on film quality, Chemical Engineering Science 65 (21) (2010) 5699–5715.

[248] S.R.L. Werner, J.R. Jones, A.H.J. Paterson, R.H. Archer, D.L. Pearce, Air-suspension particle coating in the food industry, Part I: State of the art, Powder Technology 171 (1) (2007) 25–33.

[249] P. Rajniak, F. Stepanek, K. Dhanasekharan, R. Fan, C. Mancinelli, R.T. Chern, A combined experimental and computational study of wet granulation in a Wurster fluid bed granulator, Powder Technology 189 (2) (2009) 190–201.

[250] S. Heinrich, M. Dosta, S. Antonyuk, Multiscale Analysis of a Coating Process in a Wurster Fluidized Bed Apparatus, in: G.B. Marin, J. Li (Eds.), Advances in Chemical Engineering, vol. 46, Academic Press, 83–135, 2015.

[251] K. Knop, P. Kleinebudde, PAT-tools for process control in pharmaceutical film coating applications, International Journal of Pharmaceutics 457 (2) (2013) 527–536.

[252] F.L. Laksmana, L.J. van Vliet, P.J.A. Hartman, H. Vromans, H.W. Frijlink, K. van der Voort Maarschalk, Quantitative image analysis for Evaluating the coating thickness and pore distribution in coated small particles, Pharmaceutical Research 26 (4) (2009) 965–976.

[253] H. Lin, Y. Dong, D. Markl, B.M. Williams, Y. Zheng, Y. Shen, J.A. Zeitler, Measurement of the intertablet coating uniformity of a pharmaceutical pan coating process with combined terahertz and optical coherence tomography in-line sensing, Journal of Pharmaceutical Sciences 106 (4) (2017) 1075–1084.

[254] W. Zhong, A. Yu, J. Zhou, G.and Xie, H. Zhang, CFD simulation of dense particulate reaction system: Approaches, recent advances and applications, Chemical Engineering Science 140 (2016) 16–43.

[255] L. Fries, S. Antonyuk, S. Heinrich, S. Palzer, DEM–CFD modeling of a fluidized bed spray granulator, Chemical Engineering Science 66 (11) (2011) 2340–2355.

[256] T. Kulju, M. Paavola, H. Spittka, R.L. Keiski, E. Juuso, K. Leiviskä, E. Muurinen, Modeling continuous high-shear wet granulation with DEM-PB, Chemical Engineering Science 142 (2016) 190–200.

[257] S. Poozesh, N. Setiawan, N.K. Akafuah, K. Saito, P.J. Marsac, Assessment of predictive models for characterizing the atomization process in a spray dryer's bi-fluid nozzle, Chemical Engineering Science 180 (2018) 42–51.

[258] X. Jiang, G.A. Siamas, K. Jagus, T.G. Karayiannis, Physical modelling and advanced simulations of gas–liquid two-phase jet flows in atomization and sprays, Progress in Energy and Combustion Science 36 (2) (2010) 131–167.

[259] K. Luo, M. Shao, C.and Chai, J. Fan, Level set method for atomization and evaporation simulations, Progress in Energy and Combustion Science 73 (2019) 65–94.

[260] P. Kieckhefen, T. Lichtenegger, S. Pietsch, S. Pirker, S. Heinrich, Simulation of spray coating in a spouted bed using recurrence CFD, Particuology 42 (2019) 92–103.

[261] B. Freireich, R. Kumar, W. Ketterhagen, K. Su, C. Wassgren, J.A. Zeitler, Comparisons of intra-tablet coating variability using DEM simulations, asymptotic limit models, and experiments, Chemical Engineering Science 131 (2015) 197–212.

[262] C. Pei, J.A. Elliott, Asymptotic limits on tablet coating variability based on cap-to-band thickness distributions: A discrete element model (DEM) study, Chemical Engineering Science 172 (2017) 286–296.

[263] A. Maisels, F. Einar Kruis, H. Fissan, Direct simulation Monte Carlo for simultaneous nucleation, coagulation, and surface growth in dispersed systems, Chemical Engineering Science 59 (11) (2004) 2231–2239.

[264] H. Zhao, A. Maisels, T. Matsoukas, C. Zheng, Analysis of four Monte Carlo methods for the solution of population balances in dispersed systems, Powder Technology 173 (1) (2007) 38–50.

[265] B. Freireich, C. Wassgren, Intra-particle coating variability: Analysis and Monte-Carlo simulations, Chemical Engineering Science 65 (3) (2010) 1117–1124.

[266] W. Zhang, C. You, Numerical approach to predict particle breakage in dense flows by coupling multiphase particle-in-cell and Monte Carlo methods, Powder Technology 283 (2015) 128–136.

[267] C. Rieck, A. Bück, E. Tsotsas, Monte Carlo modeling of fluidized bed coating and layering processes, AIChE Journal 62 (8) (2016) 2670–2680.

[268] A.D. McGuire, S. Mosbach, K.F. Lee, G. Reynolds, M. Kraft, A high-dimensional, stochastic model for twin-screw granulation, Part 2: Numerical methodology, Chemical Engineering Science 188 (2018) 18–33.

[269] A.D. McGuire, S. Mosbach, K.F. Lee, G. Reynolds, M. Kraft, A high-dimensional, stochastic model for twin-screw granulation, Part 1: Model description, Chemical Engineering Science 188 (2018) 221–237.

[270] R. Rioboo, M. Marengo, C. Tropea, Time evolution of liquid drop impact onto solid, dry surfaces, Experiments in Fluids 33 (1) (2002) 112–124.

[271] Q. Du, V. Faber, M. Gunzburger, Centroidal voronoi tessellations: Applications and algorithms, SIAM Review 41 (4) (1999) 637–676.

[272] C.G. Koay, Analytically exact spiral scheme for generating uniformly distributed points on the unit sphere, Journal of Computational Science 2 (1) (2011) 88–91.

[273] S. Lloyd, Least squares quantization in PCM, IEEE Transactions on Information Theory 28 (2) (1982) 129–137.

[274] C. Josserand, S.T. Thoroddsen, Drop Impact on a Solid Surface, Annual Review of Fluid Mechanics 48 (1) (2016) 365–391.

[275] C. Mundo, M. Sommerfeld, C. Tropea, Droplet-wall collisions: Experimental studies of the deformation and breakup process, International Journal of Multiphase Flow 21 (2) (1995) 151–173.

[276] A.L. Yarin, D. Weiss, Impact of drops on solid surfaces: Self-similar capillary waves, and splashing as a new type of kinematic discontinuity, Journal of Fluid Mechanics 283 (1995) 141–173.

[277] V. Gnielinski, G9 Fluid-Particle Heat Transfer in Flow Through Packed Beds of Solids, in: VDI Heat Atlas, Springer, Berlin, Heidelberg, 743–744, 2010.

[278] R.A. Meric, H.Y. Erbil, Evaporation of sessile drops on solid surfaces: Pseudo-spherical cap geometry, Langmuir 14 (7) (1998) 1915–1920.

[279] R. Zhu, S. Li, Q. Yao, Effects of cohesion on the flow patterns of granular materials in spouted beds, Physical Review E 87 (2) (2013) 022206.

[280] E. Tsotsas, Particle-particle heat transfer in thermal DEM: Three competing models and a new equation, International Journal of Heat and Mass Transfer 132 (2019) 939–943.

[281] M. Hussain, J. Kumar, E. Tsotsas, Modeling aggregation kinetics of fluidized bed spray agglomeration for porous particles, Powder Technology 270 (2015) 584–591.

[282] H.S. Fang, K. Bao, J.A. Wei, H. Zhang, E.H. Wu, L.L. Zheng, Simulations of droplet spreading and solidification using an improved SPH model, Numerical Heat Transfer, Part A: Applications 55 (2) (2009) 124–143.

[283] Z. Wang, R. Chen, H. Wang, Q. Liao, X. Zhu, S. Li, An overview of smoothed particle hydrodynamics for simulating multiphase flow, Applied Mathematical Modelling 40 (23) (2016) 9625–9655.

[284] X. Yang, L. Dai, S. Kong, Simulation of liquid drop impact on dry and wet surfaces using SPH method, Proceedings of the Combustion Institute 36 (2) (2017) 2393–2399.

[285] M. Robinson, M. Ramaioli, S. Luding, Fluid–particle flow simulations using two-way-coupled mesoscale SPH–DEM and validation, International Journal of Multiphase Flow 59 (2014) 121–134.

# Appendices

# Appendix A

# Measurement data

## A.1 List of all experiments

The summary of all experiments in this thesis is given in Table A.1.

Table A.1: List of all PTV experiments.

| Experiments Chapter | Case | Number of images | Measured variables |
|---|---|---|---|
| Chapter 5 | DE 6 - DE 6 | $2000 \times 10$ | Particle trajectory |
| | DE 6 - glass | $2000 \times 10$ | Coefficient of restitution |
| | DE 47- glass | $1000 \times 5$ | Rotation speed |
| | glass - glass | $1000 \times 5$ | |
| | MCC - glass | $1000 \times 5$ | |
| | Alumina - glass | $1000 \times 4$ | |
| | Rapeseed - glass | $1000 \times 4$ | |
| | ABS - glass | $1000 \times 4$ | |
| Chapter 6 | Low-level left | $5000 \times 3$ | Collision frequency |
| | Low-level left-center | $5000 \times 3$ | Collision velocity |
| | Low-level right-center | $5000 \times 3$ | Granular temperature |
| | Low-level right | $5000 \times 3$ | Particle trajectory |
| | High-level left | $5000 \times 3$ | |
| | High-level left-center | $5000 \times 3$ | |
| | High-level right-center | $5000 \times 3$ | |
| | High-level right | $5000 \times 3$ | |
| Chapter 7 | Binary mixture | 5000 | Granular temperature |
| | Ternary mixture | 5000 | Mixing degree |

## A.2    Particle trajectories of irregular particle rebound

The measured trajectories of irregular particles before and after collision in a time period of 100 ms are shown in Figure A.1.
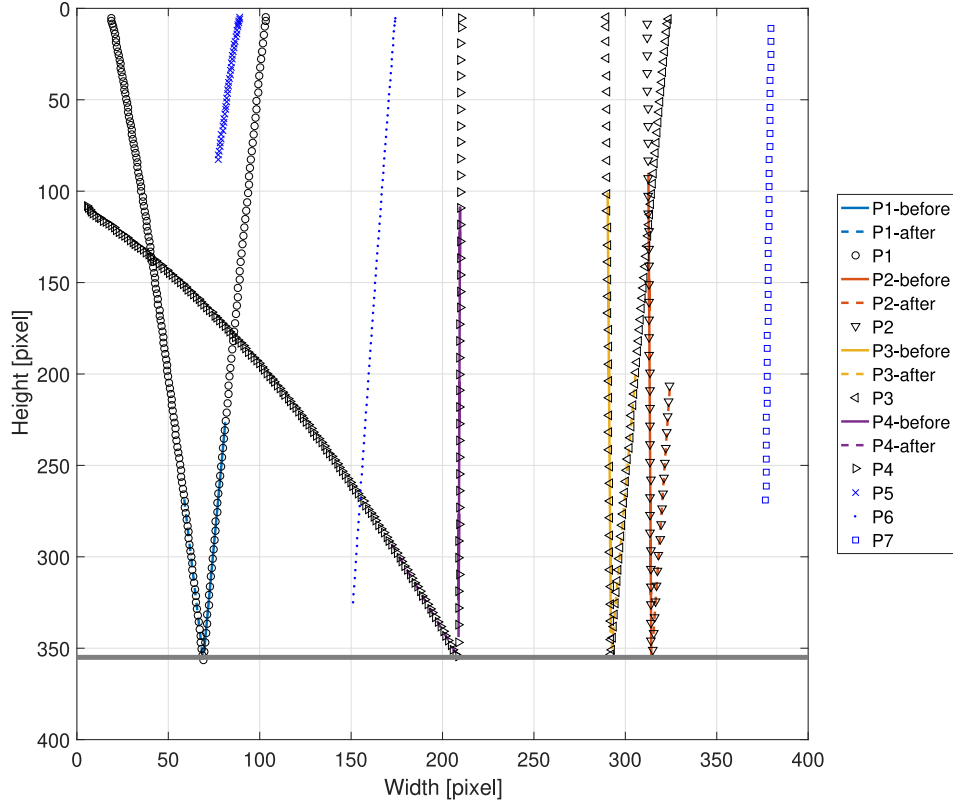


Figure A.1: Measured trajectories of irregular particles before and after collision in a time period of 100 ms.

## A.3    PTV measurement of particle dynamics data

*Instantaneous data*

The raw image, instantaneous velocity field, average velocity field, granular temperature and solid volume fraction in the low-level left at 1.68 m/s (with an interval of 20 ms) are given in Figure A.2, Figure A.3, Figure A.4, Figure A.5 and Figure A.6, respectively.

*Time-average data*

The time-average solid volume fraction and isoline of time-average granular temperature obtained from region c) at 1.68 m/s are shown in Figure A.7 and Figure A.8. All granular temperatures and main indices of particle collision dynamics are summarized in Table A.2, Table A.3 and Table A.4.
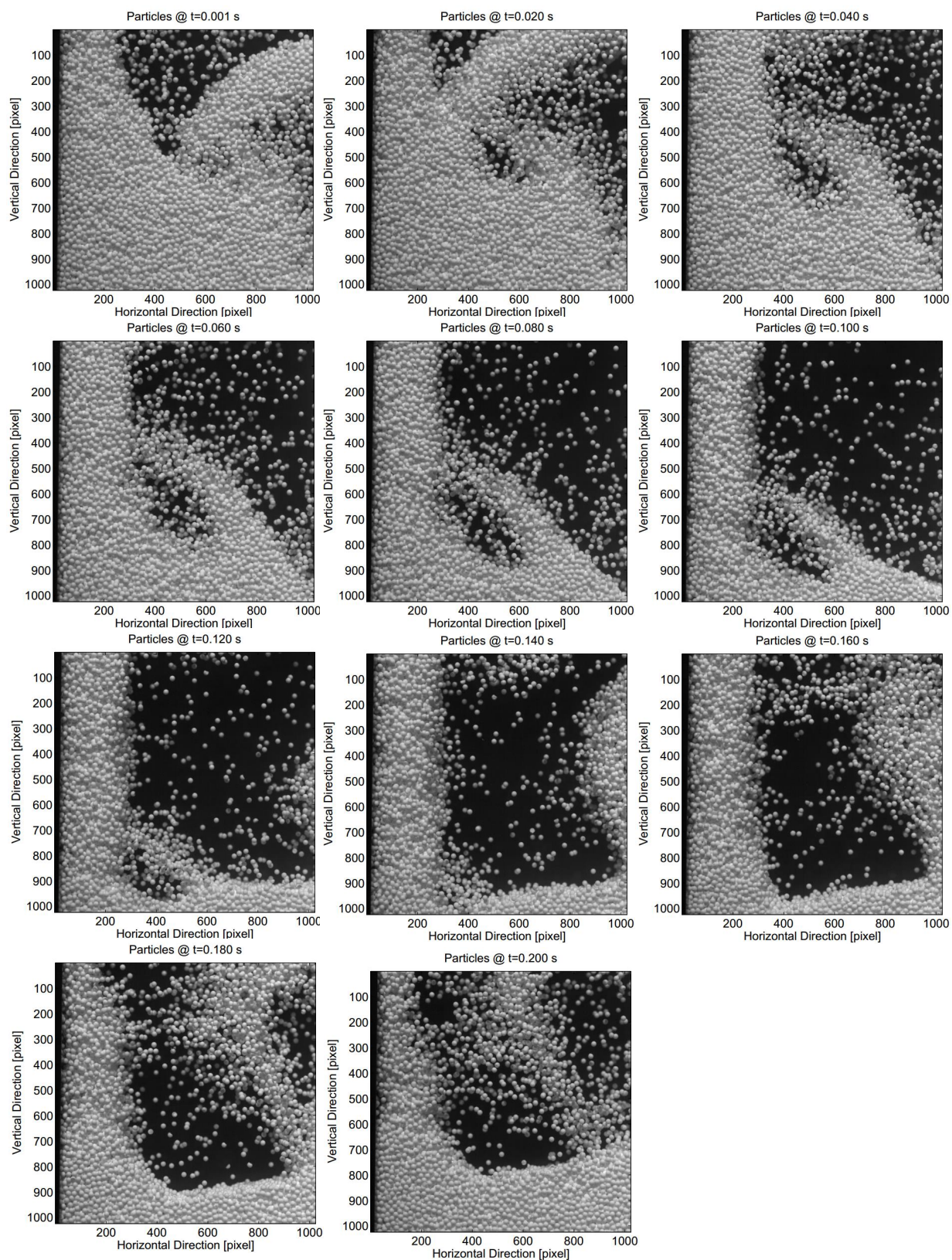
Figure A.2: Raw images.

Figure A.3: Instantaneous particle velocity fields.

Figure A.4: Average particle velocity fields.

Figure A.5: Particle granular temperature fields.

Figure A.6: Solid volume fraction distributions.

Figure A.7: Time-averaged solid volume fraction obtained from region c) at a gas velocity of 1.68 m/s.



Figure A.8: Isolines of time-averaged granular temperature obtained from region c) at a gas velocity of 1.68 m/s.

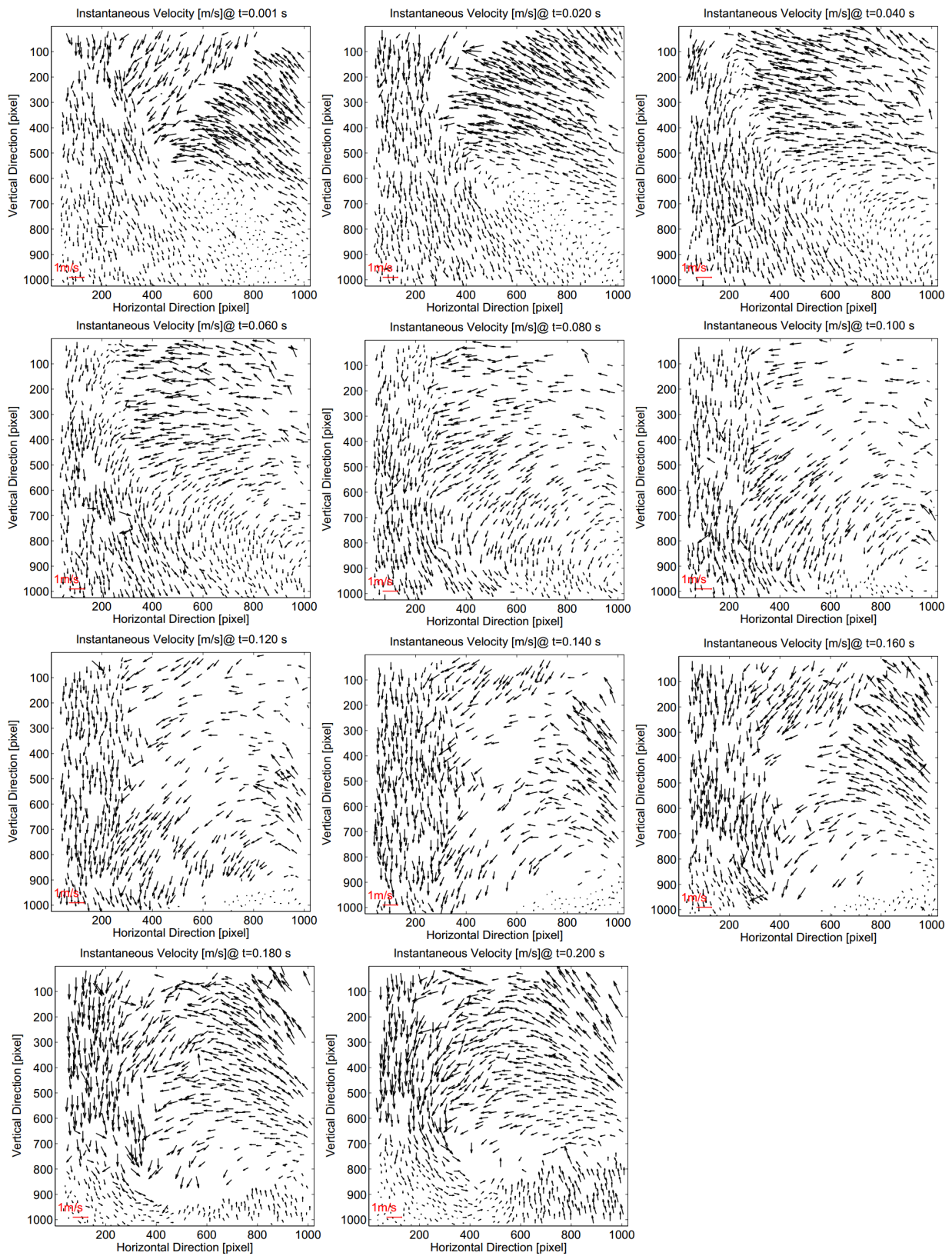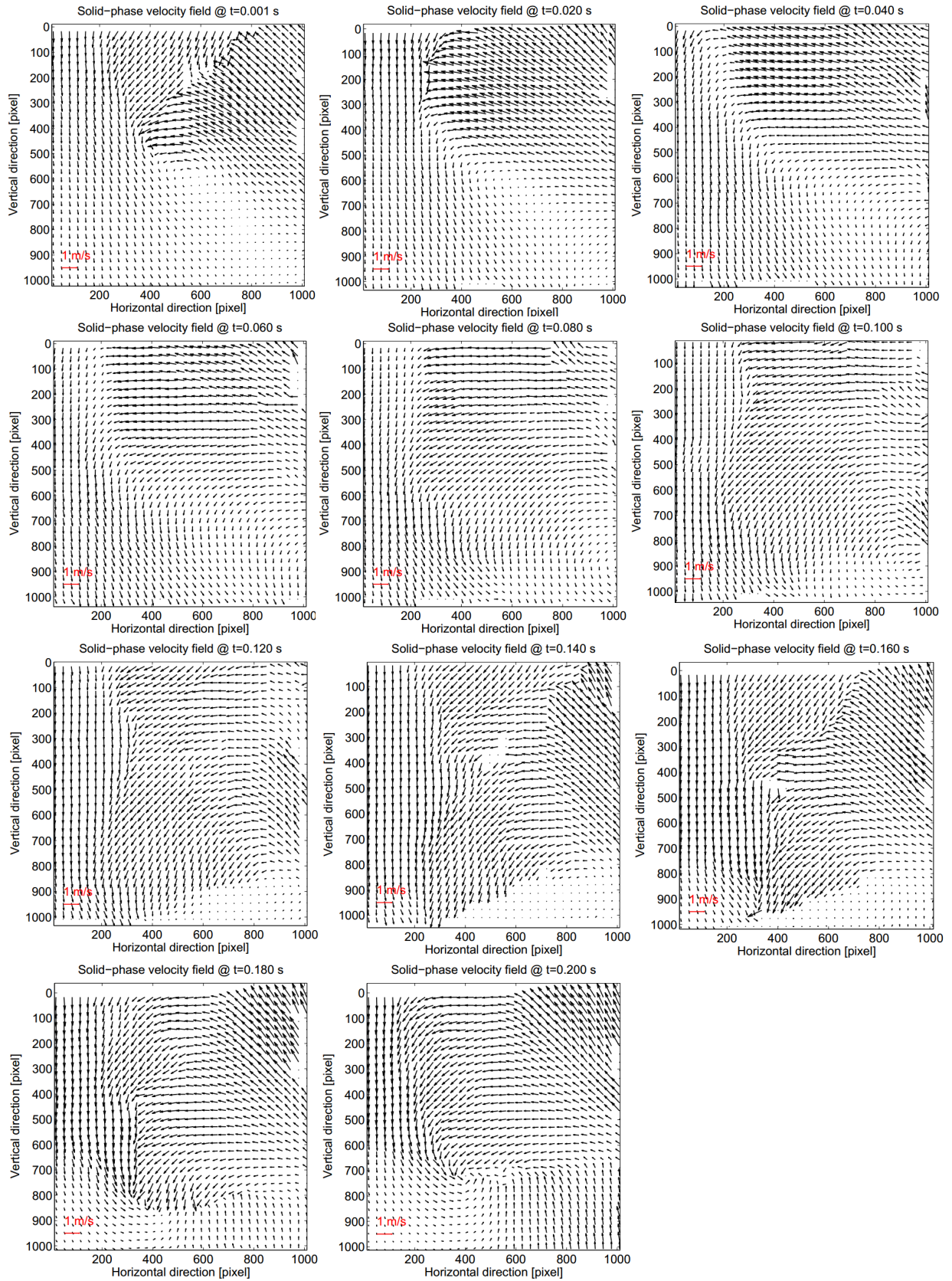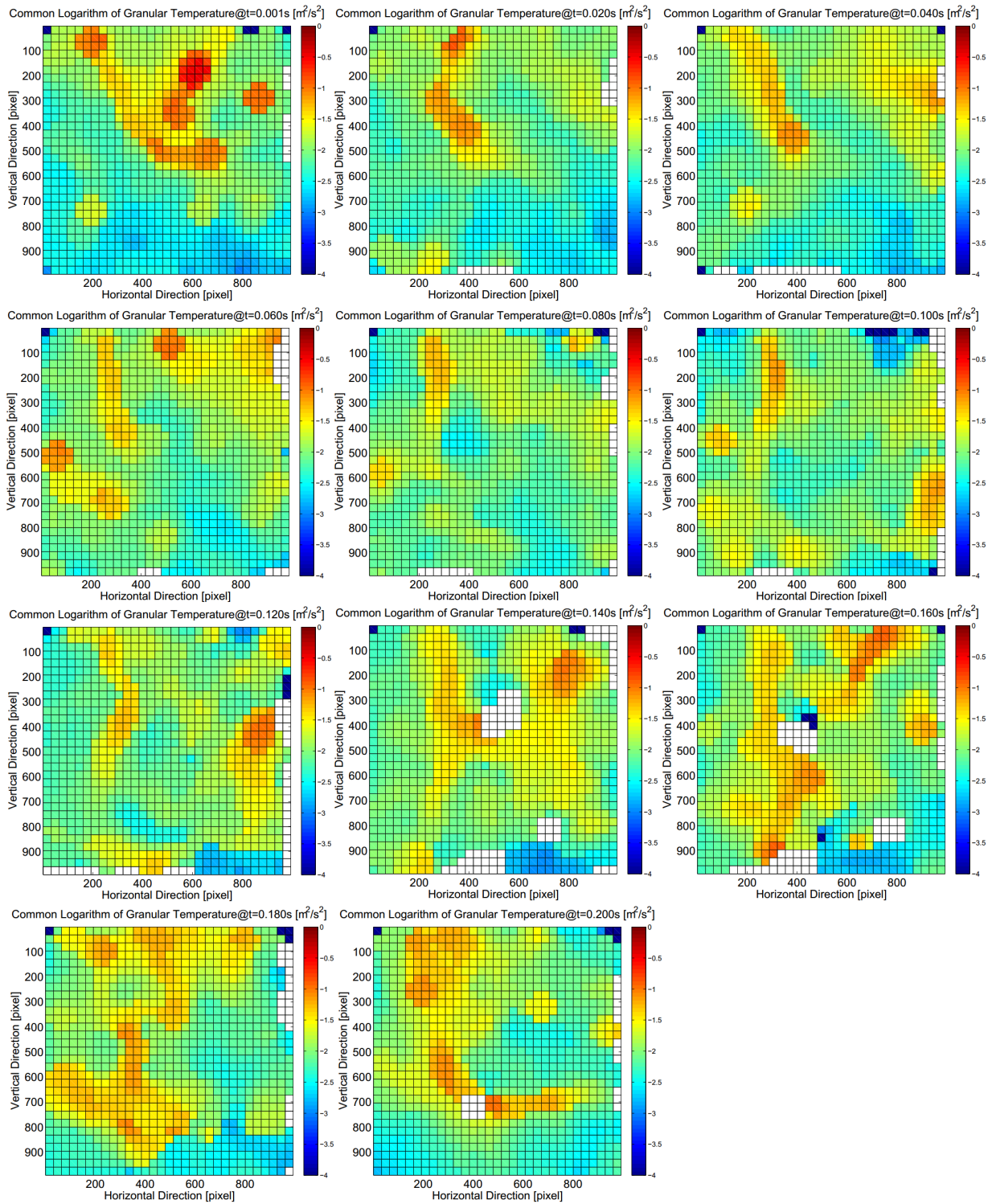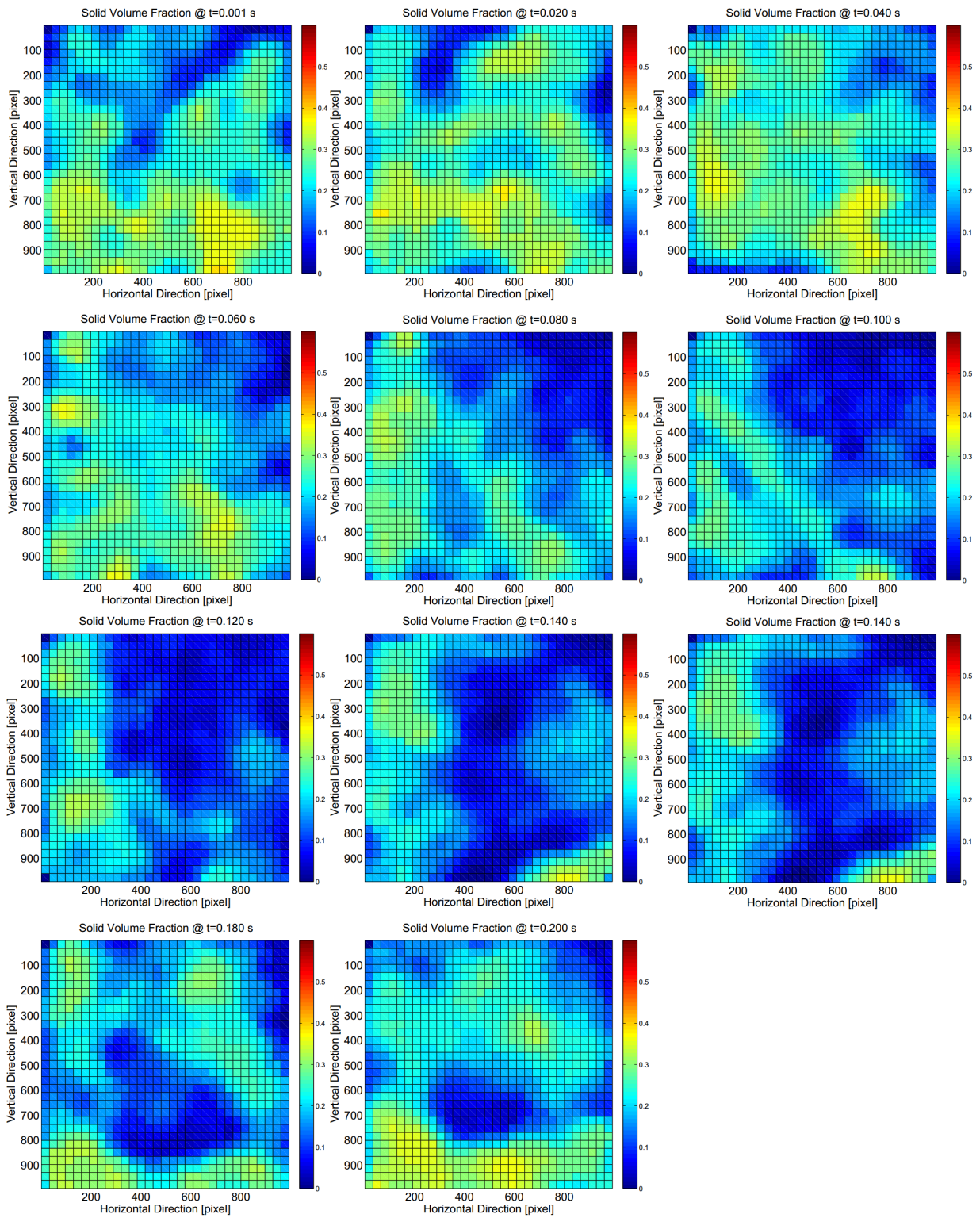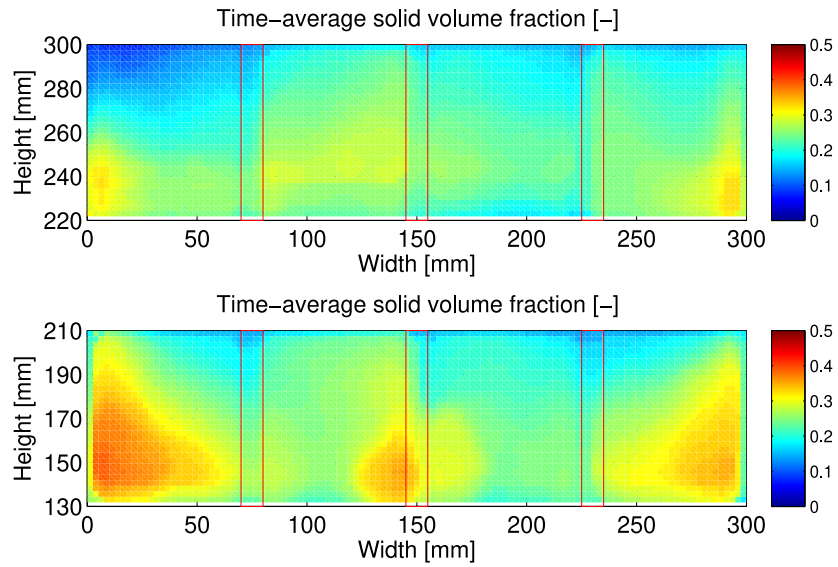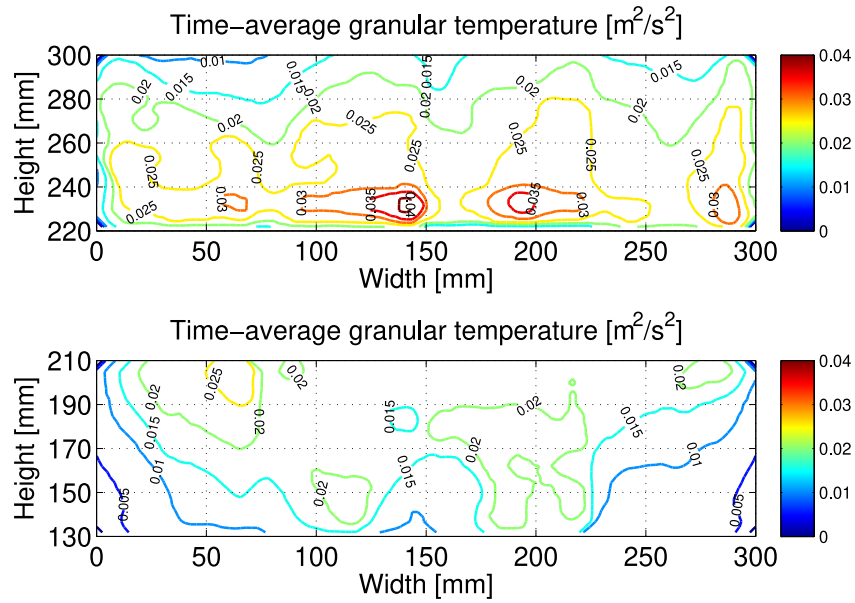Table A.2: Performance of PTV measurement and particle dynamics for different locations under different superficial gas velocities.

| Case | | PTV performance | | | | Particle dynamics | | | |
|---|---|---|---|---|---|---|---|---|---|
| Location | $U$ [m/s] | $\langle R_r \rangle$ [%] | CV [%] | $\langle \tau_p \rangle$ [ms] | CV [%] | $\langle \Phi \rangle$ [m³/(s·m²)] | CV [%] | $\langle |\boldsymbol{u}_p| \rangle_{(c)}$ [m/s] | CV [%] |
| Low-level left (1) | 1.68 | 89.2 | 7.1 | 11.5 | 91.3 | 0.048 | 6.0 | 0.223 | 31.2 |
| | 1.40 | 88.5 | 9.5 | 12.3 | 89.7 | 0.041 | 5.4 | 0.179 | 29.2 |
| | 1.12 | 90.5 | 9.7 | 12.1 | 77.5 | 0.031 | 4.8 | 0.134 | 24.3 |
| Low-level left-center (2) | 1.68 | 87.6 | 6.9 | 9.2 | 92.1 | 0.062 | 5.8 | 0.279 | 25.5 |
| | 1.40 | 88.1 | 8.4 | 9.6 | 79.8 | 0.059 | 4.4 | 0.252 | 18.4 |
| | 1.12 | 89.1 | 9.2 | 9.9 | 87.5 | 0.044 | 4.7 | 0.186 | 19.2 |
| Low-level right-center (3) | 1.68 | 88.3 | 9.3 | 8.8 | 96.7 | 0.058 | 4.8 | 0.276 | 21.4 |
| | 1.40 | 90.1 | 8.4 | 9.2 | 88.2 | 0.056 | 4.4 | 0.242 | 19.2 |
| | 1.12 | 89.7 | 9.5 | 9.1 | 82.3 | 0.038 | 3.5 | 0.168 | 14.8 |
| Low-level right (4) | 1.68 | 90.5 | 7.2 | 12.5 | 99.0 | 0.047 | 4.8 | 0.194 | 25.9 |
| | 1.40 | 89.3 | 8.3 | 12.7 | 85.7 | 0.043 | 4.3 | 0.179 | 24.1 |
| | 1.12 | 91.0 | 8.6 | 11.9 | 93.4 | 0.031 | 3.4 | 0.137 | 19.4 |
| High-level left (5) | 1.68 | 86.5 | 8.7 | 10.8 | 86.1 | 0.083 | 10.3 | 0.396 | 38.5 |
| | 1.40 | 87.5 | 9.0 | 11.7 | 91.0 | 0.059 | 8.8 | 0.279 | 29.4 |
| | 1.12 | 87.7 | 8.5 | 11.5 | 82.7 | 0.019 | 9.7 | 0.095 | 39.9 |
| High-level left-center (6) | 1.68 | 86.1 | 9.8 | 8.9 | 90.6 | 0.071 | 6.9 | 0.296 | 24.4 |
| | 1.40 | 87.7 | 8.5 | 9.1 | 86.3 | 0.061 | 7.5 | 0.279 | 26.4 |
| | 1.12 | 87.9 | 7.9 | 9.7 | 84.9 | 0.025 | 8.5 | 0.117 | 33.1 |
| High-level right-center (7) | 1.68 | 88.2 | 8.3 | 8.7 | 91.3 | 0.067 | 5.4 | 0.302 | 22.9 |
| | 1.40 | 89.3 | 7.8 | 9.3 | 88.2 | 0.052 | 5.8 | 0.268 | 23.3 |
| | 1.12 | 88.4 | 8.8 | 8.8 | 87.5 | 0.024 | 5.3 | 0.105 | 21.2 |
| High-level right (8) | 1.68 | 87.5 | 8.9 | 12.4 | 97.2 | 0.083 | 8.5 | 0.373 | 27.5 |
| | 1.40 | 88.1 | 7.8 | 12.0 | 95.5 | 0.058 | 9.0 | 0.261 | 30.9 |
| | 1.12 | 87.9 | 9.1 | 12.1 | 89.2 | 0.023 | 10.5 | 0.111 | 41.2 |

[1] $\langle R_r(t) \rangle = \sum\limits_{t=1}^{N_t}(R_r(t))$, where $N_t$ is the number of time steps.

[2] $\langle \tau_p(j) \rangle = \sum\limits_{j=1}^{N_p}(\tau_p(j))$, where $N_p$ is the number of particles.

[3] Particle dynamics are evaluated based on region (c). $\langle \Phi(i,t) \rangle = \sum\limits_{t=1}^{N_t}(\sum\limits_{i=1}^{N_i}(\Phi(i,t)))$, where $N_i$ is the number of investigation regions. Similarly, $\langle |\boldsymbol{u}_p|(i,t) \rangle = \sum\limits_{t=1}^{N_t}(\sum\limits_{i=1}^{N_i}(|\boldsymbol{u}_p|(i,t)))$.

[4] CV refers to the coefficient of variation of corresponding individual values of $R_r(t)$, $\tau_p(j)$, $\Phi(i,t)$) or $|\boldsymbol{u}_p|(i,t)$.

Table A.3: Particle granular temperature for different locations under different superficial gas velocities, based on different sizes of the investigation region.

| Case | | Region (a) | | | | Region (b) | | | | Region (c) | | | |
|---|---|---|---|---|---|---|---|---|---|---|---|---|---|
| Nr. | $U$ [m/s] | $\langle\sqrt{\Theta_{2D}}\rangle$ [m/s] | CV [%] | $\langle\frac{\sqrt{\Theta_y}}{\sqrt{\Theta_x}}\rangle$ [-] | CV [%] | $\langle\sqrt{\Theta_{2D}}\rangle$ [m/s] | CV [%] | $\langle\frac{\sqrt{\Theta_y}}{\sqrt{\Theta_x}}\rangle$ [-] | CV [%] | $\langle\sqrt{\Theta_{2D}}\rangle$ [m/s] | CV [%] | $\langle\frac{\sqrt{\Theta_y}}{\sqrt{\Theta_x}}\rangle$ [-] | CV [%] |
| | 1.68 | 0.219 | 36.4 | 1.30 | 38.5 | 0.132 | 63.6 | 1.14 | 28.3 | 0.092 | 86.7 | 1.05 | 24.9 |
| (1) | 1.40 | 0.185 | 43.9 | 1.36 | 47.2 | 0.113 | 67.8 | 1.20 | 36.1 | 0.077 | 89.3 | 1.07 | 28.2 |
| | 1.12 | 0.150 | 46.5 | 1.40 | 58.7 | 0.093 | 74.4 | 1.23 | 38.6 | 0.063 | 93.9 | 1.08 | 32.9 |
| | 1.68 | 0.245 | 32.4 | 1.45 | 43.2 | 0.156 | 49.5 | 1.22 | 31.6 | 0.104 | 74.3 | 1.03 | 24.5 |
| (2) | 1.40 | 0.229 | 28.2 | 1.46 | 44.0 | 0.147 | 54.2 | 1.25 | 33.5 | 0.099 | 80.6 | 1.07 | 26.6 |
| | 1.12 | 0.191 | 33.9 | 1.48 | 45.1 | 0.119 | 62.9 | 1.26 | 38.5 | 0.081 | 87.5 | 1.05 | 29.8 |
| | 1.68 | 0.246 | 28.3 | 1.47 | 40.4 | 0.158 | 50.2 | 1.25 | 28.8 | 0.107 | 80.5 | 1.03 | 24.5 |
| (3) | 1.40 | 0.221 | 27.4 | 1.45 | 43.3 | 0.145 | 49.3 | 1.23 | 32.1 | 0.097 | 76.1 | 1.05 | 24.6 |
| | 1.12 | 0.200 | 29.5 | 1.47 | 43.3 | 0.126 | 58.5 | 1.28 | 35.9 | 0.082 | 84.1 | 1.02 | 28.9 |
| | 1.68 | 0.203 | 33.9 | 1.31 | 44.2 | 0.125 | 61.7 | 1.23 | 34.7 | 0.084 | 82.3 | 1.05 | 27.1 |
| (4) | 1.40 | 0.181 | 36.9 | 1.32 | 38.8 | 0.111 | 63.2 | 1.25 | 31.4 | 0.075 | 84.5 | 1.07 | 26.1 |
| | 1.12 | 0.159 | 51.2 | 1.37 | 59.2 | 0.095 | 72.8 | 1.27 | 43.7 | 0.064 | 90.1 | 1.05 | 34.9 |
| | 1.68 | 0.279 | 32.1 | 1.39 | 51.1 | 0.169 | 57.3 | 1.25 | 38.9 | 0.113 | 87.4 | 1.05 | 27.8 |
| (5) | 1.40 | 0.215 | 38.6 | 1.37 | 39.1 | 0.143 | 61.2 | 1.23 | 37.3 | 0.078 | 91.5 | 1.09 | 38.2 |
| | 1.12 | 0.117 | 75.3 | 1.37 | 50.9 | 0.102 | 55.8 | 1.19 | 36.7 | 0.057 | 94.2 | 1.06 | 46.2 |
| | 1.68 | 0.263 | 30.9 | 1.47 | 60.1 | 0.170 | 47.2 | 1.31 | 33.1 | 0.127 | 70.9 | 1.02 | 27.1 |
| (6) | 1.40 | 0.209 | 38.5 | 1.43 | 52.6 | 0.135 | 56.2 | 1.28 | 39.1 | 0.088 | 81.4 | 1.07 | 34.6 |
| | 1.12 | 0.155 | 39.3 | 1.41 | 63.9 | 0.105 | 55.9 | 1.27 | 53.5 | 0.070 | 91.5 | 1.06 | 50.5 |
| | 1.68 | 0.273 | 34.1 | 1.49 | 43.6 | 0.172 | 47.9 | 1.27 | 33.6 | 0.124 | 75.1 | 1.08 | 28.5 |
| (7) | 1.40 | 0.231 | 38.5 | 1.49 | 50.1 | 0.146 | 57.4 | 1.28 | 36.5 | 0.087 | 81.3 | 1.05 | 34.2 |
| | 1.12 | 0.156 | 48.0 | 1.44 | 62.2 | 0.099 | 67.6 | 1.31 | 47.7 | 0.068 | 94.3 | 1.05 | 43.0 |
| | 1.68 | 0.252 | 27.7 | 1.46 | 51.6 | 0.170 | 45.7 | 1.23 | 35.3 | 0.112 | 71.9 | 1.04 | 27.7 |
| (8) | 1.40 | 0.213 | 34.4 | 1.40 | 46.9 | 0.143 | 52.8 | 1.17 | 39.1 | 0.077 | 82.1 | 1.09 | 33.9 |
| | 1.12 | 0.154 | 69.4 | 1.39 | 48.1 | 0.102 | 62.1 | 1.22 | 46.4 | 0.060 | 93.5 | 1.08 | 48.5 |

[1] The sizes of *regions (a), (b) and (c)* are $45 \cdot d_p$, $15 \cdot d_p$, and $6 \cdot d_p$, respectively.

[2] $\langle\sqrt{\Theta_{2D}}(i,t)\rangle = \sum_{t=1}^{N_t}(\sum_{i=1}^{N_i}(\sqrt{\Theta_{2D}}(i,t)))$, $N_t$ is the number of investigation regions, $N_i$ is the number of time steps. Similarly, $\langle\frac{\sqrt{\Theta_y}}{\sqrt{\Theta_x}}(i,t)\rangle = \sum_{t=1}^{N_t}(\sum_{i=1}^{N_i}(\frac{\sqrt{\Theta_y}}{\sqrt{\Theta_x}}(i,t)))$.

[3] CV refers to the coefficient of variation of corresponding individual values of $\sqrt{\Theta_{2D}}(i,t)$ or $\frac{\sqrt{\Theta_y}}{\sqrt{\Theta_x}}(i,t)$ in each region and each time step.

Table A.4: Particle collision dynamics and impact velocities for different locations under different superficial gas velocities.

| Case Nr. | $U$ [m/s] | *Region (a)* $\langle f_c\rangle$ [1/s] | CV [%] | $\langle \epsilon_s\rangle$ [−] | CV [%] | $t_{p,fit}$ [s] | *Region (c)* $\langle\sqrt{\Theta_{2D}}\rangle_{fit}$ [m/s] | *Collision velocity (c)* $\langle|\boldsymbol{u_{r,c}}|\rangle$ [m/s] | CV [%] | $p_1$ | $p_2$ |
|---|---|---|---|---|---|---|---|---|---|---|---|
| (1) | 1.68 | 357.9 | 22.1 | 0.274 | 20.3 | 0.77 | 0.082 | 0.124 | 17.9 | | |
| | 1.40 | 386.1 | 19.0 | 0.289 | 19.2 | 0.93 | 0.070 | 0.111 | 13.0 | 0.687 | 0.060 |
| | 1.12 | 380.3 | 16.7 | 0.267 | 11.7 | 1.15 | 0.061 | 0.104 | 10.9 | | |
| (2) | 1.68 | 359.0 | 28.2 | 0.245 | 21.2 | 0.99 | 0.091 | 0.134 | 17.2 | | |
| | 1.40 | 390.1 | 23.6 | 0.252 | 18.0 | 1.63 | 0.089 | 0.126 | 14.1 | 0.606 | 0.067 |
| | 1.12 | 441.7 | 25.0 | 0.264 | 17.9 | 2.34 | 0.078 | 0.114 | 12.8 | | |
| (3) | 1.68 | 355.8 | 30.1 | 0.240 | 25.5 | 1.00 | 0.087 | 0.138 | 17.9 | | |
| | 1.40 | 396.2 | 24.3 | 0.257 | 25.9 | 1.53 | 0.083 | 0.128 | 14.2 | 0.718 | 0.059 |
| | 1.12 | 424.4 | 21.9 | 0.263 | 21.9 | 2.28 | 0.077 | 0.117 | 12.7 | | |
| (4) | 1.68 | 370.6 | 24.0 | 0.274 | 20.5 | 0.82 | 0.075 | 0.119 | 17.6 | | |
| | 1.40 | 392.1 | 24.3 | 0.267 | 21.7 | 0.89 | 0.069 | 0.117 | 14.5 | 0.686 | 0.063 |
| | 1.12 | 398.4 | 27.0 | 0.285 | 18.1 | 1.01 | 0.058 | 0.106 | 10.7 | | |
| (5) | 1.68 | 294.1 | 36.3 | 0.194 | 34.9 | 1.52 | 0.092 | 0.159 | 27.1 | | |
| | 1.40 | 245.4 | 38.4 | 0.167 | 43.9 | 2.31 | 0.074 | 0.147 | 32.4 | 1.030 | 0.056 |
| | 1.12 | 169.1 | 81.0 | 0.064 | 97.3 | 3.68 | 0.049 | 0.140 | 33.6 | | |
| (6) | 1.68 | 280.6 | 31.5 | 0.204 | 19.8 | 1.84 | 0.098 | 0.177 | 20.1 | | |
| | 1.40 | 263.7 | 40.2 | 0.187 | 38.9 | 2.59 | 0.076 | 0.159 | 21.4 | 1.015 | 0.059 |
| | 1.12 | 234.4 | 43.4 | 0.098 | 75.1 | 2.70 | 0.061 | 0.144 | 33.1 | | |
| (7) | 1.68 | 281.5 | 33.4 | 0.203 | 20.6 | 1.93 | 0.089 | 0.181 | 20.9 | | |
| | 1.40 | 262.3 | 40.4 | 0.179 | 31.6 | 2.43 | 0.079 | 0.165 | 23.1 | 1.082 | 0.053 |
| | 1.12 | 231.9 | 45.2 | 0.118 | 53.0 | 2.86 | 0.062 | 0.132 | 28.0 | | |
| (8) | 1.68 | 299.9 | 32.3 | 0.214 | 25.7 | 2.01 | 0.090 | 0.170 | 22.0 | | |
| | 1.40 | 247.1 | 32.9 | 0.178 | 42.1 | 2.97 | 0.070 | 0.149 | 23.9 | 1.087 | 0.051 |
| | 1.12 | 180.1 | 72.3 | 0.082 | 99.1 | 3.45 | 0.055 | 0.142 | 32.4 | | |

[1] The sizes of *regions (a) and (c)* are $45 \cdot d_p$ and $6 \cdot d_p$, respectively.

[2] $\langle f_c(i,t)\rangle = \sum\limits_{t=1}^{N_t}(\sum\limits_{i=1}^{N_i}(f_c(i,t)))$, $N_i$ is the number of investigation regions, $N_t$ is the number of time steps. Similarly, $\langle \epsilon_s(i,t)\rangle = \sum\limits_{t=1}^{N_t}(\sum\limits_{i=1}^{N_i}(\epsilon_s(i,t)))$. Differently, $\langle|\boldsymbol{u_{r,c}}|\rangle$ is averaged over the individual impact velocities of individual collision events.

[3] CV refers to the coefficient of variation of corresponding individual values of $f_c(i,t)$) and $\epsilon_s(i,t)$ in each region and each time step, or $|\boldsymbol{u_{r,c}}|$ of each collision event.

[4] All Fourier transformations used to fit period $t_{p,fit}$ with 3 items.

[5] Eq. (6.15) was used to fit average square root of 2D granular temperature $\langle\sqrt{\Theta_{2D}}\rangle_{fit}$.

[6] The relationship between $\langle\sqrt{\Theta_{2D}}\rangle$ and $\langle|\boldsymbol{u_{r,c}}|\rangle$ is fitted based on the linear function ($f(x) = p_1 x + p_2$).

# Appendix B

# Simulation data

## B.1    List of all simulations

The summary of all simulations in this thesis is given in Table B.1.

## B.2    Solving governing equations of fluid phase by PISO algorithm

The PISO algorithm consists of two steps, as shown in List B.1. The velocity is first predicted using the momentum predictor. Then, the pressure and the velocity are corrected until a predefined number of iterations is reached. Afterwards, the transport equations of the turbulence model are solved.

## B.3    Solutions of HSD models

The equation of motion describing the collision of two particles with the equivalent mass $m_{eq}$ can be written in the form

$$m_{eq}\ddot{\varepsilon} + f_{dis}(\varepsilon,\,\dot{\varepsilon}) + f_{cons}(\varepsilon) = 0. \tag{B.1}$$

Considering a collision between two particles ($\rho_p = 1420$ kg/m$^3$, $d_p = 0.36$ mm, $E = 10^6$ Pa, $\sigma = 0.3$, $e = 0.7$ and an impact velocity of 1 m/s), Figure B.1 shows change of the overlap and the possible artifact attractive force during an entire collision period. The impact velocity mentioned in this thesis is the relative velocity of two particles at the initial contact instant.

Table B.1: List of all simulations.

| Chapter | Case | $N_p$ [-] | $d_{32}$ [mm] | Main model | Main phenomena |
|---|---|---|---|---|---|
| Chapter 5 | MS-DEM | 3000 | 0.13 | HSD, multi-sphere | Coefficient of restitution |
|  | SQ-DEM | 3000 | 0.13 | HSD, superquadric |  |
| Chapter 6 | CFD-DEM ($3U_{mf}$) | ca. 180000 | 1.80 | HSD, Tang drag | Collision dynamics |
| Chapter 7 | CFD-DEM (Binary) | ca. 6200 | 2.15 | HSD, MBVK, PBVK | Mixing |
|  | CFD-DEM (Ternary) | ca. 5000 | 2.15 | HSD, MBVK, PBVK |  |
| Chapter 8 | CFD-DEM (Wurster) | ca. 32000 | 2.10 | HSD, Gidaspow, Solid-drop | Residence time |
| Chapter 9 | CFD-DEM-MC (Wurster) | ca. 50000 | 1.75 | HSD, MBVK, Cohesion | Coating uniformity |

Listing B.1: Predictor in PISO algorithm.

```
0  // Momentum predictor
   // Class particleCloud contains parameters from DEM
   // Define the equation for velocity (Eq. 3.21)
                   fvVectorMatrix UEqn
                   (
5                  fvm::ddt(voidfraction,U) - fvm::Sp(fvc::ddt(voidfraction)
                       ,U)
                   + fvm::div(phi,U) - fvm::Sp(fvc::div(phi),U)
                   + particleCloud.divVoidfractionTau(U, voidfraction)
                   ==
                   - fvm::Sp(Ksl/rho,U)
10                 + fvOptions(U)
                   );

                   UEqn.relax();
                   fvOptions.constrain(UEqn);
15 //Solve the momentum predictor
                   solve(UEqn == - voidfraction*fvc::grad(p) + Ksl/rho*Us);

                   fvOptions.correct(U);
```
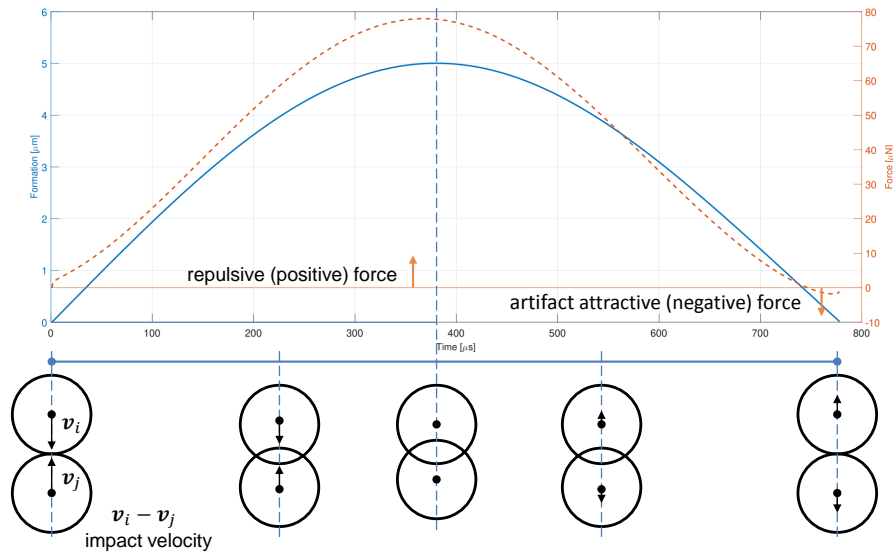


Figure B.1: Sketch of a collision event in DEM simulation by soft-sphere model.

## B.4   Typical values of various forces

The typical values of various forces (as discussed in Chapter 3) on individual particles with different sizes are listed in Table B.2 ($\rho_p = 1420$ kg/m$^3$, $E = 10^6$ Pa, $\sigma = 0.3$ and $e = 0.7$).

Table B.2: Typical drag force, contact force, capillary force, and viscous force of individual particles with different sizes.

| Normalized force | $d_p = 2$ mm | $d_p = 0.2$ mm |
|---|---|---|
| $f_d/(m_pg)$ $[-]$ | 0.015 | 0.015 |
| | $\|u - v\| = 0.5$ m/s, $\epsilon_s = 0.2$, air | |
| $f_{c,n}/(m_pg)$ $[-]$ | 0.67 | 12.01 |
| | $\varepsilon = 1$ $\mu$m, $v_{r,n} = 0.05$ m/s | |
| $f_{capillary}/(m_pg)$ $[-]$ | 3.69 | 159 |
| | $d_{inter} = 5$ $\mu$m, $d_d/d_p = 0.1$, 2 wt% HPMC | |
| $f_{vis,n}/(m_pg)$ $[-]$ | 6.47 | 64.7 |
| $f_{vis,t}/(m_pg)$ $[-]$ | 0.22 | 14.1 |
| | $d_{inter} = 5$ $\mu$m, $v_{r,n} = v_{r,t} = 0.05$ m/s, $d_d/d_p = 0.1$, 2 wt% HPMC | |

## B.5   Orthogonal grid of Wurster fluidized bed

The *blockMesh* utility was used to generate structured grids in the Wurster fluidized bed. According to Figure 4.5, the domain geometry was decomposed into several blocks with straight lines and arcs. The details of vertices, lines, blocks and patches are described in Listing B.2. The vertices arranged in inner, middle and outer regions correspond to the nozzle, internal annulus and external annulus in the Wurster coater. By this method, the final points, surfaces, hexahedra cells in the simulation domain are 84525, 249072 and 81600, respectively. The Wurster tube was inserted into the domain by the *createBaffles* utility, which makes the internal faces into boundary faces.

Listing B.2: O-grid of the Wurster fluidized bed by *blockMesh*.

```
0   FoamFile
    {
    version      2.3;
    format       ascii;
    class        dictionary;
5   object       blockMeshDict;
    }
    convertToMeters 1;
    // Geometry of the Wurster fluidized bed by 48 vertices in five layers;
    vertices
10  (
    // in the first layer
```

```
      ( 0.0028   0.0028 0.0)        // Vertex inner = 0
      (-0.0028   0.0028 0.0)        // Vertex inner = 1
      (-0.0028  -0.0028 0.0)        // Vertex inner = 2
15    ( 0.0028  -0.0028 0.0)        // Vertex inner = 3
      ( 0.0177   0.0177 0.0)        // Vertex middle = 4
      (-0.0177   0.0177 0.0)        // Vertex middle = 5
      (-0.0177  -0.0177 0.0)        // Vertex middle = 6
      ( 0.0177  -0.0177 0.0)        // Vertex middle = 7
20    ( 0.0424 0.0424 0.015)        // Vertex outer = 8
      (-0.0424 0.0424 0.015)        // Vertex outer = 9
      (-0.0424 -0.0424 0.015)       // Vertex outer = 10
      ( 0.0424 -0.0424 0.015)       // Vertex outer = 11
// in the second layer
25    ( 0.0028   0.0028 0.035)      // Vertex inner = 12
      (-0.0028   0.0028 0.035)      // Vertex inner = 13
      (-0.0028  -0.0028 0.035)      // Vertex inner = 14
      ( 0.0028  -0.0028 0.035)      // Vertex inner = 15
      ( 0.0177 0.0177 0.035)        // Vertex middle = 16
30    (-0.0177 0.0177 0.035)        // Vertex middle = 17
      (-0.0177 -0.0177 0.035)       // Vertex middle = 18
      ( 0.0177 -0.0177 0.035)       // Vertex middle = 19
      ( 0.0424 0.0424 0.035 )       // Vertex outer = 20
      (-0.0424 0.0424 0.035)        // Vertex outer = 21
35    (-0.0424 -0.0424 0.035)       // Vertex outer = 22
      ( 0.0424 -0.0424 0.035)       // Vertex outer = 23
// in the third layer
      ( 0.0028   0.0028 0.255)      // Vertex inner = 24
      (-0.0028   0.0028 0.255)      // Vertex inner = 25
40    (-0.0028  -0.0028 0.255)      // Vertex inner = 26
      ( 0.0028  -0.0028 0.255)      // Vertex inner = 27
      ( 0.0177 0.0177 0.255)        // Vertex middle = 28
      (-0.0177 0.0177 0.255)        // Vertex middle = 29
      (-0.0177 -0.0177 0.255)       // Vertex middle = 30
45    ( 0.0177 -0.0177 0.255)       // Vertex middle = 31
      ( 0.0884 0.0884 0.255)        // Vertex outer = 32
      (-0.0884 0.0884 0.255)        // Vertex outer = 33
      (-0.0884 -0.0884 0.255)       // Vertex outer = 34
      ( 0.0884 -0.0884 0.255)       // Vertex outer = 35
50 // in the fourth layer
      ( 0.0028   0.0028 0.34)       // Vertex inner = 36
      (-0.0028   0.0028 0.34)       // Vertex inner = 37
      (-0.0028  -0.0028 0.34)       // Vertex inner = 38
      ( 0.0028  -0.0028 0.34)       // Vertex inner = 39
55    ( 0.0177 0.0177 0.34)         // Vertex middle = 40
      (-0.0177 0.0177 0.34)         // Vertex middle = 41
      (-0.0177 -0.0177 0.34)        // Vertex middle = 42
      ( 0.0177 -0.0177 0.34)        // Vertex middle = 43
      ( 0.0884 0.0884 0.34)         // Vertex outer = 44
60    (-0.0884 0.0884 0.34)         // Vertex outer = 45
      (-0.0884 -0.0884 0.34)        // Vertex outer = 46
      ( 0.0884 -0.0884 0.34)        // Vertex outer = 47
);
// Build 3 blocks using 48 vertices
```

```
65  // Set the grid number and grid grading in each line
    blocks
    (
    // first block
        hex (2 3 0 1 14 15 12 13)    (12 12 7) simpleGrading (1 1 1)
70      hex (1 0 4 5 13 12 16 17)    (12 10 7) simpleGrading (1 1 1)
        hex (6 2 1 5 18 14 13 17)    (10 12 7) simpleGrading (1 1 1)
        hex (6 7 3 2 18 19 15 14)    (12 10 7) simpleGrading (1 1 1)
        hex (3 7 4 0 15 19 16 12)    (10 12 7) simpleGrading (1 1 1)
        hex (4 8 9 5 16 20 21 17)    (12 12 7) simpleGrading (1 1 1)
75      hex (10 6 5 9 22 18 17 21)   (12 12 7) simpleGrading (1 1 1)
        hex (10 11 7 6 22 23 19 18)  (12 12 7) simpleGrading (1 1 1)
        hex (7 11 8 4 19 23 20 16)   (12 12 7) simpleGrading (1 1 1)
    // second block
        hex (14 15 12 13 26 27 24 25) (12 12 44) simpleGrading (1 1 1)
80      hex (13 12 16 17 25 24 28 29) (12 10 44) simpleGrading (1 1 1)
        hex (18 14 13 17 30 26 25 29) (10 12 44) simpleGrading (1 1 1)
        hex (18 19 15 14 30 31 27 26) (12 10 44) simpleGrading (1 1 1)
        hex (15 19 16 12 27 31 28 24) (10 12 44) simpleGrading (1 1 1)
        hex (16 20 21 17 28 32 33 29) (12 12 44) simpleGrading (1 1 1)
85      hex (22 18 17 21 34 30 29 33) (12 12 44) simpleGrading (1 1 1)
        hex (22 23 19 18 34 35 31 30) (12 12 44) simpleGrading (1 1 1)
        hex (19 23 20 16 31 35 32 28) (12 12 44) simpleGrading (1 1 1)
    // third block
        hex (26 27 24 25 38 39 36 37) (12 12 17) simpleGrading (1 1 1)
90      hex (25 24 28 29 37 36 40 41) (12 10 17) simpleGrading (1 1 1)
        hex (30 26 25 29 42 38 37 41) (10 12 17) simpleGrading (1 1 1)
        hex (30 31 27 26 42 43 39 38) (12 10 17) simpleGrading (1 1 1)
        hex (27 31 28 24 39 43 40 36) (10 12 17) simpleGrading (1 1 1)
        hex (28 32 33 29 40 44 45 41) (12 12 17) simpleGrading (1 1 1)
95      hex (34 30 29 33 46 42 41 45) (12 12 17) simpleGrading (1 1 1)
        hex (34 35 31 30 46 47 43 42) (12 12 17) simpleGrading (1 1 1)
        hex (31 35 32 28 43 47 44 40) (12 12 17) simpleGrading (1 1 1)
    );
    // Create 32 quarter circles
100 edges
    (
        arc 5 6      (-0.025 0 0.0)
        arc 6 7      (0.0 -0.025 0.0)
        arc 7 4      (0.025 0.0 0.0)
105     arc 4 5      (0.0 0.025 0.0 )
        arc 17 18    (-0.025 0 0.035)
        arc 18 19    (0.0 -0.025 0.035)
        arc 19 16    (0.025 0.0 0.035)
        arc 16 17    (0.0 0.025 0.035 )
110     arc 28 29    (0.0 0.025 0.255)
        arc 29 30    (-0.025 0 0.255 )
        arc 30 31    (0.0 -0.025 0.255)
        arc 31 28    (0.025 0.0 0.255)
        arc 40 41    (0.0 0.025 0.34)
115     arc 41 42    (-0.025 0 0.34 )
        arc 42 43    (0.0 -0.025 0.34)
        arc 43 40    (0.025 0.0 0.34)
```

```
        arc 8 9      (0.0 0.06 0.015)
        arc 9 10     (-0.06 0 0.015)
        arc 10 11    (0.0 -0.06 0.015)
        arc 11 8     (0.06 0.0 0.015)
        arc 20 21    (0.0 0.06 0.035 )
        arc 21 22    (-0.06 0 0.035)
        arc 22 23    (0.0 -0.06 0.035)
        arc 23 20    (0.06 0.0 0.035)
        arc 32 33    (0.0 0.125 0.255)
        arc 33 34    (-0.125 0 0.255)
        arc 34 35    (0.0 -0.125 0.255)
        arc 35 32    (0.125 0.0 0.255)
        arc 44 45    (0.0 0.125 0.34)
        arc 45 46    (-0.125 0 0.34)
        arc 46 47    (0.0 -0.125 0.34)
        arc 47 44    (0.125 0.0 0.34)
);
// Generate patches for inlets, outlets and walls
patches
(
        patch inlet0
        (
        (0 1 2 3)
        )
        patch inlet1
        (
         (3 7 4 0)
         (0 4 5 1)
         (2 1 5 6)
         (3 2 6 7)
        )
        patch inlet2
        (
         (7 11 8 4)
         (4 8 9 5)
         (5 9 10 6)
         (7 6 10 11)
        )
        patch outlet
        (
         (36 37 38 39)
         (39 43 40 36)
         (36 40 41 37)
         (37 41 42 38)
         (38 42 43 39)
         (43 47 44 40)
         (40 44 45 41)
         (41 45 46 42)
         (42 46 47 43)
        )
        wall walls
        (
         (9 8 20 21)
```

```
        (9 21 22 10)
        (10 22 23 11)
        (11 23 20 8)
        (21 20 32 33)
        (21 33 34 22)
        (22 34 35 23)
        (23 35 32 20)
        (33 32 44 45)
        (33 45 46 34)
        (34 46 47 35)
        (35 47 44 32)
    )
);
mergePatchPairs
(
);
```

# Publication list

**Journal Papers**

1. **Z. Jiang**, T. Hagemeier, A. Bück, E. Tsotsas, *Experimental measurements of particle collision dynamics in a pseudo-2D gas-solid fluidized bed,* Chemical Engineering Science 167 (2017), 297-316. 10.1016/j.ces.2017.04.024

2. **Z. Jiang**, A. Bück, E. Tsotsas, *CFD-DEM study of residence time, droplet deposition, and collision velocity for a binary particle mixture in a Wurster fluidized bed coater,* Drying Technology, 36 (2018), 638-650. 10.1080/07373937.2017.1319852

3. **Z. Jiang**, T. Hagemeier, A. Bück, E. Tsotsas, *Color-PTV measurement and CFD-DEM simulation of the dynamics of poly-disperse particle systems in a pseudo-2D fluidized bed,* Chemical Engineering Science 179 (2018), 115-132. 10.1016/j.ces.2018.01.013

4. L. Zhang, F. Weigler, V. Idakiev, **Z. Jiang**, L. Mörl, J. Mellmann, E. Tsotsas, *Experimental study of the particle motion in flighted rotating drums by means of Magnetic Particle Tracking,* Powder Technology 339 (2018), 817–826. 10.1016/j.powtec.2018.08.057

5. **Z. Jiang**, J. Du, C. Rieck, A. Bück, E. Tsotsas, *PTV experiments and DEM simulations of the coefficient of restitution for irregular particles impacting on horizontal substrates*, Powder Technology 360 (2020), 352-365. 10.1016/j.powtec.2019.10.072

6. **Z. Jiang**, C. Rieck, A. Bück, E. Tsotsas, *Modeling of inter- and intra-particle coating uniformity in a Wurster fluidized bed by a coupled CFD-DEM-Monte Carlo approach*, Chemical Engineering Science 211 (2020), 115289. 10.1016/j.ces.2019.115289

7. L. Zhang, **Z. Jiang**, F. Weigler, F. Herz, J. Mellmann, E. Tsotsas, *PTV measurement and DEM simulation of the particle motion in a flighted rotating drum,* Powder Technology 363 (2020), 23–37. 10.1016/j.powtec.2019.12.035

**Conference Proceedings**

1. T. Hagemeier, **Z. Jiang**, A. Bück, E. Tsotsas, *Discrete analysis of particle collision behaviour in fluidized beds,* In: 7th International Granulation Workshop, Sheffield (UK), July, 2015

2. **Z. Jiang**, T. Hagemeier, Y. Yang, A. Bück, E. Tsotsas, *Particle dynamics and mixing behavior in a polydisperse gas-solid fluidized bed by color-PTV measurement,* In: PARTEC, Nürnberg (DE), April, 2016

3. T. Hagemeier, K. Zähringer, **Z. Jiang**, D. Thévenin, *Influence of wetting behavior on macroscopic film flow pattern,* In: 18th International Symposium on the Application of Laser and Imaging Techniques to Fluid Mechanics, Lisbon (PT), Paper 2.6.4, 1-17, 2016

4. **Z. Jiang**, T. Hagemeier, A. Bück, E. Tsotsas, *CFD-DEM study of residence time and collision velocity in a binary Wurster fluidized bed,* In: The 20th International Drying Symposium, Gifu (JP), August, 2016

5. **Z. Jiang**, C. Rieck, A. Bück, E. Tsotsas, *Estimation of coefficient of restitution of irregularly shaped particles on horizontal substrates,* In: 8th International Granulation Workshop, Sheffield (UK), June, 2017

6. **Z. Jiang**, C. Rieck, A. Bück, E. Tsotsas, *Modeling of particle behavior in a Wurster fluidized bed: Coupling CFD-DEM with Monte Carlo,* In: The 21th International Drying Symposium, Valencia (ES), September, 2018

7. L. Zhang, F. Weigler, **Z. Jiang**, V. Idakiev, J. Mellmann, E. Tsotsas, *Investigation of 3D particle flow in a flighted rotating drum,* In: The 21th International Drying Symposium, Valencia (ES), September, 2018

8. **Z. Jiang**, K. Chen, A. Bück, E. Tsotsas, *Novel algorithm for particle tracking velocimetry (PTV) of non-spherical particles,* In: 9th International Granulation Workshop, Lausanne (CH), June, 2019

**Oral and Poster Presentations**

1. T. Hagemeier, **Z. Jiang**, A. Bück, E. Tsotsas, *Discrete analysis of particle collision behaviour in fluidized beds,* In: 7th International Granulation Workshop, Sheffield (UK), July, 2015

2. **Z. Jiang**, A. Bück, E. Tsotsas, *CFD-DEM simulation of particle collision dynamics in a poly-disperse gas-solid fluidized bed,* In: Jahrestreffen der Fachgruppen Agglomerations- und Schüttguttechnik, Mehrphasenströmungen und Computational Fluid Dynamics, Bingen (DE), March, 2016

3. **Z. Jiang**, T. Hagemeier, Y. Yang, A. Bück, E. Tsotsas, *Particle dynamics and mixing behavior in a polydisperse gas-solid fluidized bed by color-PTV measurement,* In: PARTEC, Nürnberg (DE), April, 2016

4. **Z. Jiang**, T. Hagemeier, A. Bück, E. Tsotsas, *Discrete analysis of particle collision behavior in a pseudo-2D fluidized bed,* In: PARTEC, Nürnberg (DE), April, 2016 (Poster)

5. T. Hagemeier, K. Zähringer, **Z. Jiang**, D. Thévenin, *Influence of wetting behavior on macroscopic film flow pattern,* In: 18th International Symposium on the Application of Laser and Imaging Techniques to Fluid Mechanics, Lisbon (PT), July 4-7, 2016

6. **Z. Jiang**, T. Hagemeier, A. Bück, E. Tsotsas, *CFD-DEM study of residence time and collision velocity in a binary Wurster fluidized bed,* In: The 20th International Drying Symposium, Gifu (JP), August, 2016

7. **Z. Jiang**, C. Rieck, A. Bück, E. Tsotsas, *Measurements of the coefficient of restitution of Group A particles on different horizontal substrates,* In: Jahrestreffen der Fachgruppen Agglomerations- und Schüttguttechnik, Grenzflächenbestimmte Systeme und Prozesse, Trocknungstechnik, Lebensmittelverfahrenstechnik und Wärme- und Stoffübertragung, Bruchsal (DE), February, 2017 (Poster)

8. **Z. Jiang**, C. Rieck, A. Bück, E. Tsotsas, *Estimation of coefficient of restitution of irregularly shaped particles on horizontal substrates,* In: 8th International Granulation Workshop, Sheffield (UK), June, 2017

9. **Z. Jiang**, A. Bück, E. Tsotsas, *Investigation of residence time and collision velocity in a Wurster fluidized bed using CFD-DEM simulations ,* In: 5th International Conference on Particle-based Methods, Fundamentals and Applications, Hannover (DE), September, 2017

10. **Z. Jiang**, A. Bück, E. Tsotsas, *Influence of wetting conditions on residence time distributions in a Wurster coater: A CFD-DEM study,* In: Jahrestreffen der der ProcessNet-Fachgruppen MPH, WSUE, CFD, HTT, AuW, KRI, PMT, Bremen (DE), March, 2018 (Poster)

11. **Z. Jiang**, A. Bück, E. Tsotsas, *Verification of PTV methodology for evaluating particle-particle interactions by CFD-DEM data,* In: Jahrestreffen der der ProcessNet-Fachgruppen MPH, WSUE, CFD, HTT, AuW, KRI, PMT, Bremen (DE), March, 2018 (Poster)

12. **Z. Jiang**, C. Rieck, A. Bück, E. Tsotsas, *Modeling of particle behavior in a Wurster fluidized bed: Coupling CFD-DEM with Monte Carlo,* In: The 21th International Drying Symposium, Valencia (ES), September, 2018 (Poster)

13. **Z. Jiang**, A. Bück, E. Tsotsas, *Modeling of coating in a Wurster fluidized bed by a coupled CFD-DEM-Monte Carlo approach,* In: PARTEC, Nürnberg (DE), April, 2019 (Poster)

14. **Z. Jiang**, J.S.G. Bonilla A. Bück, E. Tsotsas, *The motion of non-spherical particles in a pseudo-2D fluidized bed: PTV measurement and CFD-DEM simulation,* In: Jahrestreffen Reaktionstechnik 2019 gemeinsam mit der Fachgruppe Mehrphasenströmungen, Würzburg (DE), May, 2019 (Poster)

15. **Z. Jiang**, K. Chen, A. Bück, E. Tsotsas, *Novel algorithm for particle tracking velocimetry (PTV) of non-spherical particles,* In: 9th International Granulation Workshop, Lausanne (CH), June, 2019 (Poster)

# Student theses

1. A.K. Singh, Influence of drag models on CFD-DEM simulations of a poly-disperse fluidized bed, Master thesis, Otto von Guericke University Magdeburg, Germany, 2017

2. D. Li, DEM investigation of the dynamics of singlet-doublet collisions during agglomeration, Master thesis, FAU Erlangen-Nuremberg, Germany, 2019

3. K. Lou, Influence of thermal conduction models on particle temperature in rotating drums by thermal DEM, Bachelor thesis, FAU Erlangen-Nuremberg, Germany, 2019